Multi-scale quantitative sedimentology of Upper Pleistocene coastal dunes from the Northern Bahamas and Western Australia

Vimpere, Lucas

How to cite

VIMPERE, Lucas. Multi-scale quantitative sedimentology of Upper Pleistocene coastal dunes from the Northern Bahamas and Western Australia. Doctoral Thesis, 2021. doi: 10.13097/archive-ouverte/unige:157371

This publication URL: https://archive-ouverte.unige.ch/unige:157371
Publication DOI: 10.13097/archive-ouverte/unige:157371

UNIVERSITE DE GENEVE

FACULTE DES SCIENCES

Section des Sciences de la Terre et de l'Environnement

Professeur Sébastien Castelltort, Directeur
Professeur Pascal Kindler, Co-directeur

Département des Sciences de la Terre

Multi-scale quantitative sedimentology of Upper Pleistocene coastal dunes from the Northern Bahamas and Western Australia

THESE

présentée à la Faculté des Sciences de l'Université de Genève pour obtenir le grade de
Docteur ès Sciences, mention Sciences de la Terre

par

Lucas Vimpere
de
Genève (Suisse)

Thèse N° 5615

FRANCE
2021

UNIVERSITÉ
DE GENÈVE
FACULTÉ DES SCIENCES

DOCTORAT ÈS SCIENCES, MENTION SCIENCES DE LA TERRE

Thèse de Monsieur Lucas VIMPERE

intitulée :

«Multi-Scale Quantitative Sedimentology Of Upper Pleistocene Coastal Dunes From The Northern Bahamas And Western Australia»

La Faculté des sciences, sur le préavis de Monsieur S. CASTELLTORT, professeur associé et directeur de thèse (Département des sciences de la Terre), Monsieur P. KINDLER, professeur ordinaire et codirecteur de thèse (Département des sciences de la Terre), Monsieur A. STRASSER, professeur (Department of Geosciences, University of Fribourg, Fribourg), Monsieur P. HESP, professeur (College of Science and Engineering, Flinders University Earth Sciences, Adelaide, South Australia), autorise l'impression de la présente thèse, sans exprimer d'opinion sur les propositions qui y sont énoncées.

Genève, le 17 novembre 2021

Thèse - 5615 -

Le Doyen

N.B. - La thèse doit porter la déclaration précédente et remplir les conditions énumérées dans les "Informations relatives aux thèses de doctorat à l'Université de Genève".

Abstract

In the age of global climate change and the ensuing growing concern about future implications for the planet, scientists are working in a joint effort to better understand Earth systems. Coastal dunes present numerous benefits for the 40% of the global population living in coastal areas and for their ecosystems but also represent a potential desertification threat if reactivated. The understanding of the triggering factors for dune instability is thus capital to better predict their future behaviour and adapt coastal management programs. The project of this thesis originates in the controversy around some coastal “chevrons” described in the Bahamas. These U-shape landforms date from the Last Interglacial, stage of the Quaternary that was characterised by a higher than present global average temperature (+ 1-2 °C) and a higher sea level (+ 6-9 m.a.s.l.). The discussion on their genesis opposes a dramatic interpretation of these “chevrons”, linked with superstorms related to warmer and unstable climate conditions, to a more classic one suggesting drier and windier conditions in the Caribbean allowing the dunes formation.

Considering the lack of clarity around the definition and the use of the term “chevron”, I first reviewed the literature mentioning them. The term “chevrons” has been used independently to describe coastal parabolic dunes in the Bahamas, Madagascar, and Western Australia where they have been correlated to wind, giant storms, and tsunamis caused by asteroid impacts. In each of these countries, a debate arose among geoscientists on the depositional processes and the validity of the terminology. This review provides with a complete and comprehensive summary of the problematic and demonstrates than “chevrons” are coastal parabolic dunes of aeolian origin.

I then further investigated the connection between the coastal parabolic dunes in the Bahamas and the particular climate conditions prevailing in the region during the Last Interglacial. First, the study of the morphology and sedimentary structures coupled with the grain size analysis of the dunes confirmed the conclusions reached in the review. The stratigraphic study then correlated the deposition of the dunes with the southward displacements of the Intertropical Convergence Zone, which lead to a deterioration of the vegetation cover under a drier and windier climate. Dunes formed during a short sea level drop during the highstand of the Last Interglacial and the ensuing regression when these conditions prevailed, following periods of significant carbonate production on the platforms.

The link between coastal aeolianites, climate conditions, and sea level variations was again investigated in Western Australia where the carbonate platform geometry is different. The formation of transverse aeolianites along the western coast of the Shark Bay region was correlated to a drier and windier climate caused by northward displacement of the Intertropical Convergence Zone, and more generally by a northward shift of the atmospheric cells. These changes in atmospheric circulation and the associated variations in ocean circulation were correlated to glacial periods whilst aeolianite-capping paleosols were correlated to interglacials stages.

Following the conclusions reached on coastal aeolianites and the climate under which they form relative to the geometry of the platform, I extended the investigation to continental parabolic dunes. Their activity during the pre-industrial and the mid. Holocene was investigated because climate conditions are well constrained for these periods. The Intertropical Convergence Zone moved north during the mid. Holocene, which resulted in the aridification of the presently-humid areas and the reactivation of continental parabolic dunes in these regions. Inversely the presently-dry regions were wetter, and dunes stabilised by vegetation. The link between dune activity, atmospheric circulation, and the related climate provides valuable information to constrain potential future climate change and define the regions the most at risk for desertification through parabolic dunes migration.

All together, these results highlight the causal relationship between parabolic dunes or coastal aeolianites and global atmospheric circulation. Further efforts should be directed towards a better understanding of the general trends of aeolian dunes activity related to climate. This would serve both future climate predictions and palaeoclimate interpretations, two important areas that are intricately intertwined.

Résumé

A l’heure du changement climatique et de l'inquiétude croissante qui entourent ses implications futures pour la planète, les scientifiques s’associent dans un effort commun pour une meilleure compréhension du système Terre. Les dunes côtières présentent de nombreux avantages pour les 40 % de la population mondiale qui vivent dans les zones côtières et pour leurs écosystèmes, mais représentent également une menace potentielle de désertification si elles viennent à être réactivées. La compréhension des facteurs déclencheurs de l'instabilité des dunes est donc capitale pour mieux prévoir leur comportement futur et adapter les programmes de gestion du littoral. Le projet de cette thèse trouve son origine dans la polémique autour de certains « chevrons » côtiers décrits aux Bahamas. Ces reliefs en forme de U datent du dernier interglaciaire, période du Quaternaire caractérisée par une température moyenne mondiale supérieure à celle actuelle (+ 1-2 °C) et par un niveau marin plus élevé (+ 6-9 m.). La discussion sur leur genèse oppose une interprétation dramatique de ces « chevrons », associés à des super-tempêtes générées par des conditions climatiques plus chaudes et plus instables, à une interprétation plus classique suggérant des conditions plus arides et venteuses dans les Caraïbes qui permettent la formation des dunes.

Considérant le manque de clarté quant à la définition et l'utilisation du terme « chevron », j'ai d'abord passé en revue la littérature qui les mentionne. Le terme « chevrons » a été utilisé indépendamment pour décrire les dunes paraboliques côtières des Bahamas, de Madagascar, et d'Australie-Occidentale, où elles ont été corrélées au vent, a des tempêtes géantes, et a des tsunamis causés par les impacts d'astéroïdes. Dans chacun de ces pays, un débat a surgi au sein de la communauté des géosciences quant aux processus de dépôt et à la validité de la terminologie. Cette revue fournit un résumé complet et exhaustif de la problématique et démontre que les « chevrons » sont des dunes paraboliques côtières d'origine éolienne.

J'ai ensuite étudié plus en détail le lien entre les dunes paraboliques côtières aux Bahamas et les conditions climatiques particulières qui prévalaient dans la région pendant le dernier interglaciaire. Dans un premier temps, l'étude de la morphologie et des structures sédimentaires couplée à l'analyse granulométrique des dunes ont confirmé les conclusions de la revue. L'étude stratigraphique a ensuite corrélé le dépôt des dunes avec les déplacements vers le sud de la Zone de Convergence Intertropicale, qui conduisent à une détérioration du couvert végétal causé par un climat plus sec et venteux. Les dunes se sont formées lors d'une brève régression survenant

dans la phase de haut niveau marin (*highstand*) du dernier interglaciaire, et durant la régression qui a suivi lorsque ces conditions ont prévalu, à la suite de périodes importantes de production de carbonate sur les plates-formes

Le lien entre les éolianites côtières, les conditions climatiques, et les variations du niveau marin a de nouveau été étudié en Australie occidentale, où la géométrie de la plate-forme carbonatée est différente. La formation d'éolianites transversales le long de la côte ouest de la région de Shark Bay a été corrélée à un climat plus sec et venteux causé par le déplacement vers le nord de la Zone de Convergence Intertropicale, et plus généralement par un déplacement vers le nord des cellules atmosphériques. Ces changements dans la circulation atmosphérique et les variations associées de la circulation océanique ont été corrélés aux périodes glaciaires, tandis que les paléosols recouvrant les éolianites ont été corrélés aux stades interglaciaires.

Faisant suites aux conclusions tirées sur les éolianites côtières et le climat dans lequel elles se forment dépendamment de la géométrie de la plate-forme, j'ai élargi l'investigation aux dunes paraboliques continentales. Leur activité pendant les périodes préindustrielle et de l'Holocène moyen a été étudiée car les conditions climatiques sont bien contraintes pour ces périodes. La Zone de Convergence Intertropicale s'est déplacée vers le nord durant l'Holocène moyen et a entraîné l'aridification des zones actuellement humides ainsi que la réactivation des dunes paraboliques continentales dans ces régions. A l'inverse, les régions actuellement sèches étaient plus humides, et les dunes stabilisées par la végétation. Le lien entre l'activité des dunes, la circulation atmosphérique, et le climat associé fournit des informations précieuses pour contraindre de potentiels futurs changements climatiques et définir les régions les plus à risque de désertification au travers la migration parabolique des dunes.

Tous ensemble, ces résultats mettent en évidence la relation de causalité entre dunes paraboliques ou éolianites côtières et la circulation atmosphérique globale. Des efforts supplémentaires devraient être dirigés vers une meilleure compréhension globale des tendances globales de l'activité des dunes éoliennes liées au climat. Cela servirait à la fois aux prévisions climatiques futures et aux interprétations paléoclimatiques, deux domaines importants qui sont étroitement liés.

Remerciements – Acknowledgements

Cette thèse, comme tout travail scientifique, est le résultat de quatre années de collaborations, d’amitiés, de discussions, et d’aventures vécues aux côtés de nombreuses personnes dont la contribution, tant humaine que scientifique, a participé à l’achèvement de ce projet.

Avant tout, j’aimerais remercier Pascal Kindler pour m’avoir accompagné tout au long de ces années. Je le remercie d’avoir eu le courage de m’accorder sa confiance lorsque j’ai fait irruption dans son bureau avec en main une idée pour un projet de master. Merci également de m’avoir offert l’opportunité de définir mon sujet de thèse en m’offrant ce doctorat. En espérant que l’amitié qui est née de ces nombreuses années de collaboration perdure.

Bien entendu, tout ceci n’aurait jamais été rendu possible sans Sébastien Castelltort qui, à la demande de Pascal Kindler, a accepté de me prendre comme son étudiant. Je le remercie pour l’accompagnement et le soutien indéfectible dont il a fait preuve tout au long de ces quatre ans tout en maintenant sa motivation qui s’est avérée contagieuse. Enfin, merci pour ce retour aux sources et aux expressions du terroir à l’accent chantant lors de nos séances café.

Une pensée particulièrement chaleureuse à mon grand-père Beghachem n Ayyur, à qui j’ai fait une promesse il y a très longtemps.

Un immense merci à ma compagne Ester pour son soutien, sa patience, et son affection dont j’ai bénéficié tout au long de ces années, et merci de m’avoir donné une fille magnifique. À vous deux, je vous dédie ce travail de thèse dont vous êtes une composante majeure.

Je tiens également à remercier ma famille, en particulier ma sœur Léa, pour tout ce qu’ils m’ont transmis, pour avoir été à mes côtés sans jamais baisser les bras, et pour avoir toujours cru en moi. A tous ceux-là, cette thèse est aussi votre réussite.

La liste de personnes du département auxquelles je tiens à faire part de mon affection est bien trop longue pour pouvoir les citer tous. Merci aux secrétaires, merci aux techniciens, merci aux professeurs, merci à mes collègues et amis, merci à toutes ces personnes qui m’ont vu grandir et qui ont partagé un bout de chemin avec moi. Les mots manquent pour leur exprimer toute ma gratitude.

Contents

List of Figures

List of Tables

Chapter 1 – Introduction

1 Aeolian sediments

1.1 Importance

The last decades have seen a major growth of interest in aeolian sediments and processes with a joint effort to understand the mechanisms leading to transport and deposition of sediment by wind (e.g., Anderson and Walker, 2006; Frank and Kocurek, 1996; Hansen et al., 2009; Smyth et al., 2014; Sweet and Kocurek, 1990; Tsoar, 1983; Walker, 1999; Walker and Nickling, 2002). Aeolian deposits are important components of the sedimentary record because they form large deposits that can be found in most climates of the world. These deposits fall into three main categories (Figure 1): sand sheets, loess blankets, and sand dunes, which are the focus of this thesis.

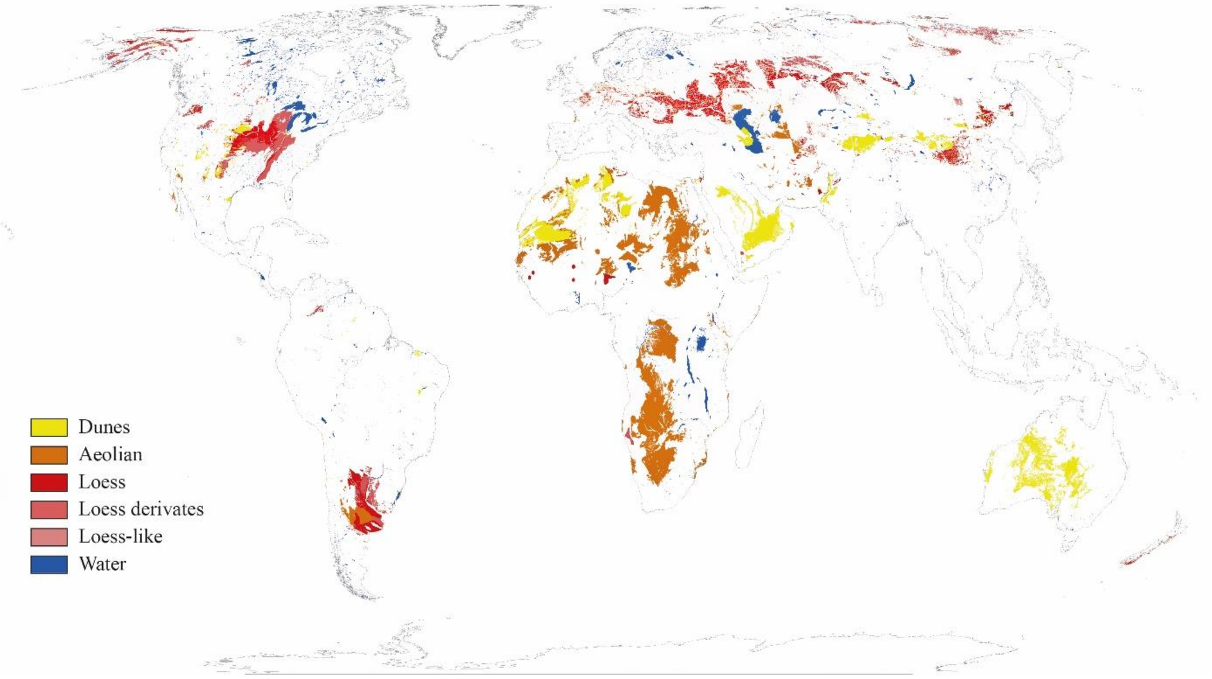

Figure 1: Global distribution of aeolian sediments (modified after Börker et al., 2018).

Several factors have contributed to the increased level of interest such as the use of present aeolian deposits and environments as potential analogues for ancient aeolian reservoirs or as a proxy for regional climate and global atmospheric changes during the Quaternary and sometimes earlier times (see Pye, 1993 and references herein). The dominance of aeolian deposits on other planets such as Mars has also favoured the development of the understanding of aeolian processes (e.g., Banham et al., 2018; Day and Catling, 2020; Vaz and Silvestro, 2014; Williams et al., 2020). More recently, the growing need for improved methods of desertification and sand control, especially in view with the forecasted consequences of global climate change, has led geoscientists to further investigate the relationship between sand transport/dune migration with climate conditions, ecosystems and anthropogenic disturbances (Vimpere et al., 2021 and references herein). Indeed, whilst sand dunes, mobile and immobile, are found at all latitudes and climates ranging from boreal to humid to arid and semiarid, most of them lie in deserts (Tsoar, 2001). Finally, coastal dune systems have been recognised as an important conservation resource offering a natural protection against sea level rise and other hazards, generating income through recreational activities, and offering a natural shelter to many endemic species.

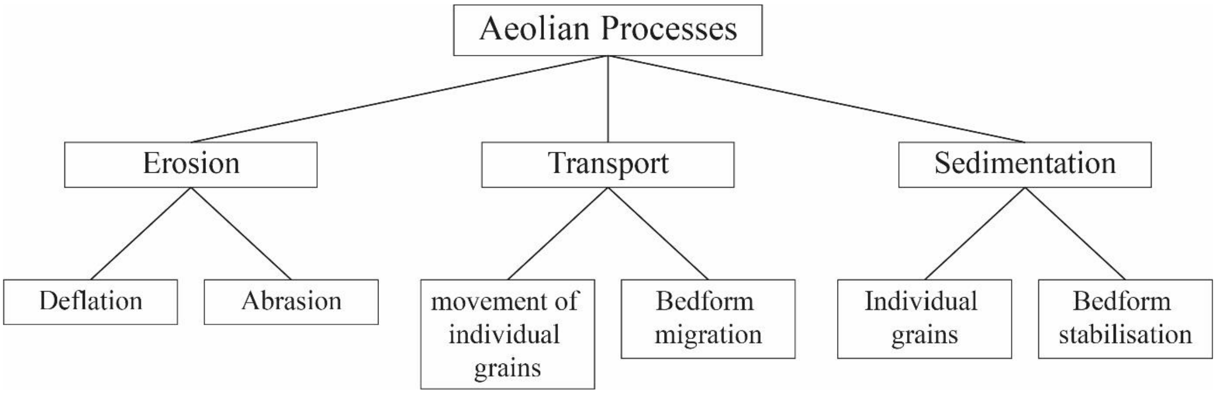

Figure 2: The nature of aeolian processes (Pye and Tsoar, 2008).

1.2 Aeolian transport

The wind effect on loose sediment is declined into three main aeolian processes which are responsible for erosion, transport, and sedimentation (Figure 2). Erosion requires more wind power than transport, which is initiated when wind blows above a certain threshold velocity. Early models for sand transport were developed during the 19th century but have been highly improved during the 20th century (e.g., Bagnold, 1941, 1936). These models estimated this *impact threshold shear velocity* of wind to be at 12 knots under dry conditions. Developed by Fryberger and Dean (1979), the presently accepted method of quantifying wind power is based on this threshold value and refers to the *drift potential* of the wind, that is its capacity to transport sand (Kilibarda and Kilibarda, 2016; Mesbahzadeh and Ahmadi, 2012; Saqqa and Saqqa, 2007; see Chapter 2). By using wind vectors (i.e., direction and speed), the Fryberger method allows to characterise wind regime properties such as the variability of the wind direction and its capacity to transport sand in the main blowing direction.

The common diameter of grains composing sand dunes ranges from 0.062 to 2.0 mm because they are not cohesive (Tsoar, 2001), contrary to finer grains such as silt and clay (< 0.050 mm) for which more energy is required to initiate transport. Different types of dunes show distinct grain size composition (Pye and Tsoar, 2008) as different mechanisms are responsible for their formation. Grain size and wind velocity define the two main different modes of particle transport referred to as *suspension load* and *bed load*. Suspension load occurs when particles are lifted from the surface and are transported over long distances by the flow without regaining contact with the bed, which usually ensues sediment being exposed to a turbulent airflow. Finer grains are transported through suspension load and ultimately deposit as loess deposits whereas most of the grains forming dunes are transported through bed load. The latter consists of *surface traction*, in which grains roll along the surface of the sediment, and *saltation*, in which grains proceed forward through a series of jump and rebound. This mode of transport lead to particles being transported along the stoss slope and over the brink of the dune to finally deposit on its slipface (Figure 3) in a process called *grainfall*, which forms grainfall lamination (i.e., foresets). Grainfall lamination alternates with sandflow cross-stratification, which forms when the angle of repose (~ 30°) is reached and sand avalanches on the dune slipface. This process of grain transport is often referred to as *grain flow*.

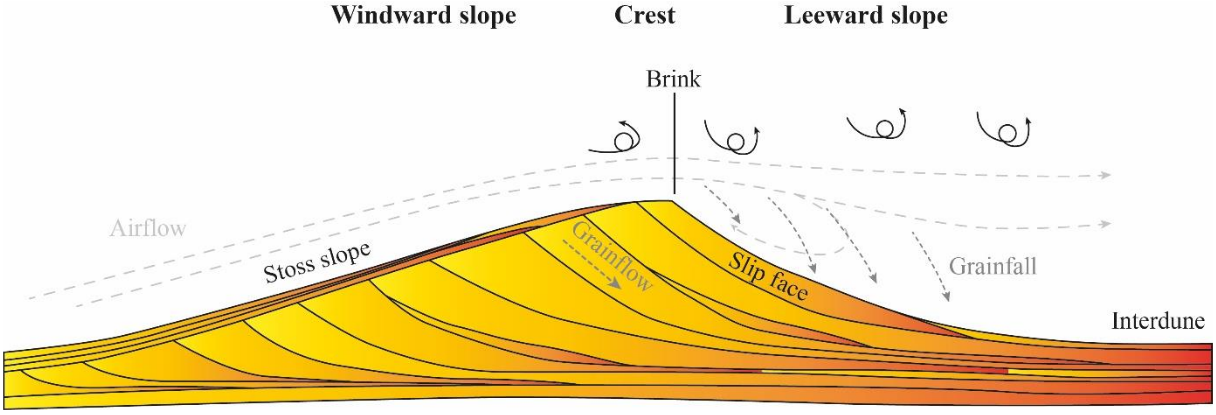

Figure 3: Typical elements of aeolian systems (modified after Ringrose and Bentley, 2015).

2 Coastal aeolianites

Fossilised aeolianites have long been observed such as the ones on the island of St Helena examined in 1836 by Charles Darwin whom already interpreted them as products of coastal dune formation during a period of lower sea level (Brooke, 2001; Darwin, 1851). The term "eolianite" was first introduced by Sayles (1931) to describe any lithified deposit of aeolian origin in Bermuda. This term does not refer to the composition of these deposits whereas another twenty denominations were used in different locations to described fossilised carbonate dunes deposited by the wind (see Table 1 in Le Guern, 2004). The commonly accepted definition for aeolianites is the one from Brooke (2001) that designates wind-driven subaerial accumulations on coasts of carbonate-dominated sediment consolidated by a carbonate cement.

Although most of aeolianites are located on coastlines (Figure 4), some have been observed hundreds of kilometres inland in the Thar Desert (Glennie, 1970; Goudie and Sperling, 1977) so that this definition might be at times slightly restrictive.

2.1 Importance

Coastal aeolianites are omnipresent between 20° and 40° in both hemispheres (Figure 4), where warm climatic conditions favour carbonate production whilst trade winds mobilise beach sediment and transport it into dunes. They constitute valuable latitudinal and climatic markers for palaeogeographic reconstitutions for periods preceding the Quaternary. They form large deposits that can reach dozens of metres in height and dozens of kilometres in length (e.g., Bahamas and Shark Bay in Western Australia). Generally, they develop as elongated transverse ridges that are parallel to the shore, with oblique, parabolic, and barchanoid being the most common morphologies (Brooke, 2001). Due to their composition, they tend to be rapidly immobilised by early cementation and pedogenic calcrete development. Aeolianites may constitute significant hydrodynamic barriers, thus limiting coastal erosion and potentially protecting littorals from sea level rise. From an economic point of view, aeolianites are extensive reservoirs showing a high primary and secondary porosity with no clay discontinuities within. Recognising these deposits in periods older than the Quaternary (Le Guern, 2004) would greatly improve the subsurface modelling and prediction for aquifers or oil and gas exploitation.

2.2 Timing of deposition

The majority of the coastal aeolianite record was constrained to icehouse periods with a significant occurrence during the Late Tertiary and the Quaternary (Abegg et al., 2001; Brooke, 2001; Dodd et al., 2001; Johnson, 1968; McKee and Ward, 1983; Smith et al., 2001) until contradictory studies mentioned and described aeolianites from greenhouse periods (Kilibarda and Loope, 1997; Kindler and Davaud, 2001). Contrary to greenhouse periods, icehouse periods present large glacio-eustatic fluctuations so that aeolianites formation and deposition were correlated to high amplitude sea level variations. Dating techniques (e.g., AAR, U-Th, TL, OSL) have been applied either directly to aeolian sediment, or on speleothems, or on palaeosol capping aeolianites to constrain the timing of dune formation relative to sea level fluctuations occurring during interglacial and glacial periods. In many places (e.g., Bahamas, Bermuda, South Australia), aeolianite formation has been linked with highstand periods (see references in Brooke, 2001). There are several reports of carbonate dunes deposited during both interglacial/glacial cycles, or glacial only (Engelmann et al., 2001; Frechen et al., 2001; Fumanal, 1995; Playford et al., 2013; Porat and Wintle, 1995; Price et al., 2001; Zhou et al., 1994), notably in Southern Victoria and Western Australia. A comprehensive review of these studies concluded that carbonate platform geometries have an influence on the relative sea level variation, and thus carbonate production and mobilisation (e.g., Le Guern, 2004).

Figure 4: Global distribution of Quaternary (black dots) and pre-Quaternary (red dots) aeolianites (modified after Brooke, 2001 and Le Guern, 2004).

In a context of a ramp (e.g., Arabian Gulf, Western Australia), the whole carbonate production system is shifted towards a lower position during a lowstand phase, subaerially exposing a large surface of the ramp for the wind to remobilise sand into coastal aeolianites. This is particularly true in regions where glacial periods are dry and windy (see Chapter 4 on Western Australia). Highstands during interglacials correspond to phases of significant carbonate production when the system shifts inland but sediment availability for transport can be restricted by a wet climate associated with a development of the vegetation cover.

The depositional model for steep-rimmed platforms, such as the one developed in the Bermuda and the Bahamas (e.g., Carew and Mylroie, 2001, 1995; Hearty and Kindler, 1993), considers that aeolianites can form during all phases of the eustatic cycle expect for the lowstand. When sea level drops, the shallow waters where carbonate precipitate cover a much-reduced surface of the platform slopes. This translates into a platform top being exposed to meteoric waters inducing karst and palaeosol formation. It is then considered that coastal dunes form during the late stage of marine transgression, highstand, and early stage of regression when carbonate production takes place and the platform top is somewhat exposed to winds reworking sediment into aeolianites.

3 Parabolic dunes

Aeolian sediments constitute a substantial part of the sedimentary accumulation on Earth, especially in continental and coastal environments. Parabolic dunes constitute an important sub-class of these aeolian deposits and develop over a wide range of climatic gradients. They are defined by two trailing arms that point upwind and that enclose a deflation basin, which is terminated by a nose being the depositional lobe that points downwind (**Error! Reference source not found.**). The airflow is channelled within the arms, resulting in an increase in shear stress and thus in sediment transport above the deflation basin. Then, the airflow reaches the stoss slope of the depositional lobe where it gets compressed and accelerated. When it passes over the crest of the nose, the flow expands and slow down, thus losing its transport capacity. The deceleration causes grainfall deposition on the lee slope of the nose, forming grainfall lamination. When the angle of repose is reached, grainflow and sandflow occur, cutting through older stratification. Contrary to other types of highly mobile dunes (e.g., barkhans), parabolic ones often form localised dune fields arranged in belts along coastlines, inland rivers and lakes shores.

They show a great diversity of morphologies that depend on wind regime, sediment supply and availability, and local vegetation characteristics. Several attempts have been made to establish a classification that would be applicable everywhere in the world. Mckee (1979) recognised three main classes of dunes: the simple, the compound, and the complex ones. Simple dunes are defined as single and isolated forms, later subclassified in lunates, hemicyclic, lobate and elongated by Pye (1993) based on their length/width ratio. The elongated parabolic dunes are the largest and can reach lengths of several kilometres. They are usually referred as hairpin or U- to V-shaped dunes, characterised by long-walled arms and a prominent high nose, and form under strong, unidirectional winds. Compound dunes consist of merged and/or superimposed smaller dunes that may occur in clusters. Their planform geometries go from simple superimposed forms to rarer and more complex en-echelon or digitate ones. They usually develop under wind regimes that present a greater directional variability, or where a dense and resistant vegetation cover like woodlands has developed. The trees force the airflow to separate in divergent directions, resulting in digitate parabolic dunes for instance. Finally, complex dunes are composed by two or more different types of dunes. As a rule of thumb, reduced sediment supply will likely lead to the formation of rather low-lying, unfilled parabolic dunes with narrow heads. On the contrary, elevated, long-walled parabolic dunes with large noses and partially-infilled deflation basins develop in areas of great sediment supply. The rate at which the depositional lobe is colonised by vegetation also seems to influence the shape of the dunes. Large, U-shaped noses are rapidly revegetated whereas narrow, V-shaped ones tend to be gradually fixated (Hesp, 2011). Long-term variations in wind directions may lead to a left- or right-handed asymmetry in dune morphology through time. Short-term changes such as seasonal directionality generally result in smaller and broader shapes with short trailing arms (e.g., hemicyclic). Some of these smaller dunes may be closed upwind by a back ridge, such as the ones in the Canadian prairies of Saskatchewan.

Parabolic dunes build up in both coastal and inland environments as soon as there is a sufficient wind power, sand supply, and sand availability defined by a moderate vegetation cover. The currently known distribution of parabolic dunes is highly influenced by the number of studies focusing on them. Therefore, it seems that these landforms preferentially form in the northern hemisphere. This bias may be induced by the higher proportion of continental mass being located in the northern hemisphere, or because most of the studies on parabolic dunes have been conducted in these regions. Based on the literature, parabolic dunes preferably develop along coastlines of sub-humid to humid zones, where they are usually found adjacent to river mouths or estuaries, and in conjunction with foredunes. It is believed a great proportion evolve from blowouts initiating in such foredunes, as simulated by the Extended Discrete Eco-geomorphic Aeolian Landscape (DECAL) model. Blowout formation usually starts when unidirectional onshore winds breach the vegetation cover. Because of the high transport potential and the relative abondance of sediments, most of the largest (i.e., elongated) parabolic dunes are located in such costal environments. Some perennial or ephemeral lakes can sometimes flood the deflation basins within these elongated dunes, like it is the case on the coast of Queensland in Australia.

Most of the inland parabolic dunes are distributed in semi-arid to arid regions of the Great Plains of North America, the Thar desert in India, and the northern part of mainland China. The dunes are found in river valleys and along lake margins, where they develop out of the fluvial and lacustrine sandy material. Contrary to their coastal counterparts, these regions present a sparse, low-ling vegetation cover enabling dunes to migrate farther from their source of sediment. Thus, inland parabolic dunes often result from the transformation of barkhan or transverse dunes when they start to migrate into a more densely vegetated area. In the case of a barkhan dune, vegetation starts by colonising and anchoring the horns whilst the remaining bare lobe keeps on migrating, as simulated by a continuous model and the Extended Discrete Eco-geomorphic Aeolian Landscape (Extended-DECAL) model. In general, the sediment supply and the wind energy are lower in continental interiors with respect to coastal areas. Consequently, inland parabolic dunes tend to be smaller with low-relief arms compared with coastal parabolic dunes. Some following migrating dunes usually override the arms of the dune ahead, thus preventing the formation of elongated dunes and favouring the development of compound forms.

Given their vegetated nature, parabolic dunes are strongly controlled by eco-geomorphic interactions. A low mobility and stabilisation of the dunes is to expect when climate conditions are favourable for the expansion of vegetation, whereas a high mobility occurs under deteriorating vegetation conditions. This remains valid if sediment supply and wind energy are high enough to allow the transport of sand. A complex framework of environmental factors controls the formation and development of parabolic dunes such as: lake or river watertable level fluctuations (Arbogast et al., 2002a, 2010; Forman and Pierson, 2003; Hansen et al., 2010; Lepczyk and Arbogast, 2005; Lichter, 1995), groundwater level (Porat and Botha, 2008), variations of wind regime or sediment supply (Hesp, 2002, p. 2002; Rawling et al., 2008; Tsoar et al., 2009; Zular et al., 2013), precipitation (e.g., Hoover et al., 2018; Lancaster, 1988; Landsberg, 1956; Stetler and Gaylord, 1996), temperature (e.g., Wolfe and Hugenholtz, 2009), wildfires (e.g., Filion and Morisset, 1983), droughts (Forman et al., 2005, 2001; Tripaldi et al., 2013), and more recently anthropogenic factors (e.g., Alexanderson and Fabel, 2015; Bertran et al., 2011; Bogle et al., 2015; Guo et al., 2018; Hesp, 2002, 2001, p. 2001; Hesp et al., 2010; Mason et al., 2009; Tsoar and Blumberg, 2002; Wolfe et al., 2008, 2007). In coastal settings, more factors intervene in the evolution of parabolic dunes and particularly on the associated stabilising vegetation. For example, a transgressive sea level cuts through the vegetation cover and induces coastal erosion, which eventually supplies sediment for parabolic dunes to form (Armitage et al., 2006; De Ceunynck, 1985; Pye and Rhodes, 1985; Pye and Switsur, 1981; Shulmeister and Lees, 1992; Tejan-Kella et al., 1990; Wolfe et al., 2008). An increased storminess comes with stronger winds, higher wind gust speeds, and a greater wave energy. These are all factors reducing the vegetation cover and therefore, triggering the formation and migration of parabolic dunes (Clemmensen et al., 2007, 2001; Hansen et al., 2010).

The projected increase in drought severity and loss of vegetation associated with climate change raises some concerns about the potential reactivation of dunes, especially the ones being stabilised by said vegetation like parabolic dunes. A resumed migration of these dunes may exacerbate the desertification caused by less precipitation and a joint rise of the global temperature (Mirzabaev et al., 2019). Aridification is now known to cause systemic and abrupt changes in ecosystems (Berdugo et al., 2020), which makes the now-stabilised state of parabolic dunes even more precarious. Like other types of dunes, they are known to be useful to humans in many ways. They perform their function of sand storage, sometimes contain large reserves of groundwater and act as a shelter for wildlife, favouring the sustainability of ecosystems in general (Pye and Tsoar, 2008). Coastal dunes also provide a natural and aesthetic protection against sea level rise, tsunamis, storm surges and flooding (Gares et al., 1979; Psuty and Rohr, 2000). These hazards are likely to grow stronger and more frequent in the current global warming context, hence the necessity to understand and preserve coastal dunes (IPCC, 2013).

4 Research questions

The idea of this PhD project was born during a field campaign in the Bahamas with Prof. Pascal Kindler, when I was doing my master under his supervision back in 2015. He introduced me to the controversy over some “chevron” dunes in the Bahamas, a term that has been applied to large, U- to V-shaped coastal dunes from the late Pleistocene. Their genesis was being debated and both aeolian processes and giant storm waves, along with their various implications for palaeoclimate, have been invoked to explain their presence in the region. The same denomination was applied later to describe similar landforms deposited during the Holocene in South Madagascar and Western Australia. In parallel to the Bahamian case, a discussion on their depositional process ensued opposing aeolian processes to giant tsunamis generated by a meteorite impact.

Question 1: What is a “chevron” dune and how does it form? The first objective of the thesis is to review the literature on “chevrons” with the aim to lay out a consistent and coherent global database, which would serve any future study focusing on these ridges. This is in order to discuss the validity and the use of the confusing term “chevron” in the scientific literature to describe large, U-shaped coastal landforms.

Question 2: Are “chevrons” in the Bahamas parabolic aeolianites or giant storm-wave deposits, and how are they linked to climate? Our study on carbonate “chevrons” in the Bahamas aims to bring some clarity on their genesis by proposing a thorough and final explanation for these landforms origin. To this end, a multi-proxy approach was adopted to characterise the “chevrons” morphology (GIS analysis), sedimentary structure (outcrop study), microfacies and granulometric inquiries (image analysis), and period of deposition (amino-acid racemization dating; AAR). These data were then compared to the ones collected for parabolic dunes and storm deposits in order to proceed by elimination and provide with some more accurate interpretations of palaeoclimate during the Last Interglacial.

Question 3: Coastal aeolianites in Western Australia: highstand or lowstand deposits? We address the timing of deposition relative to interglacial/glacial cycles, along with the palaeoclimatic conditions under which the coastal aeolianites in Shark Bay, Western Australia formed. At first, it was planned to conduct a comparative study on the large parabolic dunes lying in this region by investigating their structure and age. The loss by the USPS of the samples intended for the OSL dating and the lack of visible sedimentary structure within the dunes hindered any further investigation. However, the depositional timing of “chevrons”, and more generally coastal aeolianites, with respect to sea level fluctuations is still a matter of debate. The same question is being addressed since the 70’s for the Tamala Limestone coastal dunes in Western Australia. We investigated the stratigraphy and sedimentology (photogrammetric 3D models) of the Tamala Limestone dunes exposed in Shark Bay, the relative dating of the units (AAR), and the palaeoclimatic conditions prevailing at the time of their deposition.

Question 4: Under which climatic conditions do inland parabolic dunes form or migrate, and what is their potential as proxy for past climate of the Quaternary? Following the conclusions reached for coastal dunes in the Bahamas and Australia, the link between global climate and inland parabolic dunes activity was explored. Using the INQUA Digital Atlas of Quaternary Dune Fields and Sand Seas ages database, we report the activity of inland parabolic dunes during the last millennium and the mid-Holocene. The climate variables under which the recent dune activity occurred was then compared with the well-constrained climate of the mid-Holocene to define the potential of inland parabolic dunes as palaeoclimate proxy.

Question 5: Is there a possibility to characterise parabolic dunes at a global scale with regards to their morphology, the wind conditions under which they develop, the global atmospheric circulation, and the climatic conditions triggering their formation? An effort of building a consistent global database was made so that to extract some potential trend in parabolic dunes morphology. Then, factors influencing their shape were investigated starting with local wind conditions and later with global atmospheric circulation. Following the study on the relationship of parabolic dunes activity with climate conditions of the mid-Holocene and last millennium, the investigated period was further extended to the last 20’000 years so that glacial/interglacial cycles could be integrated in the research question.

5 Thesis structure

This thesis is compiled as a set of seven chapters, of which one (Chapter 2) is a review paper, and three (Chapter 3 to 5) are research papers. Given the structure of this manuscript, some repetition of text is likely to occur.

Chapter 2 comprises the review paper “*Chevrons: Origin and relevance for the reconstruction of past wind regimes*” and address the research Question 1.

Chapter 3 consists of the research paper “*Upper Pleistocene parabolic ridges (i.e., ‘chevrons’) from the Bahamas: Storm-wave sediments or aeolian deposits? A quantitative approach*” that discusses the research Question 2.

Chapter 4 encompasses the research paper “*Depositional timing and palaeoclimate interpretation of the Tamala Limestone aeolianites in Shark Bay, Western Australia*”, which focuses on the research Question 3.

Chapter 5 contains the research paper “*Continental interior parabolic dunes as a potential proxy for past climates*” that covers the research Question 4.

Chapter 6 presents and discusses unpublished data with the aim to extract potential trends and characterise parabolic dunes at a global scale, as defined by the research Question 5.

Chapter 7 summaries the key findings, discusses the thesis limitations for each chapter, and synthesises the outcomes of the overall project.

6 Publications and author contributions

Most of the thesis chapters have been published in international peer-reviewed journals as follows:

Review paper

Vimpere, L., Kindler, P., & Castelltort, S. (2019). Chevrons: Origin and relevance for the reconstruction of past wind regimes. Earth-Science Reviews, 193, 317-332. DOI: 10.1016/j.earscirev.2019.04.005

Research papers

Vimpere, L., Del Piero, N., Shawwa, N. A., Beguelin, K., Kindler, P., & Castelltort, S. (2021). Upper Pleistocene parabolic ridges (ie ‘chevrons’) from the Bahamas: Storm-wave sediments or aeolian deposits? A quantitative approach. Sedimentology, 68(3), 1255-1288. DOI: 10.1111/sed.12828

Vimpere, L., Del Piero, N., Le Cotonnec, A., Kindler, P., & Castelltort S. (*submitted*). Depositional timing and palaeoclimate interpretation of the Tamala Limestone aeolianites in Shark Bay, Western Australia. Aeolian Research

Vimpere, L., Watkins, S. E., Castelltort, S., (2021). Continental interior parabolic dunes as a potential proxy for past climates. Global and Planetary Change, 206, 103622. DOI: 10.1016/j.gloplacha.2021.103622

During my PhD, I also have contributed to further publications directly or indirectly related to my thesis subject.

Conference papers

Beccari, V., Adams, A., Angeloz, A., Basso, D., Caragnano, A., Del Piero, N., Dietsche, P., Eymard, I., Farley, N., Fau, M., Foubert, A., Hallock, P., Lauper, B., Lehmann, A., Maillet, M., Negga, H., Ordonez, L., Peyrotty, G., Rime, V., Rüggeberg, A., Schoellhorn, I., Spezzaferri, S., Stainbank, S., **Vimpere**, L., 2019. CUSO ESPP tropical marine ecology and sedimentology course, Maldives 2018: Preliminary results. Presented at the SwissSed Meeting, Fribourg.

Courgeon, S., Makhloufi, Y., **Vimpere**, L., Meyer, M., Samankassou, E., 2020. Depositional environment control on the geochemical signal of ancient shallow-water carbonates (Upper Jurassic, French Jura). Presented at the EGU General Assembly 2020.

Kindler, P., Godefroid, F., **Vimpere**, L., 2016. Elevated coralgal bioherms from Long Island (Bahamas): a testimony of recent tectonic uplift or of a high sea level during the Middle Pleistocene. Presented at the SwissSed Meeting, Fribourg.

Kindler, P., Revillon, S., **Vimpere**, L., Godefroid, F., 2016. Elevated coralgal bioherms from Long Island (Bahamas): a testimony of recent tectonic uplift or of a high sea level during Marine Isotope Stage 7. Presented at the Swiss Geoscience Meeting, Geneva.

Vimpere, L., Del Piero, N., Shawwa, N., Beguelin, K., Kindler, P., Castelltort, S., 2019. New sedimentological evidence for an eolian origin of the Upper Pleistocene U-shaped coastal ridges (i.e. “chevrons”) from the Bahamas. Presented at the 34th IAS Meeting of Sedimentology, Rome, Italy.

Vimpere, L., Godefroid, F., Kindler, P., 2016. Pleistocene shallowing-upward sequences in Dean’s Blue Hole, Long Island (Bahamas): evidence of differential subsidence or faulting along the SE margin of Great Bahama Bank. Presented at the SwissSed Meeting, Fribourg.

Vimpere, L., Kindler, P., Castelltort, S., 2019. V-shaped, carbonate and mixed coastal ridges (i.e. chevrons): origin and relevance for the reconstruction of past wind regimes. Presented at the Bathurst Meeting, Mallorca.

Research papers

Beccari, V., Spezzaferri, S., Stainbank, S., Hallock, P., Basso, D., Caragnano, A., Pisapia, C., Adams, A., Angeloz, A., Del Piero, N., Dietsche, P., Eymard, I., Farley, N., Fau, M., Foubert, A., Lauper, B., Lehmann, A., Maillet, M., Negga, H., Ordonez, L., Peyrotty, G., Rime, V., Rüggeberg, A., Schoellhorn, I., **Vimpere**, L., 2020. Responses of reef bioindicators to recent temperature anomalies in distinct areas of the North Ari and Rasdhoo atolls (Maldives). Ecol. Indic. 112. DOI: 10.1016/j.ecolind.2020.106128

Caragnano, A., Basso, D., Spezzaferri, S., Hallock, P., Adams, A., Angeloz, A., Beccari, V., Del Piero, N., Dietsche, P., Eymard, I., Farley, N., Fau, M., Foubert, A., Lauper, B., Lehmann, A., Maillet, M., Negga, H., Ordonez, L., Peyrotty, G., Rime, V., Rüggeberg, A., Schoellhorn, I., Stainbank, S., **Vimpere**, L., 2021. A snapshot of reef conditions in North Ari Atoll (Maldives) following the 2016 bleaching event and *Acanthaster planci* outbreak. Marine and Freshwater Research. DOI: 10.1071/MF20119

Stainbank, S., Spezzaferri, S., Beccari, V., Hallock, P., Adams, A., Angeloz, A., Basso, D., Caragnano, A., Del Piero, N., Dietsche, P., Eymard, I., Farley, N., Fau, M., Foubert, A., Lauper, B., Lehmann, A., Maillet, M., Negga, H., Ordonez, L., Peyrotty, G., Rime, V., Rüggeberg, A., Schoellhorn, I., **Vimpere**, L., 2020. Photic stress on coral reefs in the Maldives: The *Amphistegina* bleaching index. Ecol. Indic. 113. DOI: 10.1016/j.ecolind.2020.106257

In a scientific outreach effort, which I personally believe to be of major importance, I have contributed to journals focusing on science communication to the broad public:

Vimpere, L., 2021. What Caribbean coasts can tell us about the future of climate change. TheScienceBreaker 07. DOI: 10.25250/thescbr.brk461

An interview dedicated to the popularisation of my work on chevron dunes for the magazine Naturevolve meant to be published in December 2021 or January 2022.

Chapter 2 – Chevrons: Origin and relevance for the reconstruction of past wind regimes

This chapter review the literature to address the nature, definition, and formation process of “chevron” dunes.

Published as:

Vimpere, L., Kindler, P., & Castelltort, S. (2019). Chevrons: Origin and relevance for the reconstruction of past wind regimes. Earth-Science Reviews, 193, 317-332. DOI: 10.1016/j.earscirev.2019.04.005

Abstract

Since its first use in the late 80’s, the term chevron has been employed in numerous studies to describe large U- and V-shaped ridges found in or near shorelines worldwide. Most studies have so far focused on Bahamian chevrons that are exclusively of Late Pleistocene age, and on the supposed Holocene chevrons found in S-Madagascar and Australia. In the Bahamas, these deposits have been interpreted as the product of extreme storms at the end of the last interglacial (LIG) warm period. In contrast, the extensive chevrons complex exposed in S-Madagascar and on the western coast of Australia have been associated with a tsunami induced by a meteorite impact. Finally, several authors have also proposed a non-catastrophic (i.e., eolian) origin based on the recognized importance of wind-related processes in these coastal areas, and term such deposits parabolic dunes. In this paper, we collect and synthesize existing data on the morphology, sedimentology and age of these chevrons, and review the different interpretations proposed in the literature with the aim to lay out a consistent database to assist further investigations on these important coastal morphologies. In addition, we generated a synthesis of wind data at the three study areas, which highlights the relationship between present wind regimes and chevrons morphologies. The ubiquity of chevrons (likely actually parabolic dunes) in coastal areas around the globe and their relationship with coastal processes makes them crucial archives for reconstructing past wind regimes.

Figure 5: World map of chevron distribution along coasts and their approximate seaward axes, pointing to a potential source area (modified after Scheffers et al., 2008). The stars show the impact craters defined by those authors. Squares and triangles point the approximate locations of chevrons and/or parabolic dunes observed by (Bourgeois and Weiss, 2009). The authors defined three categories of bedforms according to their relationship to a coastline: "'interior' cases have no relationship to a coastline (black squares); 'small water body' cases require improbable impact scenarios (triangles); for 'oceanic coast' cases, impact hypothesis requires further evaluation (red squares)". Depending on the authors and the proposed interpretation, the number of chevrons and the associated localities change.

1 Introduction

The term "chevron" is widely used to describe U- and V-shapes and has taken several descriptive usages in structural geology (e.g., chevron folds; Ramsay, 1974), and sedimentology (e.g., small-scale laminae arrangement in oscillatory ripples; Allen, 1982). Later, using Landsat MSS images at 80 m spatial resolution, Maxwell and Haynes (1989) mapped the 10'000 km^2 of the Selima Sand Sheet, SW Egypt (Figure 5), where light-colored chevron-shaped patterns are observable migrating downwind over darker coarse sand. They described these features as active "extremely long-wavelength (130 to 1200 m) and low-amplitude (10 to 30 cm), […] irregularly spaced, light-toned, 0.5 to 2.0 km wide streaks oriented generally transverse to the dominant northerly wind direction […]" bedforms. By comparing Landsat images from 1972, 1986 and 1988, they defined a migration rate between 100 and 500 m.y^{-1} corresponding to a net movement of 83'000 m^3.y^{-1} of sand for a 10 km wide chevron. In the present review, we focus on the term "chevron" as it has been originally applied by these latter. Although the authors renamed them zibars thereafter (Maxwell and Haynes, 2001), the term was independently used for modern and Holocene coastal landforms of similar morphology in Australia (Bryant et al., 1997), and for Pleistocene ones in the Bahamas (Hearty et al., 1998).

Since their discovery, the origin of chevrons and their environmental significance have captured the attention of sedimentologists and geologists. Scheffers et al. (2008) characterized their morphology by using Google Earth© to identify 221 chevron sites along the world coastlines (Figure 5). To qualify as a chevron, the distinctive U to V-shape was used as the diagnostic criterion. They found that the common extension of a chevron field is between 10 and 50 km (49 % of their data), making such bedforms very significant sediment transport systems. Furthermore, 61 % of the identified chevrons have a kilometric lateral extension (length: 1 to 5 km, width: 10 to 1000s m), and 59 % of them display an elevation between 10 and 100 m a.s.l. The main characteristic of these bedforms is the linearity of their axes despite the different morphologies they exhibit (Figure 6). Five different chevron morphologies have been categorized, lying the foundations for a more complete classification, subsequently defined by the same authors.

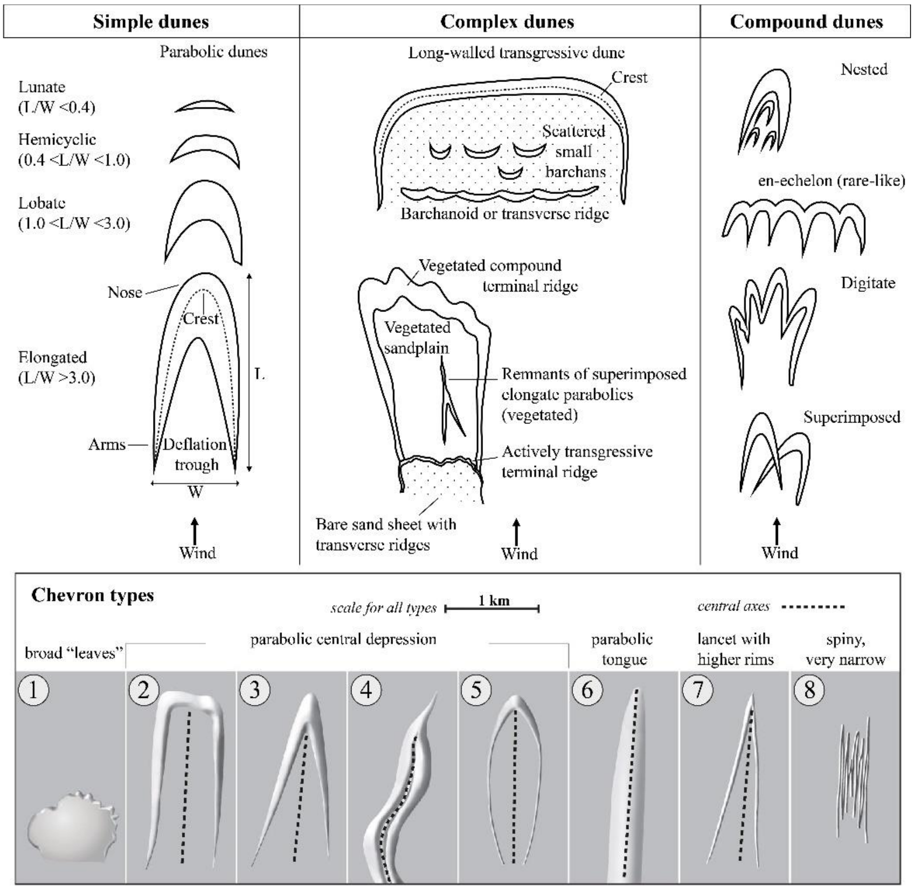

Figure 6: The three types of dunes defined by McKee (1979) and the subclassification of sample dunes according to their length:width ratio (Pye, 1993). Comparison with the eight types of chevron morphology observable around the world (modified after Scheffers et al., 2008).

Both of these systematizations are similar to the one proposed by Pye (1993) in his study of parabolic dunes in Queensland, NE-Australia, which is based on the architecture and the length/width ratio (Figure 6). Using the classification presented by McKee (1979), the morphology of dunes is subdivided in three categories : *simple*, *compound* and *complex*. Simple dunes are characterized by single forms subclassified by Pye (1993) as *lunate* when they exhibit length:width (L/W) ratio < 0.4; *hemicyclic* for 0.4<L/W<1.0; *lobate* when 1.0<L/W<3.0 and *elongate* for those with a L/W>3.0. Compound forms consist of two or more dunes of the same type that have coalesced or are superimposed, and complex dunes are composed by two or more different types of simple dunes.

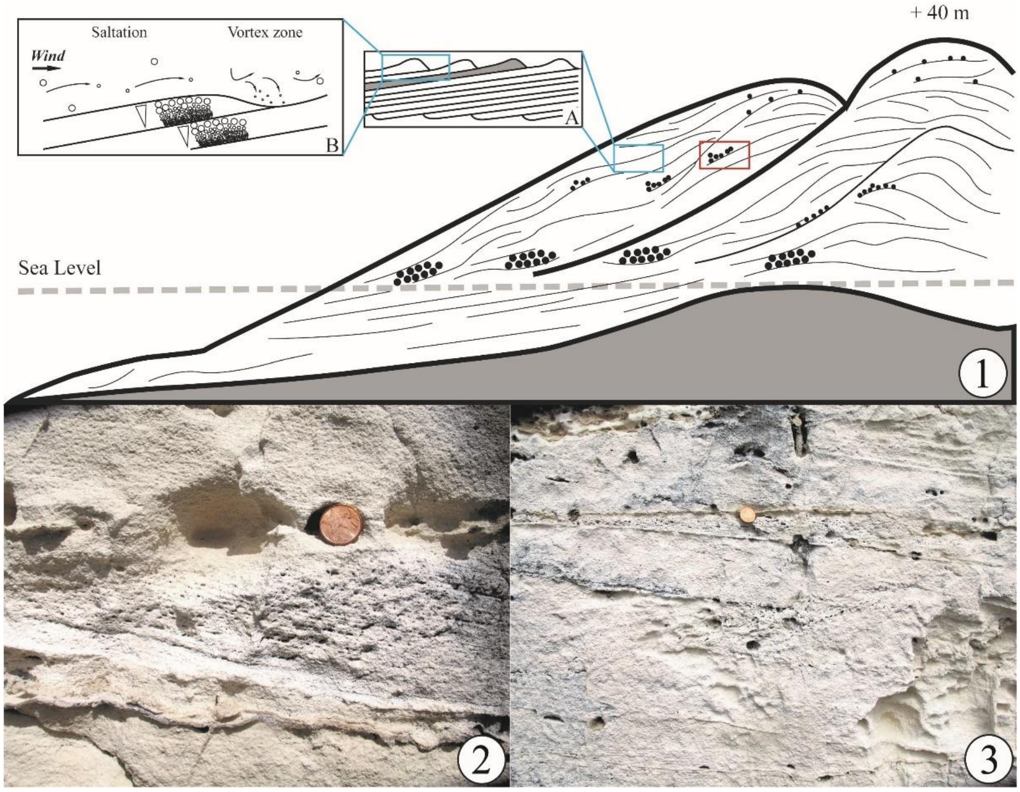

Figure 7: 1—Changing morphology of fenestrae-rich beds within chevron dunes, going from abundant tabular to slight discontinuous packages with increasing distance and elevation from shore (modified after (Hearty and Tormey, 2017). Red square indicates the position of 2 and 3. A— Subcritically translatent strata (SCTS) forming when the angle of ripple climb is lower than the inclination of ripple stoss slope (modified after Hunter, 1977). B—Formation mechanism of pine stripe laminations showing inverse grain size gradient by concentration of finer particles in the existing trough between two ripples (modified after (Fryberger and Schenk, 1988). 2 and 3—Photographs of fenestrae-rich beds of a dozen cm thick within an eolianite subparallel to the coast. Note the more pronounced pinstripe laminations within the bed rich in fenestrae in 2.

Some authors suggested a tsunamigenic origin for the chevrons from S-Madagascar and W-Australia (Abbott et al., 2005; Abbott, 2006; Abbott et al., 2006, 2007, 2010a, 2010b; Bryant and Nott, 2001; Gusiakov et al., 2009; Kelletat and Scheffers, 2003; Masse et al., 2006; Masse, 2007). Others proposed that Bahamian chevrons result from the action of large waves generated during “superstorms” (Hansen et al., 2015; Hearty et al., 2002, 1998; Hearty and Tormey, 2018a, 2018b, 2017; Tormey and Donovan, 2015). Finally, several authors proposed a non-catastrophic, wind-induced origin for the chevrons in the three mentioned regions (Bourgeois and Weiss, 2009; Engel et al., 2015a; Kindler and Strasser, 2000, 2002; Mylroie, 2018a, 2018b; Pinter and Ishman, 2008; Rovere et al., 2017, 2018). These Aeolian deposits are regarded by these authors as parabolic dunes, not chevrons.

Determining whether chevrons result from giant-storm waves, asteroid- or landslide-related tsunamis or eolian processes has important implications for the assessment of coastal hazards, landscape and infrastructure management in these regions and for the correct interpretation of genesis of coastal and near-coastal landforms, especially in the current context of climate change and sea-level rise. It is beyond the scope of this paper to present scenarios of possible coastal evolution associated with the ongoing global warming. However, research on the origin of chevrons from the Bahamas, in relation with the LIG climatic optimum, may provide "facts from the past" and a perspective of the possible consequences of the current temperature trend. In addition, although the LIG may not be a perfect analogue for present climate change, it represent an important case of a ***natural*** increase of greenhouse gas concentration in the atmosphere (Hansen et al., 2013, 2015; V. Masson-Delmotte et al., 2013; O'Leary et al., 2013), thereby providing a benchmark against which the impact of the anthropogenic addition of such gases to the atmosphere may be gauged.

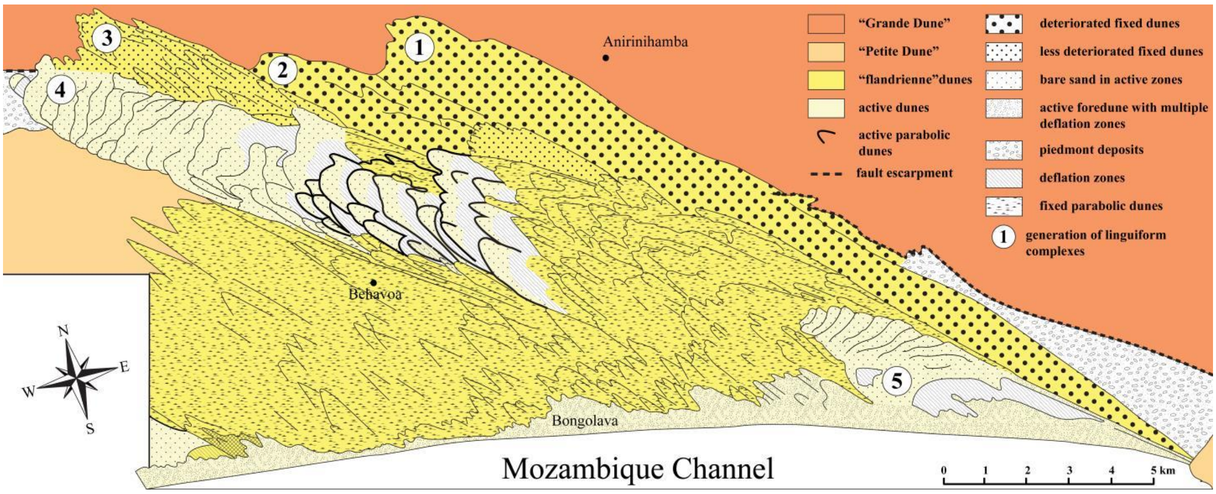

Figure 8: Geomorphological features and stratigraphic relationships of the different units composing the Fenambosy chevron (modified after Battistini, 1964). The "Grande Dune" is the oldest sandy unit in S-Madagascar coastline environment, correlated to the ancient "Aepyornien" (from 2.2 Myrs to 160'000 yrs BP). The "Petite Dune" unit corresponds to the "karimbolien" deposits (120'000-45'000 yrs BP). The "flandrienne" dunes are Holocene (6'000 yrs BP) transgression-related sandy deposits that form the chevrons in the region. The active recent dunes are depositing as foredunes on which few nebkhas can be observed. The numbers represent the different phases of deposition from the oldest (generation 1) to the youngest (generation 5).

In addition, because coastal chevrons are recognized in recent settings due to their plan-view shape, they may have been overlooked in ancient sedimentary successions. Understanding how chevrons originated could thus improve our ability to quantify past environmental conditions and extreme events that have affected coastal regions. The objectives of this paper are thus to synthesize existing knowledge on the morphology, sedimentology, age and depositional processes of these landforms.

2 The Bahamas

2.1 Morphology

In the Bahamas, chevrons are found across the archipelago but are concentrated in its northern and central part. They are exclusively located on the coast facing the Atlantic Ocean. They can be composed of multiple smaller ridges in nested sets that extend several kilometers across several islands, with asymmetrical SW-pointing seaward-dipping crests (Hearty et al., 1998; Hearty and Tormey, 2017).

2.2 Sedimentology

As most deposits from the last interglacial (i.e., MIS 5e), apart from reefal complexes, chevron ridges display an oolitic composition with a subordinate skeletal content (Hearty et al., 1998; Kindler and Hearty, 1996). Hearty et al. (1998) described the chevron's sedimentary features as: "[…] subparallel, aggrading beds with few interruptions or truncations". It was later emphasized that steep foresets are absent in Bahamian chevrons, and that pedogenic features as well as eolian strata are rare (Hearty and Tormey, 2017). Thin (5 to 20 cm thick) fenestrae-rich beds have also been observed within chevrons and coastal ridges oriented parallel to the coastline (Bain and Kindler, 1994; Hearty et al., 2002; Hearty and Tormey, 2017; Kindler, 1991; Kindler and Strasser, 2002, 2000). Detailed descriptions of exposures from several localities on different Bahamian islands have resulted in the definition of three types of fenestral beds changing with elevation and distance from the shore (Hearty and Tormey, 2017; Tormey and Donovan, 2015). From the lowest and most proximal to the highest and most distal locations, fenestral beds are respectively unlaminated, abundant and tabular, and end up forming slight, discontinuous packages. Intermediate morphologies can be observed at moderately elevated and inland positions (Figure 7). Last but not least, mm-thin, inversely graded laminae, identified as SCTS (Hunter, 1977) and outcropping as "pin-stripe laminations" Fryberger and Schenk (1988) have been observed in the chevrons (Kindler and Strasser, 2002, 2000).

2.3 Geochronology

In the Bahamas, the most widely used dating method is amino-acid racemization (AAR) geochronology, which consists in measuring the ratio between alloisoleucine and isoleucine (A/I) in shells or whole-rock samples. U/Th-calibrated A/I measurements on whole-rock samples yield a ratio of 0.48 ± 0.04 for the first part of the last interglacial (MIS 5e), and 0.40

± 0.03 for the later portion of this substage (Hearty and Kaufman, 2009, 2000). Only one chevron located in Miller’s Settlement on Long Island has been directly dated by AAR. The authors obtained two A/I ratios averaging at 0.46 (Appendix 1), and correlated the chevron to the late Pleistocene (Aminozone E; MIS 5e II; Hearty and Kaufman, 2000). The other ridges are correlated to the latter based on their petrography, stratigraphic position and dating of associated deposits such as mega boulders or runup deposits (Hearty et al., 2002, 1998; Hearty and Tormey, 2017; Kindler, 1991; Kindler and Strasser, 2000).

Table 1: Comparison of some bedform characteristics measured for chevrons around the globe and other common bedforms (Bourgeois and Weiss, 2009).

	Grain diameter, D (m)	Bedform length, L (km)	Bedform height, H (m)	L/H (m/m)	L/D (m/m).10^4
Subaqueous sand ripples, typical	0.00015	0.00015	0.01	15	0.1
Subaqueous sand dunes, typical	0.00015	0.015	1	20	10
Washington State giant ripples	0.02-0.3	0.04-0.1	1-5	20	≈0.03-0.2
Washington State parabolic dunes	≈0.001	≈0.3	≈3	≈100	≈25
Oolite chevrons, Bahamas*	0.002	3-10*	8-25	≈400	150-500
Australia "chevrons"	0.002	0.5-3	≈3-30†	≈100-200	25-150
Madagascar "chevrons"	0.002	0.5-3	≈3-30†	≈100-200	25-150

* Not regularly repeating.

† Estimates based on general characteristics in literature.

3 Australia

3.1 Morphology

Based on aerial photographs investigation in Australia, and particularly in W-Australia, chevrons show a very extended distribution around the country and different morphological appearances (Kelletat and Scheffers, 2003). These authors observed similar ranges of sizes, field extensions and nesting as in the Bahamas. The ridges are one to several kilometers in length, heights of 10 m to more than 120 m. They usually have straight axis that may be perpendicular, parallel or oblique to the coast, but can sometimes bend in two directions with a 90° shift. They described landward-narrowing, sharply marked outer contours, often covered by vegetation and soil even in the dry bush. At least two generations were defined according to their degree of erosion and vegetation cover. Active beaches act as sources of sediment, but chevrons also developed at locations where there is no apparent source of sand. However, each of the studied location has been the subject of a previous publication in the literature, describing climbing and clifftop dunes all along the Australian coast, including parabolic ones (Hesp and Chape, 1984; Short, 2014, 2006, 2005, 1988; Woodroffe, 2002). Jennings (1967) postulated that cliff-top dunes imply cliff recession or erosion of a sand ramp after the deposition. Since sand can be blown up slopes up to 60° (Pye and Tsoar, 2008), and deposited in the zone of reduced wind velocity near the crest of escarpments (Bowen and Lindley, 1977; Jackson, 1975; Marsh and Marsh, 1987), cliff-top dunes do not require a nearby source, nor a change in sea-level or tectonic regime. (Kelletat and Scheffers, 2003) also studied Cape Melville area, located on the coast of Queensland, NE-Australia, where they observed two different generations of inactive ridges, interpreted as chevrons. Again, previous work (Jennings, 1957; Lees et al., 1990; Pye, 1993b, 1983, 1982a, 1982b; Pye and Mazzullo, 1994; Pye and Rhodes, 1985; Short, 2014, 1988; Shulmeister and Lees, 1992; Tejan-Kella et al., 1990; Ward, 2006) interpreted variations in **parabolic dune** morphology all along the Queensland coast as the result of changes in wind regime, local topography, sand availability and vegetation.

3.2 Sedimentology

All studies performed on the chevron ridges from Australia mostly consist of geomorphic descriptions based on aerial photographs and/or field observations, but no thorough sedimentological or petrographic study has been conducted yet. However, the sedimentology of parabolic coastal dunes in Queensland (later named chevrons by (Kelletat and Scheffers, 2003; Scheffers et al., 2008) has been studied before the use of the term “chevron” became widespread (Pye, 1993b). Drilling data demonstrate a long history of coastal dune building in this region with several generations of deposits, separated by soil horizons with different degrees of pedogenesis, that extend more than 40 m below the surface. Eolian deposits supposedly accumulated during both highstand and lowstand periods. The Holocene marine transgression, and probably earlier ones, have trimmed sandy coastlines and provided the material for dunes to migrate landward from these eroding shorelines. The migration coupled with a partial stabilization yielded to the formation of parabolic dunes or chevrons of large size. Chevrons have nonetheless been described on the southern headland of Jervis Bay where they form two lines of deposits, respectively lying at +30 and +130 m a.s.l., and consisting of sand mixed with cobbles and fine shell hash (Bryant et al., 1997; Bryant and Nott, 2001).

3.3 Geochronology

Using ^{14}C dating on various deposits attributed to tsunamis, including chevron dunes, Bryant and Nott (2001) obtained Holocene ages from 0 to almost 7 ka BP. Kelletat and Scheffers (2003) briefly mentioned that chevrons have been dated (1) at around 123’000 ± 5000 BP without specifying the location, and (2) at 1080 AD in at least one place in W-Australia, but again without referencing their source. They mostly interpreted chevrons as Holocene deposits because of their relation to active coastline, with an older Holocene age shown by their basal erosion by beach ridges. Later, relative age indicators such as the density of the vegetation cover, the sharpness of contours, the co-existence of several generations of ridges and their relationships to the modern coast have been used based on satellite images (Scheffers et al., 2008). The coast of Queensland is far better known as stratigraphic studies have been conducted along several zones (Lees et al., 1990; Pye, 1993b; Pye and Switsur, 1981). The petrographic and diagenetic analyses coupled with ^{14}C and TL ages, when reassembled, define a stratigraphic column composed of seven units named from A to G (from top to bottom). The oldest observed record of eolian activity in this region was dated from middle Pleistocene (Appendix 1).

4 Madagascar

4.1 Morphology

A complete study has been conducted in the southern part of Madagascar to investigate its geomorphological components and define a stratigraphic column (Battistini, 1964). The Ampalaza “chevron” has been defined by the author as linguiform complexes of parabolic dunes whereas the Fenambosy “chevron” combines fixed parabolic and active transverse dunes. Battistini (1964) recognized three sub-complexes within the Ampalaza dunefield (Figure 8):

1. The first linguiform field is the oldest and innermost one. The ridges composing it are altered by the erosion and entirely covered by the vegetation.
2. The second and most extended one corresponds to an intermediate progradation phase. With a length of about 30 km and a width of 2.5 to 4 km, it composes 30% of the chevron. Fixed by the vegetation for the most part, it overlies older sandstones to reach an altitude of 77 m.a.s.l. Only the NW extremity is still active and migrates according to the general orientation.
3. Between the second sub-complex and the sea, the third phase of progradation consists of active bare sand that overlies the dunes of the second phase in some places. It is 2 to 4 km wide and 18 km long.
4. Regarding the Fenambosy dunefield, five phases have been defined (Figure 8):
5. The youngest one is an active foredune coming from the beach with numerous deflation zones and nebkhas.
6. A second one on the eastern part of the field, composed of active bare sand migrating

as transverse dunes that overlie older fixed parabolic dunes in the innermost part.

7. A middle part very extended and covered by the vegetation. It strictly consists of parabolic dunes that can be more or less elongated.
8. A migrating inner part 12 km long and 2 to 2.5 km wide that reaches the altitude maxima. Some large parabolic dunes (about 15) show active bare sand migrating NW and the associated deflation zones where nebkhas may develop. A transition to transverse dunes can be observed landward where the absence of vegetation allows a rapid migration of the ridges.
9. NE of the fresh active linguiform complex, an older phase of sand migration displays smoothed reliefs. The ridges, now partially eroded, climbed up the fault escarpment to reach an altitude of 211 m.a.s.l.

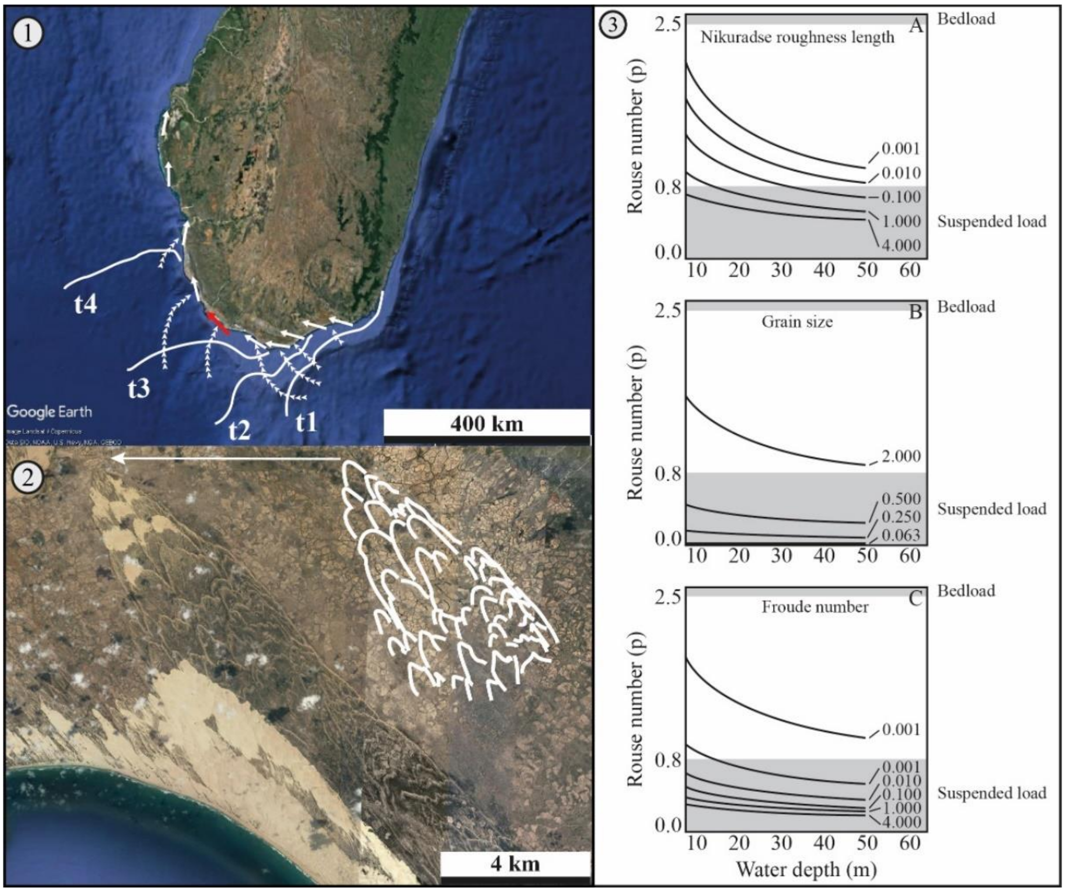

Figure 9: 1— Satellite photograph of the southern part of Madagascar. The arrows show the chevrons orientations, and specifically the Ampalaza chevron (red arrow). The timelines of wave crests modeled by Bourgeois and Weiss (2009) are represented by the uniform white lines, and angles of wave approach by arrowed ones. 2— Enhancement of the Ampalaza chevron with the main ridges outlined in white (Bourgeois and Weiss, 2009), showing the general orientation subparallel to the coast. 3— Plots of Rouse number (p) versus water depth to show the type of sediment transport under varying ks (A), D (B) and Fr (C) represented by the lines (Bourgeois and Weiss, 2009). Grain size is kept constant (D = 1 mm) in A for all cases; as Fr = 1.0 and ks = 1 m in B; plus D = 1 mm and ks = 1 m in C.

Chevrons from S-Madagascar have been morphologically compared to those described in the Bahamas and Australia, and to subaqueous dunes and ripples in the Palouse region, E-Washington State, using a sedimentological approach (Bourgeois and Weiss, 2009). These authors concluded that chevron grain diameter (D), length (L), height (H), L/H and L/D ratios are highly similar in all the studied regions (Table 1: Comparison of some bedform characteristics measured for chevrons around the globe and other common bedforms (Bourgeois and Weiss, 2009).; Bahamian chevrons slightly differ from the others but have the same order of magnitude). Unlike the rather isolated chevrons in the Bahamas than can be found nested, and the large complex extending along the Australian coastlines, the chevrons in Madagascar form massive linguiform complexes of dunes (Figure 9). Later, other authors used and described the mentioned ridge complexes as parabolic dune fields (Hesp, 2011, p. 2011; Hesp and Walker, 2013).

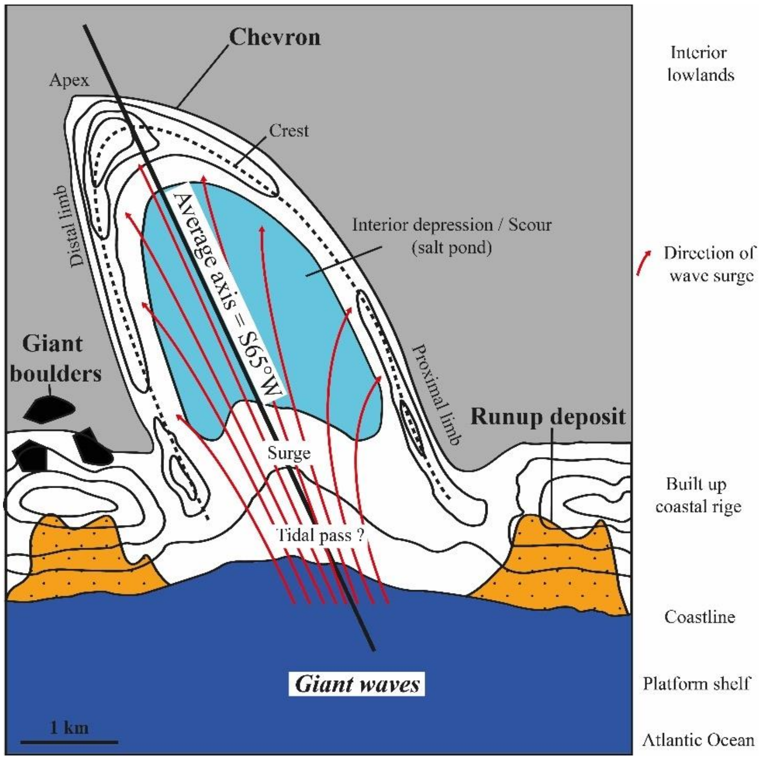

Figure 10: Schematic map of a chevron, associated giant boulders landward of highlands and runup deposits on older built-up ridges, following the impact of a giant wave coming from the Northern Atlantic Ocean (modified after Hearty et al., 1998).

4.2 Sedimentology

The source of sediment for the Fenambosy chevron is the eastern part of the active beach. This 10 km long zone is located between Malaimpioka Cape and the locality Bongolava. Battistini (1964) suggested that longshore drift towards the West accumulates sediments on this beach because the presence of a steep rocky cliff in the West. Being more resistant to the erosion, it induces a local low sediment supply. The active front part (generation 4; Figure 8) is still migrating fast but is already disconnected from the littoral source by the fixation of the parabolic dunes. As a result, a new generation of dunes (generation 5; Figure 8) is migrating from the beach on the vegetated parabolic dunes. The Menrandra mouth is located to the West of the Ampalaza chevron and acts as the main source of sediment. The associated lagoon is reformed each year during the dry season.

4.3 Geochronology

According to the stratigraphy defined by Battistini (1964), all chevrons in S-Madagascar are correlated to the “flandrienne” transgression that occurred around 6’000 yrs BP. They now partially cover the older “Petite Dune” unit correlated to the “karimbolien” high sea-level (120’000 to 80’000 yrs BP), which roughly corresponds to the Eemian or LIG. During the Holocene transgression, a dense psammophile vegetation that partly fixed the migrating bare sand, inducing the formation of parabolic dunes (Lebigre et al., 2001). The stratigraphic relationships between the different units are summarized in Figure 8 for the Fenambosy chevron, and in Appendix 2 for the Ampalaza chevron.

Radiocarbon-dated archeological discoveries (Blench, 2010; Burney, 2004), coupled with the presence or absence of oral history in S-Madagascar, made it possible to approximately constrain the chevron maximum age at ca. 500 AD (Gusiakov et al., 2009). Based on the general appearance and vegetation cover, a mid-Holocene age (7’000-4’000 years) was proposed. The authors suggest that because there are fragile, unconsolidated features, chevrons would not have been preserved after the Younger Dryas climatic change. Older detailed studies conducted in the region correlate the chevrons to the “post-karimbolien” period that occurred between 120’000 and 45’000 (Battistini, 1964; Lebigre et al., 2001).

5 Emplacement mechanisms

5.1 Giant storm wave hypothesis

Building up on an hypothesis formulated by Hearty et al. (1998), and integrating recent assessments on the LIG climate (DeConto and Pollard, 2016; Engel et al., 2015a; Hansen et al., 2013, 2015; P. Hearty et al., 2007; Kopp et al., 2009; O’Leary et al., 2013), Hearty and Tormey (2017) reiterated the giant-wave theory for the formation of chevrons in the Bahamas. There, chevrons are associated with large boulders and runup sediments, thereby seemingly constituting a “trilogy” of long-period wave deposits (Hearty et al., 2002, 1998; Hearty and

Tormey, 2017). Chevrons were accumulated in lowlands delineated by older ridges, the lower portions of which were potentially the source of the large boulders, whereas sand sheets were deposited over the ridges by wave runup (Figure 10).

This trilogy can be observed in North Eleuthera, near the Glass Window bridge, where chevrons occur close to megaboulders and run-up deposits. Seven boulders with a volume ranging from 500 to 1000 m^3, and weighting from about 300 to 2000 tons lie in the vicinity of the bridge (Hearty, 1997). Evidences for their erratic origin consist of high-angle bedding (30° to 75°; Hearty and Tormey, 2017) and their stratigraphic position above younger units. Because no major tsunami struck the Bahamian coastlines in historical times, the storm-wave hypothesis appeared as the most plausible one. The authors referred to a "diminutive analogue", called "Perfect Storm" that generated a wave responsible for the horizontal displacement of the GW bridge weighting 510 tons. The natural rock bridge painted by Winslow Homer in 1895 was also washed away by storm waves (*https://www.eleuthera-map.com/rage-glass-window-bridge-1.htm*).

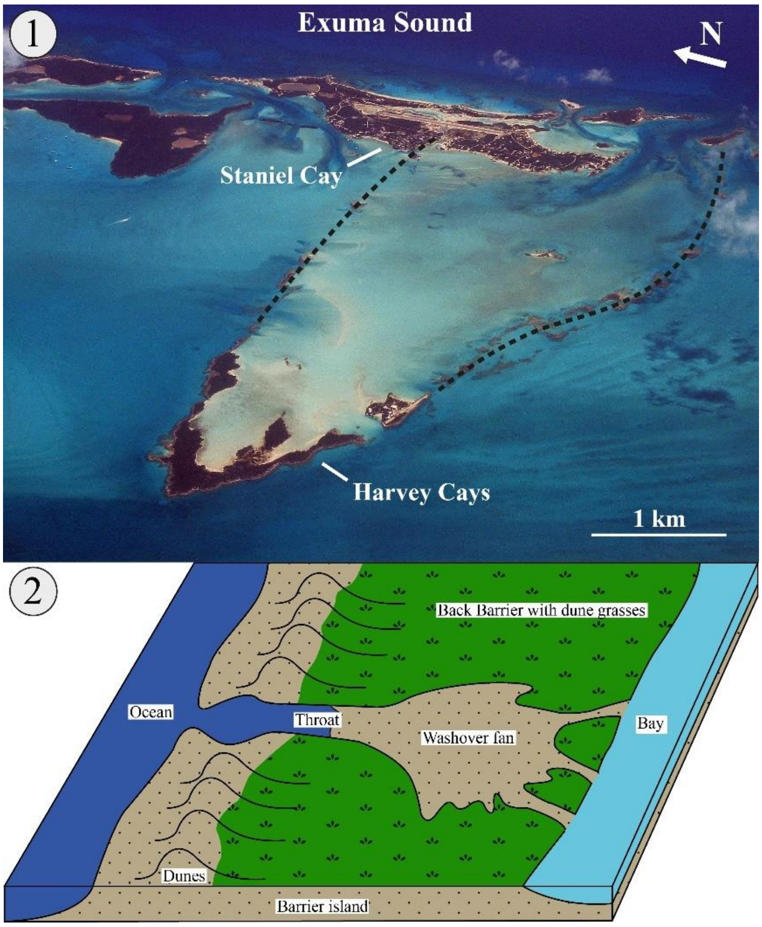

Figure 11: 1— Aerial photograph of a partially eroded chevron near Staniel Cay in the Exumas, Bahamas (photo from P. Kindler). 2— Comparison with a typical washover fan morphology on a barrier island (modified after (Donnelly et al., 2006).

Runup deposits observed near chevron dunes are composed of stacked sequences of tabular, seaward-dipping beds showing fenestrae-rich levels. The composition is the same as chevrons and consist of a well-sorted oolitic grainstone. They can be associated with scour structures and rip-up breccia in some places, advocating for the erosive power of storm waves runup (Hearty et al., 1998; Hearty and Tormey, 2017; Tormey and Donovan, 2015). Furthermore, the changing character (scarcity and continuity) of fenestral beds within chevrons and runup deposits appears to reflect an attenuation of large waves on coastlines (Hearty and Tormey, 2017; Tormey and Donovan, 2015).

The LIG sea level history remains moderately well understood despite the numerous studies conducted (see Hansen et al., 2015 for a review of past studies). Climatic transitions between glacial and interglacial periods are strongly affected by insolation change (Hays et al., 1976), as it drives the growth and decay of Northern Hemisphere ice sheets. The warm-season insolation anomalies were negative during the MIS 5e, which was supposed to trigger the decay of ice sheets. To answer this paradox, several studies proposed that East and West Antarctic ice sheets and basins collapsed during this period, resulting in an abrupt sea level rise (DeConto and Pollard, 2016; Hansen et al., 2015; Hollin, 1965; Mercer, 1978; Neumann and Hearty, 1996; Wilson, 1964). For Hansen et al. (2015), the injection of fresh melt water in the Atlantic has dramatically increased the pressure gradient at the surface, strengthening northeasterly winds that would have contributed to the generation of long-period waves, amplified thereafter by local coastal bathymetry, reflection and refraction (Hearty and Tormey, 2017).

5.2 Cosmogenic tsunami hypothesis

In Australia, most of the chevrons have been correlated to the Holocene (cf. Chap. 3.3), enabling some authors to cross-check the geological imprint of tsunamis with oral traditions and mythologies (Bryant et al., 2007; Masse, 2007; Masse and Masse, 2007). Several studies mention the impact of past intense tsunamis on Australian coastlines, especially on the west coast (Bryant, 2014; Gusiakov et al., 2009). Imbricated boulder fields located onshore, in particular along the East coast (Bryant, 2014; Gusiakov et al., 2009), evoke the concrete block that was moved 150 m from the coastline during the Japan tsunami of 1983 (Gusiakov et al., 2009). Because chevrons orientation does not necessarily coincide with the dominant wind direction, and their limits occur far above any deposits of recorded storms or seismogenic and volcanic tsunamis, a cosmogenic impact was suggested as a probable formation process (Abbott, 2006; Abbott et al., 2007; Bryant, 2014; Gusiakov et al., 2009; Kelletat and Scheffers, 2003; Masse, 2007; Scheffers et al., 2008). Another argument was the presence of chevron fields along cliffed coasts where a source of available sediment is absent (Scheffers et al., 2008), and the extent of these complexes, especially on the South-Madagascar coast where they climbed the major fault escarpment reaching heights of more than 200 m.a.s.l with inland penetration about 45 km (Gusiakov et al., 2009).

By extending chevrons orientations, Kelletat and Scheffers (2003) predicted an impact zone in the Indian Ocean at the same latitude as Perth. The large Burckle crater (29 km in diameter) was then discovered and related to the Madagascar and W-Australia chevrons (see Gusiakov et al., 2009 for a review of past studies). Because of its subtle morphology, the authors are certain that the crater cannot be interpreted as a submarine volcano, which usually have a more pronounced relief, or as a fault-block basin, that do not adopt a circular shape even within the Southwest Indian Ridge. Deep cores taken in the crater area revealed impact ejecta, of which the most diagnostic ones are: 1) melted droplets of NiO at the base of pure Ni grains, 2) nearly pure carbon spherules, and 3) calcite rhombohedrons at a depth where ocean waters are undersaturated with respect to calcite (Abbott et al., 2005; Gusiakov et al., 2009). The ages obtained for chevrons (cf. Chap. 4.3) were correlated to the estimated Holocene age (4’500 to 5’000 y BP) of the Burckle impact crater located in the S-Indian Ocean (Abbott, 2006; Abbott et al., 2007, 2006; Gusiakov et al., 2009; Kelletat and Scheffers, 2003; Masse, 2007; Masse et al., 2006; Scheffers et al., 2008; Scheffers and Kelletat, 2003).

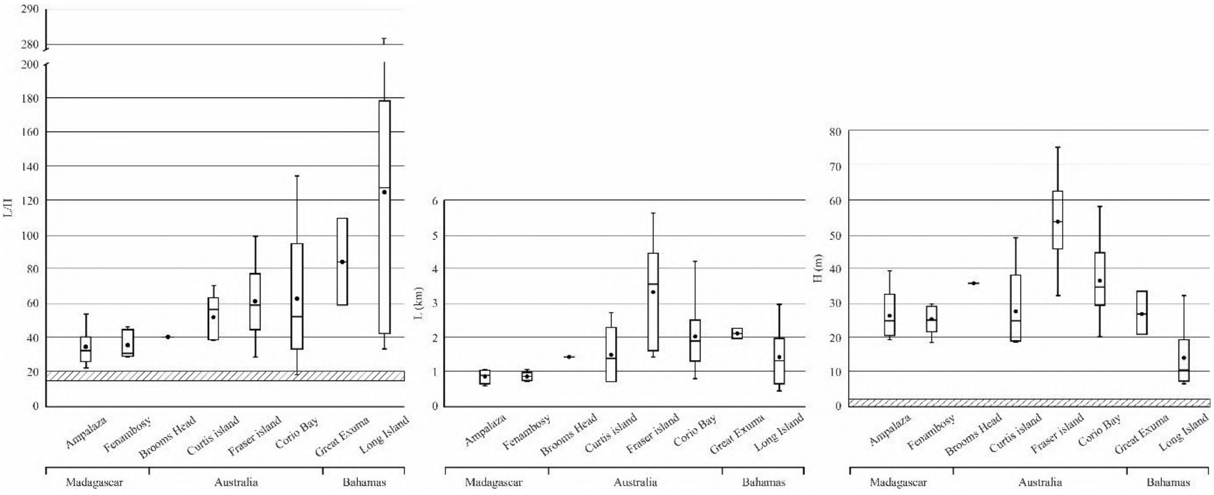

Figure 12: Distribution of L, H and L/H ratios for each location of the three studied regions where stripped zones indicate the range of subaqueous dunes, after Bourgeois and Weiss (2009), for each parameter. It does not appear on the L graph because of a much smaller order of magnitude.

5.3 Eolian hypothesis

In the Bahamas, a few studies argued that fenestral porosity does not only occur in intertidal environments (Bain and Kindler, 1994; Kindler, 1991; Kindler and Strasser, 2002, 2000), implying their occurrence in chevrons may not be necessarily related to large waves.

High-elevation fenestrae have been observed in eolianites of early MIS 5e, middle Pleistocene, and Holocene age in the Bahamas (Engel et al., 2015), which disagrees with Hearty et al. (1998) who restricted these features to the late MIS 5e chevrons and runup deposits. Stieglitz and Inden (1969) had already interpreted fenestrae within a spillway as the results of heavy rains. Moreover, Kindler and Strasser (2002, 2000) observed pin-stripe laminations in the run-up deposits and chevron ridges, and argued that such extensive, mm-thin lamina with an erosive base, that show an inverse grain-size grading in well-sorted sands devoid of gravel-size debris of marine origin, are typical eolian features. They further agreed that backwash-generated, low-angle cross-strata can also display inverse grain-size grading, but at a larger scale (1-2 cm thick) and are not as extensive. In addition, they reasoned that chevron morphology does not correspond to that of washover fans (Figure 11), which exhibit landward dipping plane beds (Schwartz, 1982), and point in a downwind direction paralleling the axes of the northeasterlies that constantly blow the Atlantic coast of the Bahamas (Kindler and Strasser, 2000).

The more complete sedimentological assessment of Malagasy chevrons by Bourgeois and Weiss (2009) and their comparison with the Palouse parabolic dunes suggest a similar formation process for both bedforms (Table 1). Their measurements of bedform characteristics show two distinct ranges for subaqueous and eolian deposits. They added that features similar to chevrons are common in continental interiors, sometimes related to bodies of water. They also modelled the wave approach pattern and compared it to the orientations of chevrons along the Malagasy coast (Figure 9). Considering a small impact in deep water and the regional bathymetry, the resultant refraction and reflection involved when potential tsunamis approach the S-Madagascar coastline are not aligned with chevron orientations. The wave crests would have been parallel to the shore and with a perpendicular approach to it. Finally, they modelled the transport conditions occurring in a flow able to deposit a chevron. They have listed several factors influencing basic bedforms characteristics (L and H): settling velocity, shear stress, flow depth, bed erodibility (e.g., vegetation) and roughness (k_s), sediment supply, flow structure and grain size (D). They defined dunes as features scaled by excursion length of grains, where sediment availability and flow depth (h) are the limiting factors of growth with a ratio of H <0.5h. Given that the majority of chevrons have an elevation between 10 and 100 m.a.s.l (Scheffers et al., 2008); the minimum flow required would have reached more than 200 m.a.s.l.. Moreover, the Rouse number (p) is an indicator of the type of transport adopted by particles under specific flow conditions. When it exceeds 2.5, bedload transport prevails, whereas when it is inferior to 0.8, only suspension load conditions occur and so the wash out of the bedform (Shen and Julien, 1993). This dimensionless number is a relationship between grain settling velocity (w_s), shear velocity (u_*) and the von Kármán constant (Vanoni, 1975; Yalin, 1977). By examining p and h under varying $k_{s,}$ D and Froude number (Fr), none of the modelled configuration generates pure bedload transport resulting in an instability of the bedform (Figure 9). Therefore, they concluded by rejecting the tsunami hypothesis and by defining the chevrons in Madagascar as parabolic dunes.

5.4 Associated deposits

Concerning the megaboulders described in Eleuthera, Rovere et al. (2017) used geological field surveys to model wave propagation and define boulder transport equations. They concluded that a storm of a "normal amplitude", meaning of historical intensity, combined with the high sea-level during MIS 5e could have transported the megaboulders from the cliff-edge, thus nuancing the "super storms" and "giant waves" assumption. Following this publication, Hearty and Tormey (2018a) and Rovere et al. (2018) exchanged comments by mutually criticizing each other's methodology.

The impact-generated tsunami explanation, mostly carried by the Holocene Impact Working Group, sparked controversy given its potential significance for past climate reconstructions and future previsions. In fact, the Burckle crater represents one case among hundreds others listed in the Expert Database on Earth Impact Structures (*http://tsun.sscc.ru/nh/impact.php*), defined as "more liberal" than the Earth Impact Database (*http://www.unb.ca/fredericton/science/research/passc/*). Pinter and Ishman (2008), in a concise dissertation and later cited by Bourgeois and Weiss (2009), quoted Carl Sagan (undated), "extraordinary claims require extraordinary evidence" while challenging the mega-tsunami interpretation. They qualified the Burckle crater as "dimple" and stipulated the absence of the associated "impact ejecta" for the K-T impact. According to them, the latter is more likely to be the result of the accumulation of micrometeorites that fall constantly on the surface of the Earth.

6 Methods

6.1 GIS analysis

Digital elevation models (DEM) were GIS analysed to quantify the geomorphological parameters of chevrons in the Bahamas, Madagascar and Queensland. The Fundamental Horizontal Accuracy (FHA) is about 5 m for Queensland, approximatively 12 m for south Madagascar and the Bahamas, whereas the Fundamental Vertical Accuracy (FVA) is

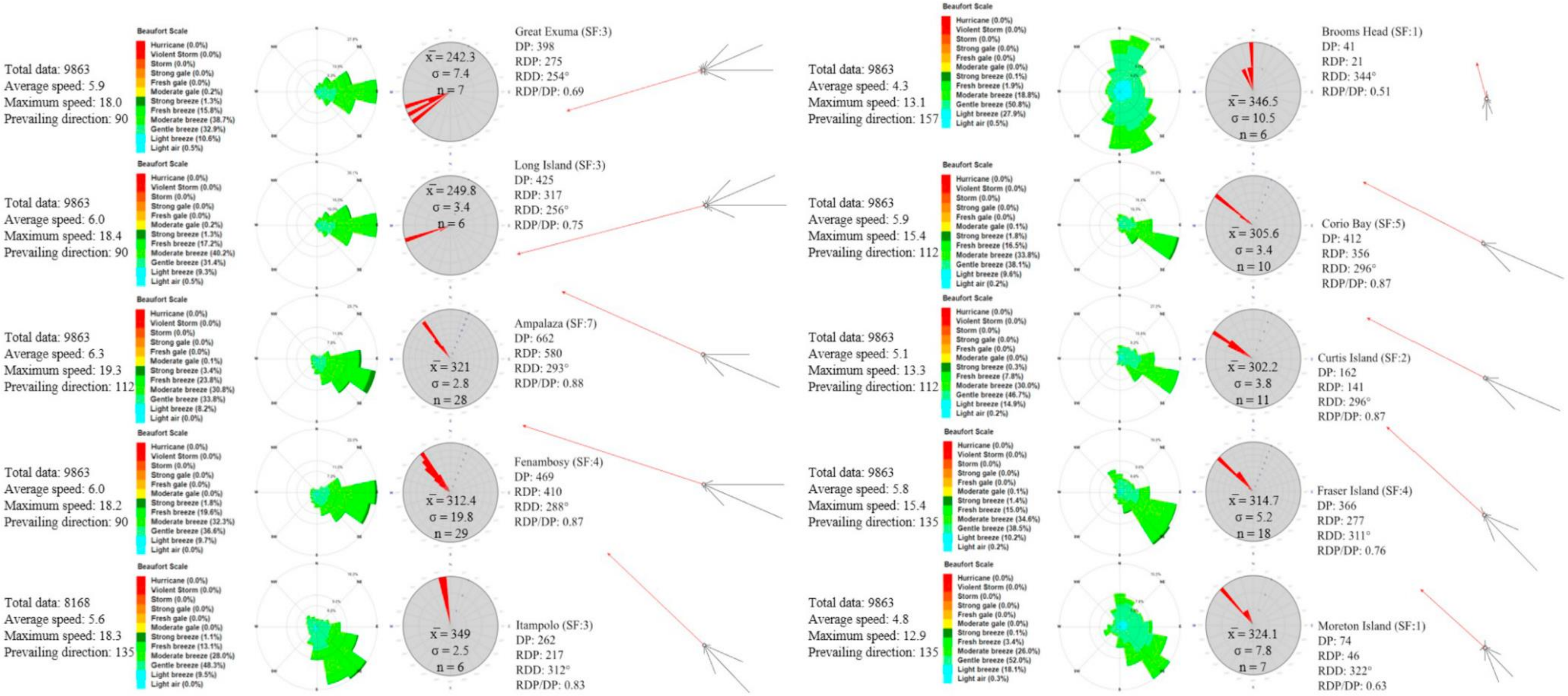

Figure 13: Columns 1-3 and 6-8: Wind regimes analyses with average and maximum speed plus the prevailing direction of wind. Proportions of each Beaufort class expressed in percentages of the time wind blew, next to windroses. Column 4 and 9: Rose diagrams showing the measured orientations of chevron ridges with the average direction, standard deviation and number of measurements. Column 5 and 10: Sand roses obtained by DP analysis with total DP, RDP, RDD and RDP/DP.

respectively of 0.8 m and of 0.0 to 2.0 m (ICSM, 2010; Wessel et al., 2018). Three bedform characteristics were precisely quantified (Figure 12) to generate a database comparable to that proposed by Bourgeois and Weiss (2009), which was partially based on estimations from the literature: L (km), W (km) and H (m). L is the mean of the lengths of both arms, W is the mean of at least three values measured between the shortest arm and the lobe (defined as where the topography significantly increases beyond the trend of the arm crest), and H is the maximum height measured between the crest and the average altitude of the surrounding floor. For each location, chevrons directions were measured and plotted as rose diagrams (Figure 13) with their mean ($\overline{x}$), standard deviation (σ) and number of measurements (n).

Table 2: Fryberger's classification of wind regimes (Fryberger and Dean, 1979) using DP analysis and the corresponding studied locations (this study).

DP (vu)	DP (m3 m-1 year-1)	Energy of wind direction	Locations
< 200	< 17	Low	Brooms Head, Moreton island, Curtis island
200 - 400	17 - 33	Intermediate	Itampolo, Fraser island, Great Exuma
> 400	> 33	High	Corio Bay, Long Island, Fenambosy, Ampalaza
RDP/DP	**Variability**	**Probable category**	**Locations**
< 0.3	Low	Complex / Obtuse bimodal	
0.3 - 0.8	Intermediate	Obtuse / Acute bimodal	Brooms Head, Moreton island, Great Exuma, Long Island, Fraser island
> 0.8	High	Wide / Narrow unimodal	Itampolo, Curtis island, Corio Bay, Fenambosy, Ampalaza

6.2 Wind analysis

The wind speed-direction data measured by satellite were collected from the POWER Release-8 database of NASA (Stackhouse et al., 2018), and wind parameters were estimated at the 10-m height according to the meteorological convention. They range from January 1st 1990 to January 1st 2017, at the rate of one measurement per day, and were collected for Great Exuma and Long Island in the Bahamas; Ampalaza, Itampolo and Fenambosy in S-Madagascar; and five costal locations (Brooms Head, Corio Bay, Curtis Island, Fraser Island and Moreton Island) in Queensland (Appendix 3). Analyses of wind regimes were performed with WindRose PRO© and plotted as wind roses (Figure 13). The latter express the distribution of wind speed and direction, using the Beaufort scale where the label "Moderate breeze" corresponds to the impact threshold shear velocity of wind. The amount of data used, the average and maximum speed (in $m.s^{-1}$), and the prevailing wind direction are calculated for each place. To avoid any bias pointed out by several studies (Bullard, 1997; Miot da Silva and Hesp, 2010; Pearce and Walker, 2005; Silva et al., 2008), the collected wind speed data, expressed in $m.s^{-1}$, were converted in knots (kts) when applying the Fryberger method.

6.3 Sand drift potential analysis: the Fryberger method

The Fryberger method (Fryberger and Dean, 1979) uses wind direction and speed to calculate the sand drift potential for the 16 compass points (N, NNE, NE, ENE, E, ESE, SE, SSE, S, SSW, SW, WSW, W, WNW, NW and NNW). Taking up the equation of Lettau (1978), Fryberger and Dean (1979) added the weighting factor for velocity classes (stronger winds have greater weightings) and simplified the equations into:

$$Q \propto V^2(V-V_t)t$$

where Q is the rate of sand drift expressed in vector units (vu), $V^2(V-V_t)$ is the weighting factor expressed as a function of the wind velocity V at 10 m height, and the impact threshold shear velocity of wind V_t at 10 m, and t the time wind blew expressed as a percentage. The impact threshold shear velocity (estimated at 12 knots under dry conditions; Fryberger and Dean, 1979) is the minimum velocity of a fluid required to initiate saltation of quartz sand grains (Bagnold, 1936). When carbonate grains are of similar size, shape and density (e.g., ooids), the transport threshold is very similar to that of quartz (Prager et al., 1996).

Once the drift potential values are calculated for all wind speed-direction data, it is possible to retrieve the resultant drift potential (RDP), also expressed in vector units, and the corresponding resultant drift direction (RDD). Because values vary over several order of magnitude, a scale factor (SF) representing a reduction factor was allocated to sand roses for comparison and ease of presentation. A fourth variable, the ratio RDP/DP, was calculated to understand the variability of the wind direction. Ranging from 0 to 1, a high RDP/DP stands for a unidirectional wind regime whereas a low ratio suggests multidirectional winds cancelling each other's DP (Fryberger and Dean, 1979). By combining these variables, the type of wind regime can be categorized (Table 2).

7 Results

Chevrons exhibit lateral extensions ranging from 0.45 to 5.7 km, heights between 7 and 75 m, and L/H ratios going from 18 to 282 (Figure 12). During the past thirty years, winds have blown with an average speed above the impact threshold shear velocity (~5.5 $m.s^{-1}$) in most studied places, except at Brooms Head and Moreton Island (Figure 13). In Great Exuma and Long Island, wind conditions with the capacity to trigger saltation represent respectively 56% and 59% of the time. In South Madagascar, it is 58% in Ampalaza, 54% in Fenambosy and 42%

in Itampolo. Finally, wind blows above the threshold 21%, 52%, 38%, 51% and 30% of the time respectively in Brooms Head, Corio Bay, Curtis Island, Fraser Island and Moreton Island.

Chevrons (aka parabolic dunes according to many authors in many of the mentioned locations) azimuths show a narrow distributivity with a maximum standard deviation of 19.8 for the Fenambosy site, and a strong correlation with RDD (Figure 14). DPs indicate a wide variety of environments in terms of wind energy, but every time under a system that tends to be unimodal with RDP/DP ratios within obtuse/acute bimodal to wide/narrow unimodal ranges (Table 2).

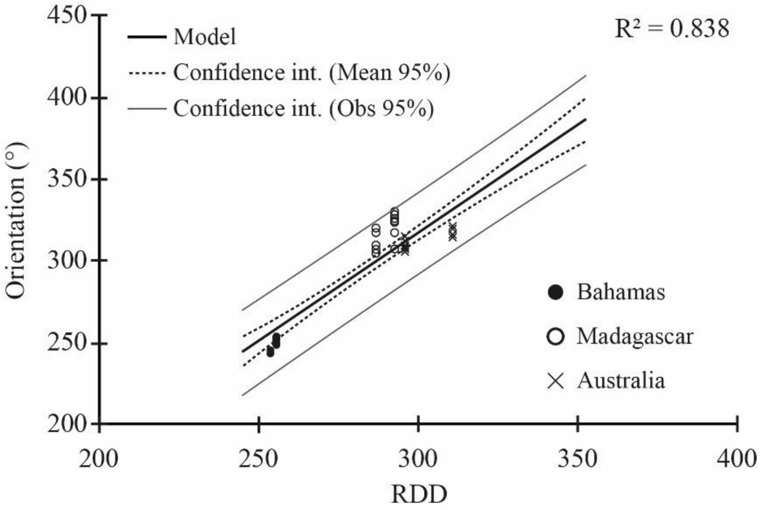

Figure 14: Linear regression model for chevrons azimuths on RDD showing a strong correlation between the two variables.

8 Discussion

The morphological parameters of chevrons need to be interpreted by region for obvious reasons such as difference in composition, ground, vegetation, precipitation rate, climatic zone and sediment supply. Since the most extended and highest dunes are not necessarily the ones associated with the greatest DP, RDP or the most unimodal wind regimes, L and H should be controlled by other factors (Hack, 1941; Hugenholtz, 2010; Rubin and Hunter, 1982; Wasson and Hyde, 1983). However, distribution of L, H and L/H of chevrons is undoubtedly above the range of subaqueous bedforms and correspond to values given for parabolic dunes (Bourgeois and Weiss, 2009; N. Lancaster, 1994).

The wind regimes and drift potential analyses reveal that wind blows above the impact threshold shear velocity with an acute bimodal or unimodal configuration most of the time, and for the great majority of the studied locations. Despite wind regimes being low, intermediate and high energy environment, the dominant Beaufort class to blow and actively induce grain mobilization in every region is the “moderate breeze” (5.5 to 7.9 m.s^{-1}). In this environment, chevrons azimuths are strongly correlated to RDD (Figure 14), which suggests an eolian origin for these deposits. The studied chevrons lie in different regions corresponding to different climate zones, vegetation type, sediment availability and composition. The Bahamas and South-Madagascar are classified as tropical savanna climates (*Aw*) according to the Köppen climate classification (Peel et al., 2007a), which have a pronounced dry season (less than 60 mm of precipitations for the driest month) and a wet season that receives less precipitation than the similar tropical monsoon season. Usually, this category is characterized by tall grass and short deciduous trees or rampant-type vegetation. The studied areas in Queensland lie in a humid subtropical climate zone (*Cfa*), defined by hot and humid summers, and mild to chilly winters. The vegetation comprises evergreen trees, shrubs and bushes. The annual precipitation ranges from 1000 to 2000 mm, moistening sand and increasing the impact threshold minimum. The different types of vegetation, which plays a key role in stabilizing the arms of the dune and driving the parabolic shape, act differently on sand migration in the considered regions. Nonetheless, the recurrence of the “U” and “V” shape, the correlation between chevrons azimuths and RDD, and the similar type of wind regimes agrees with Wolman and Miller (1960) and Bagnold (1941), who showed that net transport, dune form and orientation are parameters controlled by recurring winds above the impact threshold rather than by brief sporadic episodes of wind gusts.

As it has been a major argument to seek for alternative explanations concerning their formation, the Fryberger method proves that chevrons are effectively aligned with the dominant ***drift potential*** direction, which agrees with the principle of Occam’s Razor cited by Bourgeois and Weiss (2009): the simpler explanation is usually the better. Regarding the numerous arguments given in the literature and the new data provided in this study, it is reasonable to argue that chevrons are mostly, if not all parabolic dunes and that scientists should get rid of the term “chevron”, which has proven to be confusing, and provides little to no indication of the true genesis of most deposits claimed to be such.

So not only does wind regime control the orientation of landforms, but it is also a major component of processes shaping parabolic dune complexes or dune-field systems. One of the most interesting aspect of the data is the correlation between present wind regimes and some morphological parameters of Holocene or Pleistocene-dated chevrons. Thus, the latter seem to act as paleo-wind proxies arguing for unchanged wind regimes, at least of drift potential directions, since the LIG. Wind regimes during Holocene are more easily studied because it is a recent period, but as stated by Opdyke (1961), the wind belts during the Pleistocene were similar to the present ones, despite a significant difference in global temperature (Mackenzie, 1964). Given the wide distribution of “chevrons” on the world’s coasts (Figure 5), they could be useful to reconstruct global paleo-wind circulation at different periods of the recent past.

9 Conclusions

We have reviewed the distribution, morphology, sedimentological characteristics, geochronology, and the different interpretations pertaining to the mode of formation of chevron ridges. We further proposed a general wind-related analysis in three coastal locations along three oceans in two different climate zones. The main conclusions of this review and of our new analysis are as follows:

- chevron ridges are commonly found lying on or near coastlines but can also be observed in continental interiors.
- there are eight different types of so-called chevron, actually parabolic dune, morphologies, six of which exhibit a central depression framed by elevated crests. Alleged chevrons have a km-scale length, tens to thousands m-size width and a plurimetric thickness. The measured values for these morphological parameters are well above the range of subaqueous bedforms and correspond to values given for parabolic dunes.
- sedimentological features commonly present within chevrons are subparallel, low-angle, aggrading, seaward dipping beds with few interruptions and truncations. An alternation with cm-scale, fenestrae-rich beds can be observed in the Bahamas occurrences. Some authors have also observed subcritically climbing translatent strata (SCTS) which are typical of eolian transport.
- the age of the studied chevrons extends from the LIG and the Late Holocene.
- Chevrons azimuths show a narrow distributivity and a strong correlation with the resultant drift direction (RDD) of the wind, whereas in many cases, they are not aligned with the dominant swell or estimated wave directions associated with possible tsunamis, or similar.

The presence of characteristic eolian sedimentary features (SCTS) within chevrons and the correlation of their morphology with wind regimes rather suggest that strong unidirectional, constantly blowing winds reworking exposed subtidal to intertidal and backshore sediments are a more plausible explanation for their origin than a rapid dramatic hydrodynamic process.

Consequently, the term “chevron” should be banned from the literature if it is to be used as defined in this paper, in order to avoid any possible confusion. Finally, these deposits appear to be a useful tool to reconstruct wind environments of the past and constrain paleoclimatic models.

10 Acknowledgments

This project was funded by the department of Geology of the University of Geneva. Many thanks to the Earth Observation Center at the German Aerospace Center (DLR) for generously providing the DEMs needed. We acknowledge André Strasser for his guidance during the initial stages of writing this review. We thank Patrick Hesp for his detailed and helpful review that provided us the guidance to improve this manuscript.

Chapter 3 – Upper Pleistocene parabolic ridges (i.e., “chevrons”) from the Bahamas: storm-wave sediments or aeolian deposits? A quantitative approach.

This chapter addresses the formation process of “chevron” dunes in the Bahamas and how they are correlated to past climate conditions in the region.

Published as:

Vimpere, L., Del Piero, N., Shawwa, N. A., Beguelin, K., Kindler, P., & Castelltort, S. (2021). Upper Pleistocene parabolic ridges (ie ‘chevrons’) from the Bahamas: Storm-wave sediments or aeolian deposits? A quantitative approach. Sedimentology, 68(3), 1255-1288. DOI: 10.1111/sed.12828

Abstract

The Upper Pleistocene (Marine Isotope Stage 5e; ∼120 ka) stratigraphic record from the Bahamas comprises large, km-long parabolic ridges of oolitic composition, that point landward, and have been up to now called “chevrons”. A debate about their genesis has led previous researchers to consider two processes of deposition: 1) a catastrophic event involving giant storm-generated waves produced by specific climatic conditions at the end of MIS 5e; 2) a more uniformitarian process which characterises “chevrons” as aeolian parabolic dunes because of their similar morphology. Since there are few unequivocal sedimentological criteria to discriminate aeolian from water-deposited sediments, only a quantitative, multi-method approach could provide enough arguments to produce a viable diagnosis on the genetic processes involved. Following this reasoning, the quantification of the morphological parameters of “chevrons”, a precise study of their sedimentary structures on previously and newly discovered sections, and several statistical grain-size analyses, all advocate for an aeolian origin. Moreover, when the aforementioned characteristics of “chevrons” are compared with those of storm deposits (e.g., washovers) and parabolic dunes occuring elsewhere on Earth, the dissemblance with the former and the resemblance with the latter is evident. Amino-acid racemization (AAR) dating, together with stratigraphic and petrographic investigations, constrain the “chevrons” age to the late part of MIS 5e. Their occurrence during this specific time interval can be explained by both strengthened easterly winds and drier climatic conditions

associated with a changing vegetation cover. Fixation of the arms by a sparse vegetation, coupled with the loose "chevron" nose sediment migrating farther inland, form the peculiar U-shaped morphology of these ridges.

1 Introduction

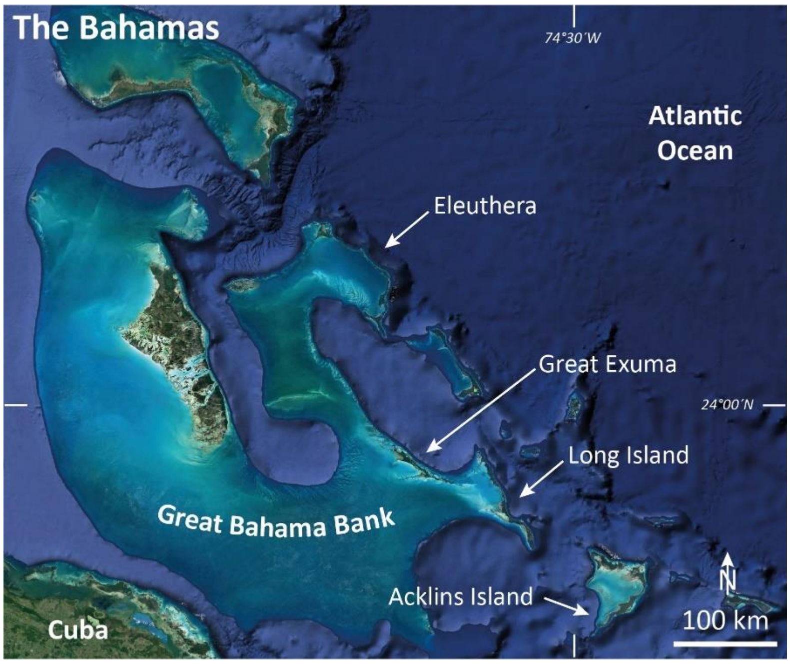

Figure 15: Google Earth satellite image of the Bahamas with the location of the four studied islands.

Up to now called "chevrons", the peculiar V- and U-shaped oolitic ridges of Late Pleistocene age exposed on several Bahamian islands have drawn the attention of numerous researchers for almost two decades (Bourgeois and Weiss, 2009; Donovan and Tormey, 2015; Engel et al., 2015b; Hansen et al., 2020, 2016, 2013; Hearty et al., 2015, 2002, 1998; Hearty and Tormey, 2018b, 2018a, 2017; Kindler and Strasser, 2002, 2000; Mylroie, 2018a, 2018b; Rovere et al., 2018, 2017; Tormey, 1999; Tormey et al., 2018, 2016; Tormey and Donovan, 2015; Vimpere et al., 2019). However, despite the numerous studies pertaining to these landforms, both their formation mechanism and their climatic significance remain uncertain and controversial. Two conflicting hypotheses have so far been proposed: (1) Hearty et al. (1998) first suggested that large, long-period waves generated by distant "superstorms" dumped sediments in a hairpin form onto the islands at the end of the substantially warmer Last Interglacial period (LIG; Marine Isotope Stage 5e; 126-113 ka BP; Thompson et al., 2011); (2) by contrast, Kindler and Strasser (2002, 2000) inferred a wind-driven formation process for these deposits because of the number of similarities between "chevrons" and aeolian parabolic dunes.

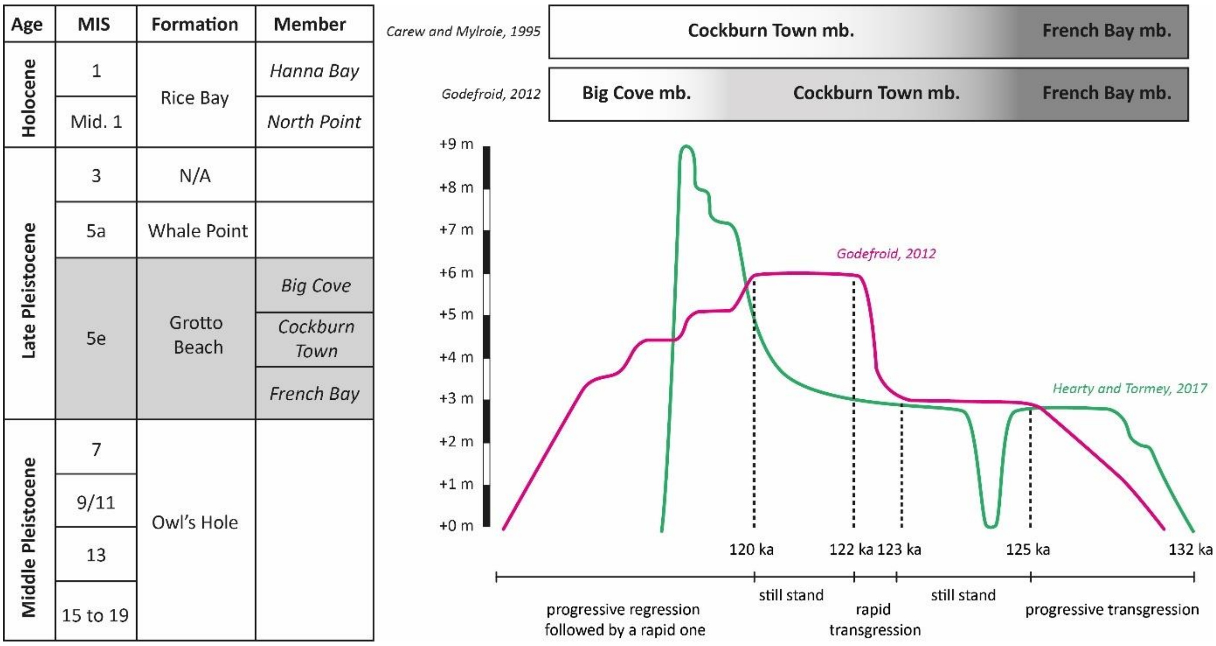

Age	MIS	Formation	Member
Holocene	1	Rice Bay	*Hanna Bay*
	Mid. 1		*North Point*
Late Pleistocene	3	N/A	
	5a	Whale Point	
	5e	Grotto Beach	*Big Cove*
			Cockburn Town
			French Bay
Middle Pleistocene	7	Owl's Hole	
	9/11		
	13		
	15 to 19		

Figure 16: Stratigraphy of the Bahamas islands and its relationship to sea level during the LIG. Description of the eustatic phases and ages correspond to the sea-level curve proposed by Godefroid (2012). Note that the boundaries between members cannot be attributed precisely to a specific sea-level stand.

The first assumption concurs with the so-called "ice-surge hypothesis" (DeConto and Pollard, 2016; Hansen et al., 2016; Hollin, 1965; Mercer, 1978; Neumann and Hearty, 1996; Wilson, 1964), which portrays a rapid transgression and catastrophic climatic changes at the end the LIG linked to a collapse of Antarctic ice sheets. These events would have facilitated the formation of giant waves by chain-reaction, notably by strengthening pressure, temperature and moisture gradients adjacent to warm tropical waters (Hearty and Neumann, 2001). Hearty et al. (2002, 1998) and Hearty and Tormey (2017) further identified a "trilogy" of field evidence for long-period wave deposits in the Bahamas: (1) the "chevrons", which accumulated in lowland areas under this morphology because of the rapid loss of wave kinetic energy; (2) seven "megaboulders", up to 2'000 tons in weight, some of which stand on top of a 20 m-high cliff at one location in Eleuthera; and (3) stacked, seaward-dipping "run-up" deposits including scour structures and "rip-up" breccias. The occurrence of fenestral porosity in both "chevrons" and "run-up" deposits is presented as an additional evidence of a wave-induced origin for these landforms because fenestrae (i.e. keystone vugs) are commonly associated with wave-swash action (e.g. Dunham, 1970).

The second hypothesis relies on the morphological resemblance between aeolian parabolic dunes and "chevrons" (Engel et al., 2015b; Kindler and Strasser, 2002, 2000) and on the alignment of the latter with the present resultant drift direction of carbonate sand generated by north-easterly winds (Vimpere et al., 2019). The occurrence of rhizoliths, land snails, and the omnipresence of climbing translatent stratification (CTS) within "chevrons" and "run-up" deposits further argues for an aeolian origin, as these fine structures are by and large considered as diagnostic of wind processes (Caputo, 1993; Frébourg et al., 2008; Fryberger and Schenk, 1988; Hunter, 1977; Loope and Abegg, 2001; Loucks and Ward, 2001; McKee and Ward, 1983; White and Curran, 1989). In this hypothesis, fenestral pores are interpreted as resulting from the effect of rainfall. This formation process has been observed in modern coastal dunes (Emery, 1945; Frébourg et al., 2008) and in a subaerial dam spillway (Stieglitz and Inden, 1969), and also reproduced experimentally (Bain and Kindler, 1994). Fenestrae have also been described from aeolianites of Holocene (Engel et al., 2015; Loucks and Ward, 2001) and Pleistocene age (Bain and Kindler, 1994; Frébourg, 2010). Finally, the morphological and sedimentological disparities between well-identified storm deposits (e.g. washover lobes, conglomeratic berms) and "chevrons" (Engel et al., 2015b; Kindler and Strasser, 2002, 2000; Mylroie, 2018a, 2018b; Vimpere et al., 2019) does not agree with a wave origin for the latter. Regarding the "megaboulders", Rovere et al. (2018, 2017) used a wave model to demonstrate the needlessness of evoking "superstorms" as an emplacement mechanism when hurricanes of historical intensity can transport boulders of such sizes. Because of their geographically limited distribution, Mylroie (2008) proposed a cliff-rollback model (boulders rolling down from the cliff edge to overlie a younger unit), which was discussed as the best option by peers (Hasler et al., 2010; Kindler et al., 2010; Viret, 2008).

This study provides new quantitative data on the morphology, sedimentology, granulometry and timing of deposition of "chevrons" from the islands of Eleuthera, Long and Great Exuma. "Chevrons" from Acklins Island were only considered for remote measurements as no field data have been collected there. We aim at resolving the controversy regarding the formation and the significance of these landforms. Figuring out whether these Upper Pleistocene V- and U-shaped ridges from the Bahamas result from large-storm action or from aeolian processes is certainly of importance in the present-day context of anthropologically induced global climatic changes and sea-level rise.

2 Settings

2.1 Geographical settings

Located to the East of Florida and to the North of Cuba, the Bahamian archipelago is composed of a series of isolated, flat-topped carbonate platforms extending for more than 1'000 km along a NW-SE axis. This study concerns three islands situated on the Great Bahama Bank

(GBB; Eleuthera, Great Exuma and Long) and Acklins, which is located on the Crooked-Acklins Bank to the South of GBB (Figure 15). The area was long considered as slowly subsiding in a tectonically stable context (J. Carew and Mylroie, 1995; Lynts, 1970; Mullins and Lynts, 1977), but this tectonic stability has recently been questioned (Kindler et al., 2011; Mulder et al., 2012). Most of the islands are elongated and narrow in shape (Figure 15), and essentially composed of a complex 3D arrangement of wind-blown carbonate sediments of Quaternary age. High-energy conditions along the Atlantic coastlines and quiet lagoonal environments on the bank side lead to sediments being mostly transported from East to West, parallel to the constantly blowing easterlies.

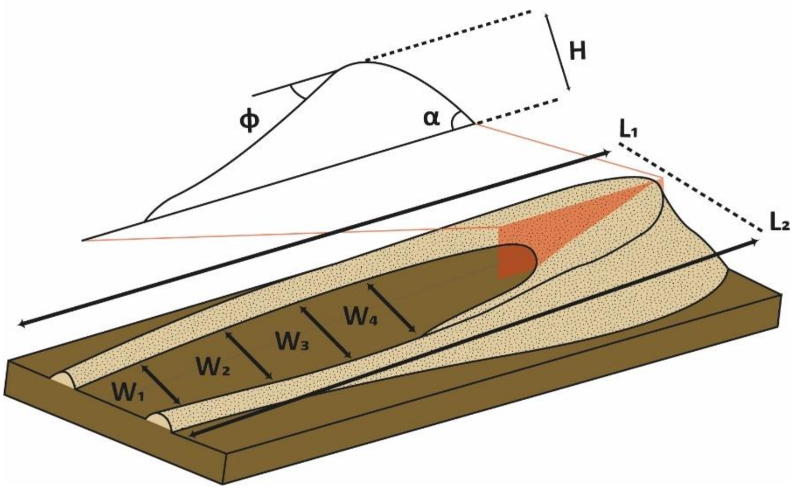

Figure 17: Illustrative sketch of an ideal parabolic dune showing the different morphological parameters measured.

2.2 Present-day and LIG climate in the Bahamas

The Bahamas are located in the tropical monsoon climate zone as defined in the Köppen classification and experience two main seasons largely determined by the movements of the Intertropical Convergence Zone (ITCZ). In the winter, the southward motion of the ITCZ induces temperate-warm, dry, and windy conditions over the archipelago, whereas in the summer its northward shift results in a hot and humid climate with weaker trade winds (Kottek et al., 2006; Peel et al., 2007b). The Bahamian climate is mostly influenced by the latitudinal extension of the archipelago, which leads to a climatic heterogeneity between the northern and southern part. Indeed, whilst temperature is rather constant throughout the archipelago in the summer, it is clearly warmer in its southern part in the winter (Sealey, 2006). Moreover, the average yearly rainfall is 850 mm, but regional variations range from 700 mm to 1500 mm/y (Wolcott et al., 2018), the southern part of the archipelago being much drier than the northern one.

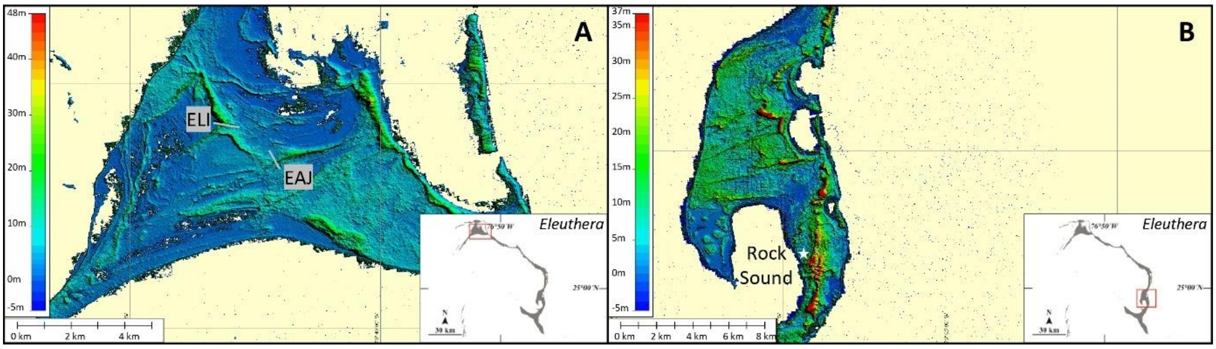

Figure 18: A) DEM of the area near North Eleuthera Airport showing the location of the two sections describing alleged "chevron" arms (ELI and EAJ; e.g. Hearty et al., 1998). No characteristic U- or V-shaped morphologies are discernible. See text for more explanations. B) DEM of the area near Rock Sound Airport, South Eleuthera, where "chevrons" have been identified (e.g., Hearty et al., 1998). No characteristic U- or V-shaped morphologies are visible. See text for more explanations.

The LIG is commonly known as one of the warmest interglacial periods of the last 800 kyr (Past Interglacials Working Group of PAGES, 2016) with a global average temperature estimated at 1.5-2°C warmer than the pre-industrial one (Hansen et al., 2016), and a sea level rise of 6 to 9m above the present one associated to significantly reduced ice sheets (Dutton et al., 2015). As such, it has been used as a potential analogue for future climate models (Hansen et al., 2020; Valérie Masson-Delmotte et al., 2013). Prolonged anomalies of the ITCZ position have long-term effects on the climatic conditions in the tropics, which have been linked with changes in sea surface temperature (SST) and salinity (SSS), Atlantic Meridional Overturning Circulation (AMOC), and ice sheets extent (Gibson and Peterson, 2014; Hoffman et al., 2017; Peterson and Haug, 2006; Zhuravleva and Bauch, 2018). In the Bahamas, a southward shift of the mean annual position of the ITCZ is usually related to cooler and drier stadials with intensified trade winds, whereas a northward shift is linked to higher temperatures, increased precipitation, and weakened trade winds. By studying faunal assemblages, the isotopic signal and XRF data, Zhuravleva and Bauch (2018) advocate a warm/humid and cooler/drier early/late MIS 5e, respectively, which correlates with a SST being higher during the early MIS 5e than during the late MIS 5e (Hoffman et al., 2017). They also determined that a sudden southward displacement of the ITCZ at around 127 ka BP interrupted a warm phase in the early part of MIS 5e and induced an abrupt "Younger Dryas-like event".

2.3 LIG stratigraphy and sea-level history of the Bahamas

The studied V- or U-shaped ridges belong to the Grotto Beach Formation (GBF), which has been correlated to the LIG. The GBF generally overlies the Owl's Hole Formation (Carew and Mylroie, 1985; Figure 16), which comprises both bioclastic and oolitic-peloidal calcarenites of Middle Pleistocene age (Hearty and Kaufman, 2000; Kindler and Hearty, 1996).

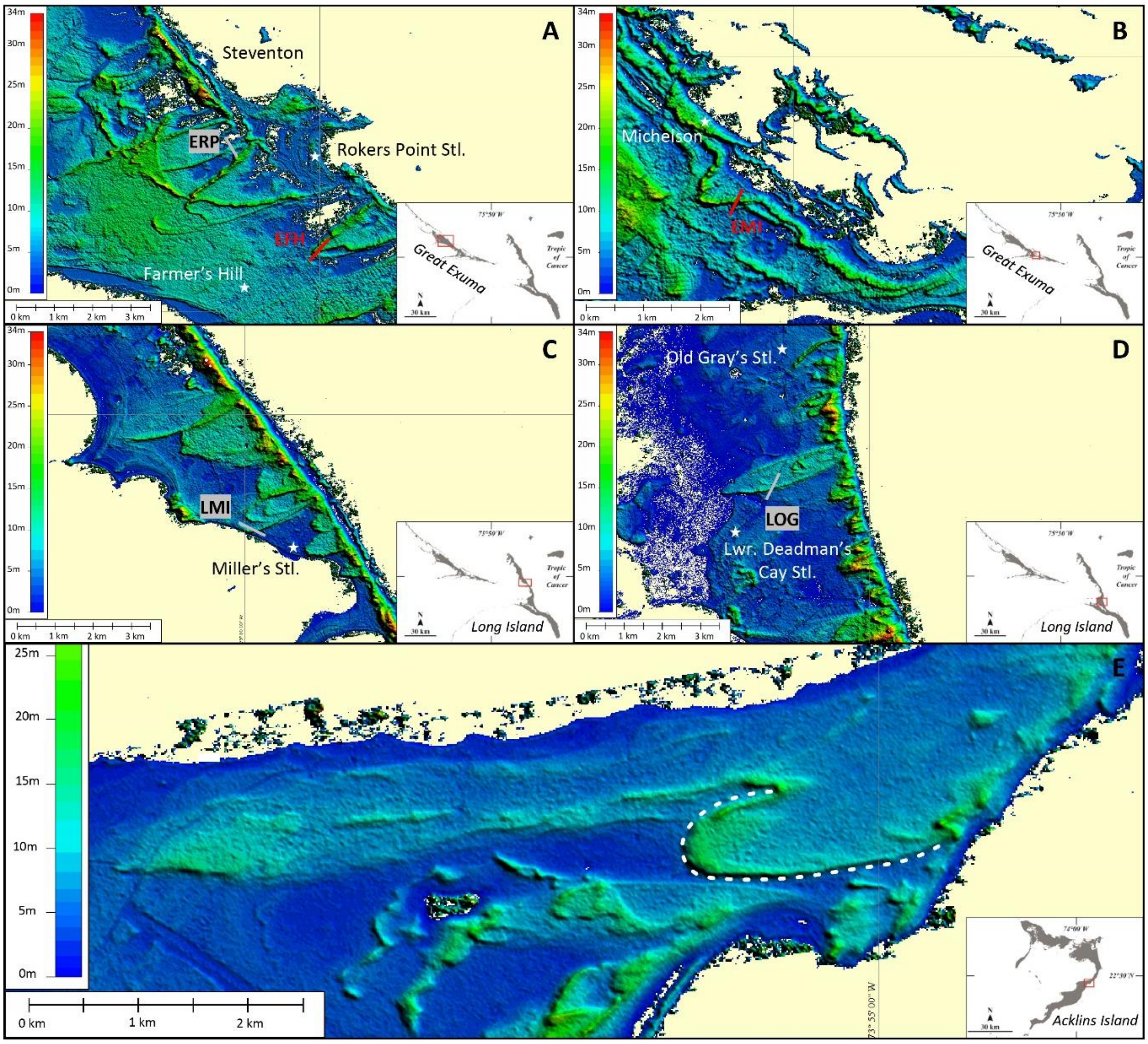

Figure 19: DEMs showing "chevron" morphologies: (A) on the northern part of Great Exuma (EFH = Farmer's Hill section; ERP = Rokers Point Settlement section); (B) at the Michelson section (EMI) on the southern portion of Great Exuma; (C) near Miller's Settlement on Long Island (LMI; e.g. Hearty et al., 1998); (D) near Old Gray's Settlement in the central part of Long Island (LOG; e.g. Hearty et al., 1998); and (F) on Acklins Island where no field data were collected. Refer to text for more details.

It is capped either by bioclastic aeolianites generally correlated to MIS 5a (Almgreen Cay Fm.; Hearty and Kindler, 1993; Whale Point Fm., Kindler et al., 2010) or by the Holocene Rice Bay Formation (Carew and Mylroie, 1985), which includes (1) oolitic-peloidal aeolianites (North Point Mb.; Carew and Mylroie, 1985), and (2) a shallowing-upward succession of mostly bioclastic sediments deposited in beach to dune environments (Hanna Bay Mb.; Carew and Mylroie, 1985). The GBF comprises three members (from base to top):

The *French Bay Member* (FBM; Carew and Mylroie, 1985) consists of a well-preserved oolite showing sedimentary structures typical of the subtidal, intertidal, and mostly the aeolian depositional environments (e.g. Caputo, 1995). It can be correlated with the early part of the LIG based on its position relative to the well-dated overlying unit (see below) and amino-acid racemization (AAR) data (Hearty and Kaufman, 2000). The FBM has been interpreted as transgressive-phase aeolianites of the GBF (Carew and Mylroie, 1985, 2001; J. L. Carew and Mylroie, 1995), or as deposits corresponding to a distinct highstand at the beginning of MIS 5e (Hearty and Kaufman, 2000; Hearty and Kindler, 1993; Kindler and Hearty, 1996).

The *Cockburn Town Member* (CTM; Carew and Mylroie, 1985) comprises coral boundstone/rudstone and shell-rich floatstone corresponding to ancient reefal and lagoonal settings, respectively. The reefal facies is particularly well-represented in Mayaguana (Godefroid, 2012) and Great Inagua (Skrivanek et al., 2018; Thompson et al., 2011). U-Th ages from well-preserved coral samples range between 130 and 116 ka BP (Chen et al., 1991; Kindler et al., 2011; Thompson et al., 2011), allowing correlation with MIS 5e.

The *Fernandez Bay Member* (Hearty and Kindler, 1993), or *Boat Cove Member* (Godefroid, 2012), corresponds to a shallowing-upward succession of oolitic to bioclastic sediments deposited in subtidal, intertidal and aeolian environments, and itconformably overlies the CTM. It can be correlated with the late part of the LIG because of its position above the CTM, and because of AAR data (Hearty and Kaufman, 2000). This succession possibly records a distinct sea-level highstand at the end of MIS 5e (Hearty and Kaufman, 2000; Hearty and Kindler, 1993; Kindler and Hearty, 1996), but can alternatively be interpreted as the regressive-phase deposits of the GBF (Carew and Mylroie, 1985; J. Carew and Mylroie, 1995; J. L. Carew and Mylroie, 1995). Considering the uncertainties pertaining to the sea-level history during the LIG (e.g. Barlow et al., 2018), this specific point remains an open question.

3 Methods

3.1 Morphology

To quantify the specific morphological parameters of "chevrons", we used a Digital Elevation Model (DEM) of the Bahamas generated by the satellite TanDEM-X and provided by the German Aerospace Centre (DLR). The product is a grid given at 0.4 arcsec at the equator (~12 m) with absolute horizontal (AHA) and vertical (AVA) accuracies (respectively expressed as a circular and linear error at 90% confidence level) higher than 10 m. The relative vertical accuracy (RVA) is about 2 m for a slope ≤ 20% and about 4 m for a slope > 20% (Wessel et al., 2018). The length (L), width (W), height (H), stoss-slope angle (φ), slip-face angle (α), L/W and L/H ratios were measured (Figure 17; Appendix 4) on 10 "chevrons" located on three of the studied islands: Great Exuma, Long and Acklins. The collected data were then compared to the ones measured on 95 aeolian parabolic dunes, located in nine countries (Australia, Brazil, Denmark, Libya, Netherlands, Scotland, Spain, USA and Wales) and covering the tropical, subtropical, and temperate zones worldwide (Appendix 5). The same global DEM was used for parabolic dunes measurements. Following the methodology used by Yan and Baas (2017), L expresses the average longitudinal distance between the front of the apex and the tips of the arms:

$$L = {}^{1}\!/_{2}\,(L_1 + L_2)$$

W is the average dune width between the tips of the arms and the lobe, obtained from at least five measurements:

$$W = \sum_{i=1}^{n} {}^{W_i}\!/_{n}$$

The estimations of sand volumes were made by calculating the pile volume defined by computing sample elevations along the perimeter of the ridge. By assembling these elevations, we generated a terrain surface that represents the "chevron" base and allowed us to calculate its volume. Since "chevrons" lie on lowlands, the possibility of having an older substrate forming reliefs below their base is negligible as well as the uncertainty on the sand volume.

3.2 Field method

After recognition of the "chevrons" on the DEM, satellite and drone images were scrutinized to find potential roadcuts or sections exposing their nose part. Sedimentary structures were examined in detail at every exposure. Each dip value of large-scale cross-beds is a calculated average of 20 values taken in the field. Small-scale sedimentary structures were described following the classification developed by Hunter (1977) in siliciclastic deposits and adapted to carbonate rocks by Loucks and Ward (2001). Following their classification, we apply the term bounding surfaces to describe truncation surfaces of different orders of magnitude. First-order bounding surfaces are the most extended, cut across cross-bedding and other dune structures, and are often associated to the development of a protosol. Thus, they represent long-term exposure surfaces and are labelled as such. Second-order bounding surfaces are less extended, bound sets of cross-strata and are truncated by the first order bounding surfaces. Therefore, they illustrate short-term reactivation surfaces that may correspond to short stops in the sedimentation or to a change in the wind direction. We paid particular attention to the occurrence of three stratification types: (1) *climbing translatent stratification* (CTS), which consists of mm-thin, inversely graded laminae generated by the migration of wind ripples across the dune; (2) *grainfall lamination*, which corresponds to mm- to cm-thick laminae produced on the lee side of dunes where flow separation occurs; and (3) *sandflow cross-stratification* that forms cm-thick, lens-shaped laminae resulting from sand avalanching on the dune slip face.

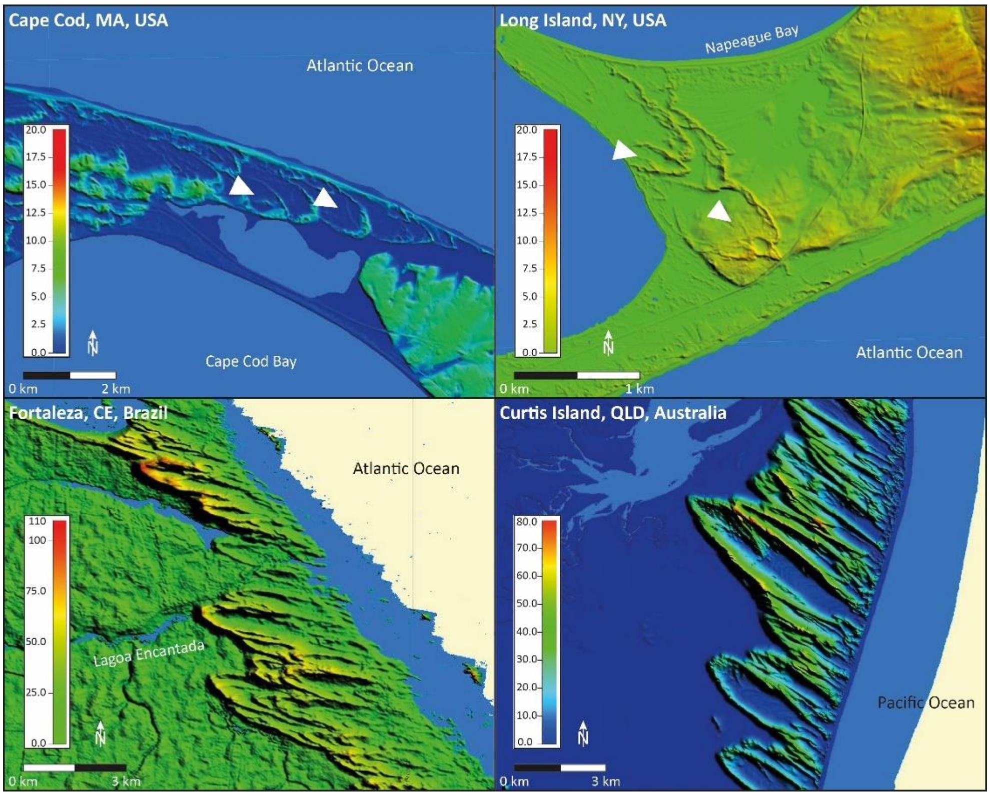

Figure 20: Four examples of the studied 95 parabolic dunes around the world. Note the exceptional dimensions of the coastal dunes in Brazil and along the east coast of Australia (C and D) compared to the ones developing on the eastern coast of the USA (A and B). The formers are more elongated with a narrower deflation basin at their centres whereas the latter are flat-lying, splayed landforms.

3.3 Comparative microfacies analyses

Oriented samples collected in the field (n = 147) were cut, impregnated with blue epoxy, thin-sectioned and then analysed under a Zeiss axioscope petrographical microscope connected to a Leica dfc 450c camera to ascertain their composition, diagenetic alteration, and micro-sedimentary structures such as CTS.

To further clarify the depositional process at the origin of "chevrons", we compared by image analysis the granulometry of these landforms to that of well-identified, *coeval* aeolian and beach deposits. Samples were taken from foresets, topsets and backsets, as well as from planar, wedge-planar and trough cross-beds to avoid representativity bias. Image analysis requires high-resolution scans of thin sections (4000 dpi), which were acquired using a Nikon Super Coolscan 4000. Grain-size investigation was performed by manually measuring in 2D the long-axis diameter of 250 grains per section, using a random grid automatically generated in the image-analysis software *JMicroVision* (Roduit, 2007). This type of grid prevents potential uncertainties generated by a recursive (i.e. regular) one not suited to the mean grain size (Neilson and Brockman, 1977), although the homogeneous character of the studied oolitic deposits avoids any over-representation of large or small particles. The nature of ooids and peloids, being spherical or ovoidal well-rounded carbonate grains, makes the underestimation of a particle diameter generated by the random nature of the section negligible (Higgins, 2000).

The computation of grain-size statistics was done with GRADISTAT v.8 (Blott and Pye, 2001), which is an Excel macro that provides a rapid calculation based on the mathematical "method of moments" (Friedman and Johnson, 1982; Krumbein and Pettijohn, 1938) and the method of Folk and Ward (1957). It uses both metric and logarithmically transformed scales ($\varphi = -\log_2(d)$; where d is the grain diameter), with the same number of classes as the ones proposed by Friedman and Sanders (1978), but with a slightly modified nomenclature (Appendix 6). Calculated parameters include the mean grain size, sorting, skewness, kurtosis and seven different cumulative percentile values (D_{10}; D_{50}; D_{90}; D_{90}/D_{10}; $D_{90} - D_{10}$; D_{75}/D_{25} and $D_{75} - D_{25}$).

3.4 Amino-acid racemization (AAR) dating

In the Bahamas, amino-acid racemization (AAR) chronology has successfully been used to date whole-rock samples and shells of terrestrial gastropods (e.g. Hearty, 2010; Hearty and Kaufman, 2009, 2000; Hearty and Kindler, 1993; Hearty and Schellenberg, 2008). This rapid and inexpensive method commonly provides a reasonable time frame of targeted periods of deposition. Avoidance of possible biases in AAR data was ensured by carefully sampling "chevrons" away from any alteration source and soil (>1 m from the surface). Samples for AAR analysis were collected from grainfall and grainflow laminae in nose sections and from CTS beds in the arm sections.

Four whole-rock "chevron" samples were cleaned until there was no more crust or bacterial mats left to limit the contamination of the supposedly closed amino-acid system by oxidised or externally derived material (Walker, 2005). This operation was made with a small stainless-steel chisel. Then, the samples were powdered to a size comprised between 250 μm and 1 mm. This powdering was performed in a mortar with a pestle, both made of agate, to avoid any type of contamination. It was done softly to prevent any possible warming up of the sample in order to keep a realistic ratio of amino acids (Hollin et al., 1993; Miller and Brigham-

Grette, 1989). Once the samples were powdered, particle sorting was done by dry sieving to constrain the desired range of sizes. Finally, knowing that further procedures would use dilute HCl to remove 30% of the sample mass to reduce the possibility of contamination by cements and organic residues on grain surfaces, we chose a minimum weight of powder of 50 g. Samples were sent to the Amino Acid Geochronology Lab of the Northern Arizona University where the amino-acid content was measured by reverse phase high-performance liquid chromatography (Kaufman and Manley, 1998; Whitacre et al., 2017). D/L-glutamic-acid (Glu) ratios were found to be the most appropriate ratios (Hearty and Kaufman, 2009; Rutter, 1985; Rutter et al., 1979) to date oolitic sediments, and are the only ones used in this study. The conversion method of Whitacre et al. (2017) was applied to our data to calculate the Alloisoleucine/Isoleucine (A/I) values in order to compare them with the database generated in the Bahamas (Hearty and Kaufman, 2009, 2000).

4 Results

4.1 Morphology

4.1.1 "Chevrons" description

The series of ridges located in the vicinity of North Eleuthera Airport do not meet the essential V- or U-shaped morphology to qualify as "chevrons". Indeed, the two sections supposedly exposing "chevron" arms (ELI and EAJ; Hearty et al., 1998; Hearty and Tormey, 2017; Tormey, 1999) cut across distinct linear ridges that are parallel and, respectively, perpendicular to the NW-SE trending Atlantic shoreline (Figure 18A). These straight-lined hills form the western and southern limits of a subdued area where an array of smaller, WNW-ESE oriented ridges occurs. Similarly, the "chevron" located to the North of Rock Sound Airport in South Eleuthera consists of two rectilinear, parallel, WSW-ENE trending ridges that stretch from the Atlantic coast to the lagoon shoreline (Figure 18B). Consequently, the alleged Eleuthera "chevrons" will not be further described as such in the following chapters. On Great Exuma, the "chevrons" are mostly concentrated in the Steventon - Farmer's Hill area (northern part of the island; Figure 19A), where they form several nested sets. A smaller, immature but well-defined one occurs near Michelson (southern part of the island; Figure 19B). Its arms are connected to a breached ridge, which is parallel to the shore. On Long Island, well-identified, elongated, and narrow "chevrons" essentially occur along the Atlantic coast in the central and northern part of the island (Figure 19C and D, Appendix 7). Finally, the U-shaped landform observed on Acklins Island is strongly asymmetric with the NW arm being much shorter than the SE one (Figure 19E).

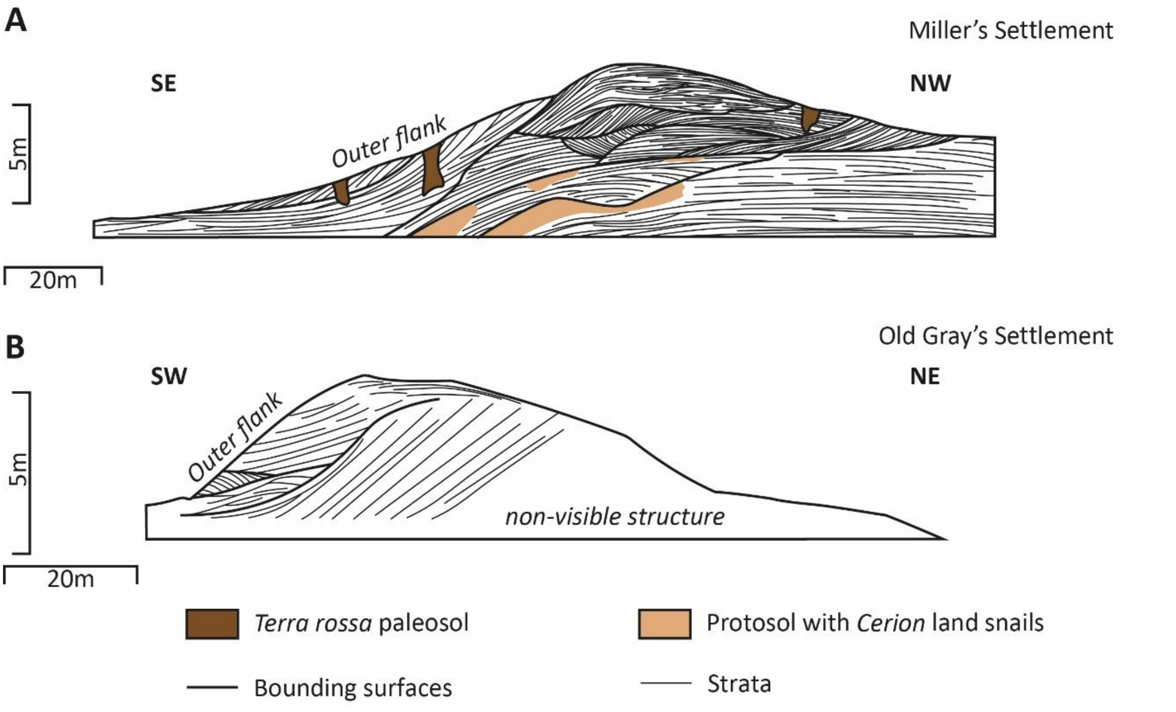

Figure 21: Sketches showing two examples of the internal architecture of "chevron" arms; both exposures are located on Long Island: A) Miller's Settlement (LMI, Figure 18C); B) Old Grays' Settlement (LOG, Figure 19D). Note marked difference in slope angle between the outer and the inner flanks. Sections are retrieved from the DEM and represent the actual morphology of "chevrons" arms.

4.1.2 Morphological parameters of "chevrons" (Appendix 4)

The Bahamian "chevrons" are mostly km-scale landforms, ranging from 0.4 to 3.0 km in length (average = 1.6 ± 0.78 km) and from 0.3 to 1.2 km in width (average = 0.6 ± 0.28 km). They are low-lying deposits between 7 and 33 m high. The mean ratios of these parameters give L/W = 2.68 ± 1.43; L/H = 112.31 ± 76.03 and W/H = 43.12 ± 19.97. They represent consequent volumes of transported sand with a pile volume (see section. 3.1) averaging at 4.97 ± 3.10^6 m^3. Measurements show the typical difference between a steep lee face (11 ± 2°) and a gentle stoss face (2 ± 1°), which characterizes sediment bodies deposited under a unidirectional flow.

4.1.3 Morphological parameters of aeolian parabolic dunes (Appendix 5)

Parabolic dunes (Figure 20), like "chevrons", are mostly km-scale bedforms, ranging from 0.1 to 5.6 km in length (average = 1.07 ± 1.03 km) and from 0.04 to 3.2 km in width (average = 0.38 ± 0.42 km). They show a high variability of height, going from 4 to 90 m and averaging at 29 ± 19 m. The different ratios of these parameters display a high variability: L/W 3.03 ± 1.52; L/H = 47.18 ± 38.11 and W/H = 17.59 ± 15.64. The typical parabolic dune displays a consequent volume of 6.94 ± 22.10^6 m^3. Once again, the difference between the lee (18 ± 9°) and the stoss face (6 ± 5°) is evident with these measurements.

4.2 Sedimentology

4.2.1 Sedimentary structures

The "chevron" arms are asymmetrical in cross-section with the outer flank slightly steeper than the inner one (Figure 21), and mostly composed of low-angle, tabular-planar cross-beds that show a concave-downward aspect towards the edges of the ridge, perpendicularly to its main axis (Figure 22A and B). When the ridge is elongated, the arms present steep foresets (Figure 22C) that are dipping towards the outside, perpendicular to the main ridge axis. It is common to find shallow trough cross-beds cross-cutting other cross-bed sets, mostly near the top of the ridge where they meet topsets or backsets. The sets are composed of either symmetrical or asymmetrical laminae. Front-lobe exposures (Figure 22D and E) reveal dm- to m-thick, tabular to wedge-shape sets of landward-dipping, high-angle cross-strata (dip value up to 30°) that can undeniably be identified as foresets. Indicators of pedogenesis such as rhizoliths, land-snail shells (*Cerion* sp.), and protosols are common within the studied "chevrons". Whatever the nature of the section and the part of the ridge observed, extensive mm- to cm-scale laminae were encountered at every outcrop and can be classified in three groups:

1) In the arm sections, most of the observed laminae do not show an erosional base and follow the pre-existing topography as tabular sets of strata, qualifying as grainfall laminae (Figure 23A). They locally separate sandlfow cross-stratification (Figure 23B), occurring on the outer flanks of the arms, but are barely visible due to the small difference in grain size. By contrast, the grainfall-sandflow alternation is well preserved and often displayed in the nose sections, especially at the front lobe toe (Figure 23C).
2) Due to the steepness of the exposures (i.e., roadcut walls), the lenticular shape of sandflow cross-strata is generally not visible. However, these structures occur in a few sections that cut across the "chevron" slip faces. They are enhanced by grainfall laminae, which are more competent (i.e., cemented) and show sharp, straight basal contacts dipping at high angles (20 to 30°). Grainflow and grainfall stratification are usually observed in their tabular shape but can be found wedging out into bottomsets when the base of the foresets is exposed. In aeolianite foresets, slump sandflows sometimes form

high-angle asymmetric folds in their lower part (Figure 23D; McKee, 1966, p. 66; Mckee and Bigarella, 1972; Pye and Tsoar, 2008).

3) By contrast, CTS are *ubiquitous* in the studied arm sections (Figure 23A) and locally present in front-lobe sections where they interfinger with grainfall lamination and sandflow cross-strata. Their relief is enhanced due to the preferential cementation of the finer part of the inversely graded lamina, which tends to retain pore water more easily because of its high surface tension (Fryberger and Schenk, 1988). CTS are commonly associated with dm-thick fenestrae-rich beds, which may be capped by highly cemented laminae (Figure 23A). Fenestrae are particularly abundant in the "chevron" arms and have been observed at elevations up to 30 m above sea level.

4.2.2 Petrography

The bulk of the investigated deposits consists of pure oolitic to peloidal grainstones (Figure 24). Ooids show different stages of vadose diagenesis that are primarily controlled by their original mineralogy and the packing of the tangential needles forming the cortices (Loucks and Patty, 2017). The major process affecting these grains is the recrystallisation of aragonite and high-Mg calcite into low-Mg calcite with a partial leaching initially affecting the cortices. The rare bioclasts mostly include *Homotrema sp.,* red algae and *Halimeda* sp. (Figure 24). All carbonate grains originated in the ocean and were washed onto the beach, from where they were transported to form the observed subaerial bedforms.

Grainfall laminae form thin levels of fine-grained, well-sorted sand, usually well-cemented. Sandflow laminae are thicker, coarse-grained, poorly sorted, and poorly cemented layers alternating with the thinner grainfall laminations (Figure 24A). Both are delimited by an abrupt change in grain size. CTS are also delimited by abrupt changes of grain size but usually form laminae of equal thickness that show an internal inverse grain-size gradient (Figure 24B). A differential cementation within a lamina, between a highly cemented basal unit and a poorly cemented upper unit, may resemble grainfall and sandflow, respectively. In both cases, low-Mg isopachous and pore-filling blocky cements develop in the fine-grained layers whereas low-Mg calcite, with meniscus and pendant geometries, cement the coarser-grained layers (Figure 24A and B). This vadose cementation is by far the dominant type observable in "chevrons" (Figure 24F) and aeolianites. In contrast to "chevrons" and aeolianites, beach to subtidal deposits do not show such a clear lamination and are generally more cemented (Figure 24C, D and E). In these deposits, typical marine phreatic fabric such as high-Mg and aragonite, fibrous to bladed isopachous cements can be found (Figure 24D and E). Fenestrae are common within “chevrons”, aeolianites, and beach/intertidal deposits.

4.2.3 Granulometry

Grain-size analysis was carried out on 11 beach, 9 aeolianite and 6 “chevron” samples from three Bahamian islands: Eleuthera, Great Exuma and Long (Supp. Data). Among the beach samples, 27% are qualified as fine sand, 27% as medium sand, 9% as coarse sand, and 36% are classified in the gravelly sand textural group. For aeolian samples, 55.5% are composed of fine sand, 33% of medium sand, and 11% of coarse sand. Finally, “chevrons” consist of finer material with half of the corresponding samples being respectively fine-grained, and the other half qualifying as medium sand.

4.3 Amino-acid racemization dating

A/I ratios calculated from D/L Glu ratios measured on the four samples collected from the studied “chevrons” range from 0.39 to 0.48 (Table 3). These values can be assigned to the aminozone E, which has been correlated to MIS 5e by comparison with U-Th ages of stratigraphically equivalent reef terraces (Hearty and Kaufman, 2009, 2000). In particular, the age of the samples gathered from the Farmer’s Hill (Great Exuma; EFH in Figure 19A and Figure 22E) and Miller’s Settlement (Long Island; LMI in Figure 19C and Figure 22A) sections could correspond to the first depositional phase identified in the LIG (5eI; Hearty and Kaufman, 2009, 2000), whereas that of samples from the Rokers Point Settlement section (Great Exuma; ERP in Figure 19A and Figure 22B) and from the Old Gray’s Settlement (Long Island; LOG in Figure 19D and Figure 22E) sections could coincide with the second phase of deposition (5eII).

5 Discussion

5.1 Depositional nature of “chevrons”

5.1.1 Morphological criteria

Based on qualitative morphological observations, other authors (e.g., Engel et al., 2015; Kindler and Strasser, 2002, 2000) previously interpreted Bahamian “chevrons” as aeolian parabolic dunes. In this paper, we provide *quantitative* data that support this interpretation. The comparative 95 dunes (Appendix 5), despite being of different age and composition, were selected because they lie in similar coastal environments (Figure 20) and were all characterised and defined as aeolian parabolic dunes by previous studies. If “chevrons” were deposited by coastal aeolian processes, they are expected to share some morphological criteria, or at least to be of the same order of magnitude as the studied parabolic dunes.

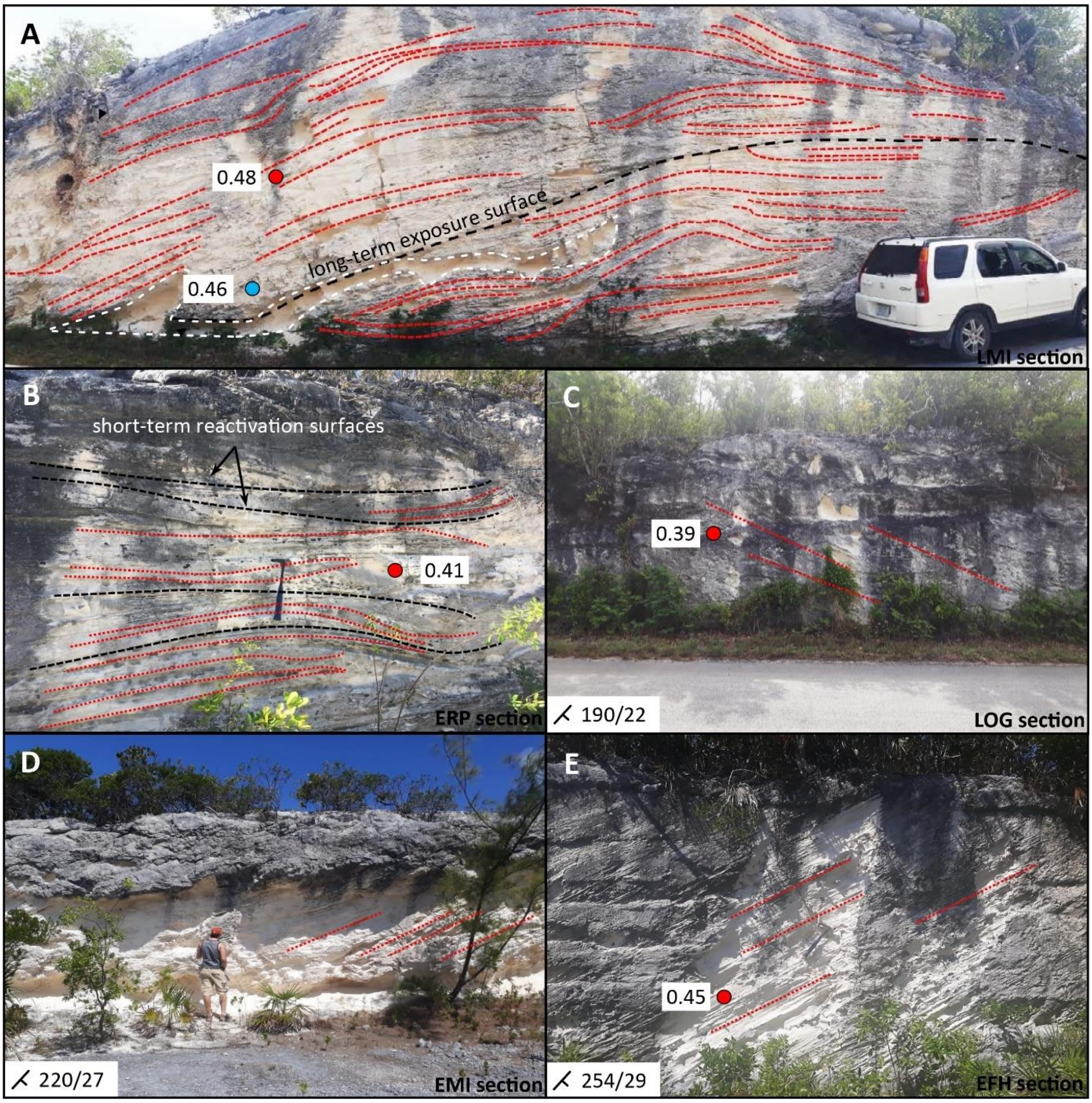

Figure 22: "Chevron" arm sections (A and B) usually display low-angle to sub-horizontal aggrading beds (red dashed lines) and bounding surfaces (black dashed lines). A) Arm section LMI (Figure 19C) where a long-term exposure surface crosscuts the general bedding and show early signs of pedogenesis (white dashed line). B) Arm section ERP (Figure 19A) showing short-term reactivation surfaces delimitating sets of cross-strata. Outcrop is approximatively 4m-high. C) Arm section LOG (Figure 19D) showing steep (22°) foresets dipping S. Their orientation indicates a development of the arm perpendicular to the main axis of the ridge. All AAR ratios obtained in these sections correlate with MIS 5e (red: this study; blue: Hearty et al., 1998). Outcrop is approximatively 4m-high. D) View of an arm section (EMI, Figure 19B) close to the apex of the ridge, showing steep foresets (27°); the dip direction indicates a migration towards the SW. Outcrop is approximatively 3m-high. E) View of a nose section from Great Exuma (EFH, Figure 19A); steep (29°) foresets, dipping towards the SW and aligned with the ridge axis, are visible all along the exposure.

L/W ratios, "chevrons" and parabolic dunes are both described as lobate or elongated with $1.04 < L/W < 5.29$ (Figure 25A). A linear regression modelled from the whole cluster shows a mean L/W ratio = 2.44 with a relatively high coefficient of determination ($R^2 = 0.71$). L/H ratios (Figure 25B) display a larger spread, but once again, "chevrons" plot within the parabolic-dune cluster. Further, the ratio between the stoss-slope and the lee-face angles (φ/α) of "chevrons" and parabolic dunes follows an exponential law with a good level of confidence ($R^2 = 0.61$). In other words, the stoss-slope angle exponentially increases with the lee-side angle (Figure 25C). Further, similarly to aeolian bedforms, the concave lee face of "chevrons" is steeper than the convex stoss slope, indicating a migration by grainfall and avalanching of the material transported from or through the deflation basin. Finally, although the W/H plot (Figure 25D) shows that "chevrons" tend to be slightly wider than high compared to the majority of aeolian dunes, their ranges overlap.

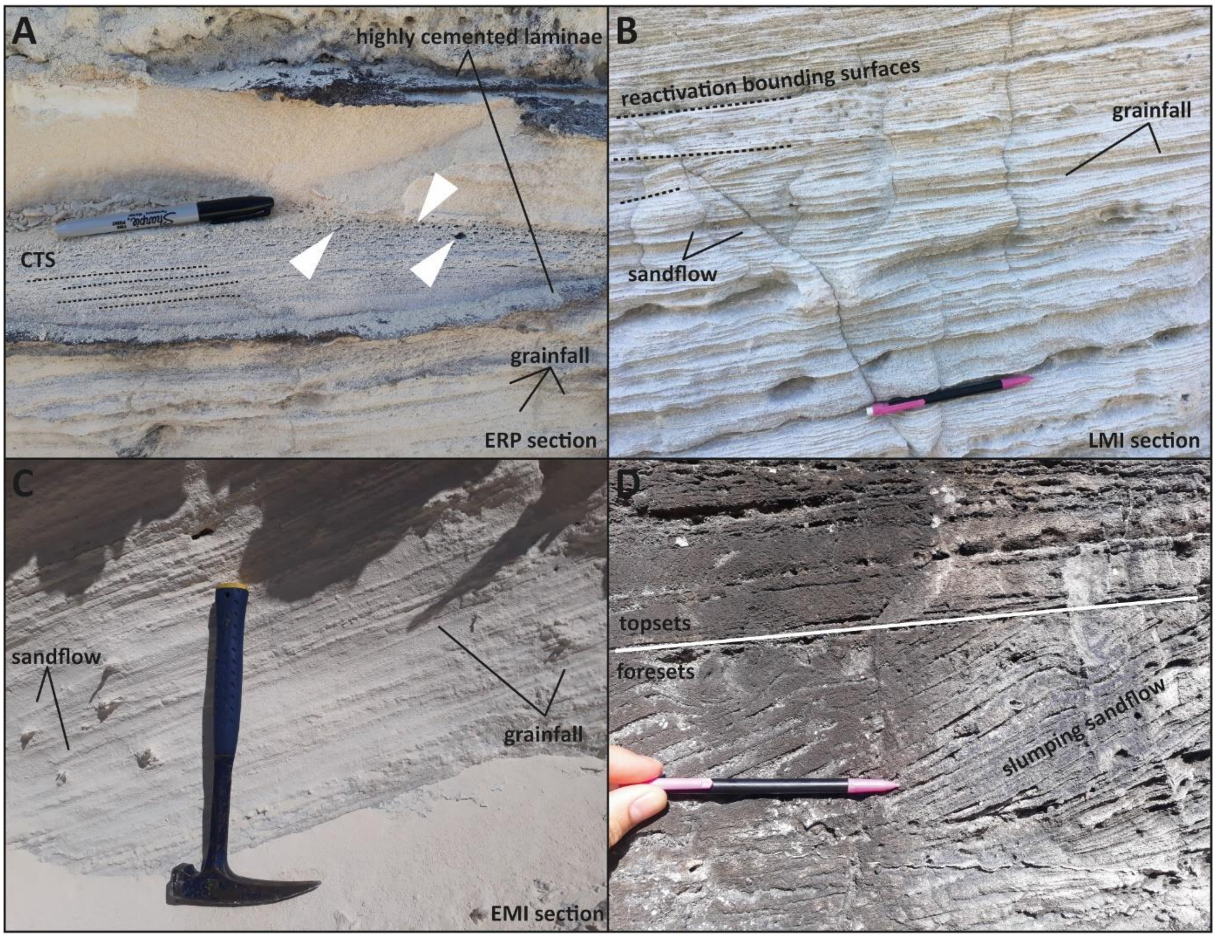

Figure 23: A) a thin bed showing the association of fenestrae (white triangles) crosscutting CTS, bounded by highly cemented laminae. Below and above, grainfall lamination of sub-horizontal aggrading beds are visible. B) Grainfall-sandflow laminae alternation composing the low-angle bedding of the arm section, with some reactivation surfaces. C) Alternation of grainfall and sandflow laminae within foresets. D) Topsets truncating underlying foresets (EX15; N 23°27'47.12"; W 75°43'55.98") where high-angle asymmetric folds correspond to the basal layer of a slumping sandflow lobe (McKee, 1966; Mckee and Bigarella, 1972; Pye and Tsoar, 2008).

As discussed in previous reports (Engel et al., 2015b; Kindler and Strasser, 2002, 2000; Mylroie, 2018a), interpreting "chevrons" as storm-wave deposits does not agree with our present-day knowledge of the latter. Indeed, recent hurricane sediments consist of *localised* sand sheets, conglomeratic berms, and washover fans or lobes (Figure 26; Donnelly et al., 2006; Donnelly and Sallenger, 2007; Mattheus and Fowler, 2015; Morton et al., 2007; Williams, 2011) that are several orders of magnitude smaller than "chevrons" (Table 4 in Morton et al., 2007; Jamison-Todd et al., 2020) and never display such a V-shaped morphology (Engel et al., 2015). Finally, sandy storm deposits are systematically thinning landward with slopes ranging from 1° to 5° whereas "chevrons", like parabolic dunes, are thickening as they progress inland (Figure 19 and Figure 20) with the highest elevation lying near the ridge apex (Hearty et al., 1998; Hearty and Tormey, 2017; Vimpere et al., 2019).

5.1.2 Sedimentological criteria

Hearty et al. (1998, 2002), Hansen et al. (2020, 2016), Hearty and Tormey (2017), and Tormey (1999) excluded an aeolian origin for the "chevrons" because of the scarcity of steeply dipping foresets in these landforms. However, as emphasized by Goudie (2011), high-angle strata are relatively rare among the foreset beds of aeolian parabolic dunes. Moreover, most "chevron" exposures are roadcuts that obliquely transect their arms and nose, thus exposing apparent dip angles of strata that are less than the true dip values. Lastly, recently discovered (Figure 22E) and previously described outcrops of "chevrons" (e.g., Fig. 2 in Hearty et al., 1998) undeniably display large-scale, steeply dipping foresets. These sedimentary structures are thus more common than formerly assessed, and this occurrence reinforces the resemblance of "chevrons" with aeolian parabolic dunes. This similarity is further supported by the presence of CTS *throughout* these deposits (Engel et al., 2015; Kindler and Strasser, 2002, 2000; this paper), i.e. not only in "a few small (1-2 m^2) patches" (Hearty et al., 2015).

Furthermore, the internal architecture of the "chevron" arms (Figure 21) is practically identical in cross-section to that of the arms of parabolic dunes (Figure 27). Stratification steepens from the inside part (the deflation basin) towards the outer flank where grainfall and grainflow are the main processes controlling sand movement. Low-angle, planar cross-beds prevail in the internal side of the arms (Figure 22A and B), whereas steep foresets constitute the external side of the arm (Figure 22C). These structures indicate a migration from the deflation basin towards the outside, perpendicularly to the main orientation of the parabolic dune (McKee, 1966; McKee and Bigarella, 1979).

Finally, comparing the internal structures of washover deposits (e.g. Schwartz, 1982) with those of "chevrons" (Figure 26 and Figure 28) underlines the dissimilarities between the two. Washover sediments pile up during one single and sudden event (i.e., a storm) and consequently, do not include pedogenic features. In contrast, "chevrons" accumulate under discontinuous aeolian processes, which leads to the formation of protosols during the sedimentation breaks. Moreover, in strike section, washover deposits display subhorizontal stratification (Figure 28A) but lack cross-bed sets and highly inclined sets (except for washovers where the flow carried sediments into a standing body of water; Schwartz, 1982). In contrast, a complete strike section across a "chevron" (Figure 28B) shows the classic aeolian succession of backsets, topsets and foresets. Backsets dip seaward at medium angle whilst steep topsets dip landward, thus indicating a landward migration of the ridges (Rowe and Bristow, 2015b). To sum up, all sedimentological observations indicate an aeolian rather than a storm-wave origin for the Bahamian "chevrons".

5.1.3 Granulometric criteria

Applying the Folk and Ward method to the collected granulometric data (Appendix 8) indicates a pure (100% of sand) sandy composition for both "chevron" and aeolian sediments, whereas coarser beach material is made up of slightly gravelly sand (98.2% of sand and 1.8% of very fine gravel; Figure 29A). The same trend is also observable when comparing mean grain sizes which amount to 272.4 µm (1.876 φ) and 271.3 µm (1.882 φ) for "chevrons" and aeolianites, respectively, and to 377.2 µm (1.407 φ) for beaches.

The sorting is somewhat better within "chevrons" (1.593 µm; 0.671 φ; moderately well sorted) and aeolianites (1.542 µm; 0.625 φ; moderately well sorted) than in beach deposits (1.954 µm; 0.966 φ; moderately sorted). These values are to be considered carefully because the three types of deposits do not show a normal or gaussian distribution (Figure 29B), but rather a bimodal one for "chevrons" ($M1_{ch}$ = 196.0 µm; $M2_{ch}$ = 327.5 µm) and aeolianites ($M1_a$ = 231.0 µm; $M2_a$ = 655.0 µm), and a polymodal one for beaches ($M1_b$ = 231.0 µm; $M2_b$ = 327.5 µm; $M3_b$ = 655.0 µm).

The Lilliefors test, a derivative of the Kolmogorov-Smirnov test for cases where parameters of the normal law, mean, and variance are unknown, was applied as a normality test. It systematically rejects the hypothesis that beach, aeolian and "chevron" grain-size distribution are normally distributed with p-values <0.0001. Taken by sample, 36% of beach sediments are unimodal, 9% bimodal, 36% trimodal and 18% polymodal (Supp. Data). Aeolianites are considerably more unimodal deposits (78%) but contain 11% of bi- and polymodal samples. "Chevrons" show 50% of bimodal, 33% trimodal and 17% polymodal

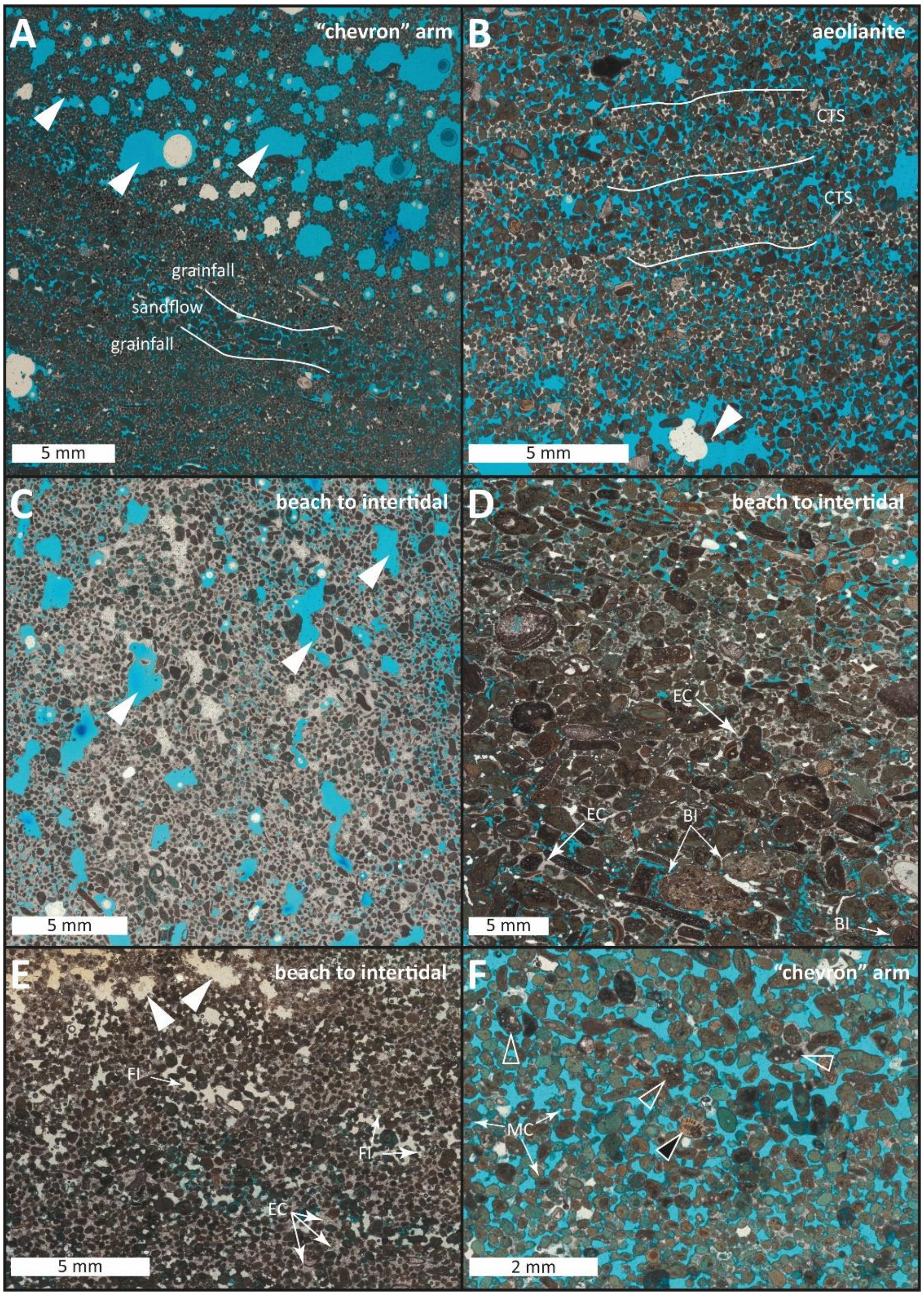

Figure 24: (A) Thin-section view of fenestrae (white arrows) and the alternating grainfall–sandflow laminae in 'chevron'arms (EX11; ERP section). (B) Thin-section view of climbing translatent stratification (CTS) in an aeolianite on Long Island (LV18; N 23° 5'57.24"; W 74°59'19.20"). Unlike grainfall–sandflow sets, there is an inverse grainsize gradient within each lamina, the basal section of which (finer part) is usually highly cemented compared to the top one (coarser part). Fenestrae are also frequent in these aeolian deposits (white arrow). (C), (D) and (E)Moderately sorted beach-to-intertidal deposits of MIS 5e age from: (C) the Boiling Hole (EL1; N 25°25'41.46"; W76°35'18.60") and (D) Gregory Town (EL21; N 25°24'33.00"; W 76°33'17.22") on Eleuthera; (E) intertidal depositson Long Island (LI146; N 23°32'5.54; W 75°15'13.33"). (C) Shows a well-preserved fenestral porosity with a complete cementation by sparite, illustrating a freshwater phreatic environment. (D) Presents a higher skeletal contentand a coarser grain size than aeolian and 'chevron' deposits. The first generation of bladed isopachous cement (BI) and the following pore-filling equigranular sparite (EC) are indicators of first a marine phreatic, and then a freshwater environment. (E) Displays grains that are first bound by a typical marine phreatic cement (i.e., fibrous isopachous; FI), here followed by a sparitic one (EC). Fenestrae are typical of this kind of environment (whitearrows). (F) Close-up showing the typical petrography of a 'chevron' arm outer flank (LI107; LOG section). Note the predominance of ooids and peloids versus bioclasts; the latter are mostly represented by Halimeda sp. (blank triangles) and Archaias sp. (black triangle). Grains are connected by meniscus cement (MC), indicating a vadose environment.

distribution. To sum up, beach sediments tend to have a uni- to polymodal distribution, whereas aeolian sands are unimodal and "chevrons" are mostly bimodal. The cumulative percentile values D_{10}, D_{50} (the median) and D_{90} are respectively of 157.0 µm, 261.4 µm and 500.9 µm for "chevrons"; 166.3 µm, 258.4 µm and 527.3 µm for aeolianites; and 181.2 µm, 340.4 µm and 983.6 µm for beaches. Because of the non-normal character of distributions, skewness and kurtosis values may just serve as indicators at best. However, it is worth mentioning that, despite being all coarsely skewed, the distribution is mesokurtic for "chevrons", leptokurtic for aeolianites, and platykurtic for beaches. These graphical observations were then confirmed by applying the Wilcoxon-Mann-Whitney statistical test to compare the different grain-size populations. Some approximation was used to compute the p-values, and the continuity correction has been applied. The null hypothesis H0, which considers no difference between the compared grain-size populations, was rejected when comparing beach samples with aeolian and "chevron" sediments with p-values <0.0001. Conversely, it cannot be rejected when comparing aeolian and "chevron" grain-size populations because of a p-value computed at 0.868.

To sum up, these quantitative analyses and statistical tests demonstrate that the granulometry of "chevrons" is akin to that of aeolianites, and that both differ from that of beaches, suggesting further a deposition by wind and not by water. The studied aeolianites are mostly foredunes, which are constantly fed by a close profusive source of well-sorted sediment from the beach. Thus, they commonly display a unimodal grain-size distribution. By contrast, parabolic dunes (i.e., "chevrons") are migrating further inland, thus moving away from coastal sources of sediment. In this case, a bimodal grain-size distribution indicates that dunes have incorporated sand from the deflation basin (Brookfield and Ahlbrandt, 2000; Pye and Tsoar, 2008).

5.2 Origin of high-elevation fenestral porosity

The "chevrons" mostly consist of an alternation of dm-thick, finely laminated (CTS) beds and of non- or poorly laminated intervals of equal thickness comprising numerous fenestrae (Figure 23A), which can be observed at elevations exceeding 30 m. As stated above, one school of thought (e.g. Hearty et al., 2002, 1998; Hearty and Tormey, 2017; Wanless et al., 1989) suggests that fenestral porosity formed by large-wave action, concurrently with the deposition of "chevrons", and that aeolian structures were produced on the surface of these deposits during periods of relative quiescence between "superstorms". The other group (e.g. Kindler and

Strasser, 2002, 2000; Mylroie, 2018a, 2018b) proposed that fenestrae were generated by heavy rainfall on the previously wind-deposited "chevrons". We believe that both hypotheses are improbable. To begin with, the formation of fenestral porosity by swash action up to 30 m should have been accompanied by an erosion of the dune topography and/or by an input of coarse-grained (possibly shelly) material, which is never the case. Secondly, although the creation of rain-induced fenestrae has been observed in modern dunes (Emery, 1945), it is a rare phenomenon that cannot account for such extensive features. Further, the presence of such fenestrae in fossil aeolianites (e.g., Bain and Kindler, 1994) is speculative because they have never been observed in association with more typical features such as raindrop imprints.

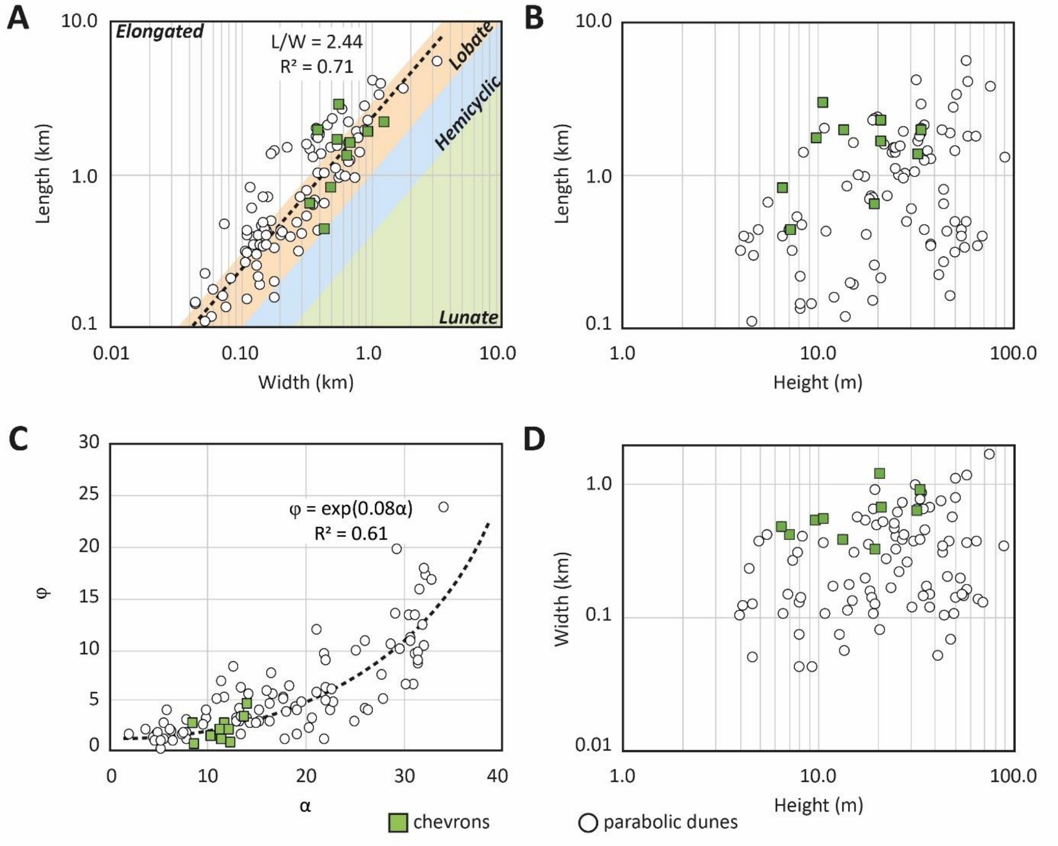

Figure 25: Comparative plots of "chevron" (green squares; this study) versus parabolic-dune (white circles; data from Appendix 5) morphological parameters A) L/W plot: parabolic aeolian dunes and "chevrons" are either lobate or elongated according to Pye's (1993) classification of simple parabolic dunes. The elongation (L/W) of all measured ridges follows a linear law with a good level of confidence. B) L/H plot: it represents the flatness of the studied landforms and shows a scattered population with rather flat "chevrons". C) φ/α plot: the stoss-slope angle (φ) increases exponentially with the lee-face angle (α) for all V-shaped ridges. D) W/H plot: it shows a scattered population where "chevrons" are among the widest landforms compared to their heights.

It has long been known that fenestrae are polygenetic features that are not necessarily generated by swash action in the intertidal zone (Kindler, 1991; Shinn, 1983, 1968). They can be related to the decay of organic matter such as plant roots and/or microbial mats, which are common in aeolian sediments. Relying on the observation of fungal endoliths and sparmicritized zones associated with elevated fenestrae in a Pleistocene aeolianite from

Table 3: AAR ratios measured on "chevron" samples from Great Exuma and Long Island and obtained by RP chromatography. A/I values were calculated following a log2 transformation of the DL-Glu ratios, following to the method developed by Whitacre et al. (2017). The AAR database developed for the Bahamas (Hearty and Kaufman, 2009) was used to corelate the A/I ratios to the corresponding phases of the MIS 5e.

Sample No.	DL Asp	DL Glu	DL Ser	DL Ala	DL Val	DL Phe	DL Ile	DL Leu	A/I calculated from DL-Glu	Associated MIS
EX10	0.478 ± 0.010	0.445 ± 0.003	0.388 ± 0.008	0.728 ± 0.008	0.388 ± 0.006	0.509 ± 0.004	0.345 ± 0.004	0.661 ± 0.003	0.453 ± 0.003	Early 5e
EX11	0.455 ± 0.016	0.424 ± 0.005	0.349 ± 0.025	0.691 ± 0.006	0.370 ± 0.012	0.520 ± 0.032	0.353 ± 0.037	0.667 ± 0.032	0.414 ± 0.005	Latest 5e
LI107	0.492 ± 0.004	0.413 ± 0.009	0.254 ± 0.097	0.665 ± 0.012	0.340 ± 0.006	0.439 ± 0.005	0.295 ± 0.011	0.587 ± 0.045	0.394 ± 0.009	Latest 5e
LI133	0.520 ± 0.006	0.461 ± 0.001	0.364 ± 0.025	0.775 ± 0.015	0.419 ± 0.002	0.521 ± 0.019	0.390 ± 0.035	0.704 ± 0.017	0.483 ± 0.001	Early 5e

Providenciales (Caicos Platform), Kindler et al. (2009) further proposed that fenestral zones represented immature pedogenic horizons where the cemented grainstone was patchily altered by plant and fungal activity. We tend to support this hypothesis because of the unequivocal association of parabolic dunes with a stabilising vegetation (e.g. Durán and Herrmann, 2006; Durán and Moore, 2013; Tsoar and Blumberg, 2002; Yan and Baas, 2015). Furthermore, the higher density of fenestral beds in "chevron" arms, with respect to the apices, can be explained by the formation process of parabolic dunes implying a fixation of the trailing arms by vegetation while bare sand composes the migrating nose (e.g., Goudie, 2011).

With one exception (Blackwatch Pass, Bermuda, Kindler and Strasser, 2000; Rowe and Bristow, 2015a, 2015b), elevated fenestrae have always been observed in well-sorted oolitic-peloidal grainstone and in association with CTS (Figure 24B; Fig. 6 and 7 in Hearty et al., 1998; Fig. 3 in Kindler and Strasser, 2002). Thus, the occurrence of such pores could also result from the interaction of vadose water (but not necessarily heavy rainfall) with the peculiar grain shape and size of the oolites, and with the tight packing and low permeability of the CTS.

5.3 Megaboulders of Eleuthera

As previously stated, Hearty et al. (1998, 2002) and Hearty and Tormey (2018a, 2017) repeatedly argued that a "trilogy" of sedimentary features, including the "chevrons", "runup" deposits and the megaboulders from North Eleuthera, offered an unequivocal testimony of superstorms producing giant, long-period waves in the northeast Atlantic Ocean at the end of the LIG. Based on new quantitative data, we substantiate here earlier reports (e.g., Kindler and Strasser,

2000) according to which the "chevrons" must be interpreted as aeolian parabolic dunes. Because they display also numerous aeolian structures (e.g. CTS), we further support the interpretation of "run-up" deposits as climbing (Kindler and Strasser, 2000) or advancing (Rowe and Bristow, 2015b) dunes. It is beyond the scope of this paper to discuss the age of emplacement of the megaboulders, and whether they represent the remnants of a tower karst (Mylroie, 2018a, 2008), were rolled down from a higher elevation, or deposited by large waves related to bank-margin collapse (Hearty, 1997), a tsunami (Hearty, 1997; Kelletat et al., 2004), a superstorm (Hearty et al., 1998; Hearty and Tormey, 2018a, 2017), or a hurricane of historical intensity during a period of higher than present sea level (Rovere et al., 2018, 2017). However, we assert that the aforementioned deposits must not be regrouped in a "trilogy" as we consider "chevrons" and "run up" deposits to be the result of long-term aeolian transport on several islands, whereas the megaboulders from North Eleuthera have likely been emplaced by a violent, short-term event at one location.

5.4 Age of "chevrons"

Based on AAR data from this and Hearty et al.'s (1998) studies, the Bahamian "chevrons" can be assigned to MIS 5e, but the AAR-dating method is not precise enough to unequivocally correlate these deposits with a specific interval of this substage. Considering their morphological position (Hearty et al., 1998) and the occurrence of cross-beds dipping below modern sea level (Kindler and Strasser, 2002), previous authors suggested that "chevron" deposition occurred during the rapid regression that ensued MIS 5e, when large amounts of mostly oolitic shelf sediments became available for reworking by wind or waves (Hearty et al., 2015; Kindler and Strasser, 2000; Neumann and Hearty, 1996). This timing and scenario are likely correct for the low-elevation "chevrons" located near platform margins (e.g., Harvey Cays, Exumas; Fig. 2 in Hearty et al., 1998), but questionable when applied to the higher ridges positioned in a more bankward position (e.g., the landforms on Great Exumas, Figure 19A and B). The latter were probably emplaced during or before the previous LIG highstand (interval 5 of Hearty and Tormey, 2017; Hearty et al., 2007) ca. 118 ka BP (Kerans et al., 2019; Skrivanek et al., 2018).

5.5 Paleoclimatic and paleoceanographic settings during the formation of "chevrons"

Kindler and Strasser (2000) already addressed the question of the climatic and oceanographic conditions on GBB during the formation of "chevrons". To sum up, the

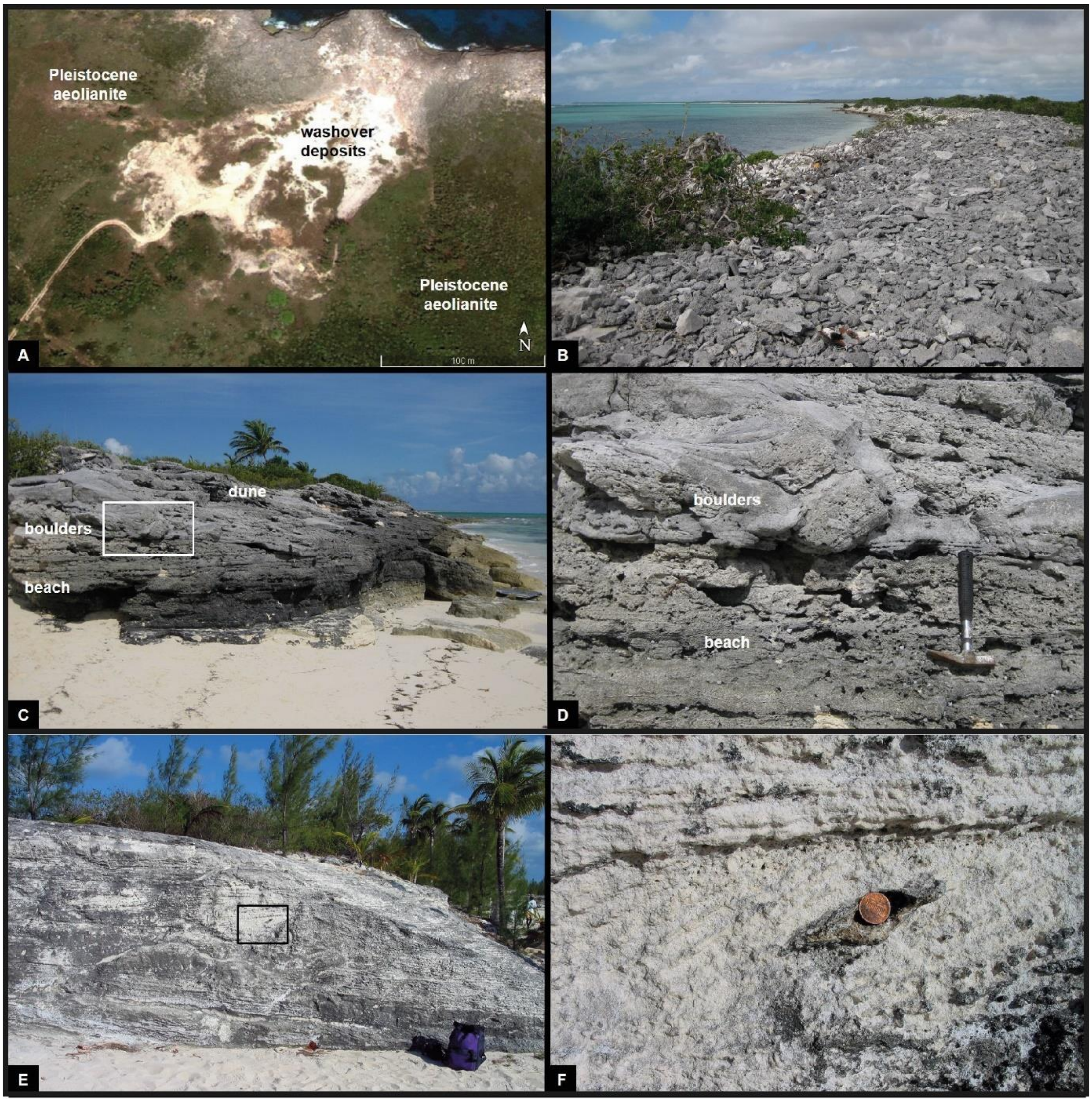

Figure 26: Examples of storm deposits of Recent, Holocene, and Late Pleistocene age. A) Satellite view of partly quarried, recent, sandy to conglomeratic washover deposits capping a sea cliff ca. 1 km to the SE of Boiling Hole (Eleuthera). Coordinates: N 25°25'36.48"; W 76°35'21.89". Note lobe shape of deposits. Image Google Earth. B) Conglomeratic storm berm along the southern coast of Great Inagua. Coordinates: N 20°55'28.99"; W 73°30'3.89". Clasts mostly consist of dm-sized coral debris derived from an adjacent reef. Top of the berm is about 2.5 m above sea level. C) Coastal exposure along the coastline of Flamingo Bay (Mayaguana). Coordinates: N 22°24'31.85"; W 72°59'15.00". Outcrop shows a shallowing-upward succession of beach and dune deposits of Holocene age (Hanna Bay Formation). A boulder layer representing a fossil storm berm is interstratified between the beach and the dune deposits. White rectangle shows the position of D. Hammer is 35 cm long. Top of the exposure is ca. 2 m above sea level. D) Close-up view of the boulder layer mentioned in C. Hammer is 35 cm long. E) Roadcut leading to Rainbow Beach (Eleuthera). Coordinates: N 25°20'2.33"; W 76°25'53.01". Exposure consists of coarse to very coarse, sandy oolitic deposits of MIS 5e age. Coarse grain size, predominant subhorizontal stratifications. and small antidunes identify these beds as fossil washover deposits. Interestingly, sediments came from the open sea located to the left and were transported bankward (i.e. to the right) into a lagoon. These deposits overlie bioturbated lagoonal sediments (not visible on the photograph). Bag for scale is 50 cm high. Black rectangle shows the position of F. F) Close-up view of small antidune in MIS 5e washover deposits. Flow moved from left to right. Structure behind the coin (for scale) is a rhizolith.

environment was potentially windier and certainly drier than today to prevent the rapid cementation of carbonate sands (e.g. Kindler and Mazzolini, 2001) that would hinder dune migration. That climatic conditions were drier during the formation of "chevrons" and of coeval linear dunes is attested by the occurrence of nebkhas within these deposits (Kindler and Strasser, 2000; Tormey, 1999). Indeed, nebkhas, or "coppice dunes", characterise areas of low precipitation ranging from 200 to 300 mm/y (García-Romero et al., 2019). In comparison, today's annual rainfall across the Bahamas varies between 600 and 1500 mm (Wolcott et al., 2018). Lower precipitation rates likely induced a change in both vegetation type and cover, which directly impacts the roughness of the terrain (e.g. Jerolmack et al., 2012; Levin et al., 2008), and thus on how the wind is slowed down during its progression inland. Drier climatic conditions generally result in a shrubbier vegetation at these latitudes, representing a lower surface roughness (De Chiffre, 2001), which increases the wind capacity to transport sediment (drift potential; Fryberger and Dean, 1979) without necessarily blowing harder. Such a setting could have resulted from a slight northward migration of climatic belts (Perlmutter and Matthews, 1992) placing GBB in the same conditions as those presently affecting the southern Bahamas. These speculations are supported by recent climate models advocating for a higher surface temperature, diminished precipitation, and a grassier type of vegetation during a great part of the MIS 5e (Nikolova et al., 2013; Scussolini et al., 2019).

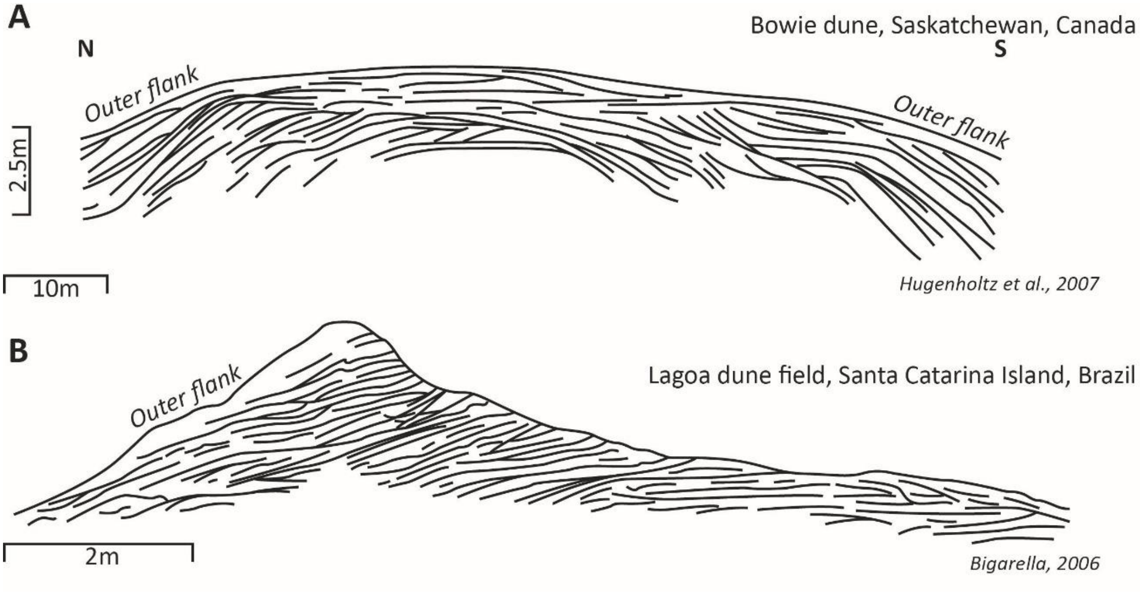

Figure 27: Arm sections described in aeolian parabolic dunes from Canada and Brazil. Similarities with "chevron" arms (Figure 21) include an outer flank generally steeper than the flank facing the deflation basin, cross-bed sets dipping towards the outside, and an analogous size.

Furthermore, considering the reconstruction of the Bahamian climate during MIS 5e proposed by Zhuravleva and Bauch (2018), the following scenario can be envisaged. An important phase of carbonate (i.e., ooid) production occurred early in MIS 5e, when warm and humid conditions associated with weak trade winds prevailed. The elevated "chevrons", that have migrated further inland, could correspond to a sedimentation phase taking place during the "Younger Dryas-like event" (ca. 127 ka BP) when climate was drier and windier due to a sudden southward motion of the ITCZ. Deposition of the low-elevation "chevrons" followed a second phase of carbonate production, and likely occurred during the stepwise regression that ensued the second (or the main) MIS 5e highstand (Figure 16), when the ITCZ shifted again to the South.

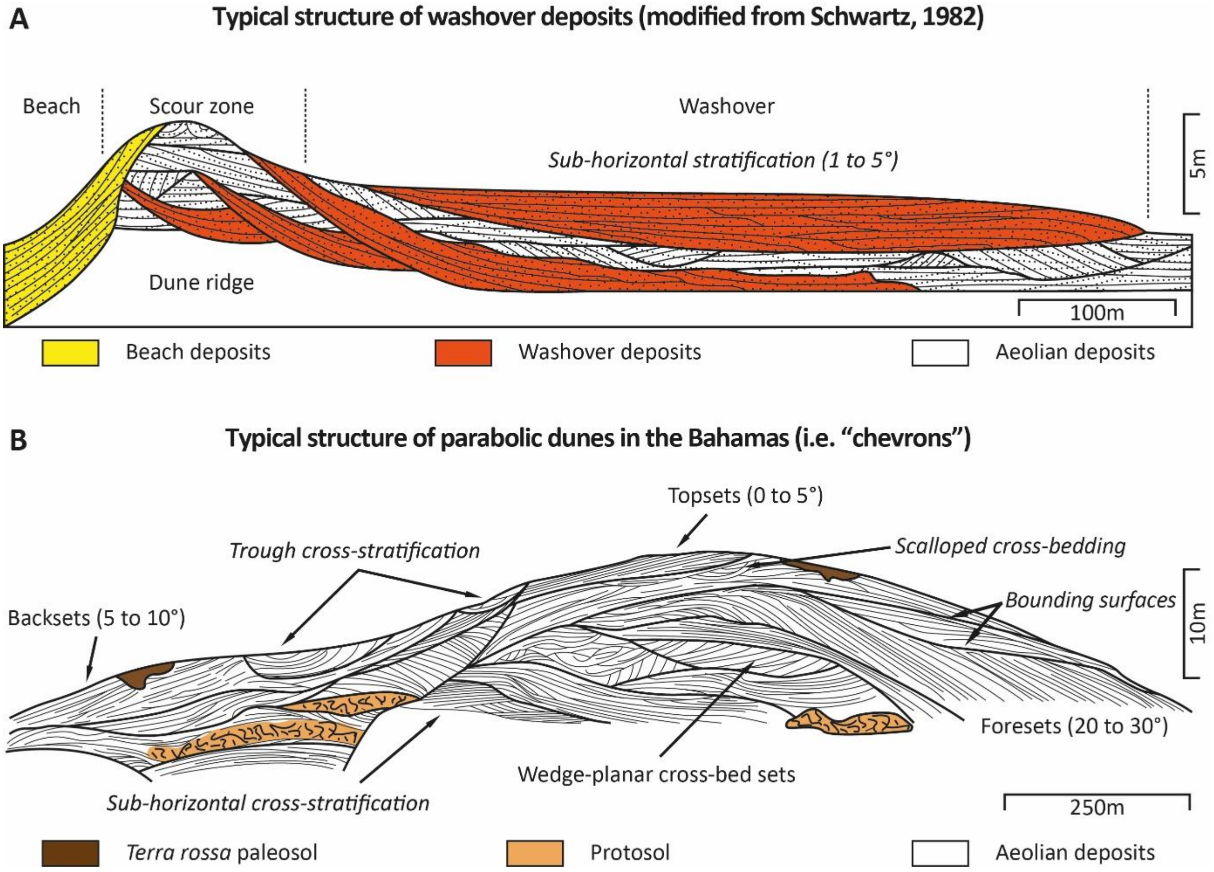

Figure 28: A) Typical morphology and internal structure of washover fans deposited on a hard substrate. They present a thinning-landward lobe shape, with a sub-horizontal stratification. Several lobes can be superimposed or found interfingering with aeolian sediments. B) Reconstruction of the internal structure of "chevrons", based on the different sections observed in the field, and shown as a strike view through an arm and the nose. Note the greater complexity of these deposits when compared with typical aeolian features.

Thus, a protracted influence of trade winds, a lowering of the moisture content in the sediment, and both a vegetation cover and type subsequently dropping within the ideal range for parabolic dune formation (Goudie, 2011 for a summary; Hanoch et al., 2018) would have favoured the deposition of these ridges by increasing the erosional power of wind on loose foredunes, forming blowout features of different stages (e.g. Hesp, 2011). The wind would have reworked these foredunes and the fine part of the beach material (explaining the matching of some grain-size populations within the ridges; Figure 29), sorting out the latter during the migration processes. These conditions would have lasted until after the onset of the regression (as shown by the foresets dipping below modern datum), when the shelf sediments became exposed, spanning the whole highstand in agreement with the recent models proposed for carbonate aeolianites (Frébourg, 2010; Rowe and Bristow, 2015a).

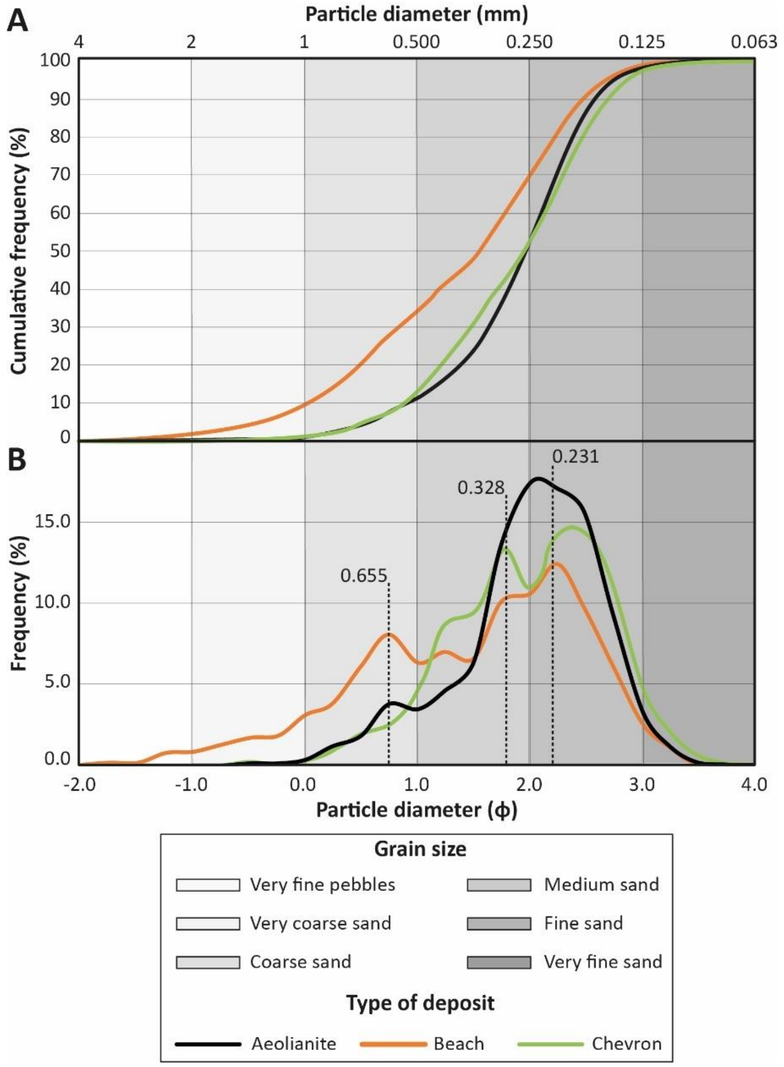

Figure 29: A) Cumulative frequency curves of grain-size populations measured for "chevrons" (green lines), aeolianites (black lines) and beach deposits (orange lines). The latter are composed of coarser sediments, whereas "chevrons" and aeolian dunes show a similar distribution. B) The distribution type is more easily read on a frequency plot. "Chevrons" and aeolianites have a bimodal distribution, whereas beaches show a polymodal distribution. Values at dashed lines show the common modes between types of deposits, indicating a reworking of material of one by the other, or a common source.

6 Conclusions

The new morphological, granulometric, sedimentological, and age data on Bahamian "chevrons" presented in this study, as well as a detailed review of previous papers pertaining to these peculiar landforms bring out the following conclusions:

- The morphological parameters measured on the "chevrons" from Great Exuma, Long, and Acklins islands perfectly correlate with those of more than 95 aeolian parabolic dunes worldwide.

- The occurrence of numerous aeolian structures in these deposits, along with strong dissimilarities with storm-related deposits, confirm that "chevrons" are wind-deposited bedforms.
- Quantitative granulometric analyses and several statistical tests show that the granulometry of "chevrons" is akin to that of aeolianites, but differs from that of beaches, further suggesting that they have been deposited by wind and not by water.
- Considering the polygenetic nature of fenestral porosity and the unequivocal relationship between vegetation and parabolic dunes, it is reasonable to assume that high-elevation fenestrae are related to plant or fungal activity, and/or to the particular fabric of the well-sorted oolitic-peloidal aeolianites.
- AAR data constrain the "chevron" age to MIS 5e, and geomorphological criteria further indicate they have probably been formed during two distinct late phases of this time interval.
- The notorious "chevrons" from Eleuthera Island are linear ridges.

To sum up, the peculiar and controversial Bahamian "chevrons" are aeolian parabolic dunes that have been deposited during the MIS 5e highstand and the ensuing regression, when climatic conditions in the northern Bahamas were drier and windier than today due to a southward displacement of the average annual position of the ITCZ. These conditions were coupled to a shrubbier/grassier vegetation, inducing the formation of a fenestral porosity, and fixing the trailing arms while a migrating nose was advancing downwind farther inland.

7 Acknowledgements

This project was funded by the Department of Earth Sciences of the University of Geneva. Our gratitude goes to the Earth Observation Centre at the German Aerospace Centre (DLR) for generously providing the DEMs needed. Dr. Ian Spooner at Acadia University helped this project by allowing us to use his drone in the field. We would like to acknowledge the Amino Acid Geochronology Lab of the Northern Arizona University for their efficiency and for remaining available to discuss the results. We thank François Gischig for the excellent quality of the thin sections. Comments of André Strasser, Ryan C. Ewing and Massimiliano Ghinassi greatly improved the paper. The authors declare no conflict of interest associated with this publication.

Chapter 4 – Depositional timing and palaeoclimate interpretation of the Tamala Limestone aeolianites in Shark Bay, Western Australia.

This chapter addresses the sedimentology and stratigraphy of the Tamala Limestone in the Shark Bay region, in Western Australia. Based on the collected data, correlations are made between episodes of aeolian deposition and paleoclimate conditions in the region.

Submitted as:

Vimpere, L., Del Piero, N., Le Cotonnec, A., Kindler, P., & Castelltort S.. Depositional timing and palaeoclimate interpretation of the Tamala Limestone aeolianites in Shark Bay, Western Australia. Aeolian Research

Abstract

The carbonate units grouped under the name "Tamala Limestone" outcrop for a thousand kilometres along the coast of Western Australia. The extensive Zuytdorp Cliffs shaping the northern half of the coastline up to Shark Bay expose and offer an exceptional access to the stratigraphy of this formation.

The regional survey of the Shark Bay region, which combines both stratigraphic and sedimentological analyses, reveals that the Tamala Limestone is a dry accumulating aeolian system composed of large transverse dunes migrating parallel to the prevailing winds. Accordingly, the amino acid-data show an aging of the units towards the east. Episodes of carbonate aeolian sedimentation correlate with the successive glacial intervals of the Pleistocene whilst palaeosols are correlated with breaks in the sedimentation during interglacial intervals.

Palaeoclimate reconstructions reveal that sea level and sea surface temperature of the Indo-Pacific Warm Pool were lower during glacial intervals. The weakened Leeuwin Current, which flows along the western coast of Australia and is the main source of precipitation, contributed to the aridification of the region. Consequently, and associated with a northward migration of the Hadley and Ferrel cells, periods of glaciation were drier. By contrast, paleosols developed through dissolution of the carbonate units during more humid interglacial intervals.

1 Introduction

The Tamala Limestone is a Mid- to Upper-Pleistocene calcareous formation predominantly comprising a complex of stacked aeolian units that is exposed along much of the Western coast of Australia. Extending from Shark Bay in the north to Esperance in the south, it is considered as to be the widest deposit of aeolianites of this age in the world (Wakelin-King and Webb, 2020). Initially known as the "Coastal Limestone" within the Perth Basin (Saint-Smith, 1912), it was then known as the "Tamala Eolianite" in the Shark Bay area (Logan, 1968), to finally be renamed as "Tamala Limestone" by Playford et al. (1976) so that a lithological rather than a generic term would be used. The type section was defined at Womerangee Hill where the unit is exposed up to 250 m above the present sea level (Playford et al., 2013).

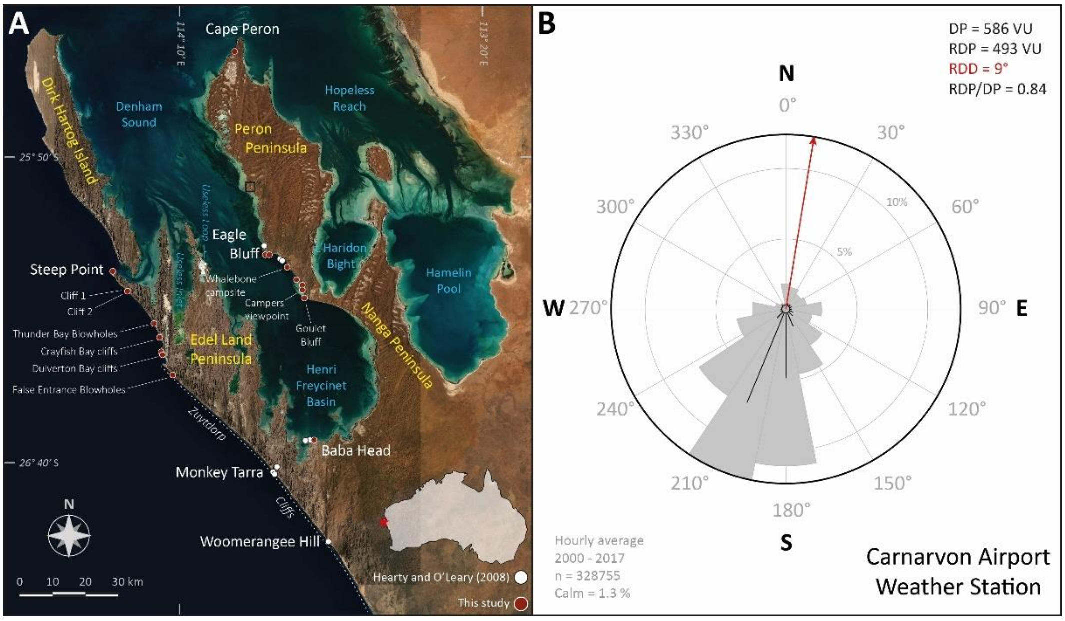

Figure 30: A: Shark Bay texture map generated by the draping of image satellites (Sentinel-2) over the Tandem-X digital elevation model (± 12 m; Wessel et al., 2018). The white and red dots represent the studied sites for AAR from Hearty and al. (2008) and this study, respectively. B: Wind frequency rose and Fryberger analysis (sand rose) generated from the Carnarvon Airport station data. DP = Drift Potential; RDP = Resultant Drift Potential; RDD = Resultant Drift Direction.

With a length of 210 km, the Zuytdorp Cliffs are likely the longest on Earth (Wakelin-King and Webb, 2020) and offer an exceptional insight of the Tamala Limestone's stratigraphy, which has been correlated with climate and sea-level fluctuations (Hearty and O'Leary, 2008; Jorgensen, 2012; Lipar and Webb, 2014; Playford et al., 2013). However, the exact timing of deposition has been hindered by the lack of precise dating techniques available for this interval of the Quaternary. Consequently, connections with glacioeustatic sea levels and palaeoclimate have not been clearly established.

New sections of the Tamala Limestone in the Shark Bay area are presented in this paper with a particular focus on the Zuytdrop Cliffs. The aim of this study is to: (i) investigate the mechanism of transport of dune sands (e.g., migration vs. aggradation), (ii) define the palaeowind direction under which they accumulated, (iii) constrain their timing of deposition and the associated palaeoclimate conditions taking place during their emplacement.

2 Settings

2.1 Geomorphology

Shark Bay is a subtropical region of Western Australia (26 °S) located in the Southern Carnarvon Basin, from which the uniform Carnarvon carbonate ramp extends seaward. Shark Bay shallow sea is separated from the Indian Ocean to the west by the Edel Land Peninsula, the Dirk Hartog Island, and the three Dorre, Bernier and Koks islands (Figure 30). The Nanga and the Peron Peninsulas form a complex that divides the sea into two major zones of shallow, metahaline-to-hypersaline waters: Hamelin Pool and Henri Freycinet Harbour Basin. The west coast of Edel Land consists of an escarpment that extends for 210 km from Steep Point in the north to Kalbarri in the south (27.7 °S; 114.2 °E). The Zuytdorp Cliffs reach 250 m in height and sharply truncate the Tamala Limestone, thus offering an exceptional insight into the aeolian stratigraphy. The formation of the Zuytdorp Cliffs has been suggested to be a result of a displacement along the normal Zuytdorp Fault, which was likely active during the Pleistocene and possibly during the early Holocene (Playford, 2003; Playford et al., 2013).

2.2 Quaternary sedimentation

The Quaternary geology of the region predominantly consists of the Pleistocene aeolianites of the Peron Sandstone and the Tamala Limestone, both of which overlie the underlying Tertiary and Cretaceous formations. The red Peron Sandstone is exposed on the Nanga and Peron Peninsulas where it is irregularly onlapped or interfingered by the Tamala Limestone, notably on the west coast of the Peron Peninsula at Eagle Bluff. The Tamala Limestone itself is mostly found on the Edel Land Peninsula and Dirk Hartog Island, where it reveals large pristine aeolian structures such as cross-beds. It is still debated if the Peron Sandstone is older or is the lateral stratigraphic equivalent of the Tamala Limestone and formed from the concentration of the siliciclastic material through the leaching of carbonate aeolianites. The interdune areas such as Useless Inlet, Useless Loop, or Boat Haven Loop form some bays that have been flooded during past marine transgressions, such as the ones from the Middle and

Late Pleistocene (Le Guern, 2004). The high sea levels associated with these intervals led to the deposition of the marine carbonates of the Dampier and the Bibra Formations, respectively, which are sporadically outcropping along the shoreline re-entrants. The surface of the region is mostly covered by the Carrarang Sand and the Denham Sand. The Carrarang Sand is a carbonate sand that composes the seif, parabolic, barchan, massive and undulating dunes on Edel Land Peninsula whilst the Denham Sand is the red sand forming the large parabolic and transverse dunes on the Peron Peninsula (Playford et al., 2013). Most of the dunes are currently stabilised by vegetation. The ^{14}C ages retrieved along a transect from the bare sand dune field feeding from the Dulverton Bay beach indicate a deposition during the late Pleistocene to early Holocene (Le Guern, 2004).

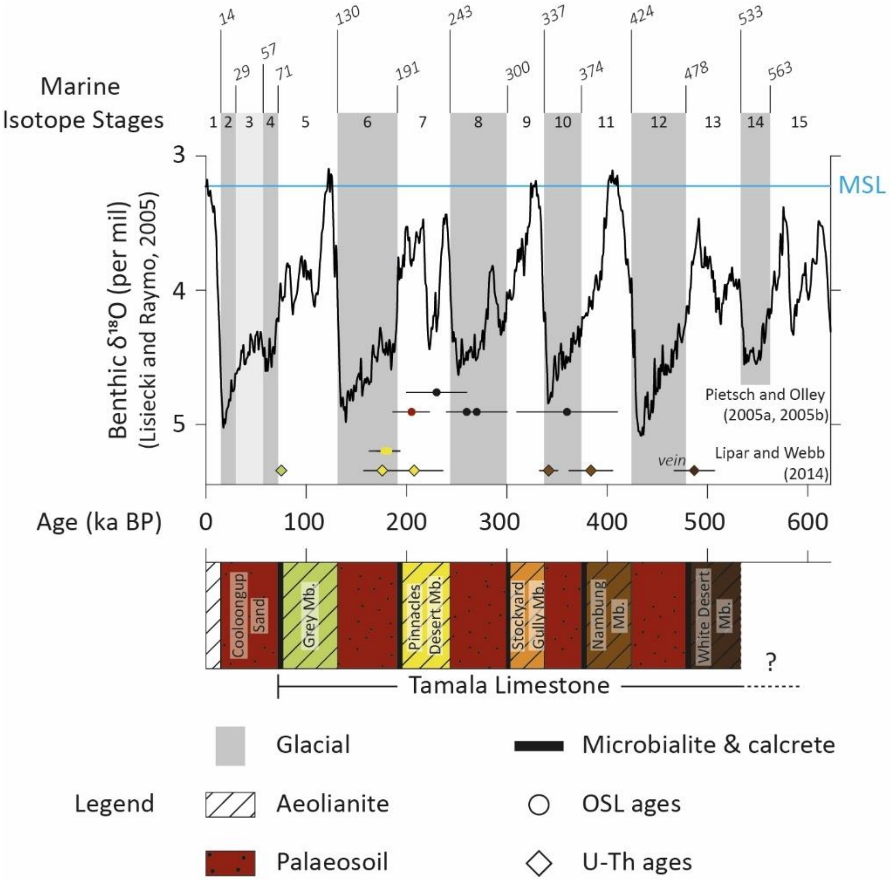

Figure 31: Glacial-interglacial cycles (Lisiecki and Raymo, 2005) and the associated stratigraphic column of the Tamala Limestone defined in the Swan Coastal Plain (Lipar and Webb, 2014). Black and red dots are OSL ages measured in aeolianites and paleosols, respectively, at the Womerangee Hill type section of the Tamala Limestone (Playford et al., 2013). The colours of the OSL and U-Th ages measured by Lipar and Webb (2014) refer to the corresponding members of the Tamala Limestone from which the samples were taken.

The sands that are feeding the Carrarang Sand and that fed the Tamala Limestone have a similar composition, which likely indicates a unique source of sediment throughout the Late Quaternary. Out of the eleven compositionally different depositional zones defined by James et al. (1999), the *Quartzose Skeletal Sand*, the *Planktic Intraclast Sand* and the *Skeletal Sand* are the ones currently feeding the active dune fields of the Carrarang Sand, and were probably the ones feeding the Tamala Limestone dunes. These sands are predominantly calcareous with the terrigenous part representing 0 - 30% of the sediment. Consequently, the aeolianites of the Tamala Limestone consist of fine-to-coarse, carbonate sand that is moderately cemented by sparite in most cases. The main component is largely skeletal and represented by rounded fragments of molluscs, foraminifera, red algae (Corallinaceae) and echinoderms. The siliciclastic part mostly consists of quartz and feldspathic sand, and rarely exceed 10% in the aeolian units (Le Guern, 2004, Hearty and O'leary, 2008). The latter are capped by paleosol horizons of variable thickness and stiffness, with a texture going from sandy to calcretised (Lipar and Webb, 2014; Smith et al., 2011).

2.3 Depositional timing of the Tamala Limestone

So far, two dating methods have been used on samples that were directly retrieved from the Zuytdorp Cliffs (Figure 31). Pietsch and Olley (2005a, 2005b) have reported five Optically Stimulated Luminescence (OSL) ages from the type section of the Tamala Limestone located at Womerangee Hill (Playford et al., 2013). Measured from the top of the section, the calculated ages are ~260 ka at 33m, 360 ±30 ka at 85 m, 270 ±30 ka at 120 m, 205 ±18 ka at 132 m, and 230 ±30 ka at 215 m. Since they show age inversions, these data were assumed problematic by the authors who then concluded that the whole section was likely deposited circa 250 ka ago, which corresponds to the glacial MIS 8.

Subsequently, Hearty and O'Leary (2008) attempted to date samples retrieved from the Monkey Tarra and the Womerangee Hill sections on the Zuytdorp Cliffs by amino acid racemization (AAR). They have interpreted the upper and middle beds of both sections as early Pleistocene in age, based on the measured A/I ratios. The lower beds, however, show low to non-detectable levels of amino acids and may have been deposited during the earliest Pleistocene and/or the Pliocene. By comparison with the Bahamas, the authors interpreted aeolian units as highstand deposits whereas paleosols and calcretes were correlated to glacial periods. Problematic A/I values in both sections decrease in stratigraphically lower units, which translates into an age inversion.

Further south onto the Swan Coastal Plain, five members of the Tamala Limestone have been recognised and dated by both OSL and U-Th over the last 500 ka (Lipar and Webb, 2014). The Tamala Limestone Formation is subdivided into five members that are stratigraphically separated from each other by paleosols. The whole formation is believed to date from MIS 13 at least to MIS 5, and is capped by the Cooloongup Sand dated to the Last Glacial Period (LGP; MIS 4 to 2), which could correlate with the Denham Sand defined in Shark Bay (Playford et al., 2013). Most of the U-Th ages were retrieved from microbialites capping the aeolian carbonate units and underlying paleosol levels, except for the one obtained in a vein intersecting the White Desert Member. These ages were interpreted by the authors as the end of the periods of aeolian accumulation. Therefore, and in agreement with Hearty and O'Leary (2008), Lipar and Webb (2014) correlated aeolian sedimentation and paleosol formation to interglacial and glacial periods, respectively. By contrast, two OSL ages measured within aeolianites of the Pinnacles Desert Member indicate a deposition during the glacial MIS 6 (Figure 31).

To summarise, the age and depositional timing of the Tamala Limestone in the Shark Bay region remains poorly constrained. The remoteness and difficulty of access lead to data scarcity, adding to the lack of proper dating technique for such material of Pleistocene age. However, the different dating methods applied to the Zuytdorp Cliffs sediment converge towards a depositional period ranging from the Middle to the Late Pleistocene.

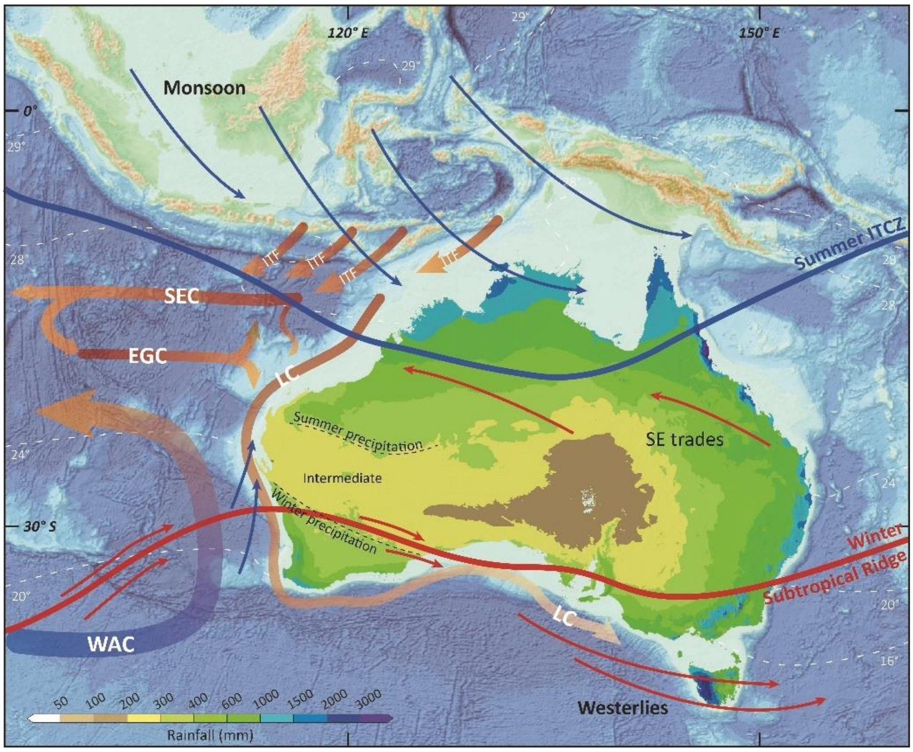

Figure 32: Map of Australia and Southeast Asia showing the multi-decadal rainfall map of Australia along with the prevailing atmospheric and oceanic circulation features. The rainfall map is based on 30-year averages calculated over the 1986-2015 period (Australian Bureau of Meteorology: www.bom.gov.au). The limits between the different rainfall zones of Western Australia are represented by the black dashed lines (van der Kaars and De Deckker, 2002). White dashed lines indicate the modern mean annual SST estimates (World Ocean Atlas, 1998; Barrows and Juggins, 2005) with the 28°C line delimitating the IPWP. Prevailing summer (blue) and winter (red) winds, including summer ITCZ and winter Subtropical Ridge positions, are indicated (modified from Courtillat et al., 2020). Major oceanographic currents include: ITF = Indonesian Throughflow; SEC = Indian and Pacific Ocean South Equatorial Current; EGC = East Gyral Current; WAC = Western Australian Current; LC = Leeuwin Current (modified from Petrick et al., 2019).

2.4 Climate

Shark Bay has a semi-arid climate with hot and dry summers (from November to March) that contrast with mild winters (from April to October). The average annual temperature is 26.5 °C, with a peak in February and a plunge in July. Although the mean annual rainfall is 230 mm, the mean annual evaporation rate reaches up to 2000-3000 mm (Australian Bureau of Meteorology: www.bom.gov.au). Most of the precipitation is concentrated during austral winters and coincide with a weakening of the southerly winds that blow during the whole year (Appendix 9). By contrast, austral summer in the region is hot, dry, and windy. Data from the Carnarvon Airport station (24.89 °S; 113.67 °E) show that winds are predominantly blowing from the south in the region (Figure 30). The slightly modified Fryberger analysis (Fryberger and Dean, 1979) developed by Kilibarda and Kilibarda (2016) is used in this study to quantitatively characterise the present wind regime in the region. Under this method, four indicators are calculated:

- The drift potential (DP), which is expressed in vector units (VU) and measures the total capacity of the surface wind to drag sand.
- The resultant drift potential (RDP) that represents the net DP, which corresponds to the vectorial sum of the DP values in each compass direction.
- The resultant drift direction (RDD) that defines the direction of the RDP.
- The ratio RDP/DP that characterises the directional variability of wind regimes.

According to the values defined by Fryberger and Dean (1979), results indicate a high-energy (i.e., DP > 400 VU), unidirectional (i.e., RDP/DP > 0.8) wind regime with a preferential direction of sand transport towards the north (RDD = 9°).

The climate in Western Australia is greatly influenced by larger climate systems with a planetary scale influence and can be divided into three major zones. The climate in North West Australia is indirectly affected by the Indo-Pacific Warm Pool (IPWP), an extended zone of warm (≥ 28 °C; Yan et al., 1992) surface waters characterised by low salinity and nutrient content. This “heat engine” is also sometimes referred to as the “steam engine” of the world because of the high convective clouds that are generated above it (De Deckker, 2016), which ultimately are the source of the moisture that causes the high rainfall during the Australian summer monsoon (ASM). The latter relies on the seasonal movement of the Intertropical Convergence Zone (ITCZ), which brings rain and northwesterly winds in the northern part of the country when it migrates southward (Figure 32) during the austral summer (Courtillat et al., 2020; Reeves et al., 2013).

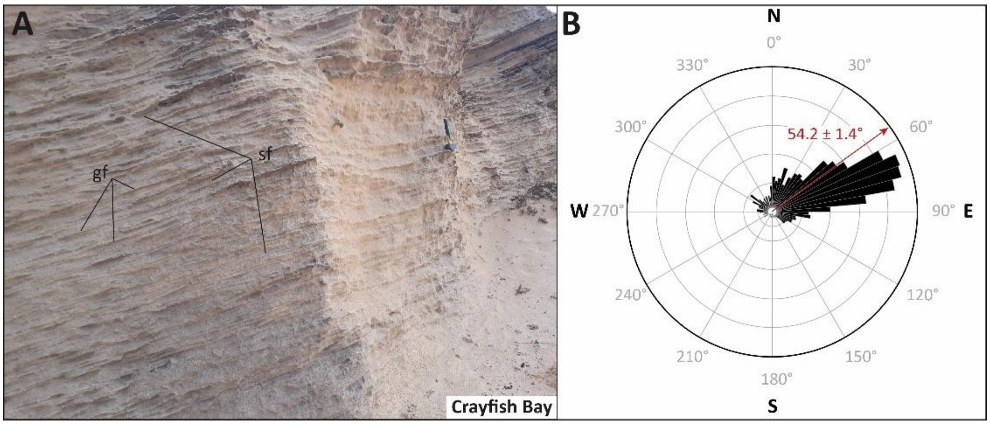

Figure 33: A: Typical sedimentary structures of the Tamala Limestone exposed along the Zuytdorp Cliffs include the planar-tabular cross-beds, which are constituted by an alternation of sandflow (sf) and finer grainfall (gf) strata. B: Rose diagram of the 1832 cross-beds dip directions measured on 3D models generated for four locations of the Zuytdorp Cliffs: Steep Point, Cliff 1, Cliff 2, and False Entrance Blowholes (Figure 30). The von Mises probability density function indicates that dunes of the Tamala Limestone were migrating ENE.

Conversely, Southwest Australia experiences dry and hot summers whilst most of the precipitation occurs in winter (McBride, 1987; Suppiah, 1992). During this season, both the ITCZ and the limit of the subtropical ridge move northward. The strong westerlies and the cold, humid fronts associated with a zone of high pressure are then displaced towards the centre of the country (Figure 32). The strength and westward position of westerlies, and thus the amount of moisture brought onto the continent, is also influenced by the Indian Ocean Dipole (IOD). During a positive phase, the sea surface temperatures (SST) are lower in the eastern Indian Ocean region than in the western part, which causes droughts in Australia through the suppression of the local convection and the reduction of precipitation (Cai et al., 2014).

The region of Shark Bay is located at the centre of a coastal belt (25 to 27 °S) that is not dominated by a single climatic system. Whilst the influence of the westerlies diminishes to the north of this belt, that of the ASM decreases to the south (Courtillat et al., 2020). The Indonesian Throughflow (ITF) transports a part of the IPWP waters along the coast of Western Australia (Current et al., 1996; Gordon and Fine, 1996; Spooner et al., 2005; Wijffels et al., 2002), where it eventually mixes with water from the central Indian Ocean to form the Leeuwin Current (LC). The latter is a surface current of slightly salted, warm waters that flows southward following the coastline and preventing upwelling (Godfrey and Ridgway, 1985; Tomczak and Godfrey, 2003). It is weakest during the hot and dry summer, when the opposite southeasterlies are the strongest and the ITCZ is in its southern position. Since the contraction/expansion of the IPWP and the intensity of the ITF are strongly linked to the IOD phases and the El Niño-Southern

Oscillation (ESO), so is the Leeuwin Current (Saji et al., 1999; Webster et al., 1999) being strengthened during la Niña and weakened during el Niño events (Spooner et al., 2011). Particularly strong events dominated by La Niña makes the LC strong enough to extend up to the southern coast of Australia and the Tasman Sea (De Deckker et al., 2012). The evaporation of the warm LC waters is a key contributor to the winter precipitation in the region of Shark Bay.

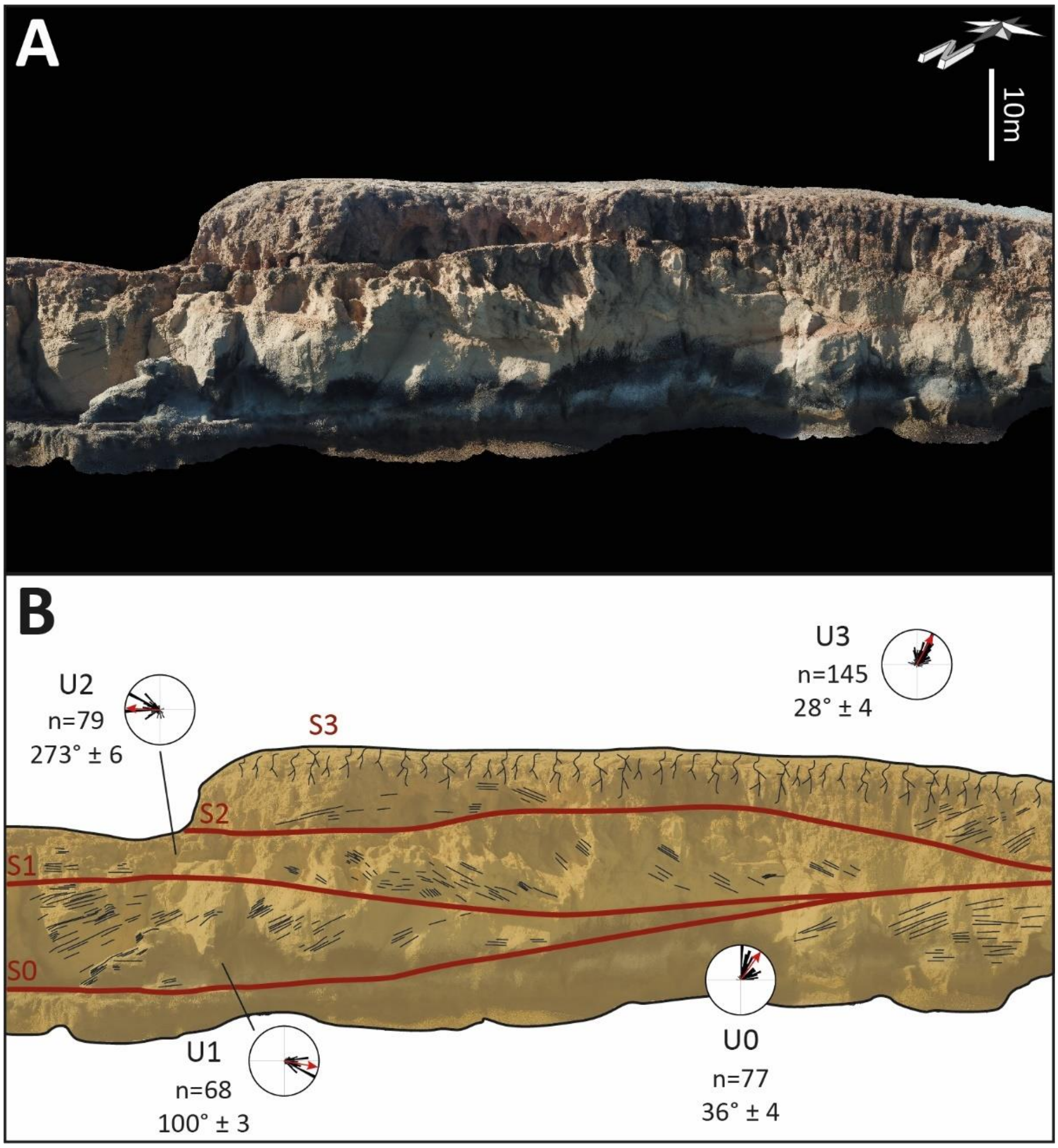

Figure 34: The 3D model (A) of Steep Point and the (B) stratigraphic interpretation showing the distribution of the measured cross-strata dip directions for each unit, along with the mean direction vectors (red arrows).

3 Methods

3.1 3D models

High-resolution virtual outcrop models were generated using UAV imagery. The UAV used is a DJI™ Mavic Pro Platinum equipped with an onboard camera with a 12.71M pixels, 1/2.3” (CMOS) sensor and a 78.8° FOV, 26mm f/2.2 lens with limited distortion. Still pictures are acquired in a portion of a circle facing the outcrop faces, at 10 to 30m away from the rock face. In total, 361 photographs were taken of the False Entrance Blowholes, 65 of the Cliff 1, 112 for the Cliff 2, and 414 of the Steep Point outcrops. Those photographs are then processed using Agisoft Metashape™, in which they are aligned, georeferenced and orientated. Then, a dense point cloud is generated for each outcrop, at this stage algorithmic artefacts, commonly water and/or sky-related, as well as isolated points are cleaned. Finally, a mesh is created using the clean point cloud, and a draping texture is generated. The final model is georeferenced then exported to be processed in VRGS™ (Virtual Reality Geoscience Studio) to measure the dip and dip direction of cross-beds. Mean direction vectors for each unit were calculated by applying a von Mises probability density function to the data.

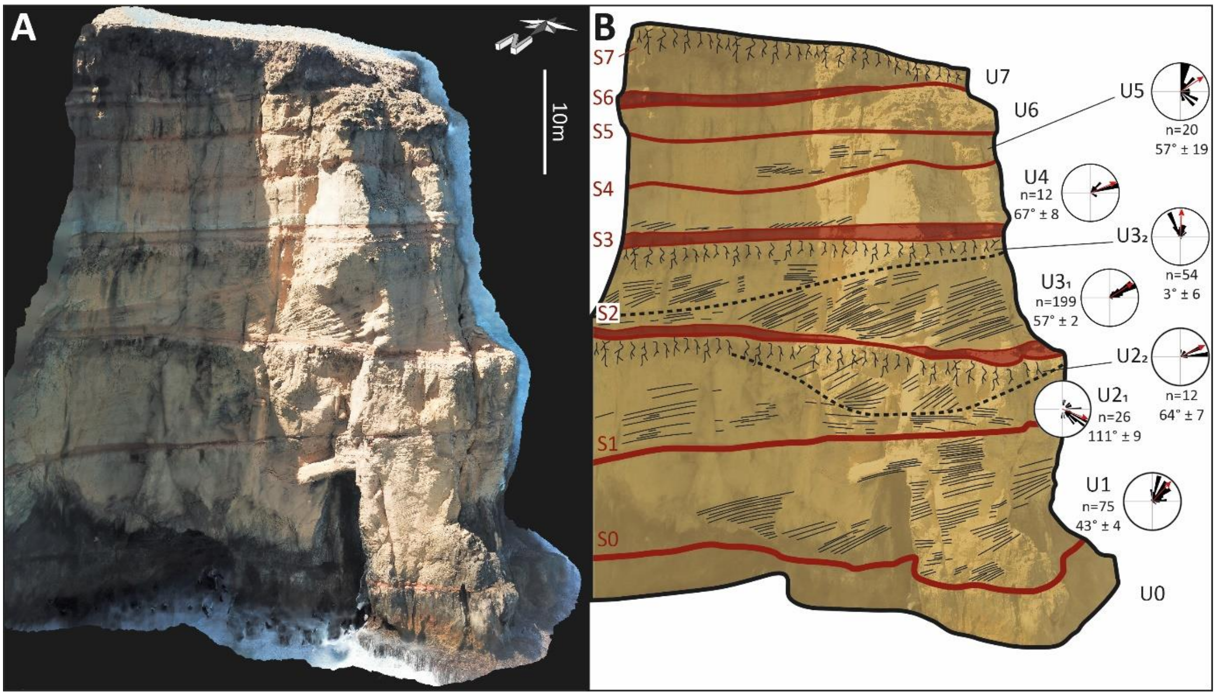

Figure 35: Photogrammetry-generated 3D model (A) of Cliff 1 next to the stratigraphic interpretation and dip direction measurements (B).

3.2 Whole-rock amino acid racemization (AAR) dating

Altogether, 48 samples were retrieved from aeolianites of the Tamala Limestone, using a hammer and a chisel. A total of 34 samples were collected when rappelling down the Zuytdorp Cliffs. Considering their exposure to the elements (wind, spray, varying temperature, and humidity), the sampling was done away from paleosol levels (>1 m below) and a 20 cm-deep square was first carved in the cliffs each time to limit a potential bias. The samples were then sent to the Amino Acid Geochronology Laboratory of the Northern Arizona University where the amino acid content was measured by reverse phase high-performance liquid chromatography (Kaufman and Manley, 1998). After a bleaching of 30% of their total mass with 2M HCL, two sub-samples analyses were conducted for each sample through a 22h-long hydrolysis.

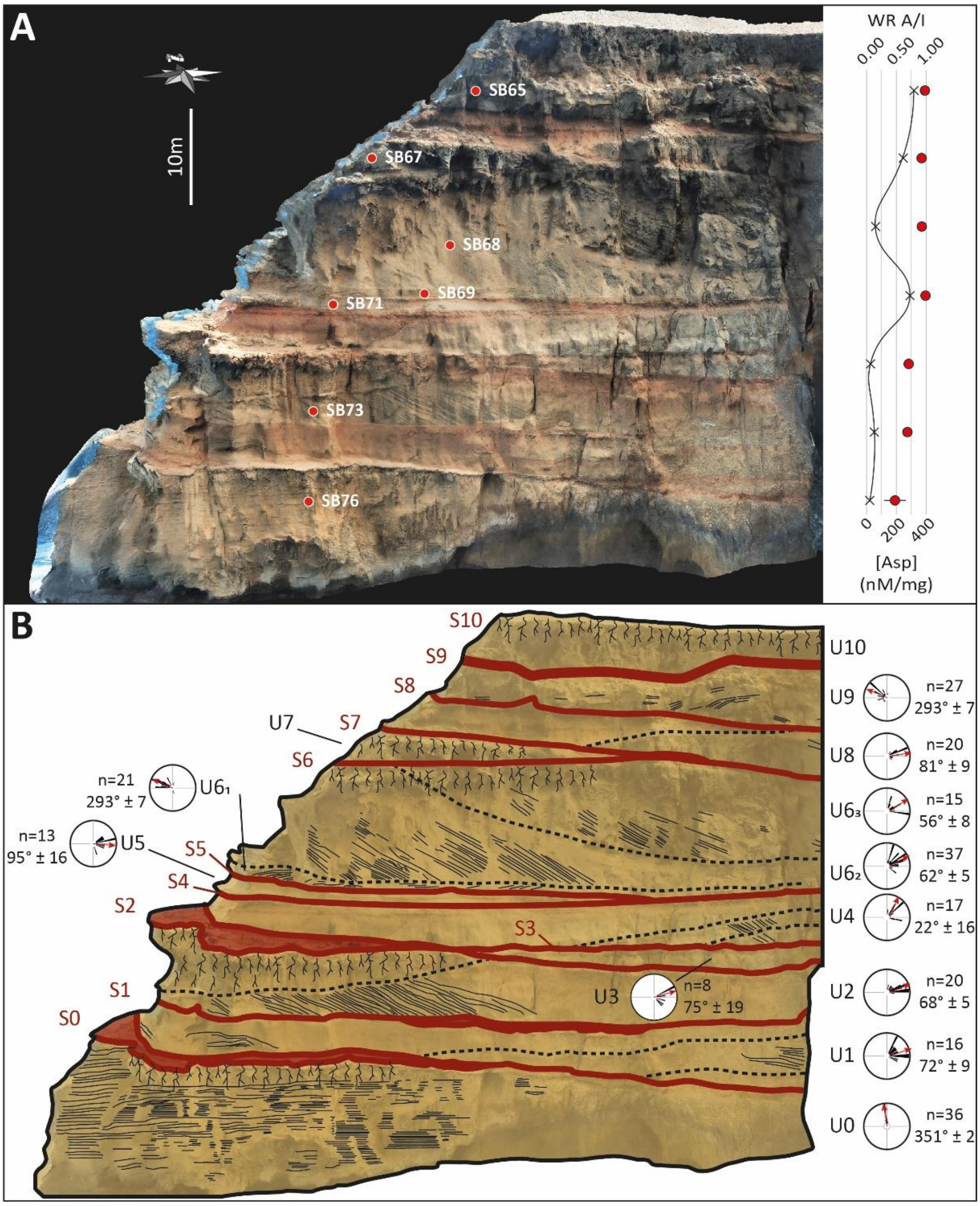

Figure 36: A: 3D model of Cliff 2 showing the sampled units and the associated A/I values and amino acid concentrations decreasing downwards. B: Stratigraphic interpretation of Cliff 2 showing the distribution of the measured cross-strata dip directions for each unit, along with the mean direction vectors (red arrows).

The conversion method of Whitacre et al. (2017) was applied to the present data to calculate the Alloisoleucine/Isoleucine (A/I) values in order to compare them with the database provided by Hearty and O'Leary (2008). The whole-rock (WR) approach seems preferable considering the skeletal nature of the dominant material. Organisms have control over the symmetry of amino acids contained in their shells, which influences the initial DL ratios (Hearty and Kaufman, 2009). The WR-AAR method averages the DL ratios of all the organisms, matrix and cement constituting the samples, resulting in an estimation of the average age of deposition of the sediment.

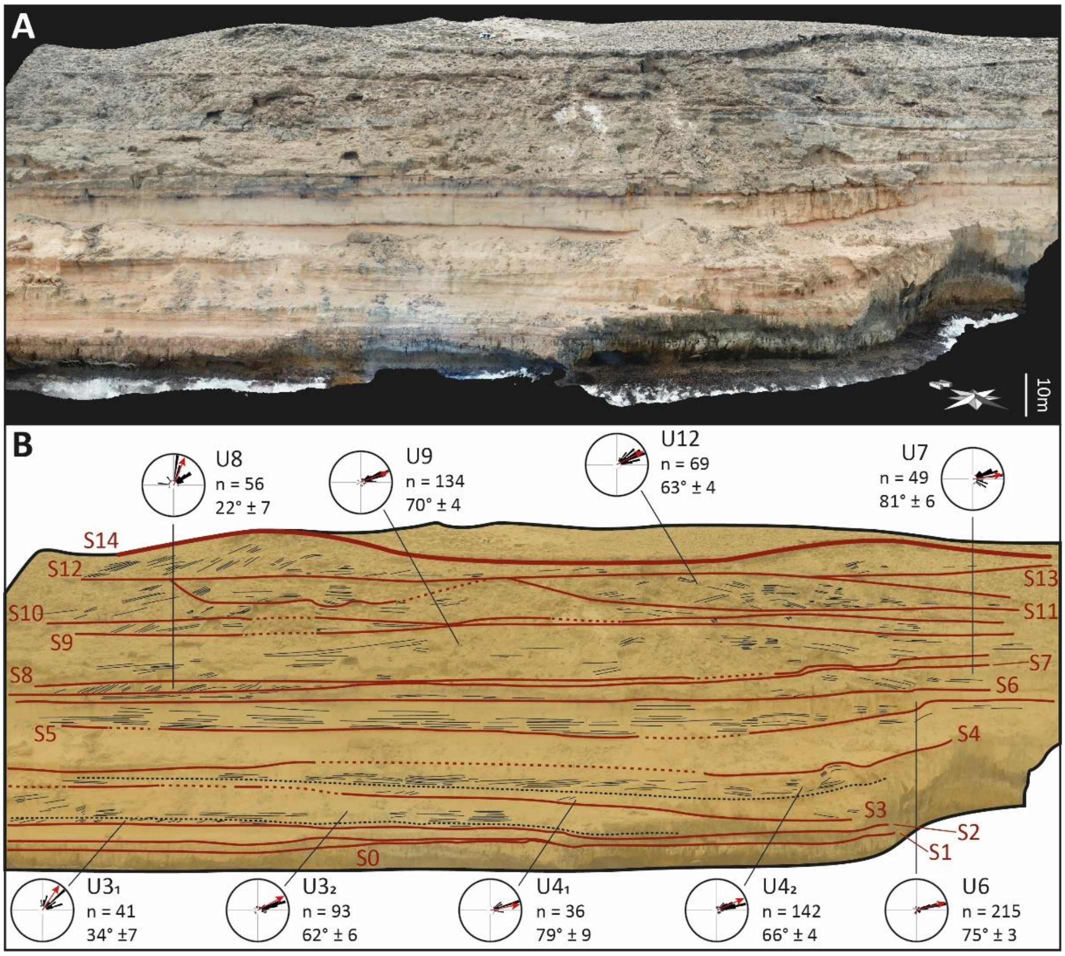

Figure 37: Model of the southernmost studied section at False Entrance Blowholes.

4 Results

4.1 Stratigraphy and sedimentology of the Zuytdorp Cliffs sections

The height and the number of units composing the cliffs become greater southward where they reach their maximum at Womerangee Hill, the Tamala Limestone type locality. Generally, the stratigraphy is defined by a stack of alternating carbonate units that are overlain by subsequent red paleosol horizons. Paleosols range from a light-yellow to deep red colour and can be sandy, nodular or calcretic. They may be rich in rhizoliths or gastropods and reach up to 2 m in thickness. Some less-developed soil horizons are present within the carbonate units where they appear as loose, sandy layers usually light-yellow or light orange in colour. The carbonate units are characterised by high-angle, tabular- to wedge-planar cross-bed sets that are

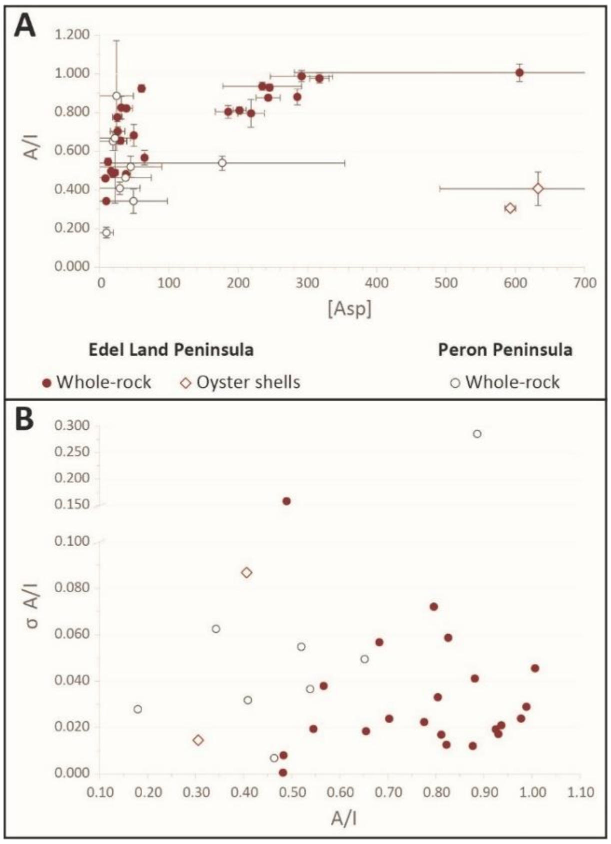

Figure 38: A: A decrease in amino acid concentration correlates with a decrease in the measure DL-Asp ratio and therefore, in the subsequently calculated A/I ratio. The oyster shells were sampled at Baba Head in a shelly storm-surge layer (sb36 and sb39 in Table 4). Samples from the Peron Peninsula show lower amino acid concentrations and A/I ratios compared with the ones from Edel Land Peninsula. B: The uncertainty increases with the A/I value.

metric to decametric in size. They mostly consist of an alternation of fine-grained grainfall and thicker coarse-grained sandflow strata (Figure 33A). A total of 1832 dip and dip directions were measured on four photogrammetric 3D models (Figure 33B). These measurements indicate that the majority (55 %) of the cross-beds dip at angles higher than 20°, and 40% at more than 30°. Most of these beds (80 %) are dipping ENE whereas the second cluster (14.6 %) of orientation indicates a NW direction. The resultant mean vector has an orientation of 54.2 ±1.4°, which corresponds to a general NE orientation of the cross-strata.

Four different units were defined at Steep Point, the northernmost location, where carbonate intervals are about 10 m-thick and underlie thin (~1 m), well-cemented soil horizons (Figure 34). The mean dip orientation of the cross-beds from the units 0 and 3 is NE whereas units 1 and 2 show an ESE and W orientations, respectively.

South of Steep Point, seven couplets carbonate-paleosol were identified at Cliff 1 with a thickness ranging from 5 to 15 m (Figure 35). A bounding surface and a protosoil divide the units 2 and 3, respectively, into four subunits from which orientation measurements were made separately. Overall, the general sedimentary structure of the cliff is pointing ENE, which is also the case for the units 2_2 and 4. The units 1 and 3_1 indicate a NE orientation of cross-beds whereas the ones forming the unit 3_2 are dipping north. Contrary to the others, unit 5 does not present a unimodal distribution of the measured orientations but rather a bimodal one with cross-beds dipping towards the N-NE and SE. Only the unit $U2_1$ indicates a sedimentary structure dipping towards the SE.

Cliff 2 only lies 300 m to the SE from Cliff 1 but displays a more complex stratigraphy. Ten units compose Cliff 2, of which four are subdivided into two or more subunits by bounding surfaces, sometimes represented by protosoils (Figure 36). Most of the cross-beds are dipping E to NE except for the ones from unit 0 that are dipping N, and from units 6_1, and 9 that are inclined towards the NW.

The southernmost studied cliff, located at False Entrance Blowholes, is composed by 15 units separated by 14 visible paleosol horizons (Figure 37). All carbonate units show a unimodal distribution of cross-beds orientations uniformly indicating an ENE dip direction.

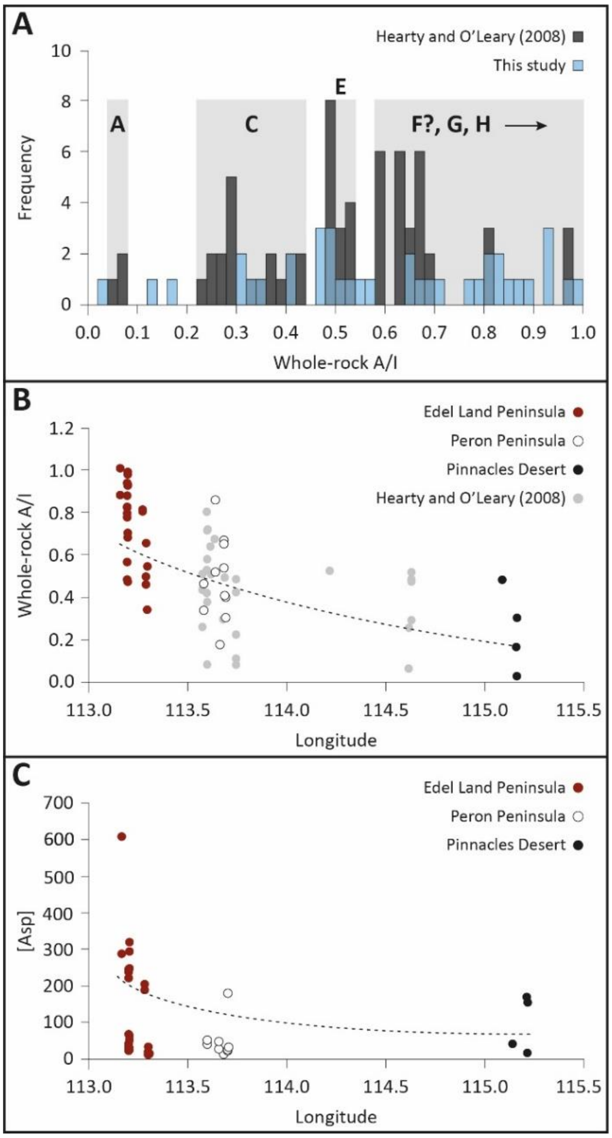

Figure 39: A: Histograms of whole-rock A/I values from this study along with the ratios and aminozones defined by Hearty and O'Leary (2008). The eastward (i.e., inland) decrease in both A/I values (B) and amino acid concentrations (C) representing the increasing diagenetic state (i.e., aging) of sediments.

4.2 Whole-rock AAR

The samples collected in the Shark Bay area have A/I ratios ranging from 0.179 to 1.006, and amino acid concentrations varying from 9 to 633 nM/mg (Table 4). Out of the 48 analysed samples, 24 showed low concentrations of amino acids, defined as < 80 nM/mg (Hearty and O'Leary, 2008), and 4 of them could only be analysed once. Nine samples had amino acid concentrations below the detection limit. In general, uncertainty becomes greater with a higher A/I ratio, which increases with the amino acid concentration (Figure 39). Both A/I ratios and the corresponding amino acid concentration values exponentially decrease towards the east (Figure 40).

In total, 12 samples were collected from six different sites (Figure 30) along the cliffs of the west coast of the Peron Peninsula. The Tamala Limestone can be seen overlying the Peron Sandstone at three locations, going from North to South: Eagle Bluff (Figure 40), an unnamed headland south of the Whalebone Campsite (Figure 41A), and another one north of Goulet Bluff that will be referred to as Campers Viewpoint in this study (Figure 41B). At Eagle Bluff, the two samples from the same unit of the ESE-facing cliff yielded A/I ratios of

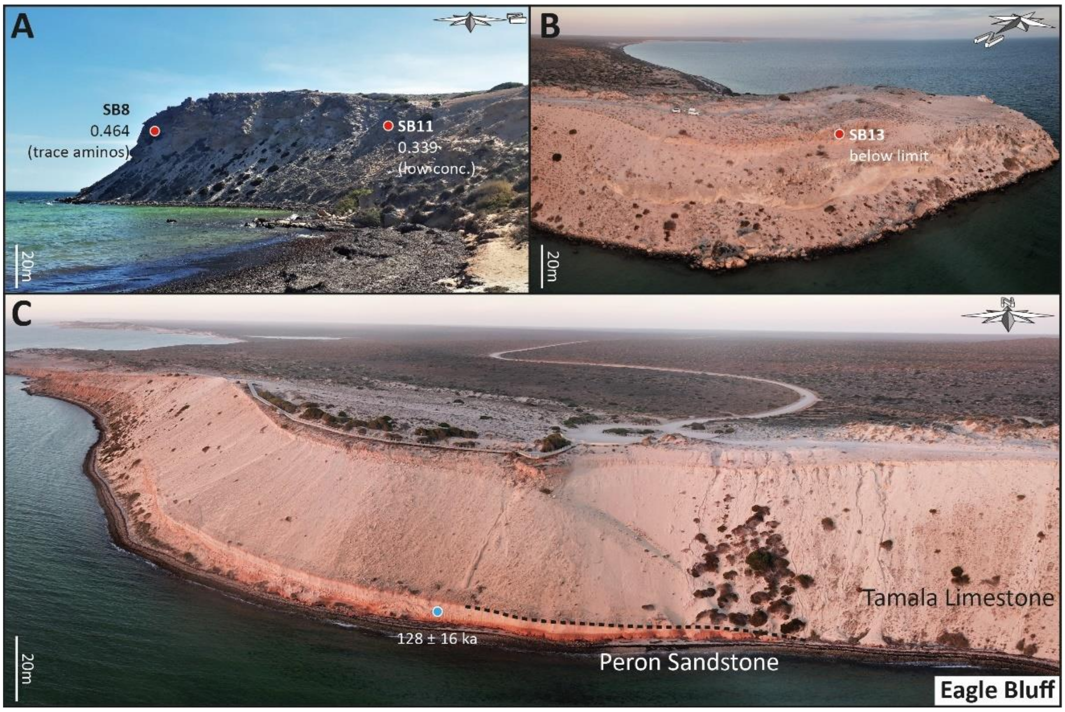

Figure 40: Three samples from the top carbonate unit at Eagle Bluff were samples within the ESE- and WNW-facing cliffs (A and B). C: Cliff exposing the Tamala Limestone overlying the Peron Sandstone, from which an OSL age has been retrieved by Pietsch and Olley in 2005 (Playford et al., 2013), at Eagle Bluff.

0.464 ±0.005 and 0.339 ±0.051, and low concentrations in amino acid (37 and 49 nM/mg). The concentrations in the sample collected within the WNW-facing cliff were below the detection limit therefore no A/I ratio could be retrieved from it. At the Whalebone Campsite, two samples from the limestone that were taken within the fine and the coarse lamina of cross-beds gave ratios of 0.518 ±0.035 (45 nM/mg) and 0.857 ±0.132 (24 nM/mg), respectively. South of the Whalebone Campsite, the loose sediment being blown off on top of the red sandstone and the carbonate bluff displayed a ratio of 0.179 ±0.034 and a low concentration in amino acid (10 nM/mg). Another ratio of 0.538 ±0.023 (177 nM/mg) was measured from the limestone bluff lying north of the Campers Viewpoint. At the Campers Viewpoint, the limestone and the underlying red calcareous sandstone yielded an A/I value of 0.669 (measured only once, 22 nM/mg) and 0.651 ±0.027 (20 nM/mg), respectively. Finally, the limestone at Goulet Bluff produced an A/I ratio of 0.408 ±0.023 and a concentration value of 29 nM/mg.

Along the west coast of the Edel Land Peninsula, six locations were investigated for aminostratigraphy (Figure 30). The top and the middle units at Steep Point yielded A/I ratios of 1.006 ±0.019 and 0.881 ±0.019, respectively (Figure 42A). The upper unit showed a mean concentration (606 nM/mg) that is nearly twice higher than the one measured in the underlying unit (285 nM/mg). A total of ten samples were collected within the cliffs forming the southernmost studied section at False Entrance Blowholes (Figure 42B). The decrease of A/I values from stratigraphically lower units correlates with the decreasing trend in the concentration of amino acids. The carbonate units from Cliff 2 yielded ratios in a descending order of 0.977 ±0.010, 0.930 ±0.008, 0.925 ±0.008, 0.988 ±0.012, 0.703 ±0.012, 0.681 ±0.030, 0.473 ±0.106 (Figure 36).

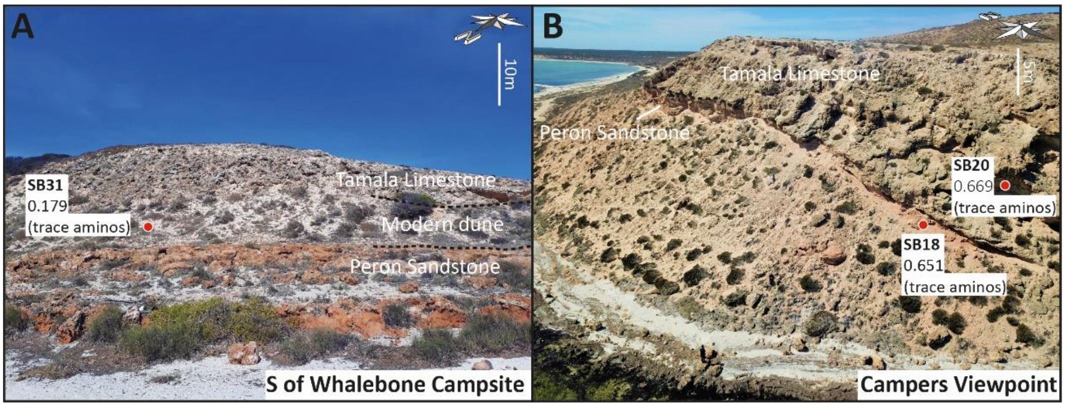

Figure 41: The Tamala Limestone can be seen overlapping the Peron Sandstone in different locations along the Western Coast of the Peron Peninsula. South of the Whalebone Campsite (A), a modern dune feeding from the adjacent beach is presently migrating on top of both the Tamala Limestone and Peron Sandstone.

The top and intermediate units of a cliff at Thunder Bay Blowholes gave A/I values of 0.812 ±0.008 and 0.804 ±0.016, respectively, with a concentration in amino acids slightly higher in the uppermost unit (Figure 44A). The cliffs terminating the beach of Crayfish Bay, also named Epineux Bay, on its northern shore were also investigated (Figure 44B). From the top to the base of the Crayfish Bay section, the retrieved A/I values decrease from 0.655 ±0.016, to 0.497 (measured once), and to 0.461 (measured once), which correlates with the decreasing concentrations in amino acids (30.5, 17, and 9 nM/mg). One sample from an immature protosoil within the uppermost unit, and another one from the unit below had concentrations of amino acids below the detection limit. Finally, the uppermost unit of the cliffs at Dulverton Bay (also named False Entrance) was sampled twice (Figure 44C). Samples showed similar concentrations of amino acids (12 and 10 nM/mg) and yielded A/I ratios of 0.545 ±0.012 and 0.342 (measured once).

Whilst the concentration values in amino acids are evidently decreasing towards the base of the section, the calculated A/I ratios display a greater variability with no clear trend. In descending order, A/I values were calculated at 0.937 ±0.009, 0.794 ±0.035, 0.877 ±0.005, 0.483 ±0.005, 0.566 ±0.023, 0.825 ±0.028, two samples below the detection limit, 0.776 ±0.011, and 0.822 ±0.006. Of the corresponding amino acid concentration values, only the first three were above the significative limit of 80 nM/mg.

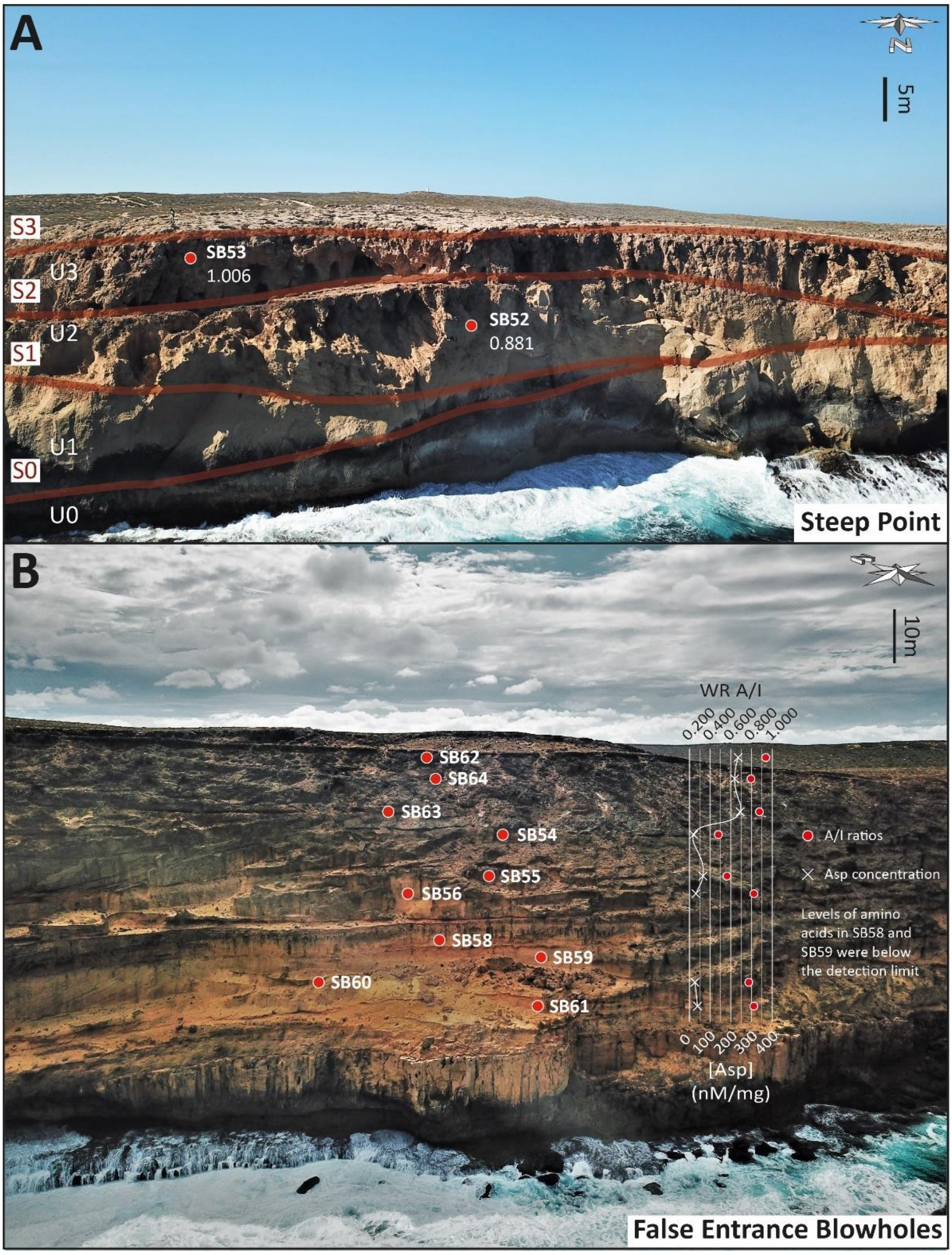

Figure 42: A: Stratigraphy and A/I values from Steep Point, the northernmost investigated section in this study. Each aeolianite is capped by a red, bioturbated paleosol horizon. B: At False Entrance Blowholes, the southernmost studied section, the AAR analysis show the characteristic decrease in amino acid concentrations in the stratigraphically lower units. Whole-rock A/I ratios from the bottom aeolianites are considered unreliable because associated with very low level of amino acids.

5 Discussion

5.1 Whole-rock AAR

Only one third of the processed samples showed levels of amino acid concentration that were high enough to ensure trustworthy subsequent A/I ratios (Figure 39). Most of these are close to the equilibrium value settled at 1.3 (Hearty and Kaufman, 2009, 2000), which makes them less reliable. This is emphasised by an uncertainty increasing with A/I values, and ratios being significantly different between samples coming from the same unit (Figure 40 and Figure 44). The distribution of the measured A/I ratios is similar to the one published by Hearty and O'Leary (2008), with values concentrating within the aminozones they have defined for the region (Figure 40A). However, our data show inconsistencies such as the bottom unit at Cliff 2 and the top one at Dulverton Bay, both correlating with the aminozone E. The latter was assigned to MIS 5e by Hearty and O'Leary (2008), which would indicate that the entire Tamala Limestone complex in Shark Bay was deposited during this unique highstand. This observation does not corroborate the age interpretations made for the Zuytdorp Cliffs succession by previous authors (Playford, 2013; Hearty and O'Leary, 2008).

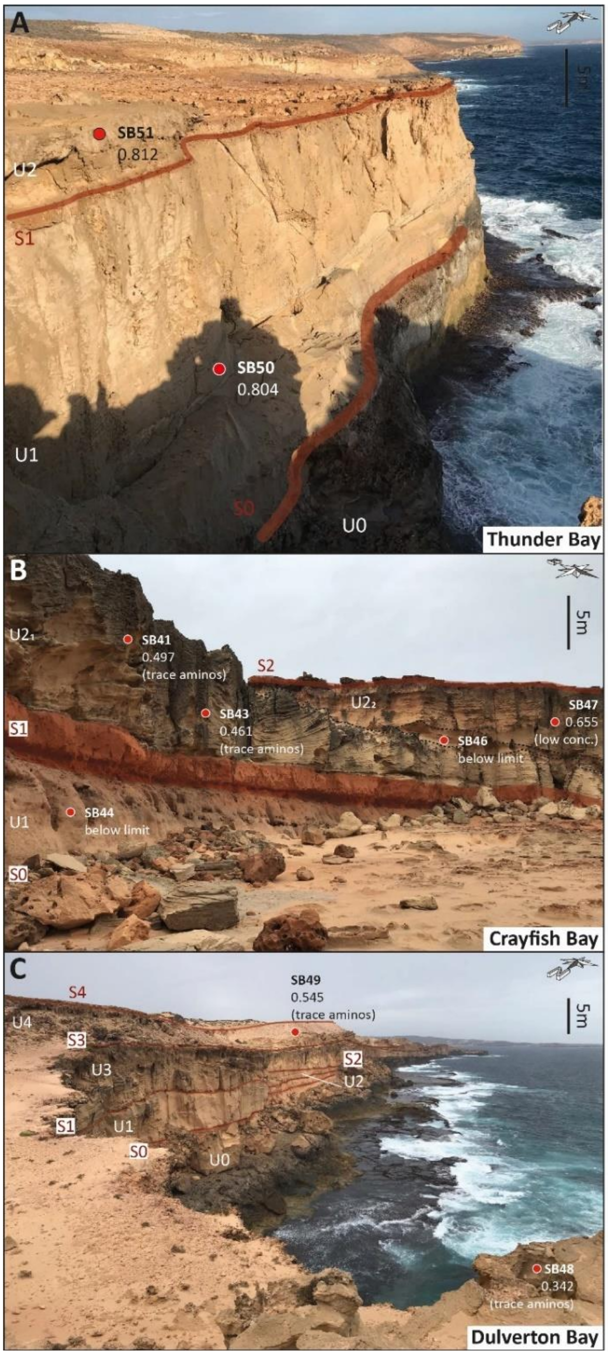

Figure 43: Stratigraphy and A/I ratios at three locations of the Zuytdorp Cliffs, from north to south: A: Thunder Bay; B: Crayfish Bay; and C: Dulverton Bay.

Generally, the concentrations in amino acids and the A/I values retrieved from the Tamala Limestone on the Peron Peninsula are lower than the ones measured on samples from the Edel Land Peninsula (Figure 40B and C). Lower A/I ratios indicate younger units but the reliability of the measurements is highly dependent of the amino-acid concentration within the carbonate. It is already known that amino acid concentration decreases with the age of the sample and the state of diagenesis (Hearty and Kaufman, 2000; Hearty and O'Leary, 2008; Roof, 1997), so this observation either indicates that carbonate units tend to be older or that the degree of carbonate diagenesis increases towards the East. Previous studies that have been conducted in the Perth Basin have demonstrated that

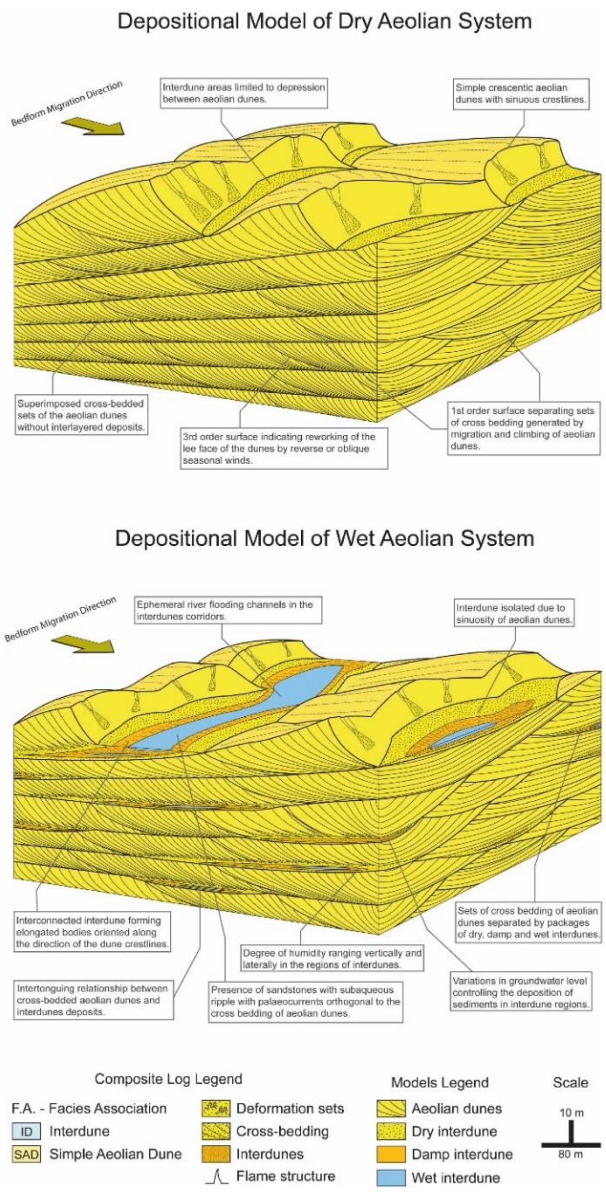

Figure 44: Architectural models for dry and wet aeolian systems (Jones et al., 2016).

the yellow sand overlying the Tamala Limestone formed by residual accumulation of the siliciclastic material after the dissolution of the carbonate units (Bastian, 2010, 1996, 1994; Newsome, 2000; Playford et al., 2013). The authors pointed out the progressive leach-out of heavy minerals most susceptible to weathering towards the east, so from the youngest to the oldest units. The inland ageing of the units was later confirmed by U-Th dating of successive coastal ridges of the Swan Coastal Plain and the Geraldton Sandplains (Lipar and Webb, 2014). The progressive loss in amino acid observed towards the east in Shark Bay therefore indicates an increase in the diagenetic state of the limestone, which correlates with the inland ageing of the deposits. This is also supported by the systematically observed decrease in both A/I value and amino acid concentration in stratigraphically lower units along the studied transects (Figure 36 and Figure 42). As already suggested by Hearty and O'Leary (2008), the lowering trend of amino acid values is time-dependent and can be used for a relative dating of the Tamala Limestone units. However, further accurate dating will require a robust calibration with absolute dating techniques (e.g., U-Th, or OSL) to compensate for the lack of accuracy of the AAR method. Nevertheless, these data refute the interpretation that the carbonate units of the Tamala Limestone at the Zuytdorp Cliffs formed during one single glacial episode (MIS 8, Playford et al., 2013), but rather suggest that deposition took place during various intervals of the Quaternary.

5.2 Type of aeolian dunes

The Tamala Limestone exposed along the Zuytdorp Cliffs present the characteristic aeolian alternation of grainfall and sandflow cross-strata (Figure 33A; Hunter, 1977; Kocurek, 1996, 1991, 1981; Uličný, 2004). Some sets of cross-strata from the investigated sections are more than 10 m-thick (Figure 35), which implies a much greater height of the dune. A minimum dune height of 10 m can be inferred from the average thickness of sandflow strata reaching up to 5-8 cm (Kocurek and Dott, 1981; Romain and Mountney, 2014). These estimations fall into the range (10-20 m) of the seif and parabolic dunes marking the current topography of the Edel Land Peninsula (Figure 30).

There is a predominance of the sandflow strata, most of which reaching the base of the slope, over the grainfall strata. Such extended sandflow strata are typical of aeolian dunes that had well-developed slipfaces during most of their periods of deposition, when sandflow processes were the main contributors to dune migration (Kocurek, 1991). It also characterises dune crestlines that were oriented transverse to prevailing effective palaeowinds (Jorgensen, 2012; Kocurek, 1991).

5.3 Aeolian system geometry

Dry aeolian sedimentary systems are characterised by a water table lying beneath the surface of accumulation, thus having a very minor influence on sedimentation (Mountney, 2011). The associated interdunes are either thin deposits (<1 m) or constitute first-order bounding surfaces (Figure 45) separating cross-bedded sets of aeolian strata when reduced to isolated interdune depressions (Kocurek and Havholm, 1993; Lancaster and Teller, 1988). By contrast, aeolian accumulation in wet aeolian systems occurs when the water table rises, which results in aeolian strata being separated by thick, extensive interdune horizons (Figure 45) over which they climb during periods of downwind migration (Kocurek et al., 1993; Loope and Simpson, 1992). The interdune units in these systems are often characterised by a reddish colour, horizontal wind ripple lamination, adhesion structures, current ripple cross-lamination and planar lamination (e.g., Jones et al., 2016), which are indicative of wet sediment surfaces (Ahlbrandt and Fryberger, 1981; Fryberger et al., 1983; Hunter, 1980; Kocurek, 1996, 1991, 1981; Kocurek and Fielder, 1982).

The stack of landward-advancing dunes of the Tamala Limestone observable along the Zuytdorp Cliffs represents a dry aeolian system with regional-scale interruptions of sedimentation. Because the red horizons separating aeolian sets of strata are heavily bioturbated (e.g., high density of rhizoliths) and do not present the typical features of wet interdunes, they constitute paleosols (Kocurek, 1988; Mountney, 2006a, 2006b) marking regional breaks in the aeolian accumulation. The thicknesses of the carbonate units and the size of the cross-strata

Table 4: Amino acid concentrations and A/I ratios measured by reverse phase (RP) chromatography on whole-rock samples from Shark Bay, the Geraldton Sandplains, and the Swan Coastal Plain (based on the Interim Biogeographic Regionalisation for Australia, IBRA7). Alloisoleucine/Isoleucine (A/I) values were calculated following a log2 transformation of the DL-Asp ratios, following to the method developed by Whitacre et al. (2017).

Area	Location	#	Lat.	Long.	DL Asp	±	[Asp]	A/I
Peron	Cape Peron	sb3	-25.54	113.49	ND	ND	ND	ND
	Eagle Bluff	sb7	-26.09	113.58	ND	ND	ND	ND
		sb8	-26.09	113.58	0.586	0.005	37	0.464
		sb11	-26.09	113.58	0.520	0.051	49	0.339
		sb13	-26.09	113.58	ND	ND	ND	ND
	Whalebone Campsite	sb14	-26.13	113.64	0.611	0.035	45	0.518
		sb15	-26.13	113.64	0.740	0.132	24	0.857
	S of Whalebone Campsite	sb31	-26.16	113.66	0.408	0.034	10	0.179
	N of Campers Viewpoint	sb30	-26.18	113.68	0.620	0.023	177	0.538
	Campers ViewPoint	sb20	-26.20	113.68	0.673	ND	22	0.669
		sb18	-26.20	113.68	0.666	0.027	20	0.651
	Goulet Bluff	sb28	-26.22	113.69	0.558	0.023	29	0.408
Edel Land	Baba Head	sb39	-26.61	113.69	0.554	0.064	633	0.401
		sb36	-26.61	113.69	0.500	0.013	593	0.305
	Steep Point	sb53	-26.14	113.16	0.786	0.019	606	1.006
		sb52	-26.14	113.16	0.748	0.019	285	0.881
	Cliff 2	sb65	-26.20	113.20	0.778	0.010	317	0.977
		sb67	-26.20	113.20	0.763	0.008	245	0.930
		sb68	-26.20	113.20	0.762	0.008	61	0.925
		sb69	-26.20	113.20	0.781	0.012	292	0.988
		sb71	-26.20	113.20	0.686	0.012	26	0.703
		sb73	-26.20	113.20	0.678	0.030	50	0.681
		sb76	-26.20	113.20	0.591	0.106	22	0.473
	Thunder Bay Blowholes	sb51	-26.29	113.27	0.725	0.008	202	0.812
		sb50	-26.29	113.27	0.722	0.016	186	0.804
	Crayfish Bay	sb47	-26.33	113.29	0.668	0.010	30.5	0.655
		sb46	-26.33	113.29	ND	ND	ND	ND
		sb41	-26.32	113.29	0.602	ND	17	0.497
		sb43	-26.32	113.29	0.584	ND	9	0.461
		sb44	-26.33	113.29	ND	ND	ND	ND
	Dulverton Bay	sb48	-26.36	113.29	0.522	ND	10	0.342
		sb49	-26.37	113.30	0.623	0.012	12	0.545
	False Entrance Blowholes	sb62	-26.19	113.19	0.765	0.009	235	0.937
		sb64	-26.19	113.19	0.719	0.035	219	0.794
		sb63	-26.19	113.19	0.746	0.005	243	0.877
		sb54	-26.19	113.19	0.595	0.005	20	0.483
		sb55	-26.19	113.19	0.632	0.023	65	0.566
		sb56	-26.19	113.19	0.729	0.028	32	0.825
		sb58	-26.19	113.19	ND	ND	ND	ND
		sb59	-26.19	113.19	ND	ND	ND	ND

		sb60	-26.19	113.19	0.712	0.011	26	0.776
		sb61	-26.19	113.19	0.728	0.006	39	0.822
Southern Beekeeper's Nature Reserve	Aiyennu Cave	sb77	-29.93	115.09	0.595	0.000	38	0.482
		sb78	-29.93	115.09	ND	ND	ND	ND
Nambung National Park	Pinnacles Desert	sb79	-30.61	115.16	ND	ND	ND	ND
		sb80	-30.61	115.17	0.499	0.017	152	0.304
		sb82	-30.61	115.17	0.208	0.023	14	0.030
		sb83	-30.60	115.16	0.367	0.142	167	0.135

indicate a high ratio of accumulation over downwind migration rates, which defines a field of great aggregation compared with a field of deflation (Figure 45; Mountney, 2011). In these settings, there is a significant sediment supply and availability along with an accumulation process occurring via bedforms climbing over one another (Rubin and Hunter, 1982). The reactivation surfaces between two sub-units can form from the erosion of the dune slipface following a change of dune height, local wind direction and speed (e.g., reverse winds), or dune asymmetry (Kocurek, 1991; Mountney, 2006b; Rubin and Hunter, 1983).

5.4 Prevailing palaeowinds

The dominant planar geometry of the cross-strata, the prevailing sandflow strata, and the unimodal distribution of the cross-beds dip directions (Figure 33B) indicate landward-advancing (i.e., transgressive; Rowe and Bristow, 2015a, 2015b) dunes migrating sub-perpendicularly to the coast towards the NE. When looked at individually, the units defined for the four studied sections also show unimodal distributions of cross-strata orientations, which are interpreted as foresets. The evident dominant directions of effective palaeowinds are towards the NE and the E, with data being more or less widely distributed around these values. Only three units out of the 31 analysed indicate a NW palaeowind direction, with cross-strata dipping at high angles (~30 °). They could either be correlated with reversing winds such as the ones blowing in winter at present, or interpreted as backslope dune deposits (i.e., backset sets).

5.5 Palaeoclimate interpretations

The depositional timing of the Tamala Limestone remains an unsettled issue as of today (Hearty and O'Leary, 2008; Jorgensen, 2012; Lipar and Webb, 2014; Playford et al., 2013). The answer to the question of whether sediment accumulation occurred during interglacial or glacial periods is complicated by the lack of accuracy of the various dating methods and the alteration level of sediments. At present, the surface dunes from Carrarang Sand and the

Denham Sand are mostly stabilised by vegetation despite the aridity of the region. The deposition of such considerable extensive dunes should have occurred during periods when sand transport was substantially facilitated. This implies a close productive source of sediment (Pye and Tsoar, 2008), winds blowing above the saltation threshold (e.g., Fryberger and Dean, 1979; Kocurek and Lancaster, 1999), and likely an increase in aridity which usually correlates with a degradation of the vegetation cover.

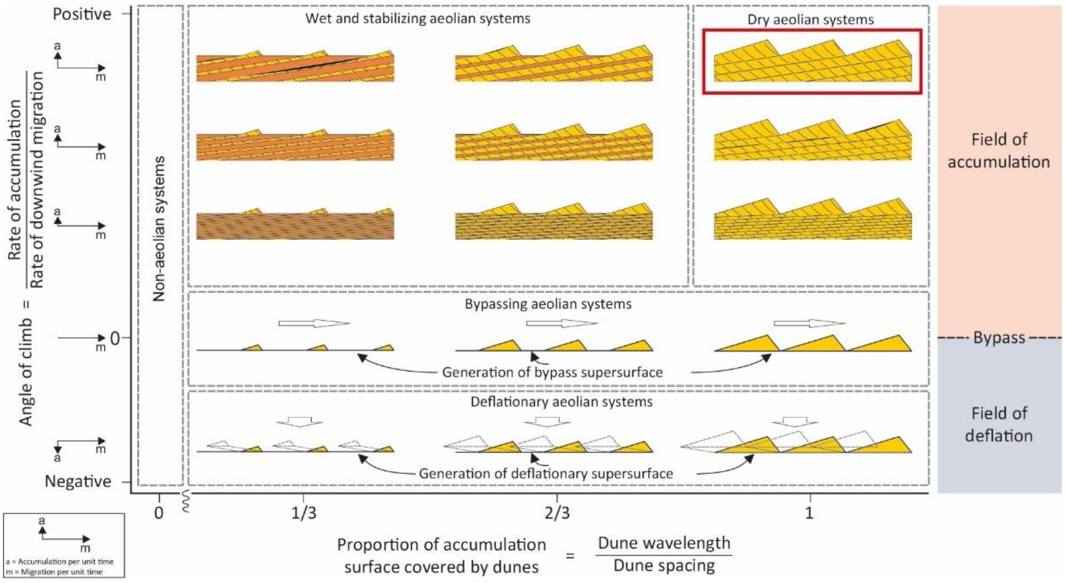

Figure 45: Modelled preserved architectures for static aeolian systems (from Mountney, 2011). A field of deflation, contrary to a field of accumulation, is defined by an angle of bedform climb of zero. The higher the angle of climb, the greater is the accumulation rate with respect to the downwind migration rate. Different architectures are generated by wet and dry aeolian systems, the former including wet interdune deposits. The Tamala Limestone at the Zuytdorp Cliffs corresponds to a dry aeolian system with a high accumulation rate (red rectangle), suggesting great sediment supply and availability from a source located close by.

During glacial periods, the decrease in sea surface temperature (SST) results in less evaporation above the Indo-Pacific Warm Pool (IPWP), which weakens the convection movement of the Hadley cell and induces the shrinking of the IPWP (Figure 46), causing the northward retreat of its southern bound (Spooner et al., 2011). This would drastically reduce the southward transport of low salinity, warm IPWP waters by the Indonesian Throughflow (ITF; Barrows and Juggins, 2005; Martínez et al., 1999). This phenomenon is amplified by the cutting off and the substantial shallowing of the ITF channels caused by a lowered sea level resulting from an increase in continental ice volume (Petrick et al., 2019). An attenuation of the feeding ITF leads to a weakening of the Leeuwin Current (LC; Reeves et al., 2013), which translates into more arid conditions along Western Australia. Models for the Pliocene and LGM indicate a reduction in rainfall up to 30% when the ITF is considerably reduced (Di Nezio et al., 2016; DiNezio et al., 2018; Krebs et al., 2011).

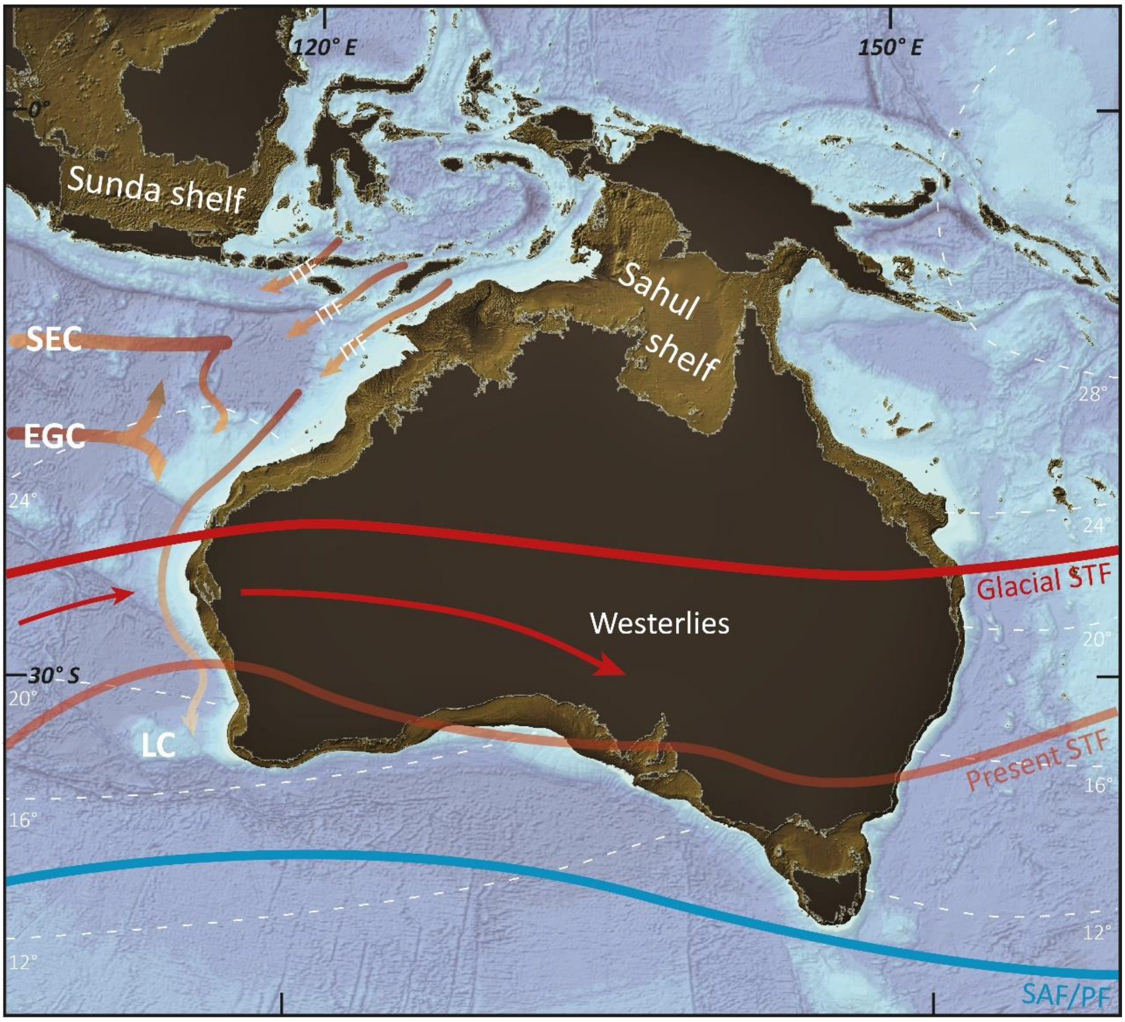

Figure 46: Maximum extent of the exposed Sahul and Sunda shelves during the LGM (-120 m) and the associated prevailing atmospheric and oceanic circulation features. White dashed lines indicate the LGM mean annual SST estimated by Barrows and Juggins (2005). Note the shrinking of the IPWP to the north compared to its modern extent and position (Figure 32). The shallowing of the Indonesian channels and straits led to a diminished transport of the IPWP waters by the ITF, which in turn led to a weakened LC (Petrick et al., 2019). This translates into less rainfall and a general aridification of Western Australia. The northward contraction and expansion of the Hadely and Ferrel cells, respectively, is illustrated by the migration north of both the STF and SAF/PF mean positions (Courtillat et al., 2020). Consequently, prevailing westerlies were blowing in the Shark Bay region.

In summary, the LC is strong during interglacials and weak during glacials, which leads to humid and arid climate conditions, respectively. This glacial-interglacial pattern in Western Australia has been demonstrated for the past 500 ka, with enhanced aeolian transport during dry glacials and increased fluvial runoff during humid interglacials (Courtillat et al., 2020; Lipar et al., 2017; Petrick et al., 2019; Spooner et al., 2011; Stuut et al., 2014). Therefore, it is unlikely that the Tamala Limestone dunes were deposited during interglacials and paleosols formed during glacials as previously suggested by some authors (Hearty and O'Leary, 2008; Lipar and Webb, 2014). It is even less likely for the MIS 5, MIS 7, and MIS 11, during which the LC was stronger than today so that climate was more humid, which would have increased the vegetation cover and limited dune mobility (Hope, 1994; Markgraf et al., 1992; Spooner et al., 2011; van der Kaars and De Deckker, 2003, 2002). The in-situ nature of the siliciclastic components of paleosol horizons (Bastian, 2010, 1996, 1994; Newsome, 2000; Playford et al., 2013; Tapsell et al., 2003) indicates a greater dissolution of the carbonate caused by intensified rainfall, correlating with interglacial periods. Moreover, the Tamala Limestone as exposed at the Zuytdorp Cliffs represents a dry aeolian system, correlating periods of deposition with glacials. A high rate of accumulation is represented by the thicknesses of the cross-strata sets, which implies a close, profusive source of sediment. During low sea levels of glacial periods, a consequent surface of the low-angle dipping Carnarvon carbonate ramp would be exposed, making sediment available to wind transport.

During the transition from a warm-humid interglacial to a cold-dry glacial, the Hadley and the Ferrel cells retreats/expands northward, respectively (Courtillat et al., 2020; De Deckker et al., 2012; Jiang et al., 2008, 2001; Jorgensen, 2012; Peterson, 1988; Scherer and Goldberg, 2007; Spooner et al., 2011; Uličný, 2004). This migration translates into a more northern position of the ITCZ, the Subtropical Front (STF), and both the Subantarctic Front (SAF)/Polar Front (PF) that are pushed closer to Australia by expanding Antarctic ice sheets (Figure 46).

It has already been shown for intervals of the Quaternary that this change in atmospheric circulation corresponds to an intensified aeolian transport (De Deckker et al., 2012; Courtillat et al., 2020). The enhanced influence of the westerlies in the Shark Bay region is shown by the palaeowind directions measured from the cross-strata and foresets orientations. This influence decreases towards the north with main wind vectors pointing more north at the Steep Point section (Figure 34) than at the False Entrance Blowing Holes section (Figure 37). Most of the studied units indicate dune migration from the west/south-west to east/north-east, which differs from the north-south orientation of the younger dunes presently lying at the surface and forming the Carrarang and Denham Sands (Le Guern, 2004). The few units indicating palaeowinds blowing from the south, if not due to secondary airflow (Frank and Kocurek, 1996; Livingstone, 1986; Sweet and Kocurek, 1990; Tsoar, 1983; I. J. Walker, 1999; Walker and Nickling, 2002), would have been deposited to conditions closer to the present ones. This reasoning applies to units showing mean wind vectors oriented towards the west and north-west which, if deposited under primary airflow or not representing backsets, would reflect the greater influence of the southeasterly trade winds of the Hadley cell in the region (Jorgensen, 2012). Overall, it seems that most the Tamala Limestone has been deposited under westerly winds prevailing in the region after a northward migration of the subtropical highs (Denton et al., 2010; Kohfeld et al., 2013). Whilst these highs seasonally bring rainfall in austral winter during their northern displacement, the long-term trend during dry glacials suggests moisture levels were not high enough to prevent dune mobilisation.

6 Conclusion

The Tamala Limestone currently exposed along the Zuytdorp Cliffs, in the Shark Bay region, shows cyclic deposition of coastal aeolianites alternating with breaks in sedimentation represented by palaeosols. The regional amino acid racemization survey coupled with a stratigraphic and sedimentological analysis, based on 3D models of the cliffs, provide new insight into the depositional timing of the Tamala Limestone aeolianites relative to glacial/interglacial cycles and the climate conditions at the time. The decrease in both A/I values and amino acid concentrations from inland units and stratigraphically lower units at the Zuytdorp Cliffs indicates a more advanced diagenetic state correlating with an aging of the units.

The Tamala Limestone is primarily constituted by landward-advancing dunes (i.e., transverse) migrating parallel to the prevailing winds. The stratigraphic layout displayed along the western coast of Edel Land Peninsula is typical of a dry accumulating aeolian system (i.e., no interdune deposits) with an important accumulation rate with respect to the downwind migration rate.

All these observations strongly suggest that the aeolian accumulation in the Shark Bay region occurred during dry/cold glacials. Lower sea levels would have exposed a consequent surface of the Carnarvon carbonate ramp where significant quantities of sediment would have been prone to transport by wind. Expanding ice sheets induced sea level drops which, coupled with lowered SST of the IPWP, would have cut off the ITF resulting in a substantially weakened LC. Consequently, diminished rainfall and moisture would have contributed to the arid climate during glacial periods. The influence of westerlies during the dunes deposition compared to today’s wind regimes correlates with northward migration of both the Hadley and Ferrel cells. Further studies to accurately date the successive units along the Zuytdorp Cliffs are warranted in order to properly constrain palaeoclimate and atmospheric circulation associated with the deposition of aeolianites in this peculiar region.

7 Author contributions

Lucas Vimpere: Conceptualisation, Methodology, Formal analysis, Investigation, Ressources, Writing - Original Draft, Writing - Review & Editing, Visualisation, Supervision, Project administration

Nicolò Del Piero: Investigation

Aymeric Le Cotonnec: Formal analysis, Writing - Original Draft

Pascal Kindler: Funding acquisition, Writing - Review & Editing

Sébastien Castelltort: Funding acquisition, Writing - Review & Editing

8 Acknowledgements

This project was funded by the Department of Earth Sciences of the University of Geneva. Our gratitude goes to the Earth Observation Centre at the German Aerospace Centre (DLR) for generously providing the DEMs needed. We would like to acknowledge the Amino Acid Geochronology Lab of the Northern Arizona University for their efficiency and for remaining available to discuss the results. We convey our warm thanks to Dave, the Chief Ranger of Cervantes who made us discover the splendid Pinnacles Desert. Dr Stephen E. Watkins greatly improved the manuscript with very valuable comments and review.

Chapter 5 – Continental interior parabolic dunes as a potential proxy for past climates

This chapter reviews the literature on continental parabolic dunes and used an OSL ages database to link periods of dune activity with global climate conditions and large-scale atmospheric circulation.

Published as:

Vimpere, L., Watkins, S. E., Castelltort, S., (2021). Continental interior parabolic dunes as a potential proxy for past climates. Global and Planetary Change, 206, 103622. DOI: 10.1016/j.gloplacha.2021.103622

Abstract

The global occurrence of parabolic dunes and their reactivation potential make them significant features in the present global landscape. Several studies have assessed the distribution and structure of parabolic dunes and their relationship to local climate factors with the aim to constrain the processes influencing their activation and potential reactivation. However, none of them have addressed the connection between recently active inland parabolic dunes and climatic conditions at a global scale, nor their potential as proxy for past climates. Here we report that the activity of 106 continental interior parabolic dunes from the last millennium is largely controlled by few *quantifiable* climate variables that are mutually influenced: aridity, type of vegetation, and wind speed. We then compare the mid-Holocene activity of 67 continental dunes with the palaeolevel of 394 lakes to confirm their relationship to past aridification, itself triggered by a northward displacement of the Intertropical Converge Zone. This study provides a quantitative tool to constrain past climates in regions where inland parabolic dunes have shown to be active, especially where other proxies are not available; along with linking continental parabolic dune activity with atmospheric circulation.

1 Introduction

Future climate change will likely result in an increase in average global temperature as well as drought frequency and severity (Coumou and Rahmstorf, 2012; IPCC, 2013). The induced vegetation loss and its impact on aeolian activity are expected to cause an intensification of desertification and land degradation (Asadi Zarch et al., 2017; Ashkenazy et al., 2012; Collins et al., 2013; Greve et al., 2019; Lancaster, 1997; Mirzabaev et al., 2019; Thomas et al., 2005; Thomas and Leason, 2005). Possible consequences of these changes include forced human migration (IPCC, 2014), decreased atmospheric carbon absorption (Lal, 2001), reduced food production (Sherr and Yadav, 1996), increased water scarcity (IPCC, 2013; Maestre et al., 2012), and ultimately conflicts (Raleigh and Urdal, 2007). It is, therefore, vital to constrain the past and present climatic factors controlling aeolian dunes activity in order to model their future mobilisation in a changing climate. One such possible method is to study parabolic dunes (Figure 47) which can be found over a wide range of latitudes and environments (Figure 48; e.g., lake shorelines, coastlines, riverbanks and continental interiors), making them an important, globally-occurring features in the present landscape (Goudie, 2011; Yan and Baas, 2015). Constraining the present eco-geomorphic systems in which parabolic dunes are currently active may therefore yield detailed insights into how the climate varied in the past.

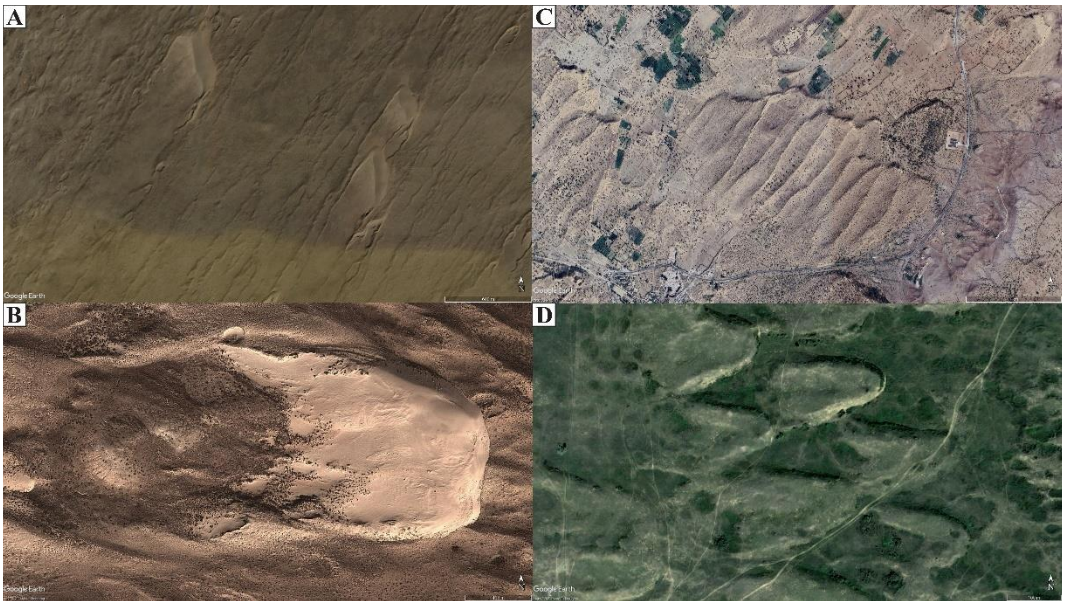

Figure 47: Examples of continental parabolic dunes around the world: (A) Great Sand Dunes, Colorado, USA; (B) Otindag desert, Inner Mongolia, China; (C) Thar desert, Rajasthan, India; and (D) Big Stick sand dunes, Saskatchewan, Canada.

Parabolic dunes typically have a U-shape or V-shape planform geometry, and are defined as asymmetric aeolian bedforms with a steep downwind “lee” slope and a much gentler upwind “stoss” slope (Hack, 1941). They result from a depositional nose migrating downwind leaving stable to semi-stable trailing arms that have been fixed by vegetation (Figure 47). Parabolic dunes located in humid regions are usually developed along large lake coastlines (e.g., Lake Michigan), or rivers, or seashores where a great majority of them evolve from blowouts within foredunes (i.e., proximal transverse dunes parallel to the shore; Hesp, 2013, 2011, 2002). In such environments, a complex framework of environmental factors governs the formation and development of parabolic dunes such as: sea level changes (Armitage et al., 2006; De Ceunynck, 1985; Pye and Rhodes, 1985; Pye and Switsur, 1981; Shulmeister and Lees, 1992; Tejan-Kella et al., 1990; Wolfe et al., 2008), lake or watertable level fluctuations (Arbogast et al., 2002a, 2010; Forman and Pierson, 2003; Hansen et al., 2010; Lepczyk and Arbogast, 2005; Lichter, 1995), variations of wind regime or sediment supply (Rawling et al., 2008; Zular et al., 2013), storminess (Clemmensen et al., 2007, 2001; Hansen et al., 2010), groundwater level (Porat and Botha, 2008), or human activity (Alexanderson and Fabel, 2015; Bertran et al., 2011; Bogle et al., 2015; Guo et al., 2018; Hesp, 2002; Hesp et al., 2010; Mason et al., 2009; Wolfe et al., 2007a, 2008). For this reason, we did not assess their potential as a palaeoclimate proxy.

On the other hand, in continental settings, parabolic dunes mostly form from the transformation of barchan aeolian dunes or transgressive dune fields (Hesp, 2011; Tsoar and Blumberg, 2002), and from the reactivation of previously stabilised sand sheets and vegetated dunes (Barchyn and Hugenholtz, 2015, 2013, 2013). This study focuses on continental interior parabolic dunes since their activity is known to be strongly controlled by sediment supply and fewer climatic factors in regards to their coastal counterparts (Yan and Baas, 2015 for a review of past work). The presence, development, activity, and transformation of inland parabolic dunes have indeed been linked with precipitation (e.g., Hoover et al., 2018; Lancaster, 1988; Landsberg, 1956; Stetler and Gaylord, 1996), temperature (e.g., Wolfe and Hugenholtz, 2009), wind regimes (e.g., Hesp, 2002; Tsoar et al., 2009), and in a more recent context, anthropogenic factors (e.g., Alexanderson and Fabel, 2015; Hesp, 2001; Hesp et al., 2010; Tsoar and Blumberg, 2002). The unequivocal relationship of parabolic dune activity with a stabilising vegetation (e.g., Durán and Herrmann, 2006; Durán and Moore, 2013; Tsoar and Blumberg, 2002; Yan and Baas, 2017), which is linked to environmental factors (Tian et al., 2018), makes them a potentially useful indicator for past Quaternary climate in regions where the availability of other proxies is limited (e.g., pollen and spores, plant macrofossils, charcoal, stable isotopes and lake sediment record).

This study aims to lay the foundations for the use of continental parabolic dunes as potential proxy for the reconstruction of past climatic conditions by quantifying the environmental factors of areas where they have been recently active, and by comparing their activity during the Holocene Thermal Maximum (e.g., Davis et al., 2003; Kaufman et al., 2020; Masson et al., 2000). Globally speaking, this period is associated with a northward shift of the Intertropical Converge Zone (ITCZ), and therefore the monsoon systems, resulting in a higher- and lower-than-present mean temperature at high and low latitudes, respectively. These changes correlate with increased precipitation in the tropics whilst temperate regions of the northern hemisphere underwent strengthened arid conditions (e.g., Braconnot et al., 2007b, 2007a, 2004; Gladstone, 2005; Kaufman et al., 2004; Kohfeld and Harrison, 2000; Mikolajewicz et al., 2003; Wanner et al., 2008). The mid-Holocene is a period of rapid and important climatic changes that is now well-constrained, making it a key period for a comparison between the continental interior parabolic dunes activity and aridity. With extreme drought and rainfall becoming more recurrent recently (Dunn et al., 2020), these aeolian landforms offer a great indicator of climate-induced land degradation.

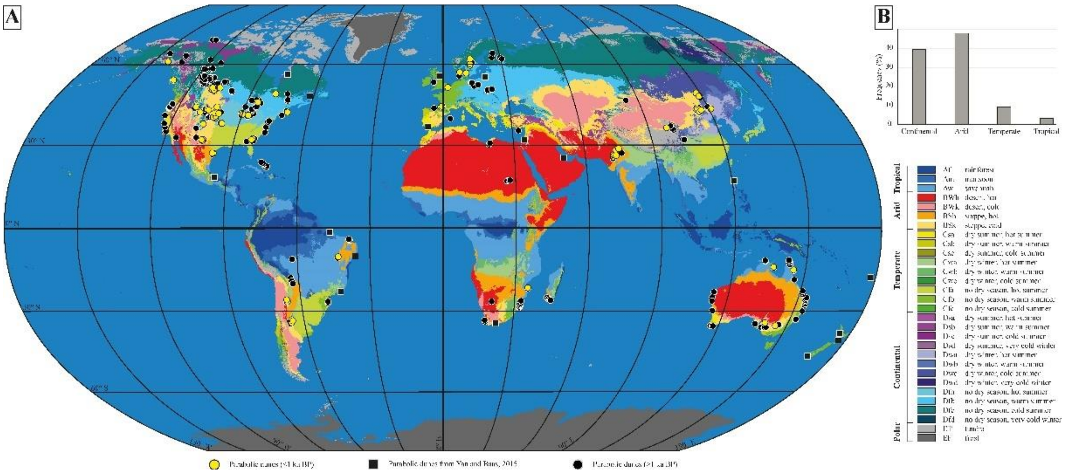

Figure 48: A) Global distribution of 798 recognised parabolic dunes based on the INQUA Digital Atlas of Quaternary Dune Fields and Sand Seas and on an extensive review of the literature (circles), as well as on the review work carried out by Yan and Baas (2015; squares). B) The majority (87%) of the parabolic dunes that have shown activity during the last thousand years are located in continental (40%) and arid (47%) climate zones, according to the Köppen classification (Kottek et al., 2006). The few that have recently migrated within temperate and tropical zones are predominantly costal parabolic dunes.

2 Methods

2.1 Dune activity database

In order to compare parabolic dunes activity to climate, a considerable global chronological database and an extensive review of the literature is required. The former is provided by the INQUA Digital Atlas of Quaternary Dune Fields and Sand Seas (Lancaster et al., 2016; https://www.dri.edu/inquadunesatlas/), and the latter is based on 244 papers mentioning parabolic dunes. Overall, 109 publications (Appendix 10) provide 1146 luminescence and radiocarbon ages for 798 different dunes (Figure 48). A total of 241 luminescence ages younger than 1 ka BP, with 75% of the age uncertainties being less than 50yrs, was obtained to constrain the activity of 115 dunes located in 12 different countries (Figure 48 and Figure 49). We excluded coastal parabolic dunes so that our database provides

218 luminescence ages for 104 recent dunes located in 8 different countries (Appendix 11). Another 97 luminescence ages and 8 ^{14}C ages constrain the activity during the mid-Holocene period (7.5 to 4.5 ka BP) of 66 continental parabolic dunes, located in 8 different countries (Appendix 12). Of these ages, 75% show uncertainties between 28 and 800 yrs. The gathered OSL ages represent the moment of burial of quartz grains, which translates into a period of dunes accumulation. In this paper, as in many others, this accumulation is interpreted as dune activity and therefore, evidence of dune remobilisation and/or migration.

2.2 Climate variables

The 104 inland parabolic dunes that have accumulated during the last 1 ka BP were compared to 6 different climate variables modelled for the modern: temperature, precipitation, aridity index, wind speed, surface roughness and mega biomes (Figure 49). Both annual surface temperature at 2 meters above sea level (m.a.s.l) and annual precipitation were derived from WorldClim v2.1 with a 5-minute resolution, which averages historical data between 1970 and 2000 AD (Fick and Hijmans, 2017). From this dataset, the Global Aridity Index (AI) database at 30 arc-second was generated by Trabucco and Zomer (2018) by computing the ratio between the mean annual precipitation and the calculated mean annual reference evapo-transpiration. For roughness length, mean surface wind speed and directionality (at 10 m.a.s.l), we used the Global Wind Atlas (GWA3) database with a resolution of 250 m at the equator, which covers a 10-years period between 2008 and 2017 AD (https://globalwindatlas.info/).

The roughness length (“z_0”) characterises the displacement of the wind velocity profile caused by the density and the height of the obstacles lying on a surface over which the wind is blowing. In a natural environment, the vegetation constitutes the main obstacle to the wind whereas human-made structures are the “roughness elements” in densely populated areas. The roughness length is a parameter of the equations (e.g., Levin et al., 2008) used to model changes of the horizontal mean wind speed near the ground along a vertical wind profile. It is a critical parameter since the size and density of potential obstacles strongly affects the shear stress wind produces on the Earth’s surface and consequently, its ability to transport sediment (Greeley et al., 1997; Levin et al., 2008; Wolfe and Nickling, 1993). The values of z_0 in GWA3 have been derived from the European Space Agency’s Climate Change Initiative Land Cover (CCI-LC) dataset v2.0.7 (*maps.elie.ucl.ac.be/CCI/viewer/download/ESACCI-LC-Ph2-PUGv2_2.0.pdf*), which provides data for the period between 1992 and 2015. The satellite data are validated with ground measurements and then processed into a landcover map where a z_0 value is attributed to each class of landcover, which includes both the type of vegetation and the type of human-modified lands (e.g., farmland, cropland, urban areas). The mega-biomes dataset is based on the same principle but differs from the CCI-LC classification in that human-modified lands are not included. In this dataset, biomes, which represent distinct plant communities that have formed in response to a shared physical climate, were grouped into broader mega-biome classes. It was modelled with a grid cell size of 3.75° width and 2.5° height for the pre-industrial period based on the HadCM3 Global Circulation Model and long pollen records (Hoogakker et al., 2016; Verheul et al., 2016).

For a more detailed analysis of wind regime, the NASA POWER Release-8 model (*https://power.larc.nasa.gov/*) was used, which is based upon a single assimilation model merging the MERRA-2 and the GEOS 5.12.4 products (Stackhouse et al., 2018). It provides the daily average of wind speed at 10 m.a.s.l. over the same period as the GWA3, with a grid cell size of 0.5° latitude by 0.5° longitude. These data enable statistical calculations to establish how often and by how much, wind is blowing above the impact threshold shear velocity, set at 11 knots (Fryberger and Dean, 1979). This value represents the lower limit, under dry conditions, from which wind initiates saltation of quartz grains (Bagnold, 1941, 1936). In other words, sand transport by wind starts at 11 knots (~5.5 m/s), which corresponds to the "moderate breeze" class of the Beaufort scale. The bigger the wind speed averaging time, the more underestimated is the blowing time of effective (≤ 11 knots) winds (Yizhaq et al., 2020). Usually, a 10-min or 1-h mean wind speed is recommended for further calculations, so that our data represent the lower spectrum of wind speeds in the studied regions.

Finally, the activity of the 66 dunes that have been active during the mid-Holocene (7.5 to 4.5 ka BP) was compared to the Global Lake Status Data Base of mid-Holocene lake levels (GLSDB; Harrison et al., 2003; Kohfeld and Harrison, 2000; Yu et al., 2001), which includes 394 sites with a strong dating control. This database is based on the relative mid-Holocene paleo-levels of lakes around the world and indicates if a given region was under wetter or drier conditions.

3 Results

The OSL ages from the last millennium are clustered into three distinct periods (Figure 50), 17 % of them are within the 1000-650 BP range (900-1300 AD), 77 % fall into the 450-50 BP range (1500-1900 AD), and only 3 % cluster after 1900 AD. Within the second group, a further distinction can be made between the 1500-1700 AD group (19 % of the ages) and the more recent 1700-1900 AD group (58% of the ages).

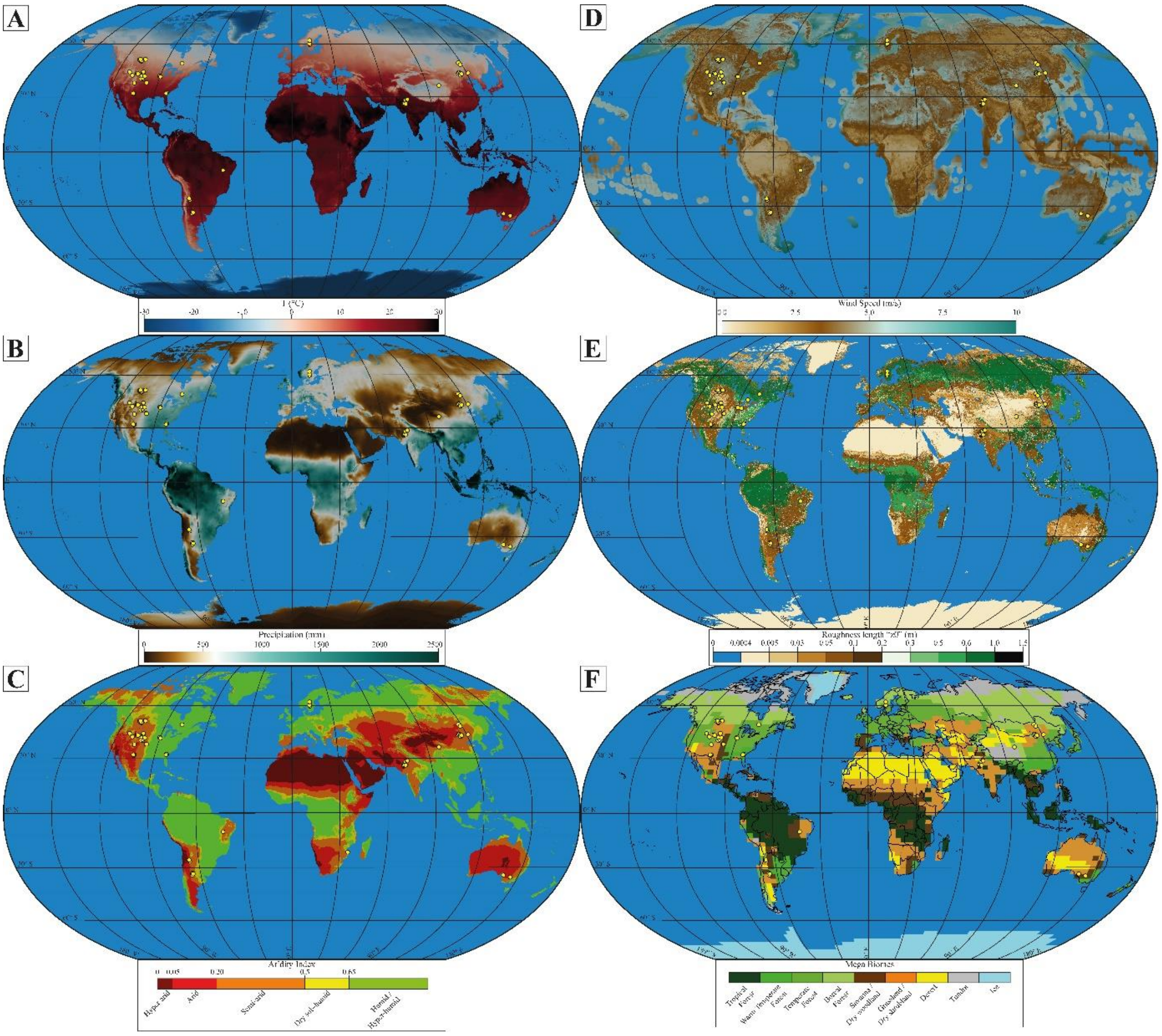

Figure 49: Global distribution of the studied 108 continental parabolic dunes that have been active during the last thousand years, overlain on the global maps of the 6 studied climate parameters: (A) average temperature, (B) average precipitation, (C) aridity index, (D) average wind speed, (E) land surface irregularity and (F) type of vegetation.

Parabolic dunes are found over a wide range of latitudes (35°S to 62°N) but the recently active ones are predominantly found (87%) in continental and arid climates (Figure 48B) as defined by the Köppen classification. We find that the regions where recent continental dunes are active have mean annual temperatures and precipitation rates ranging from -5 to 30 °C, and from 100 to 1500 mm/yr, respectively (Figure 51A and B). Of the 104 considered parabolic dunes, 90% of them reside in cold and temperate regions. In addition, approximatively 95% of the dunes prevail in areas with precipitation rates less than 800 mm/yr. About 65% are in areas receiving less than 500 mm/yr of precipitation, with a significant occurrence within the 200-500 mm/yr range. The aridity index links 89% of the active inland dunes to arid (22%) and semi-arid (67%) regions (Figure 51C). Most of the investigated regions (84%) are exposed to a gentle breeze blowing between 7 and 11 knots (3.5 to 5.5 m/s) on average throughout the 10 years of record (Figure 51D). Statistics performed on wind speed (Table 5) show that 26 regions out of the 35 studied (~74%), are exposed to daily-averaged winds blowing above the saltation threshold at least one month per year (≥ 8% of the time over the period of record). Of the 9 regions left, four can be considered as calm regions with winds reaching the threshold less than 1% of the time. The others face strong-enough winds between 2.31 and 7.91% of the time. Most of the averaged speeds range within the moderate (11 to 17 knots) and fresh (17 to 21 knots) breeze categories, with a much larger proportion falling into the former class. Generally, regions exposed more often to a moderate breeze are also proportionally more exposed to fresh breeze. Wind speed roses show the contributions, in percent, from the 12 direction sectors to the mean wind speed at the sites, and typically characterise unimodal and bimodal wind regimes (Supp. Data). The seasonal analysis show that winds are, to a greater or lesser degree, stronger during spring and autumn seasons, both in the northern and southern hemisphere (Supp. Data). Nearly all active parabolic dunes (94%) lie in areas with relatively low z_0 (0 to 0.1) indicating surfaces presenting few obstacles (Figure 51E). Up to 89% of the studied dunes occur in sparsely vegetated areas covered with a scattered low-lying vegetation (Figure 51F). These regions classify as savannah, dry woodlands, dry shrublands and grasslands mega biomes. The continental parabolic dunes activity during the mid-Holocene period correlate with drier-than-present zones whereas the stabilised dunes are observed in regions that were under wetter conditions (Figure 52).

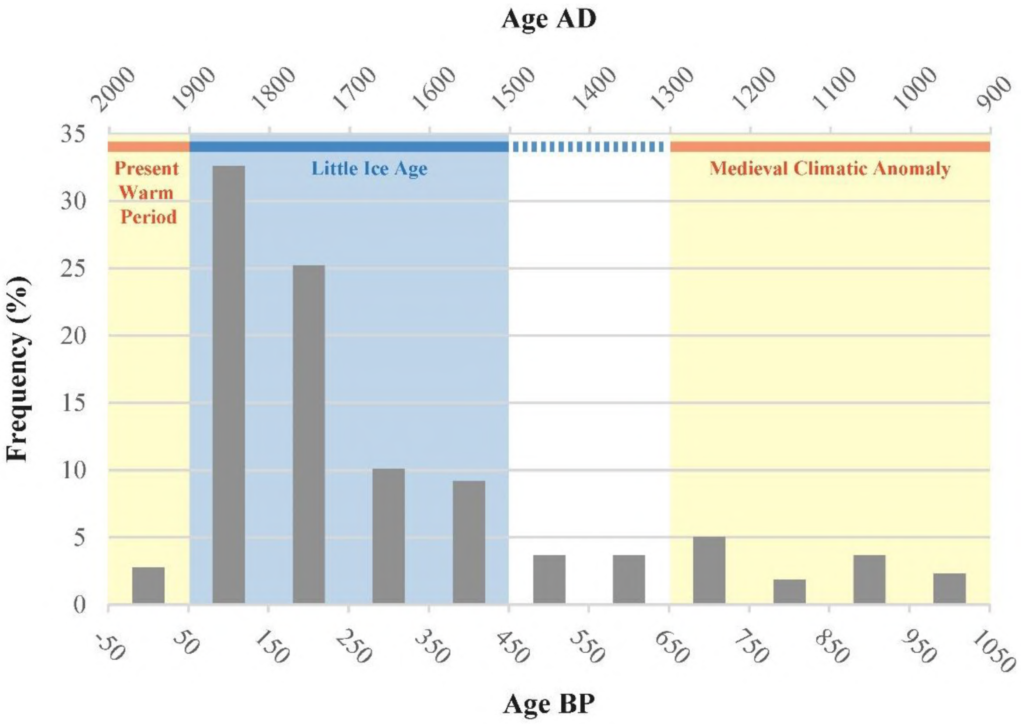

Figure 50: Frequency distribution of the OSL ages from the last thousand years relative to the MCA, LIA and the Present Warm Period.

4 Discussion

4.1 Natural factors controlling recent continental interior dunes activity

Our data show no evident direct correlation between the recent (< 1 ka BP) parabolic dune activity and the mean annual surface temperature. However, most continental parabolic dunes in this study cluster in regions receiving between 200 and 500 mm/yr, and within the 600-800 mm/yr range (Figure 51B). The aridity index represents the level of humidity of a given region and is estimated as the ratio between precipitation and potential evapotranspiration. The latter is influenced by factors such as the vegetation cover and type, solar irradiance, wind, atmospheric pressure, and the soil composition. Therefore, a region receiving a fair amount of precipitation throughout the year is not necessarily characterised as sub-humid or humid. Consequently, the peak of dune occurrence observed within the 600-800 mm/yr range of precipitation plots within the semi-arid spectrum of the aridity index (Figure 51C).

Previous studies stated that most of the inland parabolic dunes were found in arid to semi-arid areas (e.g., Yan and Baas, 2015) but did not distinguish between recently active and stabilised dunes, nor give any quantified index for these regions. In these dry continental interiors, the main sources of sediment are often small lakes and rivers (de M. Luna et al., 2011; Goudie, 2011; Hansen et al., 2009; McKenna, 2007; Yan and Baas, 2015). In such environments, dune activity relies on sediment supply, which is highly dependent on rainfall in the regional catchment basin, and sediment availability that tends to be governed by vegetation cover. In that respect sediment supply strongly controls dune construction, and thus conspicuous dune activity, whereas sediment availability influences dune reactivation and reworking as is the case for the North American dune fields (Halfen et al., 2016). The stabilising vegetation type associated with recently active parabolic dunes (i.e., savannah, dry woodlands or shrublands, and grasslands) is composed of plant functional types that are highly responsive to drought cycles (Anderegg et al., 2019; da Silva et al., 2013; Ivory et al., 2012; Liu et al., 2019; Tian et al., 2018; Trabucco and Zomer, 2014; Vicente-Serrano et al., 2006). Drought alters plants growth, height, reproduction, and causes species range shifts so that vegetation becomes scarcer and lower (da Silva et al., 2013). As a result, roughness length is diminished, which translates into a higher sediment availability and thus less energy is required for sediment transport (i.e., remobilisation) by wind (Durán et al., 2008; Durán and Herrmann, 2006).Consequently, sediment availability and thus episodes of dune reactivation are partially governed by the frequency and the intensity of drought episodes (Appendix 11). The Medieval Climatic

Anomaly (MCA) is believed to have been an arid period of the Holocene with a high frequency of severe droughts in the North Atlantic region, especially in North America (Bradley, 2003; Bradley et al., 2003; Jansen et al., 2007; Mann et al., 2009). Despite the heterogeneity of local climate conditions and the timing occurrence of dune remobilisation between different dune fields in the Great Plains, several authors recognised the MCA as a period of dune remobilisation induced by droughts (Baldauf et al., 2019; Cook, 2004; Halfen et al., 2012, 2010, 2016; Mayer and Mahan, 2004; Miao et al., 2007; Schmeisser McKean et al., 2015). In China, India, Canada and South America, dune remobilisation during the MCA interval has been attributed to climate and atmospheric-driven droughts, sometimes amplified by human activities (De Oliveira et al., 1999; Guo et al., 2018; Mason et al., 2009; Peña-Monné et al., 2015; Singhvi and Kar, 2004; Srivastava et al., 2019; Wolfe et al., 2001; Yang et al., 2013).

The majority of the ages from the last millennium correlates with the colder Little Ice Age (LIA), which follows the MCA and is marked by asynchronous mountain glacier advances (Mann, 2002; Miller et al., 2012). In the Americas, the LIA is a period of widespread droughts that were sufficient to trigger dune remobilisation (Baldauf et al., 2019; Forman et al., 2005; Halfen et al., 2012; Hall and Goble, 2016; Peña-Monné et al., 2015; Schmeisser McKean et al., 2015; Tripaldi et al., 2013; Wolfe et al., 2001, 2002b). However, droughts were less extended than during the MCA and were localised in the southern and western Great Plains (Halfen et al., 2012). The OSL ages from India correlate with a period of diminished rainfall (Roy and Singhvi, 2016; Singhvi and Kar, 2004; Srivastava et al., 2020, 2019), which coincides with an increase in droughts in northeast China (Guo et al., 2018). However, authors stress the human pressure on vegetation during this period, which resulted in a greater sediment availability in regions where climate conditions were propitious to dune reactivation. This topic will be discussed more thoroughly in the next section.

Dune construction, migration, and reworking all rely on a sufficient (i.e., above threshold) transport capacity, which sometimes must be partially erosional in order to remobilise sand (Kocurek and Lancaster, 1999). Our data show a strong correlation between recent parabolic dune activity and light wind regimes when wind speed data are averaged over 10 years. More than 80% of the dunes are located in areas exposed to gentle breeze on average, which means they are near the equilibrium just below the saltation threshold (Fryberger and Dean, 1979). Considering the range of wind speed, which is not expressed by a mean value, there is little doubt that these regions are exposed to winds powerful enough to mobilise sand for at least part of the year. Because wind data were averaged over a long period of time, they do not truly represent the full seasonal variability in wind regimes but rather characterise the average

Table 5: Analysis of wind speed data in locations where recent parabolic dune activity has been recorded.

Country	Region	Location	% above threshold	Moderate breeze 11-17 kts 5.5-7.9 m/s (%)	Fresh breeze 17-21 kts 7.9-10.7 m/s (%)	Strong breeze 21-27 kts 10.7-13.9 m/s (%)	Moderate gale 27-34 kts 13.9-17.1 m/s (%)
Argentina	Salta Province	Cafayate	0.10	0.10	0.00	0.00	0.00
	San Luis	Pampean sand sea	4.01	3.98	0.03	0.00	0.00
Australia	South Australia	Mallee	23.08	19.49	3.44	0.15	0.00
	New South Wales	Rhyola	18.00	16.14	1.85	0.00	0.00
Brazil	Bahia	rio São Francisco dunes	17.73	17.54	0.18	0.00	0.00
Canada	Saskatchewan	Bigstick	33.87	26.60	6.72	0.55	0.00
		Burstall	27.61	22.59	4.65	0.36	0.00
		Elbow	33.32	26.27	6.26	0.70	0.09
		Great Sand Hills	28.73	23.50	4.86	0.36	0.00
		Seward	36.58	28.25	7.78	0.55	0.00
		Tunstall	36.58	28.25	7.78	0.55	0.00
		Westerham	27.61	22.59	4.65	0.36	0.00
China		Horqin	28.70	23.53	4.86	0.30	0.00
		Hulun Buir Desert	26.88	22.07	4.47	0.33	0.00
		Otindag	41.68	32.05	8.82	0.79	0.03
		Tiekui Desert	7.91	7.15	0.76	0.00	0.00
India	Rajastan	Thar	11.99	10.36	1.63	0.00	0.00
Sweden	Dalarna	Haftaheden	0.00	0.00	0.00	0.00	0.00
	Jämtland	Svegssjön	0.00	0.00	0.00	0.00	0.00
	Värmland	Brattforsheden	0.12	0.12	0.00	0.00	0.00
USA	Colorado	Great Sand Dunes	11.55	9.88	1.64	0.03	0.00
		Wray Dune Field	11.55	9.88	1.64	0.03	0.00
	Georgia	Canoochee River	5.53	5.14	0.40	0.00	0.00
		Ohoopee River	2.31	2.25	0.06	0.00	0.00
	Idaho	Snake River Plain	7.75	7.36	0.40	0.00	0.00
	Illinois	Green River Lowlands	29.04	23.09	5.64	0.30	0.00
	Indiana	Fair Oaks	29.55	22.35	6.63	0.58	0.00
	Kansas	Hutchinson Dunes	37.09	27.15	9.03	0.91	0.00
	Nebraska	Nebraska Sand Hills	31.80	24.45	6.35	0.91	0.09
		South of Sand Hills	27.42	21.15	5.53	0.69	0.06
		Wray Dune Field	27.42	21.15	5.53	0.69	0.06
	New Mexico	Mescalero Sand Sheet	20.16	18.18	1.98	0.00	0.00
	South Dakota	White River Badlands	21.56	17.63	3.25	0.61	0.06
	Wyoming	Casper	41.50	26.97	12.37	2.13	0.03
		Killpecker Dunes	21.53	18.06	3.37	0.06	0.03

conditions of the studied regions. By nature, they strongly underestimate the potential of sand transport by wind in these regions but, on the contrary, give a good indication of the directional variability of winds (Yizhaq et al., 2020). In accordance with Goudie (2011), the wind regimes associated to the recently-active parabolic dunes show a unimodal or bimodal distribution (Supp. Data). We then used daily averages of wind speed to investigate with a higher precision the amount of time a defined region is exposed to wind blowing above the saltation threshold. Most of the regions where dunes have been active during the last millennium are associated with winds that can mobilise sand at least one month per year on average (Table 5). Of the four areas where winds are never, or almost never strong enough, three are in humid Central Sweden and one is in the Cafayate depression in Northwest Argentina. In these regions, it would be preferable to use raw hourly measurements of wind speed to get the full variability of it (Grange, 2014). Unfortunately, the NASA POWER Release-8 model does not provide hourly data anymore, nor wind direction. As a result, we did not assess the capacity of the wind to transport sand as defined by Fryberger and Dean (1979). It is highly probable that winds are blowing above the saltation threshold some hours a day, particularly during the windy season that is spring in Cafayate, and both spring and autumn in Central Sweden. Wind gust frequency is also to take into consideration, especially in the Cafayate region where the rugged topography of the Pre-Andean region can greatly accentuate the phenomenon (Ngo and Letchford, 2009). An increased storminess in Sweden has already been proposed as one potential reason to explain recent dune activity (Bernhardson and Alexanderson, 2018). In general, transport capacity by wind is not the limiting factor for dune remobilisation in the studied regions at present.

4.2 Human influence on recent continental interior dunes activity

The human influence on climate change has raised some concerns about the impacts in drylands (Donat et al., 2016; Fu and Feng, 2014; Huang et al., 2016; Jianping Huang et al., 2017; Ji et al., 2015), especially land use and urbanisation (J. Huang et al., 2017). For example, poor land use has contributed to land degradation by intensifying droughts in the Sahel (Charney, 1975; Taylor et al., 2002; Xue and Shukla, 1993) and East Africa (Olson et al., 2008). It has also been suggested that land surface change might lead to megadroughts in North America (Cook et al., 2016). Although human influences on drought and regional climate remain uncertain and hard to quantify (Huang et al., 2017), scientists began to investigate the Quaternary climate over drylands to better constrain this relationship. In the context of this study, it is fundamental to understand the human contribution to the reactivation of dunes that would not have been reactivated if it were only for natural factors.

The land cover classification of the 2015 ESA CCI provides more details than the Mega Biome model to analyse anthropogenic disturbance of very recent dune activity because it includes urban areas and lands modified by humans for agricultural purposes. Roughness length map is derived from the CCI database and shows that aeolian dunes are active in areas within a certain threshold of roughness length (from 0 to 0.1 m), which corresponds to a surface with scarce obstacles that could prevent sand transport by wind. Such values correlate with lands covered by the type of vegetation defined by the Mega Biome model (i.e., savannah, dry woodlands or shrublands, and grasslands) but also indicate lands principally occupied by agricultural or pastoral activities. Most of the dunes are located in semi-arid regions where conditions are close to the threshold of activity so that a small disturbance of the vegetation cover (e.g., removal by grazing) makes dunes being remobilised.

The large increase of OSL ages density during the second half of the LIA (Figure 50), during the 19th and 18th century, is indicative of a dune reactivation peak induced by a significantly greater human activity. The reactivation of the few parabolic dunes located in humid areas, as defined by their aridity indices (Figure 49C), is linked to anthropogenic modifications. In Sweden, increased storminess, charcoal production, and slash-and-burn agriculture have been correlated to parabolic dune activity around 1750 AD (Alexanderson and Fabel, 2015; Bernhardson and Alexanderson, 2018). Moreover, a combination of droughts, wildfires, bison grazing, aboriginal and then European settlers land use is believed to have caused dunes remobilisation in Illinois and Indiana during the last 600 years (Kilibarda and Blockland, 2011; Miao et al., 2010).

The human influence on dune remobilisation is indisputable when it comes to dunes in arid and semi-arid environments although the relationship appears less linear than with humid areas. A thorough review of the literature shows that dune remobilisation through degradation of the vegetation cover can be triggered by human land use solely (i.e., agriculture or grazing) or by amplification of drought impacts due to human activity (Appendix 11). During the last thousand years, land-degrading human activities in such regions have significantly contributed to the lowering of the roughness length. In Argentina for example, the combination of drought periods and impacts of European settlers activities on vegetation (i.e., wheat cultivation and overgrazing) reactivated some parabolic dunes (Peña-Monné et al., 2015; Rodríguez, 2008; Tripaldi et al., 2013). The same reasons were evoked for different deserts of eastern Inner Mongolia in China, where climatic deterioration supplanted the increased vegetation cover induced by irrigation agriculture of millet (Guo et al., 2018). The recent remobilisation of the

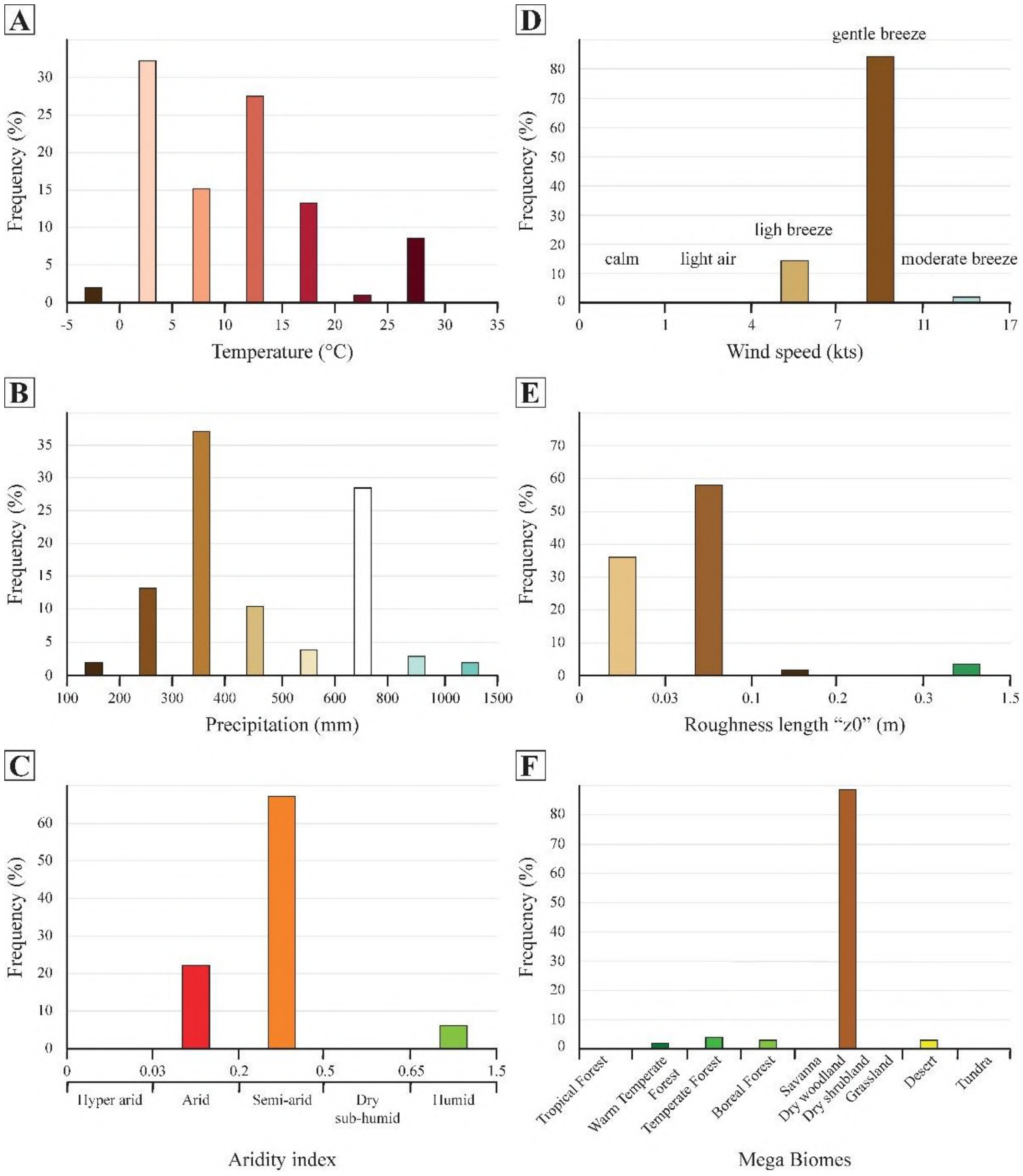

Figure 51: Frequency distribution of the recently active continental parabolic dunes as a function of the 6 studied climate variables: (A) mean temperature, (B) mean precipitation, (C) aridity index, (D) mean wind speed, (E) land surface irregularity and (F) type of vegetation.

Thar desert dunes during the last century (~1900 AD) is attributed to an increasing human pressure through grazing, cultivation, and groundwater pumping (Srivastava et al., 2019). In the northern Great Plains, dune activity has been induced by aboriginal disturbance of the landscape, which includes tree cutting, fire, and trampling from herding bison (Wolfe et al., 2007a). Forman et al. (2005) succinctly nuanced their interpretations on dune activity in the Dust Bowl area during the 1930s by linking it to severe drought coupled with farming practices. Dune activity in northern Europe has drastically increased following deforestation and intensification of agriculture during the MCA (Lungershausen et al., 2018). Reactivation of dunes caused the degradation of agricultural soils and thus triggered settlement abandonment, which led to the restabilisation of the dunes. Overall, anthropogenic modification of the environment is indissociable of dune activity for the recent period (18th century – present) and has definitely contributed to dunes reactivation in some places during earlier periods (e.g., Li and Yang, 2016; Tolksdorf and Kaiser, 2012).

4.3 Potential for new climate proxy

The results of this study suggest that the global distribution of continental parabolic dunes and their activity during the last thousand years are broadly constrained by simple climate parameters and anthropogenic activities, especially during the last 200 years. Consequently, it is important to compare with past aeolian activity to investigate the dune activity-climate relationship when human impacts were non-existent or negligible.

Precipitation and vegetation are complex to model for the Quaternary period (see the comparison model of PMIP 2). In addition, the record of proxies quantifying changes in time of these variables remains scarce and sometimes difficult to interpret (e.g., Rea et al., 2020). However, many proxies do enable a qualitative assessment of aridity in the past, which can then be compared to modelling results (e.g., Fuhrmann et al., 2019; Scheff et al., 2017). This allows a semi-quantification at least of this parameter, which has proven to be a determining factor in triggering continental parabolic dunes migration in several regions of the globe (Arbogast et al., 2010; Arbogast and Packman, 2004; Baldauf et al., 2019; Halfen et al., 2010; Latrubesse et al., 2012; Miao et al., 2007; Wolfe et al., 2006; Zieliński et al., 2011). For these reasons, aridity is often the factor studied to link dunes activity to climate.

One possible way to explore the potential of these dunes as a proxy for climate at a global scale is to study their activity during the well-constrained mid-Holocene (~8 to 5 ka BP). During this period, recent studies advocate for a global atmospheric temperature about 0.7 to 1°C higher than for pre-industrial conditions (Marcott et al., 2013), consistent with minimum extents of northern-hemisphere glaciers (Valérie Masson-Delmotte et al., 2013) and terrestrial responses to orbital forcing (Braconnot et al., 2007a, 2007b). Despite regional differences (e.g., Davis et al., 2003; Kitoh and Murakami, 2002), a global trend of warmer/colder temperatures in the northern/southern hemispheres is observed when a multi-proxy approach is adopted (Braconnot et al., 2007a; Wanner et al., 2008). An important proxy supporting this interpretation of the mid-Holocene aridity conditions in the northern hemisphere is the compilation of lakes paleo-levels provided by the GLSDB (Harrison et al., 2003; Kohfeld and Harrison, 2000). Lake level variations occur from changes in aridity (Figure 52A), expressed as the balance between

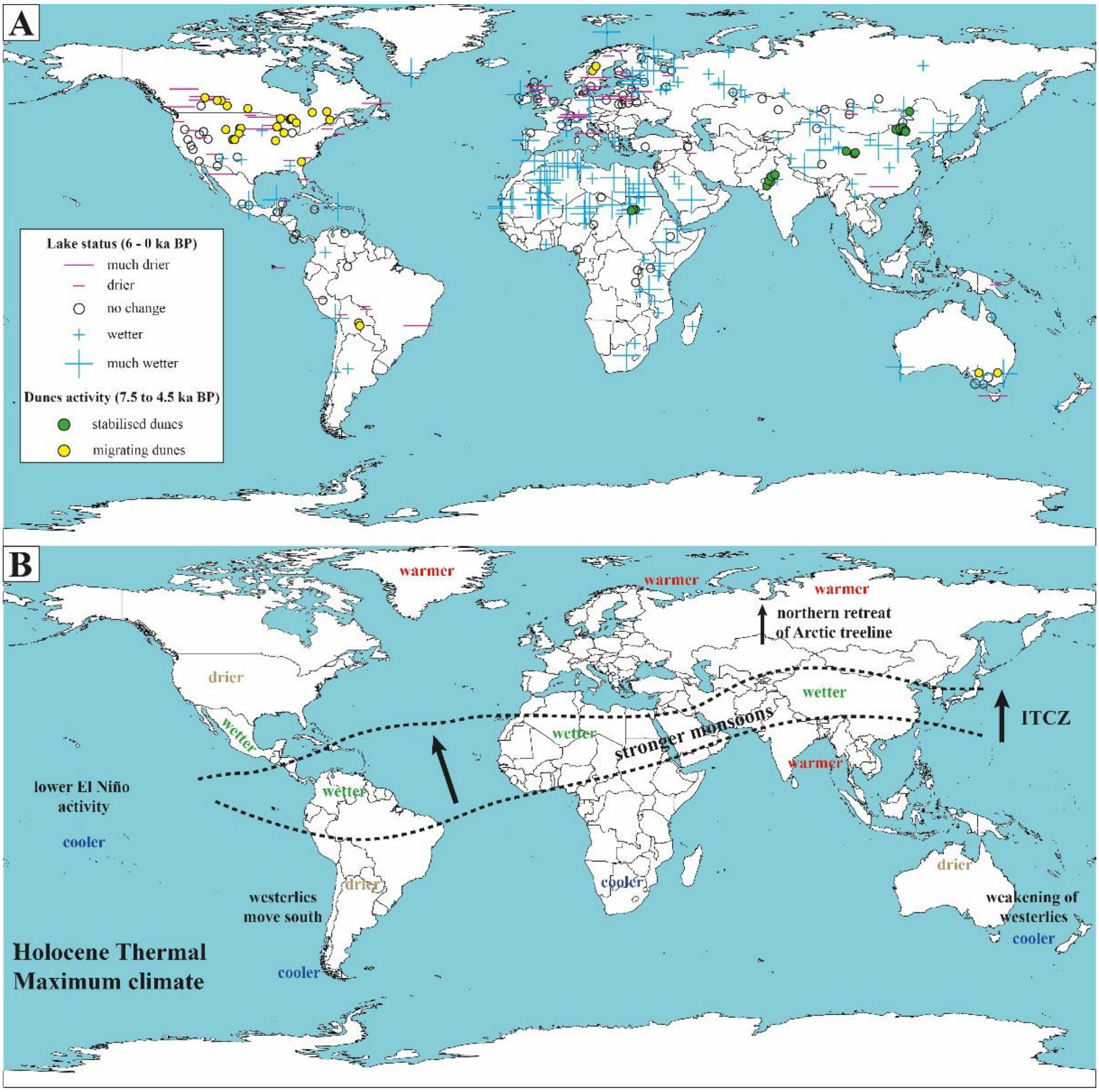

Figure 52: A) Continental parabolic dunes activity and difference in lake levels (i.e., status) at 6 ka BP compared to present (modified after Wanner et al., 2008). An increase in aridity corresponds to an aeolian activity whilst a wetter climate correlates with a cessation in both dunes migration and sedimentation. B) Global climate change during the Holocene Thermal Maximum (~6 ka BP) with respect to present day. Change in aridity in continental regions is correlated to a northern displacement of the Intertropical Converge Zone (ITCZ). This observation indirectly links the continental parabolic dunes activity to the ITCZ position.

precipitation and evaporation. In semi-arid regions, the level of closed lakes reflects changes of the equilibrium between run-off from the catchment basin and the water deficit over the lake (Kohfeld and Harrison, 2000; Kutzbach and Street-Perrott, 1985; Street-Perrott and Harrison, 1985). Therefore, a regional prolonged lowered lake level can be interpreted as a deterioration of climatic factors leading to increased aridity. The global aridification trend that occurred during the mid-Holocene is attested also by global palaeovegetation (BIOME 6000; Prentice and Webb, 1998) and atmospheric dust accumulation rate data (DIRTMAP, Kohfeld and Harrison, 2001). More specifically, the impacts of the Holocene Thermal Maximum on land surfaces differ with continental regions. In response to solar irradiance changes, induced by varying orbital parameters, the ITCZ moved north with respect to its present position (Figure 52B). This displacement caused more arid conditions to prevail at mid- to high latitudes of the northern hemisphere whilst strengthened African and Asian monsoon regimes (i.e., higher rainfall) induced wetter conditions in Central America, Africa, and Central Asia (Braconnot et al., 2007b; Wanner et al., 2008).

During this period, continental parabolic dunes in wetter-than-present regions were stabilised whereas they became activated (i.e., migrating) or partially remobilised in areas where the climate conditions were drier than the pre-industrial ones (Figure 52A). Migrating dunes seem to be almost exclusively concentrated in central South America, North America, and Scandinavia. The Chaco region in South America has indeed been reported to have been arid during the mid-Holocene, with an expansion of savanna type vegetation and an increased frequency of forest fires (Barboza et al., 2000; de Freitas et al., 2001; Mayle et al., 2000; Mourguiart and Ledru, 2003; Pessenda et al., 1998). The Great Plains of North America have experienced arid conditions during the same period, associated with a transition from boreal forest to prairie-grassland vegetation and frequent wildfires (Baldauf et al., 2019; Forman et al., 2001; Miao et al., 2007; Vance et al., 2007; Webb et al., 1993; Wolfe et al., 2006). However periods of reactivation during the mid-Holocene show a limited spatial and temporal correlation so that no conspicuously higher dune activity or construction is observable with the OSL ages (Halfen et al., 2016). Reasons have been evoked to explain this "gap" such as changes in dating methods, sampling biases, and the tendency of dune fields located at or near thresholds for aeolian activity to only record the last episodes of sand movement (Halfen and Johnson, 2013). The remobilisation of parabolic dunes in Central Sweden agrees with a scattered aeolian activity elsewhere in the country, reflecting a dry phase during the mid-Holocene (Alexanderson and Bernhardson, 2016; Bernhardson and Alexanderson, 2018; Kylander et al., 2013).

The stabilisation of continental parabolic dunes was attributed to a recovery of fixing vegetation during the African Humid Period in Sudan (Bubenzer et al., 2007). In India, the extended duration of higher monsoon and winter rainfall was evoked to explain the stabilisation of the Thar desert dunes, which show a weakly developed palaeosoil, whilst all the major saline lakes turned into perennial lakes (Singhvi and Kar, 2004). However, recent studies (Roy and Singhvi, 2016; Srivastava et al., 2020) challenge this interpretation by pointing out the nonlinear and complex relationship of dune ages with rainfall, aridity and lake levels. Nonetheless, geochemical records show a gradual weakening of the Indian Summer Monsoon (ISM) from the early to late Holocene, which translates into weaker winds and thus a reducing dune activity through the mid-Holocene (Srivastava et al., 2020). Some perennial lakes in the region maintained a high water level probably related to intensified winter rainfall, thus offsetting the reduced summer precipitation (Roy and Singhvi, 2016). In eastern China, the stabilisation process is attributed to an expansion of C_4 over C_3 vegetation, although there was a general increase of the vegetation cover (Guo et al., 2018). This expansion of vegetation and the widespread soil development that follows are concordant with a wet mid-Holocene in China (Mason et al., 2009; Yu and Lai, 2014). The “abnormal” dune activity recorded in south-east Australia, when climate was more humid, is believed to be a particularity of the Murray Basin (Lomax et al., 2011). Indeed, it acted as one of the major dust sources during the mid-Holocene whilst dust transport was limited in other basins. During the late Holocene , dust transport ceased in the Murray Basin whereas other basins became dust sources (Marx et al., 2009). During this period, the ITCZ was located further south (Shulmeister and Lees, 1995), which led to the precipitation associated with both the sub-Antarctic cyclones and the cold fronts embedded in the westerlies to remain south of the continent, being blocked by the sub-tropical high pressure belt. As a result, northern Australia was wet and southern Australia remained dry. Therefore, the Murray Basin seems to reflect the more arid conditions in the mid-Holocene and stable conditions towards the late Holocene (Marx et al., 2009).

4.4 OSL ages database uncertainties

The environmental conditions under which parabolic dunes build or are reactivated are not fully constrained due to the numerous spatial and temporal gaps of the INQUA Dune Atlas database (Lancaster et al., 2016), as it has been shown for the Great Plains of North America (Halfen et al., 2016). Uncertainties can be reduced to some extent by adopting a global approach so as to extract a general trend, but local disturbances can greatly influence dune fields and their behaviour within the same region (Halfen et al., 2016; Halfen and Johnson, 2013). The nature of the OSL dating technique tends to concentrate young ages because luminescence signals are reset when dunes are reactivated, so when the sand is exposed again. The signals from past activities are thus overwritten, which generates a gap in the dune movement history to which sampling biases contribute (Halfen et al., 2016). The constant resetting of luminescence signals within very recent dunes (< 1900 AD) may account for the small number of ages compiled in the INQUA database (Figure 50). However, the depth bias resulting from the avoidance of sampling within the upper 1-2 m of dune profiles (Hesse, 2016) and the irrelevance of dating dunes that are visibly active are more likely to explain the under-representation of very recent ages in the database. Another less plausible explanation is the currently relative stable state of dunes worldwide due to changes in land-use practice, expanding urbanisation, dune stabilisation projects, and decrease in windiness together with increase in rainfall (Gao et al., 2020; Jackson et al., 2019).

The scattered geographical and stratigraphic contexts from which come the OSL ages prevent the use of the accumulation intensity method (Thomas and Bailey, 2017), kernel, or probability density estimates so that periods of "activity" are only defined by isolated OSL ages. The decreasing precision with increasing OSL ages makes dune mobility indices (e.g., Knight et al., 2004; Lancaster, 1988; Talbot, 1984) unapplicable when studying past periods of aeolian activity because of the scale difference, as acknowledged by Knight et al. (2004). These issues impose some precautions when palaeoclimatic interpretations are made from the geographically and temporally scattered ages of the database.

5 Summary and conclusion

This study correlates the activity of recent continental parabolic dunes with *quantified* climate variables influencing each other, with the aim to define the dunes potential as a proxy for past climate. Inland parabolic dunes have recently been active in regions presenting:

- An aridity index ranging from 0.05 to 0.5, which characterises arid and semi-arid areas.
- A vegetation type corresponding to savannas, dry woodlands, dry shrublands and grasslands.
- A corresponding roughness length ranging from 0 to 0.1 m, indicating natural or human-degraded surfaces presenting a low resistance to wind.
- A unimodal or bimodal wind regime presenting seasonal wind speeds above the saltation threshold.

In summary, the continental parabolic dunes that have been active at one point during the last millennium are concentrated in semi-arid regions where the vegetation is rather scattered and low-lying, thus presenting a low resistance to wind. It has been shown that transport capacity of wind is not the limiting factor in these regions. The general wind energy is at the equilibrium, as shown by the long-term average of wind speed, thus making these zones susceptible to rapid destabilisation. This susceptibility makes the dunes prone to remobilisation when the roughness length, which correlates with the vegetation type and cover, reaches the threshold of dune activity. For the last thousand years, this phenomenon has been caused by anthropogenic disturbance and successive droughts, sometimes the former amplifying the latter.

The sensitivity of dune activity to aridity in such environments has been confirmed for the mid-Holocene period, thanks to the extended lakes palaeolevel database. Nevertheless, numerous studies have demonstrated the complexity of the relationship between climate, vegetation, and dune activity (e.g., Barchyn and Hugenholtz, 2015; Durán and Herrmann, 2006; Hesse et al., 2017; Knight et al., 2004; Lancaster and Helm, 2000; Reitz et al., 2010; Telfer and Thomas, 2007; Thomas and Bailey, 2017; Tsoar, 2005; Tsoar and Blumberg, 2002). It is thus important to state that contrary to previous studies, this one focuses only on continental parabolic dunes long-term activity at a global scale. The main reason was to avoid dealing with an overly heterogeneous database that would include several different types of dunes, lying in distinct environments, each responding to diverse climatic factors. The strong correlation between the aeolian activity and aridity conditions during the mid-Holocene period show the significance of continental parabolic dunes as a potential proxy for Quaternary climate. A global activity of dunes correlates with dry or a change towards drier conditions whereas a stabilisation period corresponds to wetter environments. This observation links the continental parabolic dunes activity with the displacements of the Intertropical Convergence Zone (ITCZ). In a global warming world, which is undergoing rapid climate change and where drought episodes tend to be longer and more severe, it is critical to assess the long-term risk represented by a potential reactivation of such widely distributed landforms, especially when it is exacerbated by anthropogenic factors.

6 Author contributions

Lucas Vimpere: Conceptualisation, Methodology, Formal analysis, Investigation, Writing - Original Draft, Writing - Review & Editing, Visualisation, Supervision
Stephen E. Watkins: Writing - Review & Editing
Sébastien Castelltort: Project administration, Funding acquisition, Writing - Review & Editing

7 Acknowledgements

This project was funded by the Department of Earth Sciences of the University of Geneva. Our gratitude goes to Prof. Nicholas Lancaster for generously providing the luminescence ages of parabolic dunes from the INQUA Digital Atlas of Quaternary Dune Fields and Sand Seas

Database. We would like to thank Prof. Pascal Kindler for his constructive comments on earlier versions of this manuscript, which helped to significantly ameliorate the quality of the work. The manuscript has been significantly improved thanks to anonymous reviewers.

Chapter 6 – Global characterisation of parabolic dunes

1 Methods

In the attempt to investigate parabolic dunes at a global level, a database was first constituted of the geomorphological characteristics that can be measured using a GIS software. Digital Elevation Models (DEMs) were collected either from national mapping agencies (e.g., AHN in the Netherlands) or from the Tandem-X WorldDEM (cf. Chapters 2 and 3), and their absolute (i.e., fundamental) accuracy are compiled in the Appendix 13. Nine morphological parameters of 326 dunes located in 11 countries were measured (Appendix 14) with the standardised method described by Yan and Baas (2015; cf. Chapter 3). The classifications of Pye (1993) and Scheffers et al. (2008) were used to categorise the different types of dunes observed (Figure 6).

The sand drift potential analysis was performed according to the method described by Kilibarda and Kilibarda (2016), which is a slightly modified version of the Fryberger method (Fryberger and Dean, 1979). This method was applied to the wind speed and direction data provided by the POWER Release-8 database of the NASA before they stopped supplying wind direction data. The data cover a period of 28 years from the 1$^{\text{rst}}$ of January 1990 to the 1$^{\text{rst}}$ of January 2017. The drift potential (DP), resultant drift potential (RDP), and the ratio between the two (RDP/DP) were calculated according to the methodology described in the Chapter 2 of this thesis so that to characterise the wind regimes.

Table 6: Statistical distribution of the morphological parameters measured on parabolic dunes

	L (km)	W (km)	H (m)	L/W	L/H	W/H	Perim. (km)	Area (km2)
Min.	0.10	0.04	1	0.6	3.5	1.29	0.360	0.007
Max.	25.32	6.73	183	9.2	779.6	279.54	59.354	149.940
Q1	0.40	0.18	11	1.7	24.9	11.57	1.176	0.081
Median	0.90	0.40	25	2.3	39.1	11.57	2.699	0.388
Q3	1.94	0.76	43	3.1	66.1	11.57	5.123	1.213
Mean	1.63	0.62	31	2.6	62.0	24.98	4.427	2.171
SD	2.43	0.72	26	1.3	82.4	28.17	5.855	9.636

2 Morphology

Out of the 326 studied parabolic dunes, 246 (75%) show a distinct parabolic central depression bounded by two well-defined trailing arms and an advancing nose. Sharp noses with straight arms and larger noses with convex arms constitute the most common forms observed (Figure 6; Scheffers et al., 2008). Size of parabolic dunes varies greatly from one location to the other, but also within the same area (Figure 53). On average, they are few hundred meters to few kilometres long, few hundred meters wide, and a dozen meters high (Table 6).

Based on the L/W ratio, most of them are lobate or elongated (Figure 55) according to the classification of Pye (1993). The ratio between wavelength and height was first used by (Bucher, 1919a, 1919b), which he called the "vertical form index", to define the flatness of submarine ripples and dunes. A slightly modified *flatness index* (L/H) was used in this study to characterise the sharpness of the relief of the dunes, which corresponds to the inversed ratio of the "*aspect ratio*" described by some authors (e.g., Lancaster, 1994). The probability density distribution (Figure 55) indicates that most of them characterise as steep (short and high) and skewed (intermediate) parabolic dunes according to the new classification defined for this project. More recently, the term "*aspect ratio*" has been applied to the ratio between the height and the width of the dune (e.g., Itzkin et al., 2020). Considering the dimensions of the studied parabolic dunes and for ease of use, this ratio was again inverted (W/H) and will henceforth be referred to as the aspect ratio. Once again, a new classification was defined to suit the particular extension of parabolic dunes (Figure 55), which predominantly characterise as convex (intermediately large and high) and round (rather broad and low-lying).

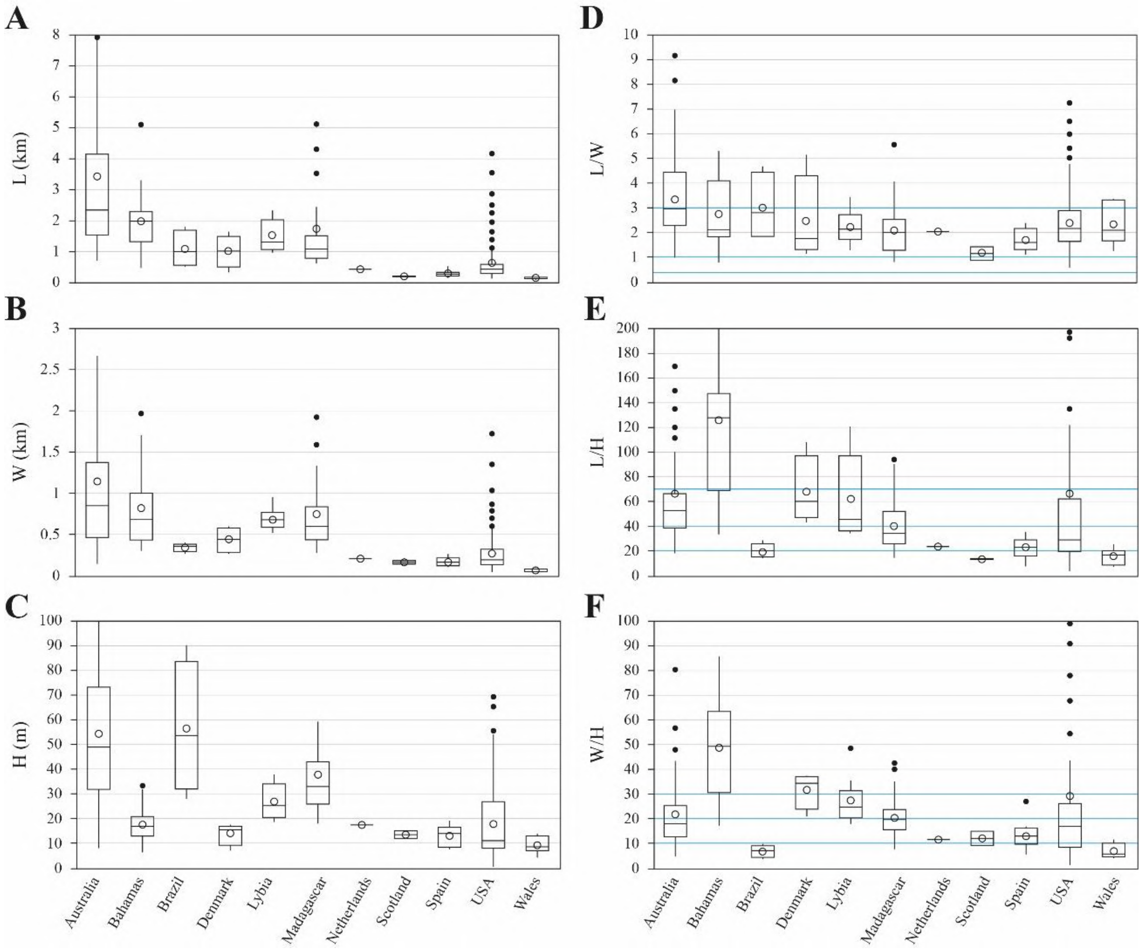

Figure 53: Distribution of the measured morphoparametres for each location studied. For the explanation regarding the blue lines, the reader is referred to the text and to Figure 55.

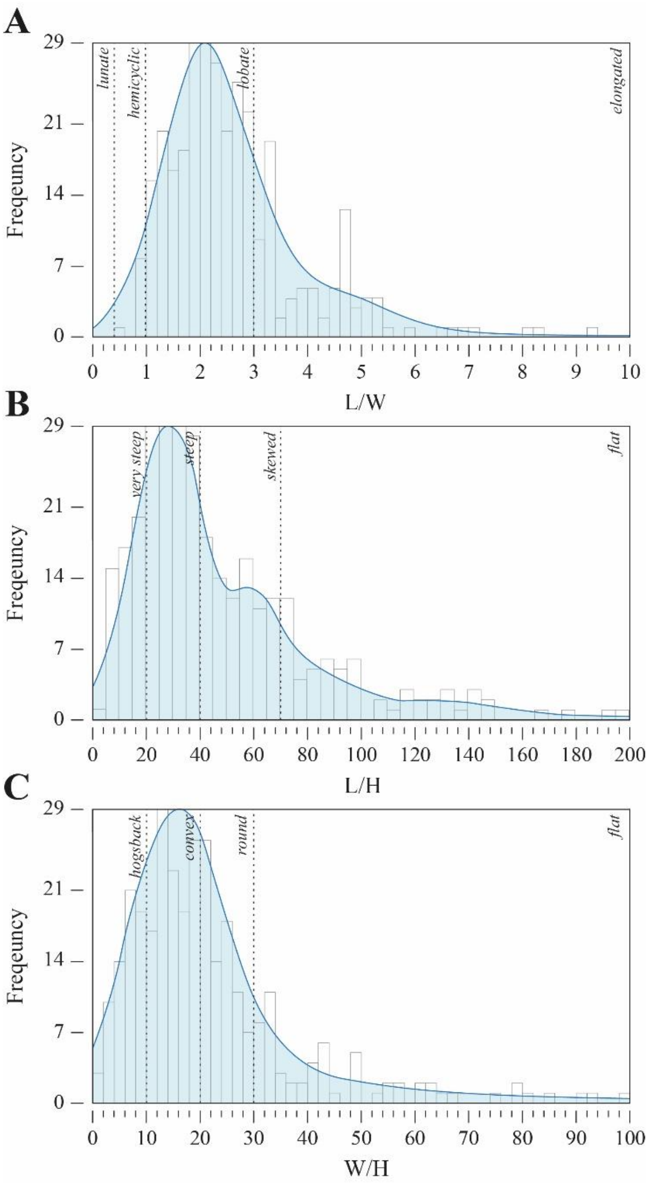

Figure 54: Frequency histograms and modelled probability density functions of: A) the elongation, B) flatness index, and C) aspect ratio. Elongation limits classification are from Pye (1993). For B and C, they were defined for this study.

The observed morphological trends seem to reflect the broad global boundary conditions for parabolic dunes to be at equilibrium. Lunate/hemicyclic dunes, especially if they are flat, are too easily erodible whereas very steep and hogsback dunes are too close to disequilibrium with regards to physical properties of the sediment (e.g., angle of repose). This argument is supported by the power laws controlling the distribution of the morphological ratios (Figure 55). The calculated coefficients of determination indicate that 79, 46, and 42 % of the variability in L/W, L/H, and W/H, respectively, can be explained by power laws, which is considerable considering the diversity of age, environment, and climate conditions under which parabolic dunes developed. Some authors suggested a potential relationship between grain size and dune shape/size, with coarse and poorly sorted sand tendentially constituting the broad and low forms (Anton and Vincent, 1986; Pye and Tsoar, 2008). That is if sediment supply (i.e., sand-producing sources such as beaches) and availability (i.e., limited by groundwater table, vegetation, or a lessened funnelling effect by widening of the openings) provide the dune with enough material to keep on building up rather than remobilising and down-wearing a limited amount of sand constituting the dune (Arens et al., 2004; Yan and Baas, 2015).

3 Wind regimes

According to the Fryberger's classification of wind regimes based on the sand drift potential analysis (Fryberger and Dean, 1979), most of the studied dunes (48 %) lie in an area

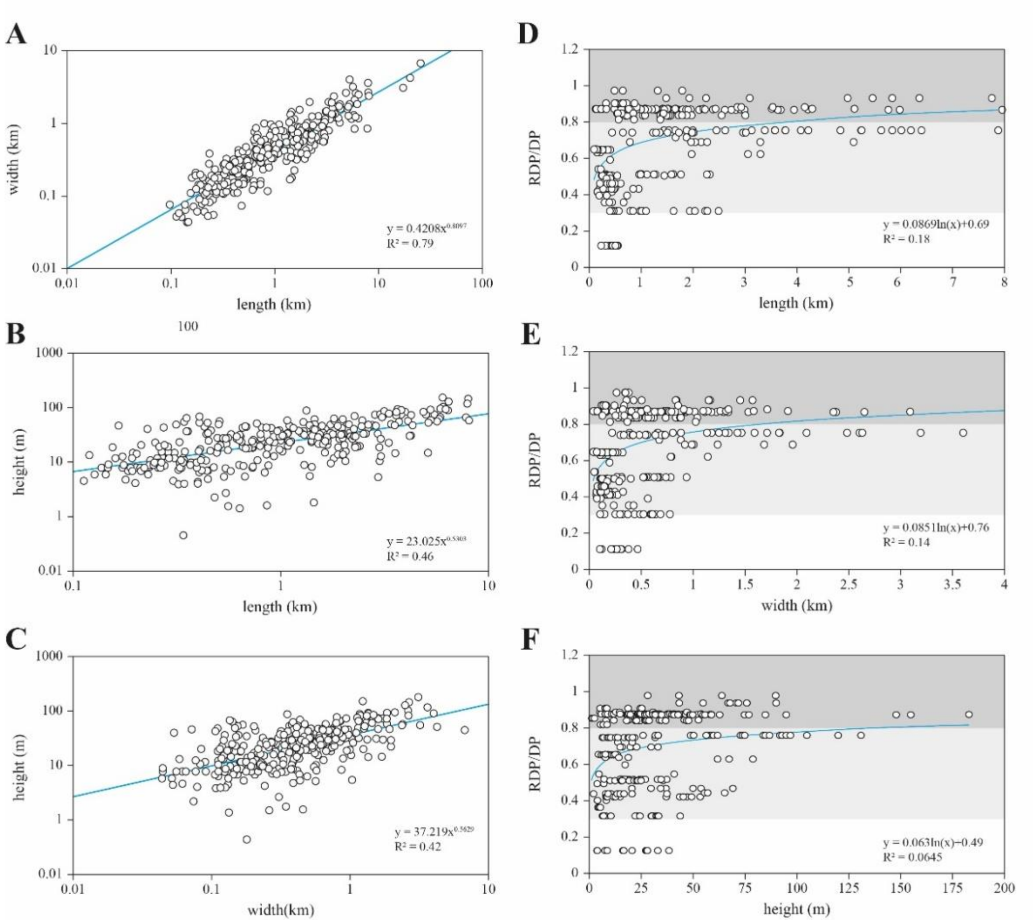

Figure 55: Power laws and the corresponding coefficients of determination computed for: A) elongation, B) flatness index, and aspect ratio. D, E, and F show the absence of any clear relationship between directional variability of the wind regimes and morphological parameters.

of low wind energy (i.e., < 200 VU). The other 27 and 25 % are located in regions being exposed to intermediate- (i.e., 200-400 VU) and high-energy (i.e., > 400 VU) wind regimes, respectively (Appendix 14). A low directional variability of wind regimes (RDP/DP) is a prerequisite for parabolic dunes formation and development as 43, 54, and only 4 % of them are presently exposed to unidirectional (RDP/DP > 0.8), intermediate (0.3 < RDP/DP < 0.8), and polydirectional (RDP/DP < 0.3) winds. However, and contrary to some interpretations made over the last decades (Pye and Tsoar, 2008 and references therein), wind regime directionality does not influence morphological parameters of parabolic dunes. Indeed, only 18, 14, and 6 % of the variability in length, width, and height, respectively, can be explained by logarithmic laws (Figure 55). It does however control the main direction of the dunes (Figure 56), with a linear relationship computed between the orientation and the RDD explaining 91 % of the variability in data. A cluster of bedform orientations measured for dunes lying on the West Coast of the USA does not fit within the 95 % confidence zone. This could be due to either the proximity of mountains with the shoreline and the subsequent topographic influence on wind,

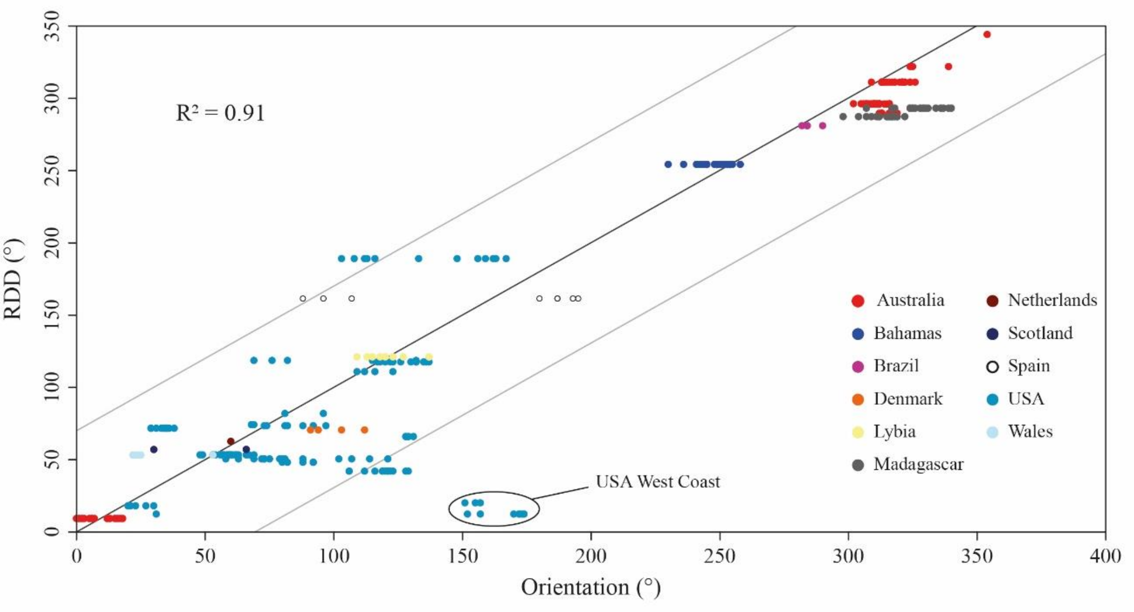

Figure 56: A strong, positive linear correlation exists between the dunes orientation and the RDD. Light grey lines represent the 95% confidence interval computed for individual observations.

or a data bias due to greater uncertainties within the models or the algorithms used to process wind speed and direction. Some inconsistencies have indeed led to the withdrawal of wind direction data that were before provided by the POWER Release-8 database. The alignment of dunes with present winds could support two interpretations: that winds have not significantly changed since the formation of the oldest dunes, or that dunes constantly realign with dominant wind direction during episodes of sand transport. In the second case, dunes that remained fossilised can be used to reconstruct palaeowind conditions and the associate climate at one particular time, given a good and consistent dating of the periods of activity.

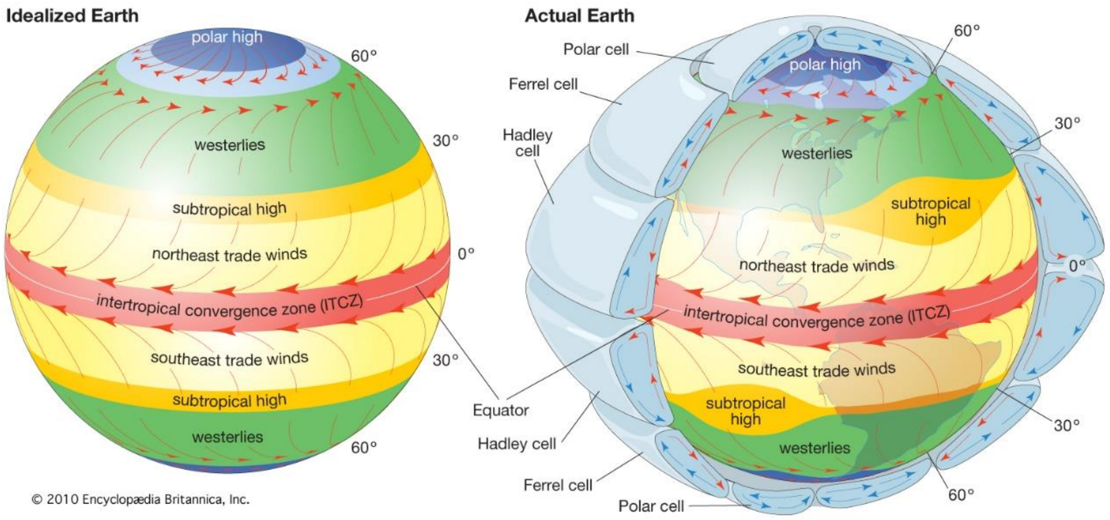

Figure 57: General pattern of atmospheric circulation for an idealised Earth with a uniform surface, and for the actual Earth. The latter show the vertical patterns of atmospheric circulation with the different atmospheric cells.

4 Global atmospheric circulation

Atmospheric circulation is defined as the large-scale movement of air within the atmosphere redistributing thermal energy on the surface of the planet. Insolation (i.e., solar irradiance) is unequally distributed at the Earth's surface with the tropics receiving twice the amount of energy than the poles (Zou et al., 2019). Coupled with the Coriolis effect caused by the rotation of the Earth, some atmospheric cells form at different latitudes (Figure 57). These cells constrain the general wind circulation at the surface of the globe with westerlies blowing towards the east-northeast at mid-latitudes within the Ferrel cells, and easterlies blowing towards the west-southwest at low latitudes within the Hadley cells. The observation of parabolic dunes being aligned with the local prevailing winds orientation (Figure 56) regardless of their age, composition, or environment (i.e., coast or continental interior), questions whether their orientation is defined by the global atmospheric circulation or not.

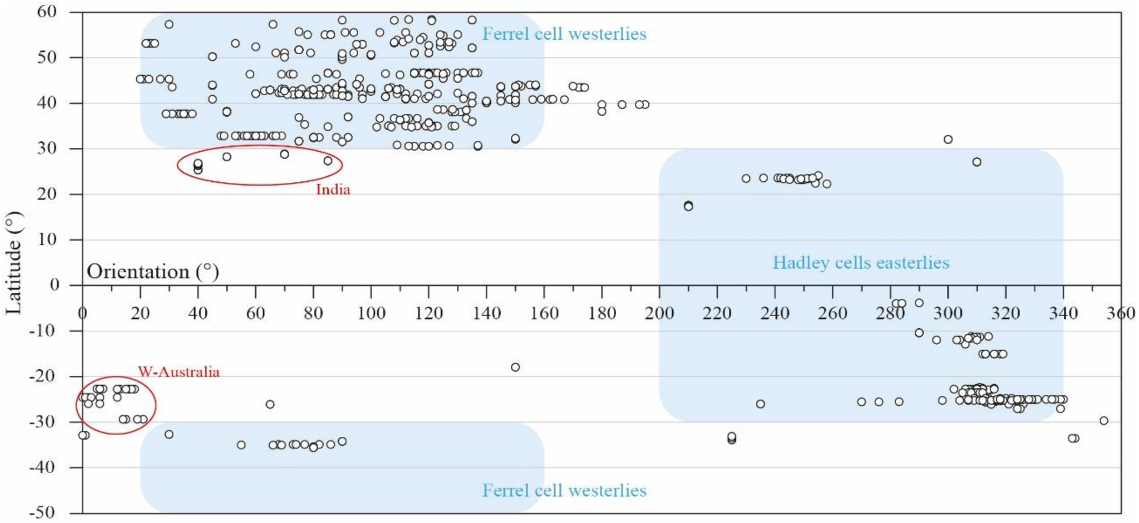

Figure 58: Parabolic dunes orientation and latitude in relation to global atmospheric circulation.

The orientation data collected by GIS analysis (Appendix 14) were combined with the ones provided by the INQUA Digital Atlas of Quaternary Dune Fields and Sand Seas database (Lancaster et al., 2016) so that the orientations of 475 dunes from 25 countries were collected. When classified according to their latitudes, a clear correlation between dune orientations and atmospheric circulation in the different cells is observed (Figure 58). Nonetheless, some dunes located in regions such as W-Australia and India (Thar Desert in Rajasthan) do not align with the trade winds. In Australia, this bias is caused by the presence of the Mascarene High, a semi-permanent subtropical high-pressure zone in the South Indian Ocean that deflects the winds in a counter-clockwise direction (Figure 59). In W-Australia, this results in a northern prevailing direction of winds hence the dunes orientation (cf. Chapter 4). The Thar Desert in India lies in a transitional south-west monsoon regime with rainfall brought by the seasonal northward displacement of the ITCZ. Parabolic dunes formation and migration occurs during the pre-monsoon period, and before the onset of rainfall, when the Indian Summer Monsoon winds blow above the threshold for sand movement (Kar, 1993; Srivastava et al., 2020; Wasson et al., 1983).

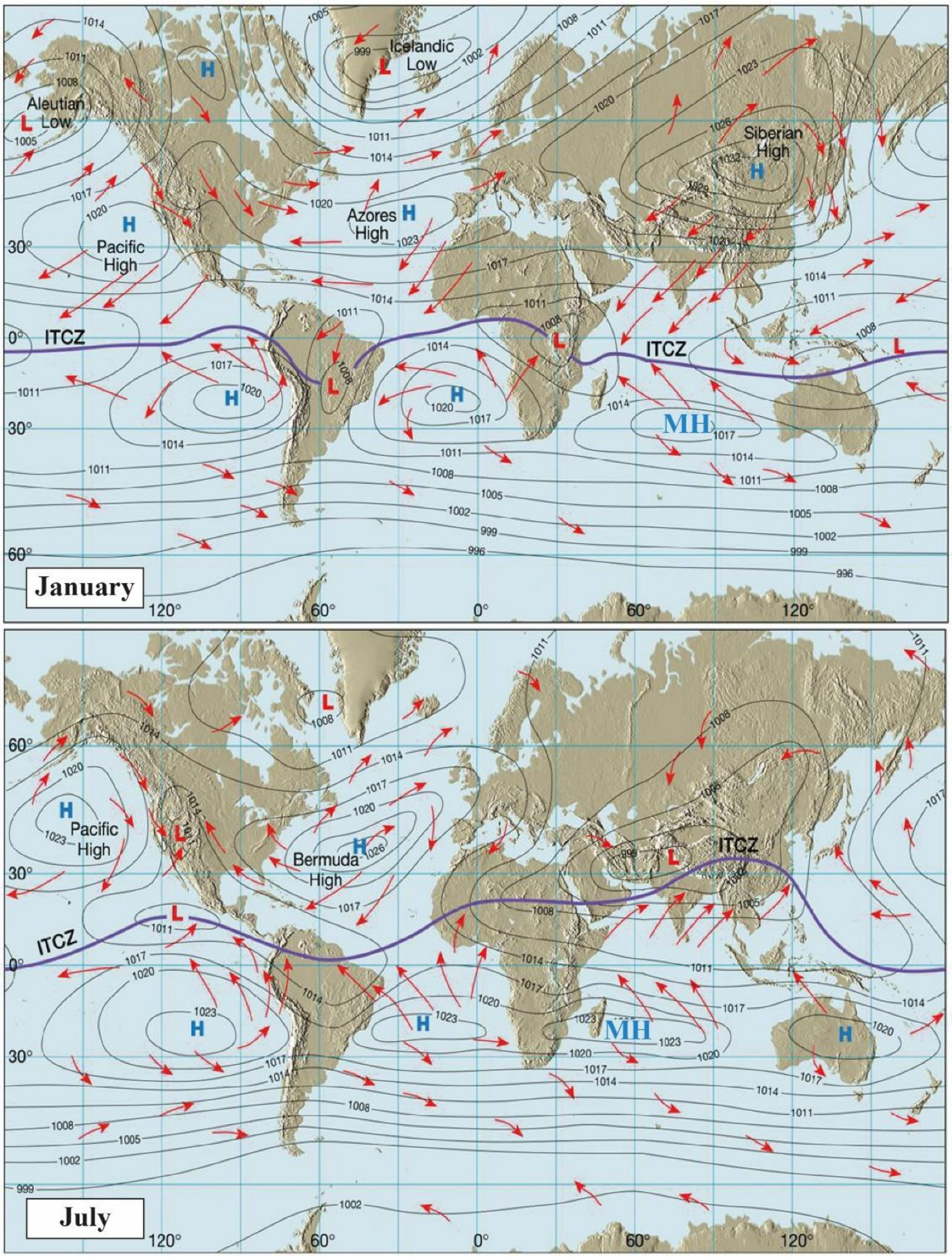

Figure 59: Seasonal changes in global atmospheric circulation with displacement of the ITCZ and the associated winds.

Overall, it seems that parabolic dunes orientation records the global atmospheric circulation within a set period. The different cells are known to contract or expand and shift position in response to interglacial/glacial cycles. During warmer periods for instance, the Hadley cell is believed to broaden whilst shifting polewards (Gastineau et al., 2009; Lu et al.,

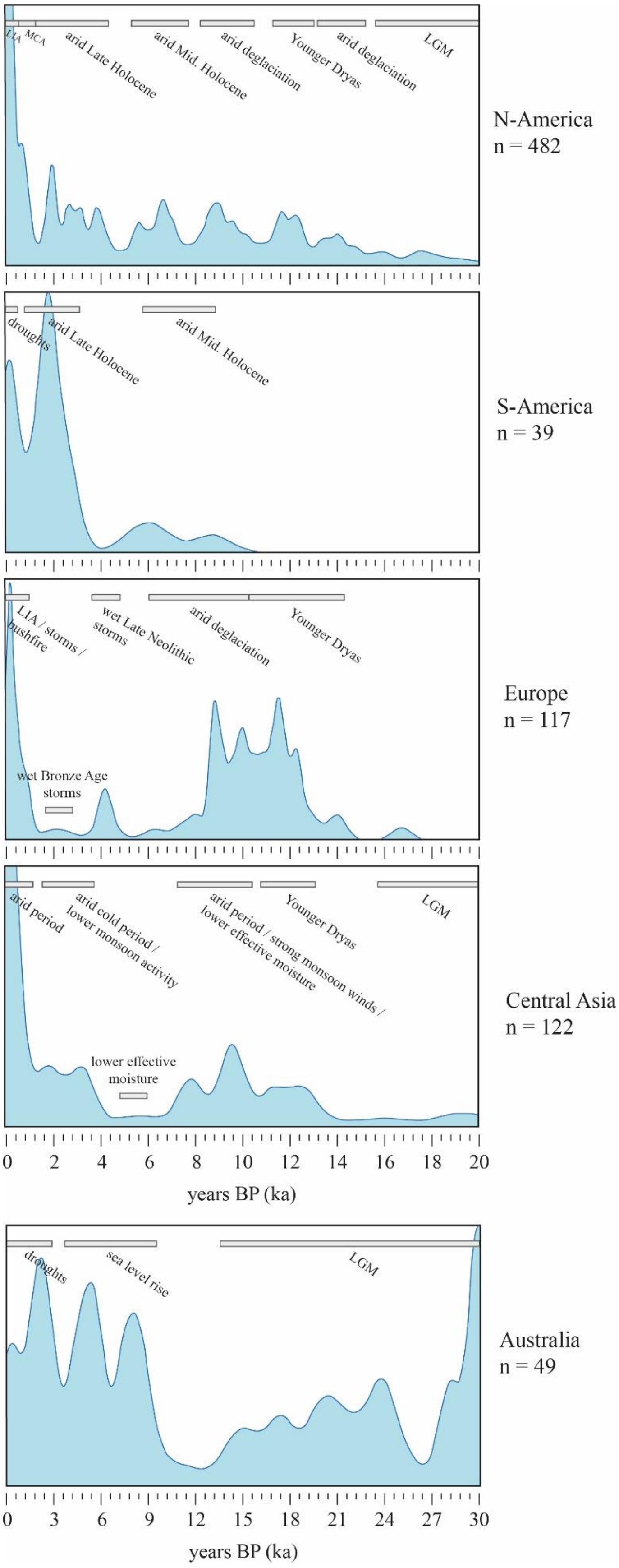

Figure 60: Probability density functions of OSL ages measured within parabolic dunes from five continents. The palaeoclimatic interpretations linked with dune activity were compiled through a review of the literature.

2007; Vallis et al., 2015). This phenomenon presents a double interest for scientists as it can be used as an indicator to predict medium to long term future shifts in direction of migration of dunes, but also as a paleoclimate proxy to determine during which cycle (i.e., glacial or interglacial) fossilised parabolic dunes formed (cf., Chapter 4).

5 Parabolic dunes activity from the last 20'000 years

Despite the issues that arise when considering a global climate rather than complex interrelated local conditions, I attempted to extract a potential global trend in dune activity with respect to global/regional climatic conditions. The luminescence ages were retrieved from the INQUA Digital Atlas database (Lancaster et al., 2016; https://www.dri.edu/inquadunesatlas/) and from 244 papers mentioning parabolic dunes that were reviewed so that 1145 luminescence and radiocarbon ages from 798 dunes distributed around the globe were compiled (Figure 48). Based on the interpretations made by the various authors, 906 ages from 367 dunes that were correlated with a period of sand accumulation (i.e., dune building or remobilisation) were extracted. Data were grouped into five different regions of the globe: North and

South America, Europe, Central Asia, and Australia. The interpretations of natural climatic conditions significance for aeolian transport were compiled from several publications addressing dune activity in these five regions (Figure 61).

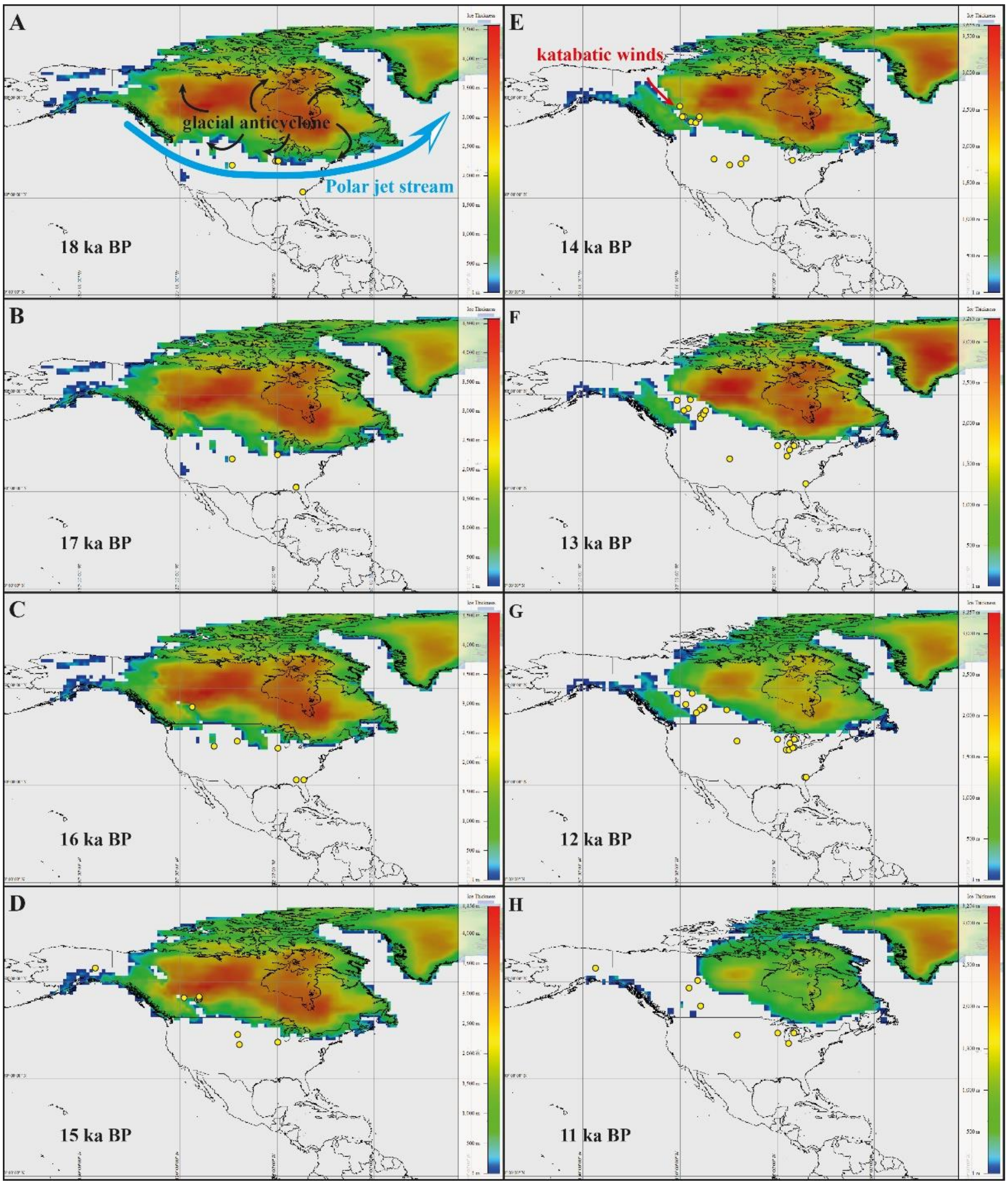

Figure 61: The modelled retreat chronology of the Laurentide Ice Sheet (Peltier, 2004) and the associated main wind circulation patterns. Yellow dots indicate the location and the time of an OSL ages measured within a parabolic dune.

Most of the periods of sand transport were correlated to arid climatic episodes occurring both during warm and cold periods. The oldest episodes of aeolian activity recorded by OSL ages occurred during the cold LGM, Younger Dryas (in the northern hemisphere), and the associated deglaciation stages. In Canada and Northern USA, phases of parabolic dunes construction took place at the northward-moving southern limit of the Laurentide ice sheet (Figure 61), following its progressive melting, and under katabatic winds blowing towards the south-east (Wolfe et al., 2007b). The subsequent episodes of dune activity correlate with the warm Mid. And Late Holocene during which the relationship with climate appears more ambiguous than for the preceding glacial interval (see Chapter 5). For example, the activity of the few parabolic dunes lying in Central Asia that show signs of activity during the Mid. Holocene was interpreted as the result of a degrading vegetation cover under a lower effective moisture (Guo et al., 2018). In Europe, the increased storminess linked with the wet and warm Late Neolithic and Bronze Age is believed to have triggered coastal parabolic dune activity (Clemmensen et al., 2007, 2001). In Australia, only in some coastal areas were the dunes reactivated following the Holocene marine transgression (Dutkiewicz and Prescott, 1997; Ellerton et al., 2020; Pye and Rhodes, 1985). As discussed in Chapter 5, parabolic dunes activity during the recent period arises from a complex interaction between anthropogenic disturbances (e.g., grazing, cropping, deforestation) and natural climatic conditions (e.g., droughts, bushfire, LIA).

Despite local climate complexities and singularities, regional and even global correlations seem possible. As stated by Halfen et al. (2016) in their review of dunefields activity in the Great Plains of North America, more dune ages are required along with a standardisation of the luminescence dating methods so that the said ages can be compared. The density and quality of palaeoclimate data decrease with age so that a good understanding of the present climate conditions under which parabolic dunes are formed and/or reactivated would be significantly helpful to constrain past climate models. Similarly, an improved knowledge of parabolic dunes behaviour during past climatic episodes would provide some valuable long-term data to better predict their future activity.

Chapter 7 – Conclusions and outlooks

1 Summary of key findings

The thesis first reviews the literature that discusses "chevron" dunes in the Bahamas, South Madagascar, and Western Australia, and offers a comprehensive summary of the observations and interpretations published in past studies. Based on this database and the correlation of regional wind regime characteristics with "chevrons" features, it is then suggested that these landforms are of aeolian origin and should be referred as parabolic dunes, not as "chevrons". Furthermore, the use of the term "chevron" has proven to be confusing as it was already referring to structural folds.

A more detailed study with a multi-proxy approach was then conducted to address the coastal carbonate landforms in the Bahamas. It confirms the conclusions reached with the review and made evident that "chevron" dunes are indeed parabolic dunes. Their formation is linked to the peculiar atmospheric circulation, sea level variations, and type of vegetation that occurred during the LIG in the Caribbean. In short, parabolic dunes in the Bahamas formed following an aridification of the region caused by the LIG climate.

The survey carried in Western Australia brings new insights into the timing of deposition of coastal carbonate dunes in the region and the climatic conditions associated to their formation. It has been shown that the aeolianites of the Tamala Limestone formation have been advancing landward (i.e., transverse) during different successive dry glacial intervals of the Pleistocene. The increased aridity during these periods is linked to changes in ocean circulation whilst the measured palaeowind directions reflect changes in atmospheric circulation.

After case studies focusing on coastal carbonate dunes, the relationship between continental parabolic dune activity and climate was further investigated at a broader global scale. Despite the prominent influence of anthropogenic activities on the recent dune activity, arid to semi-arid areas with low and scarce vegetation cover are identified as the boundary conditions favouring remobilisation, and thus activity. Using the mid-Holocene period as an analogue for potential future changes, we then demonstrate that inland parabolic dune activity is linked with large-scale atmospheric circulation, especially with the ITCZ displacements. Dune were active in regions undergoing a process of aridification, which were identified as the temperate zones whereas today's dry zones became more humid, leading to dune stabilisation.

The effort to characterise parabolic dunes at a global level and to link their activity to large-scale climate conditions was pursued further. Parabolic dunes morphoparameters were quantified and two new classifications were proposed to characterise these landforms *"flatness"* and *"aspect ratio"*. Some morphological ranges were defined that represent the boundary conditions of dunes to be at equilibrium., and power laws were computed to predict the evolution of their morphology. An assessment of the present wind regimes and sand drift potential revealed that wind energy has no influence on parabolic dunes occurrence. On the contrary, they develop almost exclusively under unidirectional wind regime although the directional variability of the winds does not influence the dunes morphology. However, dunes are aligned with the prevailing direction of present winds blowing above the threshold for sand movement. As such, parabolic dunes record the global atmospheric circulation and can potentially entomb cyclic changes in atmospheric cells if not reactivated afterwards. Based on a luminescence ages database spanning the last 20’000 years, global parabolic dune activity correlates with periods of marked aridity or changes towards more arid conditions that may occur during warm (i.e., interglacial) as well as cold (i.e., glacial) periods.

2 Discussion and potential future directions

The palaeoclimatic interpretations made for the Bahamian region are mostly based on climate models and on the study of Zhuravleva and Bauch (2018) who combined planktic foraminiferal assemblage data with δ^{18}O values in surface and thermocline-dwelling foraminifera from a core taken on the slope of the Little Bahama Bank. Unfortunately, most of the palaeoclimate reconstructions made for the subtropical western Atlantic only span the last 65'000 years (NCEI and NOAA data viewer). In this region, there is a growing need for constraining past climate conditions using multi-proxy methodologies. Speleothems are promising retainers of these environmental conditions (e.g., Comas-Bru et al., 2020, 2019; Comas-Bru and Harrison, 2019; Deininger et al., 2019; Kaushal et al., 2018; Lechleitner et al., 2018; Oster et al., 2019); constitute a suitable material for high-precision absolute dating (e.g., U-Th); and are numerous in karstic carbonate landscapes such as the Bahamian platforms (e.g., Arienzo, 2014; Arienzo et al., 2017, 2015). A regional comparative study would make possible a correlation of climate archives like speleothems with the carbonate units composing the superficial geology of the islands. The precise dating of these speleothems can both make up for the lack of precision of the AAR dating method and inform us on the sea-level history of the area. Indeed, speleothems grow when caves where they form are not flooded so that presently-underwater caves (e.g., blue holes) have dried up during past sea level falls, corresponding to glacial periods (Mylroie et al., 1995; Palmer et al., 1999). In such features,

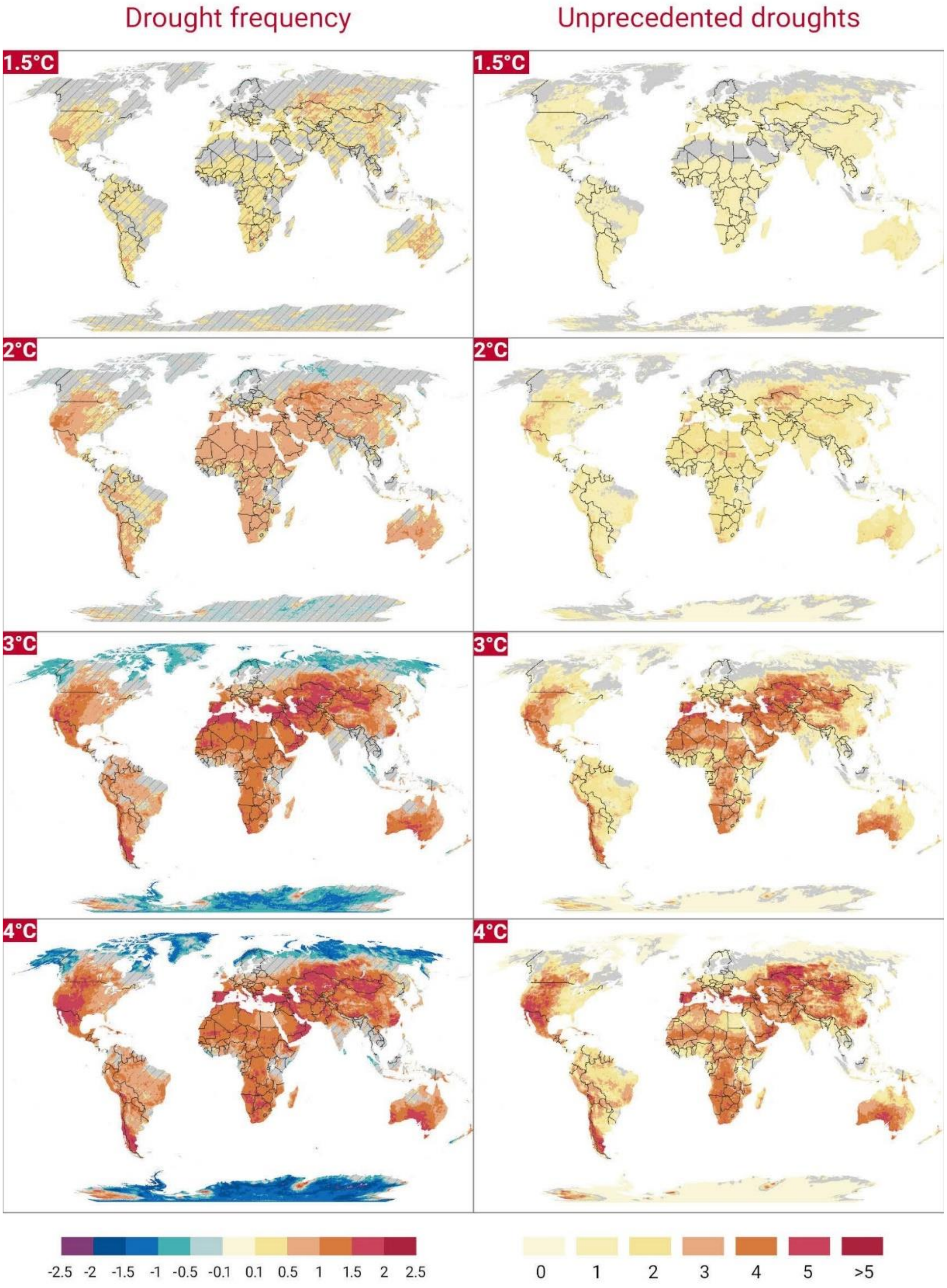

Figure 62: Modelled evolution of drought frequency (left) and drought events with stronger severity (right) than the ones recorded for the period between 1981 and 2000. First row represent data measured over the same time frame with a global temperature that is 1.5 °C higher than the pre-industrial period. From UNDRR report (2021).

stalactites forming at different depths represent markers of past sea level variations with the potential of quantifying rising/falling sea level rates whilst simultaneously recording atmospheric conditions (Bradley, 2015; Gascoyne et al., 1979; Lundberg and Ford, 1994; Richards et al., 1994; Smart et al., 1998). In this sense, they provide a way of settling the debate around a possible short sea level drop during the MIS 5e, referred as the "Younger Dryas-like event" in the chapter 3 of this thesis (Zhuravleva and Bauch, 2018). In summary, a comprehensive survey of the Bahamian speleothems by using geochemical and absolute dating analyses represents a further step in our comprehension of the interaction between past climate, sea level oscillations, and carbonate sedimentation on the islands.

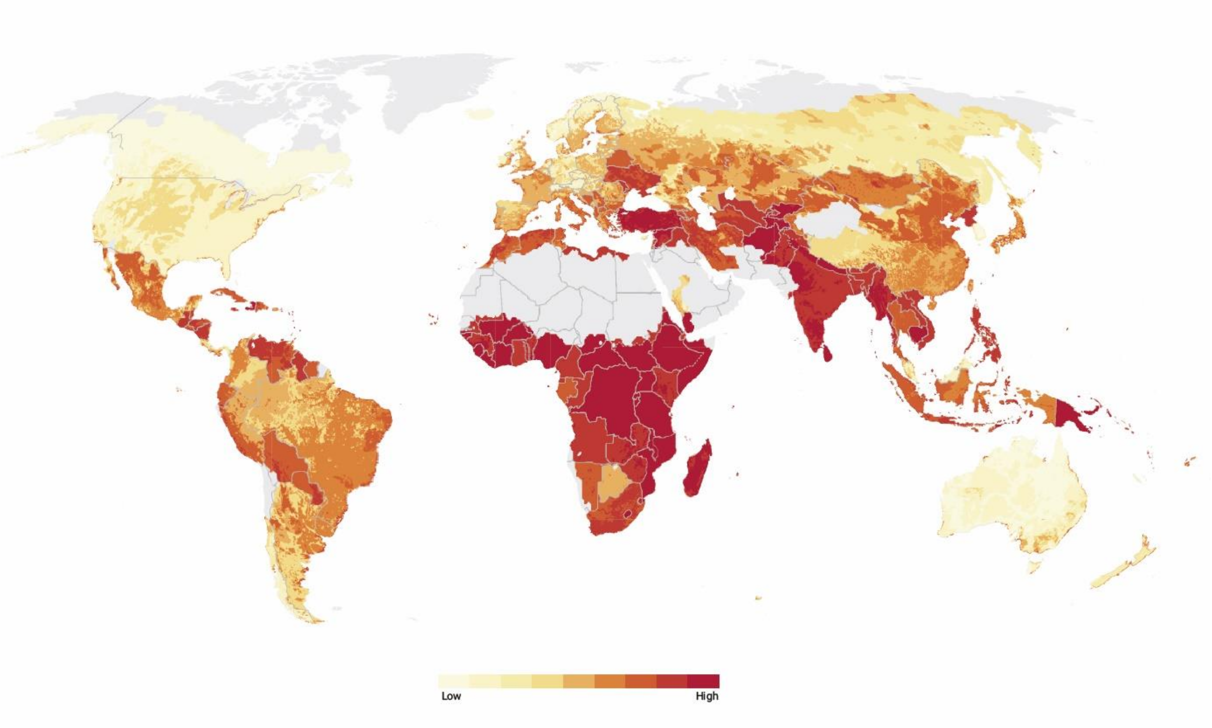

Figure 63: Global drought vulnerability map showing that presently-humid regions are the most at risk.

The Tamala aeolianites of Western Australia, and more specifically the least studied units in the Shark Bay region, constitute exceptional coastal features that definitely warrant further studies. The remoteness and difficult access of the region make its study demanding, which is probably one of the reasons why it remains understudied. The counterpart is the wilderness and the many possibilities the area still represents for scientists to make unique and authentic discoveries. Presently, the greatest issue faced by geoscientists is the timing of these aeolian deposits (Playford et al., 2013). While the composition, sedimentary structures, and stratigraphy are starting to be better understood, a consequent uncertainty on the relationship of dunes with climate and both atmospheric and ocean circulation remains. In line with our study in the Bahamas, AAR dating has proven to be inefficient to provide with a coherent and reliable aminodatabase to date the successive units. A consistent regional sampling for OSL dating offers a way to constrain the timing of deposition of the dunes more accurately. This approach has been adopted for this project until the loss of the samples and the impossibility to go back in the field due to the COVID-19 pandemic hindered any further inquiry. Accurate dating will bring highly valuable insights into the timing of carbonate aeolian deposition relative to interglacial/glacial cyclicity. It is worth to note that the interconnection between eustasy and coastal aeolian sedimentation remains a challenging question to answer, even more when different carbonate systems are considered (Abegg et al., 2001; Frébourg, 2010; Hearty and O'Leary, 2008; Le Guern, 2004; Playford et al., 2013). Our study, summarised in chapter 4, advocates for an aeolian migration and accumulation (i.e., building of the dunes) occurring during glacial intervals rather than interglacial ones as it is commonly acknowledged for the Bahamas. The contrast between Western Australia and the Bahamas can be explained by the different platform geometries, the first being a ramp whereas the second is composed by several isolated flat-topped platforms. In the case of a ramp, a lowering of sea level causes the whole production and transport systems to shift towards a lower position on the platform without reducing the area of carbonate production (Schlager, 2005). The productive area of an isolated flat-topped platform is brought lower as well by a falling sea level but is considerably reduced in the process. Sediment production is diminished then whilst transport of sediments onto the platform top is hampered by steep slopes (J. L. Carew and Mylroie, 1995). This observation is worth the investigation when looking at coastal aeolianites developing on other carbonate platforms around the world. To finish, the scarcity of both offshore and onshore palaeoclimatic data represents an opportunity for future studies. Whether the collection of new data is done by deep-sea coring or speleothems analysis, it will definitely bring new valuable elements to our general comprehension of this particular region as well as for the risk assessment related to future climate change in the most arid country on the planet.

Our attempt to put the inland parabolic dune activity within a global climate model has revealed to be a promising approach in several aspects. First, the characterisation of the present conditions causing a reactivation of stabilised dunes shows a clear link between aeolian activity and aridification. However, the definition of dune "activity" is an often-debated issue among the aeolian community, especially when it is defined by luminescence dating (Telfer and Thomas, 2007; Thomas and Bailey, 2017). Thomas and Bailey (2017) developed the Accumulation Intensity calculation method as a way to identify dune activity in an environmentally meaningful manner, although it cannot be applied on ages coming from a geographical and stratigraphic scattered context. Another factors to take into consideration is the impact of human activity on vegetation and climate, both influencing recent dune mobilisation, and the nonlinear relationship between climate, vegetation, and dune activity (e.g., Barchyn and Hugenholtz, 2012; Hesse et al., 2017). Second, the relationship between aeolian activity and aridification is verified for the warmer mid-Holocene period but surprisingly not in the regions that are presently the most sensitive to such increase in aridity.

The dunes lying in presently arid regions were stabilised during the mid-Holocene because these zones became wetter whereas the now-humid regions became more arid and subject to increased aeolian activity. This observation brings to light the importance to establish proper coastal and inland management programmes also in temperate and humid territories. Indeed, recent studies indicate that drought frequency and severity are strongly correlated to temperature, which will become an even more pivotal for drought projections with increasing global warming level (UNDRR, 2021). The central parts of the Americas, the Mediterranean, Africa, central Asia, and South Australia are the regions currently affected by an increase in drought frequency and severity and are much likely to be the most strongly affected ones in the future whilst increased precipitation in high latitude regions will reduce the occurrence and the impact of droughts (Figure 62). The modelled risk associated to droughts, and defined as a combination of hazard, exposure, and vulnerability, indicates that the current humid to sub-humid regions are the most vulnerable (Figure 63).

References

Abbott, D., 2006. Impact Craters as Sources of Megatsunami Generated Chevron Dunes. Presented at the GSA Philadelphia Annual Meeting, Philadelphia.

Abbott, D., Bryant, E., Gusiakov, V., Masse, W., Raveloson, A., Razafindrakoto, H., 2006. Report of International Tsunami Expedition to Madagascar.

Abbott, D., Bryant, T., Gusiakov, V., Masse, W., 2007. Megatsunami of the World Ocean: Did They Occur in the Recent Past ? Presented at the AGU Spring Meeting.

Abegg, F.E. (Rick), Loope, D.B., Harris, P.M. (Mitch), 2001. Modern and Ancient Carbonate Eolianites: Sedimentology, Sequence Stratigraphy, and Diagenesis. SEPM Society for Sedimentary Geology. https://doi.org/10.2110/pec.01.71

Ahlbrandt, T.S., Fryberger, S., 1981. Sedimentary features and significance of interdune deposits, in: Ethridge, F.G., Flore, R.M. (Eds.), Recent and Ancient Non-Marine Depositional Environments: Models for Exploration, SEPM Special Publication. pp. 293–314.

Alexanderson, H., Bernhardson, M., 2016. OSL dating and luminescence characteristics of aeolian deposits and their source material in Dalarna, central Sweden. Boreas 45, 876–893. https://doi.org/10.1111/bor.12197

Alexanderson, H., Fabel, D., 2015. Holocene Chronology of the Brattforsheden Delta and Inland Dune Field, Sw Sweden. Geochronometria 42. https://doi.org/10.1515/geochr-2015-0001

Anderegg, W.R.L., Trugman, A.T., Bowling, D.R., Salvucci, G., Tuttle, S.E., 2019. Plant functional traits and climate influence drought intensification and land–atmosphere feedbacks. Proc Natl Acad Sci USA 116, 14071–14076. https://doi.org/10.1073/pnas.1904747116

Anderson, J., Walker, I., 2006. Airflow and sand transport variations within a backshore–parabolic dune plain complex: NE Graham Island, British Columbia, Canada. Geomorphology 77, 17–34. https://doi.org/10.1016/j.geomorph.2005.12.008

Anton, D., Vincent, P., 1986. Parabolic dunes of the Jafurah Desert, Eastern Province, Saudi Arabia. Journal of Arid Environments 11, 187–198. https://doi.org/10.1016/S0140-1963(18)31205-9

Arbogast, A., Bigsby, M., DeVisser, M., Langley, S., Hanson, P., Daly, T., Young, A., 2010. Reconstructing the age of coastal sand dunes along the northwestern shore of Lake Huron in Lower Michigan: Paleoenvironmental implications and regional comparisons. Aeolian Research 2, 83–92. https://doi.org/10.1016/j.aeolia.2010.07.001

Arbogast, A., Hansen, E., Van Oort, M., 2002a. Reconstructing the geomorphic evolution of large coastal dunes along the southeastern shore of Lake Michigan. Geomorphology 46, 241–255. https://doi.org/10.1016/S0169-555X(02)00076-4

Arbogast, A., Packman, S., 2004. Middle-Holocene mobilization of aeolian sand in western upper Michigan and the potential relationship with climate and fire. The Holocene 14, 464–471. https://doi.org/10.1191/0959683604hl723rr

Arbogast, A., Wintle, A., Packman, S.C., 2002b. Widespread middle Holocene dune formation in the eastern Upper Peninsula of Michigan and the relationship to climate and outlet-controlled lake level. Geology 30, 55. https://doi.org/10.1130/0091-7613(2002)030<0055:WMHDFI>2.0.CO;2

Arens, S., Slings, Q., de Vries, C., 2004. Mobility of a remobilised parabolic dune in Kennemerland, The Netherlands. Geomorphology 59, 175–188. https://doi.org/10.1016/j.geomorph.2003.09.014

Arienzo, M., 2014. Subtropical Atlantic Climate Variability Record in Speleothems from the Bahamas. University of Miami, Coral Gables, Florida.

Arienzo, M., Swart, P., Broad, K., Clement, A., Pourmand, A., Kakuk, B., 2017. Multi-proxy evidence of millennial climate variability from multiple Bahamian speleothems. Quaternary Science Reviews 161, 18–29. https://doi.org/10.1016/j.quascirev.2017.02.004

Arienzo, M., Swart, P., Pourmand, A., Broad, K., Clement, A., Murphy, L., Vonhof, H., Kakuk, B., 2015. Bahamian speleothem reveals temperature decrease associated with Heinrich stadials. Earth and Planetary Science Letters 430, 377–386. https://doi.org/10.1016/j.epsl.2015.08.035

Armitage, S.J., Botha, G.A., Duller, G.A.T., Wintle, A.G., Rebêlo, L.P., Momade, F.J., 2006. The formation and evolution of the barrier islands of Inhaca and Bazaruto, Mozambique. Geomorphology 82, 295–308. https://doi.org/10.1016/j.geomorph.2006.05.011

Asadi Zarch, M.A., Sivakumar, B., Malekinezhad, H., Sharma, A., 2017. Future aridity under conditions of global climate change. Journal of Hydrology 554, 451–469. https://doi.org/10.1016/j.jhydrol.2017.08.043

Ashkenazy, Y., Yizhaq, H., Tsoar, H., 2012. Sand dune mobility under climate change in the Kalahari and Australian deserts. Climatic Change 112, 901–923. https://doi.org/10.1007/s10584-011-0264-9

Bagnold, R., 1941. The physics of blown sand and desert dunes, William Morrow&Company. ed. New York, NY.

Bagnold, R., 1936. The movement of desert sand. Proceedings of the Royal Society of London. Series A-Mathematical and Physical Sciences 157, 594–620.

Bain, R., Kindler, P., 1994. Irregular fenestrae in Bahamian eolianites: a rainstorm-induced origin. Journal of Sedimentary Research 64.

Baldauf, P., Burkhart, P., Hanson, P., Miles, M., Larsen, A., 2019. Chronology of dune development in the White River Badlands, northern Great Plains, USA. Aeolian Research 37, 14–24. https://doi.org/10.1016/j.aeolia.2018.12.004

Banham, S.G., Gupta, S., Rubin, D.M., Watkins, J.A., Sumner, D.Y., Edgett, K.S., Grotzinger, J.P., Lewis, K.W., Edgar, L.A., Stack-Morgan, K.M., Barnes, R., Bell, J.F., Day, M.D., Ewing, R.C., Lapotre, M.G.A., Stein, N.T., Rivera-Hernandez, F., Vasavada, A.R., 2018. Ancient Martian aeolian processes and palaeomorphology reconstructed from the Stimson formation on the lower slope of Aeolis Mons, Gale crater, Mars. Sedimentology 65, 993–1042. https://doi.org/10.1111/sed.12469

Barboza, F., Geyh, M., Hoffmann, R., Kruck, W., Netto, A., Merkt, J., Rojas, C., 2000. Soil formation and quaternary geology of the paraguayan chaco: Thematic mapping. Zeitschrift für angewandte Geologie 1, 49–54.

Barchyn, T., Hugenholtz, C., 2015. Predictability of dune activity in real dune fields under unidirectional wind regimes: Predictability of dune activity. Journal of Geophysical Research: Earth Surface 120, 159–182. https://doi.org/10.1002/2014JF003248

Barchyn, T., Hugenholtz, C., 2013. Dune field reactivation from blowouts: Sevier Desert, UT, USA. Aeolian Research 11, 75–84. https://doi.org/10.1016/j.aeolia.2013.08.003

Barchyn, T., Hugenholtz, C., 2012. Aeolian dune field geomorphology modulates the stabilization rate imposed by climate. Journal of Geophysical Research: Earth Surface 117, n/a-n/a. https://doi.org/10.1029/2011JF002274

Barlow, N.L.M., McClymont, E.L., Whitehouse, P.L., Stokes, C.R., Jamieson, S.S.R., Woodroffe, S.A., Bentley, M.J., Callard, S.L., Cofaigh, C.Ó., Evans, D.J.A., Horrocks, J.R., Lloyd, J.M., Long, A.J., Margold, M., Roberts, D.H., Sanchez-Montes, M.L., 2018. Lack of evidence for a substantial sea-level fluctuation within the Last Interglacial. Nature Geoscience 11, 627–634. https://doi.org/10.1038/s41561-018-0195-4

Barrows, T.T., Juggins, S., 2005. Sea-surface temperatures around the Australian margin and Indian Ocean during the Last Glacial Maximum. Quaternary Science Reviews 24, 1017–1047. https://doi.org/10.1016/j.quascirev.2004.07.020

Bastian, L.V., 2010. Comment on Hearty, P.J. and O•Leary, M.J., 2008. Carbonate eolianites, quartz sands, and Quaternary sea-level cycles, Western Australia: A chronostratigraphic approach. Quaternary Geochronology 3: 26-55. Quaternary Geochronology 5, 76–77.

Bastian, L.V., 1996. Residual soil mineralogy and dune subdivision, Swan Coastal Plain, Western Australia. Australian Journal of Earth Sciences 43, 31–44. https://doi.org/10.1080/08120099608728233

Bastian, L.V., 1994. The dune systems of the Swan Coastal Plain: subdivision based on mineral trends in the surface soils. Chemistry Centre of WA.

Battistini, R., 1964. L’Extrême-Sud de Madagascar, étude géomorphologique. Paris.

Bernhardson, M., Alexanderson, H., 2018. Early Holocene NW-W winds reconstructed from small dune fields, central Sweden. Boreas 47, 869–883. https://doi.org/10.1111/bor.12307

Bertran, P., Bateman, M., Hernandez, M., Mercier, N., Millet, D., Sitzia, L., Tastet, J.-P., 2011. Inland aeolian deposits of south-west France: facies, stratigraphy and chronology. Journal of Quaternary Science 26, 374–388. https://doi.org/10.1002/jqs.1461

Blench, R., 2010. Evidence for the Austronesian Voyages in the Indian Ocean, in: Anderson, A., Barrett, J., Boyle, K. (Eds.), The Global Origins and Development of Seafaring, McDonal Institute Monographs. pp. 239–248.

Blott, S.J., Pye, K., 2001. GRADISTAT: a grain size distribution and statistics package for the analysis of unconsolidated sediments. Earth Surface Processes and Landforms 26, 1237–1248. https://doi.org/10.1002/esp.261

Bogle, R., Redsteer, M., Vogel, J., 2015. Field measurement and analysis of climatic factors affecting dune mobility near Grand Falls on the Navajo Nation, southwestern United States. Geomorphology 228, 41–51. https://doi.org/10.1016/j.geomorph.2014.08.023

Börker, J., Hartmann, J., Amann, T., Romero-Mujalli, G., 2018. Terrestrial Sediments of the Earth: Development of a Global Unconsolidated Sediments Map Database (GUM). Geochemistry, Geophysics, Geosystems 19, 997–1024. https://doi.org/10.1002/2017GC007273

Bourgeois, J., Weiss, R., 2009. “Chevrons” are not mega-tsunami deposits - A sedimentologic assessment. Geology 37, 403–406. https://doi.org/10.1130/G25246A.1

Bowen, A., Lindley, D., 1977. A wind-tunnel investigation of the wind speed and turbulence characteristics close to the ground over various escarpment shapes. Boundary-Layer Meteorology 12, 259–271. https://doi.org/10.1007/BF00121466

Braconnot, P., Harrison, S.P., Joussaume, S., Hewitt, C.D., Kitoch, A., Kutzbach, J.E., Liu, Z., Otto-Bliesner, B., Syktus, J., Weber, S.L., 2004. Evaluation of PMIP coupled ocean-atmosphere simulations of the Mid-Holocene, in: Battarbee, R.W., Gasse, F., Stickley, C.E. (Eds.), Past Climate Variability through Europe and Africa, Developments in Paleoenvironmental Research. Springer Netherlands, Dordrecht, pp. 515–533. https://doi.org/10.1007/978-1-4020-2121-3_24

Braconnot, P., Otto-Bliesner, B., Harrison, S., Joussaume, S., Peterchmitt, J.-Y., Abe-Ouchi, A., Crucifix, M., Driesschaert, E., Fichefet, Th., Hewitt, C.D., Kageyama, M., Kitoh, A., Laîné, A., Loutre, M.-F., Marti, O., Merkel, U., Ramstein, G., Valdes, P., Weber, S.L., Yu, Y., Zhao, Y., 2007a. Results of PMIP2 coupled simulations of the Mid-Holocene and Last Glacial Maximum – Part 1: experiments and large-scale features. Climate of the Past 3, 261–277. https://doi.org/10.5194/cp-3-261-2007

Braconnot, P., Otto-Bliesner, B., Harrison, S., Joussaume, S., Peterchmitt, J.-Y., Abe-Ouchi, A., Crucifix, M., Driesschaert, E., Fichefet, Th., Hewitt, C.D., Kageyama, M., Kitoh, A., Loutre, M.-F., Marti, O., Merkel, U., Ramstein, G., Valdes, P., Weber, L., Yu, Y., Zhao, Y., 2007b. Results of PMIP2 coupled simulations of the Mid-Holocene and Last Glacial Maximum – Part 2: feedbacks with emphasis on the location of the ITCZ and mid- and high latitudes heat budget. Climate of the Past 3, 279–296. https://doi.org/10.5194/cp-3-279-2007

Bradley, R., 2015. Speleothems, in: Paleoclimatology. Elsevier, pp. 291–318. https://doi.org/10.1016/B978-0-12-386913-5.00008-9

Bradley, R., 2003. Presentation “Climate of the Last Millennium.” Presented at the HOLOCENE Working group workshop, Bjerknes center for climate research, Bergen, Norway.

Bradley, R. S., Briffa, K.R., Cole, J., Hughes, M.K., Osborn, T.J., 2003. The Climate of the Last Millennium, in: Alverson, K.D., Pedersen, T.F., Bradley, Raymond S. (Eds.), Paleoclimate, Global Change and the Future, Global Change — The IGBP Series. Springer Berlin Heidelberg, Berlin, Heidelberg, pp. 105–141. https://doi.org/10.1007/978-3-642-55828-3_6

Brooke, B., 2001. The distribution of carbonate eolianite. Earth-Science Reviews 55, 135–164. https://doi.org/10.1016/S0012-8252(01)00054-X

Brookfield, M.E., Ahlbrandt, T.S., 2000. Eolian sediments and processes. Elsevier.

Bryant, E., 2014. Tsunami: the underrated hazard, Springer. ed.

Bryant, E., Nott, J., 2001. Geological indicators of large tsunami in Australia. Natural Hazards 24, 231–249.

Bryant, E., Walsh, G., Abbott, D., 2007. Cosmogenic mega-tsunami in the Australia region: are they supported by Aboriginal and Maori legends? Geological Society, London, Special Publications 273, 203–214.

Bryant, E., Young, R., Price, D., Wheeler, D., Pease, M., 1997. The impact of tsunami on the coastline of Jervis Bay, southeastern Australia. Physical Geography 18, 440–459.

Bubenzer, O., Besler, H., Hilgers, A., 2007. Filling the gap: OSL data expanding 14C chronologies of Late Quaternary environmental change in the Libyan Desert. Quaternary International 175, 41–52. https://doi.org/10.1016/j.quaint.2007.03.014

Bucher, W., 1919a. On ripples and related sedimentary surface forms and their paleogeographic interpretation; Part I. American Journal of Science 279, 149–210.

Bucher, W., 1919b. On ripples and related sedimentary surface forms and their paleogeographic interpretation; Part II. American Journal of Science 241–269. https://doi.org/10.2475/ajs.s4-47.280.241

Bullard, J., 1997. A note on the use of the “Fryberger method” for evaluating potential sand transport by wind. Journal of Sedimentary Research 67, 499–501. https://doi.org/10.1306/D42685A9-2B26-11D7-8648000102C1865D

Burney, D., 2004. A chronology for late prehistoric Madagascar. Journal of Human Evolution 47, 25–63. https://doi.org/10.1016/j.jhevol.2004.05.005

Cai, W., Santoso, A., Wang, G., Weller, E., Wu, L., Ashok, K., Masumoto, Y., Yamagata, T., 2014. Increased frequency of extreme Indian Ocean Dipole events due to greenhouse warming. Nature 510, 254–258. https://doi.org/10.1038/nature13327

Caputo, M.V., 1995. Sedimentary architecture of Pleistocene eolian calcarenites, San Salvador Island, Bahamas, in: Curran, H.A., White, B. (Eds.), Terrestrial and Shallow Marine

Geology of the Bahamas and Bermuda. Geological Society of America. https://doi.org/10.1130/0-8137-2300-0.63

Caputo, M.V., 1993. Eolian Structures and Textures in Oolitic-Skeletal Calcarenites from the Quaternary of San Salvador Island, Bahamas: A New Perspective on Eolian Limestones, in: Keith, B.D., Zuppann, C.W. (Eds.), Mississippian Oolites and Modern Analogs. American Association of Petroleum Geologists, p. 0. https://doi.org/10.1306/St35571C17

Carcaillet, C., Richard, P., Asnong, H., Capece, L., Bergeron, Y., 2006. Fire and soil erosion history in East Canadian boreal and temperate forests. Quaternary Science Reviews 25, 1489–1500. https://doi.org/10.1016/j.quascirev.2006.01.004

Carew, J., Mylroie, J., 1995. Quaternary tectonic stability of the Bahamian Archipelago: Evidence from fossil coral reefs and flank margin caves. Quaternary Science Reviews 14, 145–153.

Carew, J., Mylroie, J., 1985. Pleistocene and Holocene stratigraphy of San Salvador Island, Bahamas, with reference to marine and terrestrial lithofacies at French Bay, in: Curran, H. (Ed.), Orlando Annual Meeting Field Trip Guidebook, Geological Society of America. Bahamian Field Station, San Salvador Island Bahamas, pp. 11–61.

Carew, J.L., Mylroie, J.E., 2001. Quaternary Carbonate Eolianites of the Bahamas: Useful Analogues for the Interpretation of Ancient Rocks?, in: Abegg, F.E. (Rick), Loope, D.B., Harris, P.M. (Mitch) (Eds.), Modern and Ancient Carbonate Eolianites: Sedimentology, Sequence Stratigraphy, and Diagenesis. SEPM Society for Sedimentary Geology, p. 0. https://doi.org/10.2110/pec.01.71.0033

Carew, J.L., Mylroie, J.E., 1995. Depositional model and stratigraphy for the Quaternary geology of the Bahama Islands, in: Curran, H.A., White, B. (Eds.), Terrestrial and Shallow Marine Geology of the Bahamas and Bermuda. Geological Society of America, p. 0. https://doi.org/10.1130/0-8137-2300-0.5

Charney, J.G., 1975. Dynamics of deserts and drought in the Sahel. Q.J Royal Met. Soc. 101, 193–202. https://doi.org/10.1002/qj.49710142802

Chen, J., Curran, H., White, B., Wasserburg, G., 1991. Precise chronology of the last interglacial period: 234U-230Th data from fossil coral reefs in the Bahamas. Geological Society of America Bulletin 103, 82–97.

Clemmensen, L., Bjørnsen, M., Murray, A., Pedersen, K., 2007. Formation of aeolian dunes on Anholt, Denmark since AD 1560: A record of deforestation and increased storminess. Sedimentary Geology 199, 171–187. https://doi.org/10.1016/j.sedgeo.2007.01.025

Clemmensen, L., Pye, K., Urray, R., 2001. Sedimentology, stratigraphy and landscape evolution of a Holocene coastal dune system, Lodbjerg, NW Jutland, Denmark. Sedimentology 48, 3–27.

Collins, M., Knutti, R., Arblaster, J., Dufresne, J.-L., Fichefet, T., Gao, X., Jr, W.J.G., Johns, T., Krinner, G., Shongwe, M., Weaver, A.J., Wehner, M., 2013. Long-term Climate Change: Projections, Commitments and Irreversibility, in: Stocker, T.F., Qin, D., Plattner, G.-K., Tignor, M.M.B., Allen, S.K., Boschung, J., Nauels, A., Xia, Y., Bex, V., Midgley, P. (Eds.), Climate Change 2013: The Physical Science Basis. Contribution of Working Group I to the Fifth Assessment Report of the Intergovernmental Panel on Climate Change. Cambridge, United Kingdom and New York, NY, USA, p. 108.

Comas-Bru, L., Harrison, S.P., 2019. SISAL: Bringing Added Value to Speleothem Research. Quaternary 2, 7. https://doi.org/10.3390/quat2010007

Comas-Bru, L., Harrison, S.P., Werner, M., Rehfeld, K., Scroxton, N., Veiga-Pires, C., SISAL working group members, 2019. Evaluating model outputs using integrated global speleothem records of climate change since the last glacial. Clim. Past 15, 1557–1579. https://doi.org/10.5194/cp-15-1557-2019

Comas-Bru, L., Rehfeld, K., Roesch, C., Amirnezhad-Mozhdehi, S., Harrison, S.P., Atsawawaranunt, K., Ahmad, S.M., Brahim, Y.A., Baker, A., Bosomworth, M., Breitenbach, S.F.M., Burstyn, Y., Columbu, A., Deininger, M., Demény, A., Dixon, B., Fohlmeister, J., Hatvani, I.G., Hu, J., Kaushal, N., Kern, Z., Labuhn, I., Lechleitner, F.A., Lorrey, A., Martrat, B., Novello, V.F., Oster, J., Pérez-Mejías, C., Scholz, D., Scroxton, N., Sinha, N., Ward, B.M., Warken, S., Zhang, H., SISAL Working Group members, 2020. SISALv2: a comprehensive speleothem isotope database with multiple age–depth models. Earth Syst. Sci. Data 12, 2579–2606. https://doi.org/10.5194/essd-12-2579-2020

Cook, B.I., Cook, E.R., Smerdon, J.E., Seager, R., Williams, A.P., Coats, S., Stahle, D.W., Díaz, J.V., 2016. North American megadroughts in the Common Era: reconstructions and simulations. WIREs Clim Change 7, 411–432. https://doi.org/10.1002/wcc.394

Cook, E.R., 2004. Long-Term Aridity Changes in the Western United States. Science 306, 1015–1018. https://doi.org/10.1126/science.1102586

Coumou, D., Rahmstorf, S., 2012. A decade of weather extremes. Nature Climate Change 2, 491–496. https://doi.org/10.1038/nclimate1452

Courtillat, M., Hallenberger, M., Bassetti, M.-A., Aubert, D., Jeandel, C., Reuning, L., Korpanty, C., Moissette, P., Mounic, S., Saavedra-Pellitero, M., 2020. New Record of Dust Input and Provenance During Glacial Periods in Western Australia Shelf (IODP Expedition 356, Site U1461) from the Middle to Late Pleistocene. Atmosphere 11, 1251. https://doi.org/10.3390/atmos11111251

Current, S.E., Current, C., Strait, S., Passage, T., Current, E.G., 1996. The WOCE Indonesian Throughflow Repeat Hydrography Sections: I10 and IR6. International WOCE Newsletter 44.

da Silva, E.C., de Albuquerque, M.B., Azevedo Neto, A.D. de, Silva Junior, C.D. da, 2013. Drought and Its Consequences to Plants – From Individual to Ecosystem, in: Akinci, S. (Ed.), Responses of Organisms to Water Stress. InTech. https://doi.org/10.5772/53833

Darwin, C., 1851. Geological observations on coral reefs, volcanic islands, and on South America: Being the geology of the voyage of the Beagle, under the command of Captain Fitzroy, RN, during the years 1832 to 1836. Smith, Elder & Company.

Davis, B.A.S., Brewer, S., Stevenson, A.C., Guiot, J., 2003. The temperature of Europe during the Holocene reconstructed from pollen data. Quaternary Science Reviews 22, 1701–1716. https://doi.org/10.1016/S0277-3791(03)00173-2

Day, M.D., Catling, D.C., 2020. Potential aeolian deposition of intra-crater layering: A case study of Henry crater, Mars. GSA Bulletin 132, 608–616. https://doi.org/10.1130/B35230.1

De Ceunynck, R., 1985. The evolution of the coastal dunes in the western Belgian coastal plain. Eiszeitalter und Gegenwart 35, 33–41.

De Chiffre, L., 2001. Measurement of surface roughness. DTU, Institut for Produktion og Ledelse.

De Deckker, P., 2016. The Indo-Pacific Warm Pool: critical to world oceanography and world climate. Geosci. Lett. 3, 20. https://doi.org/10.1186/s40562-016-0054-3

De Deckker, P., Moros, M., Perner, K., Jansen, E., 2012. Influence of the tropics and southern westerlies on glacial interhemispheric asymmetry. Nature Geosci 5, 266–269. https://doi.org/10.1038/ngeo1431

de Freitas, H.A., Pessenda, L.C.R., Aravena, R., Gouveia, S.E.M., de Souza Ribeiro, A., Boulet, R., 2001. Late Quaternary Vegetation Dynamics in the Southern Amazon Basin Inferred from Carbon Isotopes in Soil Organic Matter. Quat. res. 55, 39–46. https://doi.org/10.1006/qres.2000.2192

de M. Luna, M., Parteli, E., Durán, O., Herrmann, H., 2011. Model for the genesis of coastal dune fields with vegetation. Geomorphology 129, 215–224. https://doi.org/10.1016/j.geomorph.2011.01.024

De Oliveira, P., Barreto, A., Suguio, K., 1999. Late Pleistocene/Holocene climatic and vegetational history of the Brazilian caatinga: the fossil dunes of the middle São Francisco River. Palaeogeography, Palaeoclimatology, Palaeoecology 152, 319–337. https://doi.org/10.1016/S0031-0182(99)00061-9

DeConto, R., Pollard, D., 2016. Contribution of Antarctica to past and future sea-level rise. Nature 531, 591–597. https://doi.org/10.1038/nature17145

Deininger, M., Ward, B.M., Novello, V.F., Cruz, F.W., 2019. Late Quaternary Variations in the South American Monsoon System as Inferred by Speleothems—New Perspectives using the SISAL Database. Quaternary 2, 6. https://doi.org/10.3390/quat2010006

Denton, G., Anderson, R., Toggweiler, J., Edwards, R., Schaefer, J., Putnam, A., 2010. The last glacial termination. Science 328, 1652–1656.

Di Nezio, P.N., Timmermann, A., Tierney, J.E., Jin, F., Otto-Bliesner, B., Rosenbloom, N., Mapes, B., Neale, R., Ivanovic, R.F., Montenegro, A., 2016. The climate response of the Indo-Pacific warm pool to glacial sea level. Paleoceanography 31, 866–894. https://doi.org/10.1002/2015PA002890

DiNezio, P.N., Tierney, J.E., Otto-Bliesner, B.L., Timmermann, A., Bhattacharya, T., Rosenbloom, N., Brady, E., 2018. Glacial changes in tropical climate amplified by the Indian Ocean. SCIENCE ADVANCES 12.

Dodd, J., Hunter, R., Merkley, P., 2001. Eolianite-bearing depositional cycles in the Ste. Genevieve Limestone of Indiana and Kentucky: evidence for Mississippian eustasy., in: Abegg, F., Harris, P., Loope, D. (Eds.), Modern and Ancient Carbonate Eolianites: Sedimentology, Sequence Stratigraphy, and Diagenesis, SEPM Special Publication. pp. 151–166.

Donat, M.G., Lowry, A.L., Alexander, L.V., O'Gorman, P.A., Maher, N., 2016. More extreme precipitation in the world's dry and wet regions. Nature Clim Change 6, 508–513. https://doi.org/10.1038/nclimate2941

Donnelly, C., Kraus, N., Larson, M., 2006. State of Knowledge on Measurement and Modeling of Coastal Overwash. Journal of Coastal Research 224, 965–991. https://doi.org/10.2112/04-0431.1

Donnelly, C., Sallenger, A.H., 2007. Characterisation and Modeling of Washover Fans, in: Coastal Sediments '07. Presented at the Sixth International Symposium on Coastal Engineering and Science of Coastal Sediment Process, American Society of Civil Engineers, New Orleans, Louisiana, United States, pp. 2061–2073. https://doi.org/10.1061/40926(239)162

Donovan, B., Tormey, B., 2015. What's past is prologue: Evidence of climate instability and intense storms during the Last Interglacial on Eleuthera Island, Bahamas., in: GSA Abstracts with Programs. Presented at the GSA Southeastern Section - 64th Annual Meeting, Chattanooga, p. 75.

Dunham, R., 1970. Keystone vugs in carbonate beach deposits. AAPG Bulletin 54, 845.

Dunn, R.J.H., Alexander, L.V., Donat, M.G., Zhang, X., Bador, M., Herold, N., Lippmann, T., Allan, R., Aguilar, E., Barry, A.A., Brunet, M., Caesar, J., Chagnaud, G., Cheng, V., Cinco, T., Durre, I., Guzman, R., Htay, T.M., Ibadullah, W.M.W., Ibrahim, M.K.I.B., Khoshkam, M., Kruger, A., Kubota, H., Leng, T.W., Lim, G., Li-Sha, L., Marengo, J., Mbatha, S., McGree, S., Menne, M., Skansi, M. de los M., Ngwenya, S., Nkrumah, F., Oonariya, C., Pabon-Caicedo, J.D., Panthou, G., Pham, C., Rahimzadeh, F., Ramos, A., Salgado, E., Salinger, J., Sané, Y., Sopaheluwakan, A., Srivastava, A., Sun, Y., Timbal, B., Trachow, N., Trewin, B., Schrier, G., Vazquez-Aguirre, J., Vasquez, R., Villarroel, C., Vincent, L., Vischel, T., Vose, R., Yussof, M.N.A.B.H., 2020. Development of an updated global land in-situ-based dataset of temperature and precipitation extremes: HadEX3. Journal of Geophysical Research: Atmospheres. https://doi.org/10.1029/2019JD032263

Durán, O., Herrmann, H., 2006. Vegetation Against Dune Mobility. Physical Review Letters 97. https://doi.org/10.1103/PhysRevLett.97.188001

Durán, O., Moore, L., 2013. Vegetation controls on the maximum size of coastal dunes. Proceedings of the National Academy of Sciences 110, 17217–17222.

Durán, O., Silva, M., Bezerra, L., Herrmann, H., Maia, L., 2008. Measurements and numerical simulations of the degree of activity and vegetation cover on parabolic dunes in northeastern Brazil. Geomorphology 102, 460–471. https://doi.org/10.1016/j.geomorph.2008.05.011

Dutkiewicz, A., Prescott, J., 1997. Thermoluminescence ages and palaeoclimate from the lake Malata-Lake Greenly Complex, Eyre Peninsula, South Australia. Quaternary Science Reviews 16, 367–385. https://doi.org/10.1016/S0277-3791(97)89532-7

Dutton, A., Carlson, A.E., Long, A.J., Milne, G.A., Clark, P.U., DeConto, R., Horton, B.P., Rahmstorf, S., Raymo, M.E., 2015. Sea-level rise due to polar ice-sheet mass loss during past warm periods. Science 349, aaa4019–aaa4019. https://doi.org/10.1126/science.aaa4019

Ellerton, D., Rittenour, T., Shulmeister, J., Gontz, A., Welsh, K.J., Patton, N., 2020. An 800 kyr record of dune emplacement in relationship to high sea level forcing, Cooloola Sand Mass, Queensland, Australia. Geomorphology 354, 106999. https://doi.org/10.1016/j.geomorph.2019.106999

Emery, K., 1945. Entrapment of air in beach sand. Journal of Sedimentary Research 15.

Engel, M., Kindler, P., Godefroid, F., 2015a. Interactive comment on “Ice melt, sea level rise and superstorms: evidence from paleoclimate data, climate modeling, and modern observations that 2◦ C global warming is highly dangerous” by J. Hansen et al. Atmospheric Chemistry and Physics Discussions 15, C6270–C6281.

Engel, M., Kindler, P., Godefroid, F., 2015b. Speculations on superstorms–Interactive comment on" Ice melt, sea level rise and superstorms: evidence from paleoclimate data, climate modeling, and modern observations that 2° C global warming is highly dangerous" by J. Hansen et al. Atmospheric Chemistry and Physics Discussions 15, C6270–C6281.

Engelmann, A., Neber, A., Frechen, M., Boenigk, W., Ronen, A., 2001. Luminescence chronology of Upper Pleistocene and Holocene aeolianites from Netanya South * Sharon Coastal Plain, Israel𝔊. Quaternary Science Reviews 6.

Fick, S.E., Hijmans, R.J., 2017. WorldClim 2: new 1-km spatial resolution climate surfaces for global land areas: NEW CLIMATE SURFACES FOR GLOBAL LAND AREAS. Int. J. Climatol 37, 4302–4315. https://doi.org/10.1002/joc.5086

Filion, L., 1987. Holocene development of parabolic dunes in the central St. Lawrence Lowland, Québec. Quaternary Research 28, 196–209.

Filion, L., Morisset, P., 1983. Eolian landforms along the eastern coast of Hudson Bay, Northern Québec. Nordicana 47, 73–94.

Folk, R., Ward, W., 1957. Brazos River bar [Texas]; a study in the significance of grain size parameters. Journal of Sedimentary Research 27, 3–26.

Forman, S., Goetz, A., Yuhas, R., 1992. Large-scale stabilized dunes on the High Plains of Colorado: Understanding the landscape response to Holocene climates with the aid of images from space. Geology 20, 145. https://doi.org/10.1130/0091-7613(1992)020<0145:LSSDOT>2.3.CO;2

Forman, S., Oglesby, R., Markgraf, V., Stafford, T., 1995. Paleoclimatic significance of Late Quaternary eolian deposition on the Piedmont and High Plains, Central United States. Global and Planetary Change 11, 35–55. https://doi.org/10.1016/0921-8181(94)00015-6

Forman, S., Pierson, J., 2003. Formation of linear and parabolic dunes on the eastern Snake River Plain, Idaho in the nineteenth century. Geomorphology 56, 189–200. https://doi.org/10.1016/S0169-555X(03)00078-3

Forman, S., Spaeth, M., Marín, L., Pierson, J., Gómez, J., Bunch, F., Valdez, A., 2006. Episodic Late Holocene dune movements on the sand-sheet area, Great Sand Dunes National Park and Preserve, San Luis Valley, Colorado, USA. Quaternary Research 66, 97–108. https://doi.org/10.1016/j.yqres.2005.12.003

Forman, S.L., Marin, L., Pierson, J., Gomez, J., Miller, G.H., Webb, R.S., 2005. Aeolian sand depositional records from western Nebraska: landscape response to droughts in the past 1500 years. The Holocene 15, 973–981. https://doi.org/10.1191/0959683605hl871ra

Forman, S.L., Oglesby, R., Webb, R.S., 2001. Temporal and spatial patterns of Holocene dune activity on the Great Plains of North America: megadroughts and climate links. Global and Planetary Change 29, 1–29. https://doi.org/10.1016/S0921-8181(00)00092-8

Frank, A., Kocurek, G., 1996. Toward a model for airflow on the lee side of aeolian dunes. Sedimentology 43, 451–458. https://doi.org/10.1046/j.1365-3091.1996.d01-20.x

Frébourg, G., 2010. Carbonate coastal dunes: potential reservoir rocks? University of Geneva.

Frébourg, G., Hasler, C.-A., Le Guern, P., Davaud, E., 2008. Facies characteristics and diversity in carbonate eolianites. Facies 54, 175–191. https://doi.org/10.1007/s10347-008-0134-8

Frechen, M., Dermann, B., Boenigk, W., Ronen, A., 2001. Luminescence chronology of aeolianites from the section at Givat Olga * Coastal Plain of Israel℃. Quaternary Science Reviews 5.

Friedman, G., Johnson, K., 1982. Exercises in sedimentology. John Wiley & Sons.

Friedman, G., Sanders, J., 1978. Principles of sedimentology. Wiley.

Fryberger, S., Dean, G., 1979. Dune forms and wind regime, in: A Study of Global Sand Seas. US Government Printing Office Washington, pp. 137–169.

Fryberger, S., Schenk, C., 1988. Pin stripe lamination: a distinctive feature of modern and ancient eolian sediments. Sedimentary Geology 55, 1–15.

Fryberger, S.G., Al-Sari, A.M., Clisham, T.J., 1983. Eolian Dune, Interdune, Sand Sheet, and Siliciclastic Sabkha Sediments of an Offshore Prograding Sand Sea, Dhahran Area, Saudi Arabia1. AAPG Bulletin 67, 280–312. https://doi.org/10.1306/03B5ACFF-16D1-11D7-8645000102C1865D

Fu, Q., Feng, S., 2014. Responses of terrestrial aridity to global warming. J. Geophys. Res. Atmos. 119, 7863–7875. https://doi.org/10.1002/2014JD021608

Fuhrmann, F., Diensberg, B., Gong, X., Lohmann, G., Sirocko, F., 2019. Global aridity synthesis for the last 60 000 years (preprint). Teleconnections/Terrestrial Archives/Millenial/D-O. https://doi.org/10.5194/cp-2019-108

Fumanal, M., 1995. Pleistocene dune systems in the Valencian Betic cliffs (Spain). INQUA Subcomission on Mediterranean and Black Sea Shorelines Newsletter 17, 32–38.

Gao, J., Kennedy, D.M., Konlechner, T.M., 2020. Coastal dune mobility over the past century: A global review. Progress in Physical Geography: Earth and Environment 44, 814–836. https://doi.org/10.1177/0309133320919612

García-Romero, L., Hesp, P., Peña-Alonso, C., Miot da Silva, G., Hernández-Calvento, L., 2019. Climate as a control on foredune mode in Southern Australia. Science of The Total Environment 694, 133768. https://doi.org/10.1016/j.scitotenv.2019.133768

Gares, P., Nordstrom, K., Psuty, N., 1979. Coastal dunes: their function, delineation, and management. Center fro Coastal and Environmental Studies, Rutgers - The State University of New Jersey.

Gascoyne, M., Benjamin, G., Schwarcz, H., Ford, D., 1979. Sea-Level Lowering During the Illinoian Glaciation: Evidence from a Bahama “Blue Hole.” Science 205, 806–808. https://doi.org/10.1126/science.205.4408.806

Gastineau, G., Li, L., Le Treut, H., 2009. The Hadley and Walker Circulation Changes in Global Warming Conditions Described by Idealized Atmospheric Simulations. Journal of Climate 22, 3993–4013. https://doi.org/10.1175/2009JCLI2794.1

Gibson, K.A., Peterson, L.C., 2014. A 0.6 million year record of millennial-scale climate variability in the tropics. Geophysical Research Letters 41, 969–975. https://doi.org/10.1002/2013GL058846

Gladstone, R.M., 2005. Mid-Holocene NAO: A PMIP2 model intercomparison. Geophysical Research Letters 32. https://doi.org/10.1029/2005GL023596

Glennie, K., 1970. Desert sedimentary environments, Developments in Sedimentology. Elsevier, Amsterdam.

Godefroid, F., 2012. Géologie de Mayaguana, SE de l’archipel des Bahamas. University of Geneva, Geneva.

Godfrey, J.S., Ridgway, K.R., 1985. The large-scale environment of the poleward-flowing Leeuwin Current, Western Australia: longshore steric height gradients, wind stresses and geostrophic flow. Journal of Physical Oceanography 15, 481–495.

Gordon, A.L., Fine, R.A., 1996. Pathways of water between the Pacific and Indian oceans in the Indonesian seas. Nature 379, 146–149. https://doi.org/10.1038/379146a0

Goudie, A., 2011. Parabolic Dunes: Distribution, Form, Morphology and Change 7.

Goudie, A., Sperling, C.H.B., 1977. Long Distance Transport of Foraminiferal Tests by Wind in the Thar Desert, Northwest India. SEPM JSR Vol. 47. https://doi.org/10.1306/212F71FD-2B24-11D7-8648000102C1865D

Grange, S., 2014. Averaging wind speeds and directions.

Greeley, R., Blumberg, D.G., McHone, J.F., Dobrovolskis, A., Iversen, J.D., Lancaster, N., Rasmussen, K.R., Wall, S.D., White, B.R., 1997. Applications of spaceborne radar laboratory data to the study of aeolian processes. Journal of Geophysical Research: Planets 102, 10971–10983. https://doi.org/10.1029/97JE00518

Greve, P., Roderick, M.L., Ukkola, A.M., Wada, Y., 2019. The aridity Index under global warming. Environmental Research Letters 14, 124006. https://doi.org/10.1088/1748-9326/ab5046

Guo, L., Xiong, S., Dong, X., Ding, Z., Yang, P., Zhao, H., Wu, J., Ye, W., Jin, G., Wu, W., Zheng, L., 2018. Linkage between C4 vegetation expansion and dune stabilization in the deserts of NE China during the late Quaternary. Quaternary International. https://doi.org/10.1016/j.quaint.2018.10.026

Gusiakov, V., Abbott, D., Bryant, E.A., Masse, W., Breger, D., 2009. Mega Tsunami of the World Oceans: Chevron Dune Formation, Micro-Ejecta, and Rapid Climate Change as the Evidence of Recent Oceanic Bolide Impacts, in: Beer, T. (Ed.), Geophysical Hazards. Springer Netherlands, Dordrecht, pp. 197–227. https://doi.org/10.1007/978-90-481-3236-2_13

Hack, J., 1941. Dunes of the Western Navajo Country. Geographical Review 31, 240. https://doi.org/10.2307/210206

Halfen, A., Fredlund, G., Mahan, S., 2010. Holocene stratigraphy and chronology of the Casper Dune Field, Casper, Wyoming, USA. The Holocene 20, 773–783. https://doi.org/10.1177/0959683610362812

Halfen, A., Johnson, W., Hanson, P., Woodburn, T., Young, A., Ludvigson, G., 2012. Activation history of the Hutchinson dunes in east-central Kansas, USA during the past 2200years. Aeolian Research 5, 9–20. https://doi.org/10.1016/j.aeolia.2012.02.001

Halfen, A.F., Johnson, W.C., 2013. A review of Great Plains dune field chronologies. Aeolian Research 10, 135–160. https://doi.org/10.1016/j.aeolia.2013.03.001

Halfen, A.F., Lancaster, N., Wolfe, S., 2016. Interpretations and common challenges of aeolian records from North American dune fields. Quaternary International 410, 75–95. https://doi.org/10.1016/j.quaint.2015.03.003

Hall, S.A., Goble, R., 2016. Permian Basin Research Design 2016-2026 Volume II: Quaternary and Archaeological Geology of Southeastern New Mexico, in: Railey, J.A. (Ed.), Permian Basin Research Design 2016-2026, SWCA Environmental Consultants. SWCA Environmental Consultants-Albuquerque, Albuquerque, New Mexico, p. 185.

Hanoch, G., Yizhaq, H., Ashkenazy, Y., 2018. Modeling the bistability of barchan and parabolic dunes. Aeolian Research 35, 9–18. https://doi.org/10.1016/j.aeolia.2018.07.003

Hansen, E., DeVries-Zimmerman, S., van Dijk, D., Yurk, B., 2009. Patterns of wind flow and aeolian deposition on a parabolic dune on the southeastern shore of Lake Michigan. Geomorphology 105, 147–157. https://doi.org/10.1016/j.geomorph.2007.12.012

Hansen, E., Fisher, T., Arbogast, A., Bateman, M., 2010. Geomorphic history of low-perched, transgressive dune complexes along the southeastern shore of Lake Michigan. Aeolian Research 1, 111–127. https://doi.org/10.1016/j.aeolia.2009.08.001

Hansen, J., Kharecha, P., Sato, M., Masson-Delmotte, V., Ackerman, F., Beerling, D., Hearty, P., Hoegh-Guldberg, O., Hsu, S.-L., Parmesan, C., Rockstrom, J., Rohling, E., Sachs, J., Smith, P., Steffen, K., Van Susteren, L., von Schuckmann, K., Zachos, J., 2013. Assessing “Dangerous Climate Change”: Required Reduction of Carbon Emissions to Protect Young People, Future Generations and Nature. PLoS ONE 8, e81648. https://doi.org/10.1371/journal.pone.0081648

Hansen, J., Sato, M., Hearty, P., Ruedy, R., Kelley, M., Masson-Delmotte, V., Russell, G., Tselioudis, G., Cao, J., Rignot, E., Velicogna, I., Kandiano, E., von Schuckmann, K., Kharecha, P., Legrande, A., Bauer, M., Lo, K.-W., 2015. Ice melt, sea level rise and superstorms: evidence from paleoclimate data, climate modeling, and modern observations that 2 °C global warming is highly dangerous. Atmospheric Chemistry and Physics Discussions 15, 20059–20179. https://doi.org/10.5194/acpd-15-20059-2015

Hansen, J., Sato, M., Hearty, P., Ruedy, R., Kelley, M., Masson-Delmotte, V., Russell, G., Tselioudis, G., Cao, J., Rignot, E., Velicogna, I., Tormey, B., Donovan, B., Kandiano, E., von Schuckmann, K., Kharecha, P., Legrande, A.N., Bauer, M., Lo, K.-W., 2020. Ice Melt, Sea Level Rise and Superstorms: Evidence from Paleoclimate Data, Climate Modeling, and Modern Observations Implies that 2°C Global Warming Above the Preindustrial Level Would Be Dangerous, in: Earth and Its Atmosphere. Vide Leaf, Hyderabad. https://doi.org/10.37247/EA.1.2020.13

Hansen, J., Sato, M., Hearty, P., Ruedy, R., Kelley, M., Masson-Delmotte, V., Russell, G., Tselioudis, G., Cao, J., Rignot, E., Velicogna, I., Tormey, B., Donovan, B., Kandiano, E., von Schuckmann, K., Kharecha, P., Legrande, A.N., Bauer, M., Lo, K.-W., 2016. Ice melt, sea level rise and superstorms: evidence from paleoclimate data, climate modeling, and modern observations that 2 °C global warming could be dangerous. Atmospheric Chemistry and Physics 16, 3761–3812. https://doi.org/10.5194/acp-16-3761-2016

Harrison, S.P., Kutzbach, J.E., Liu, Z., Bartlein, P.J., Otto-Bliesner, B., Muhs, D., Prentice, I.C., Thompson, R.S., 2003. Mid-Holocene climates of the Americas: a dynamical response to changed seasonality. Climate Dynamics 20, 663–688. https://doi.org/10.1007/s00382-002-0300-6

Hasler, C.-A., Simpson, G., Kindler, P., 2010. Platform margin collapse simulation: The case of the North Eleuthera massive boulders, in: Abstracts and Program. Presented at the 15th Symposium on the Geology of the Bahamas and Other Carbonate Regions, San Salvador Island, Bahamas, Gerace Research Center, pp. 22–23.

Hays, J., Imbrie, J., Shackleton, N., 1976. Variations in the Earth’s Orbit: Pacemaker of the Ice Ages. Science 194, 13.

Hearty, P., 2010. Chronostratigraphy and morphological changes in Cerion land snail shells over the past 130ka on Long Island, Bahamas. Quaternary Geochronology 5, 50–64. https://doi.org/10.1016/j.quageo.2009.09.005

Hearty, P., 1997. Boulder Deposits from Large Waves during the Last Interglaciation on North Eleuthera Island, Bahamas. Quaternary Research 48, 326–338. https://doi.org/10.1006/qres.1997.1926

Hearty, P., Hollin, J., Neumann, A., O'Leary, M., McCulloch, M., 2007. Global sea-level fluctuations during the Last Interglaciation (MIS 5e). Quaternary Science Reviews 26, 2090–2112. https://doi.org/10.1016/j.quascirev.2007.06.019

Hearty, P., Kaufman, D., 2009. A Cerion-based chronostratigraphy and age model from the central Bahama Islands: Amino acid racemization and 14C in land snails and sediments. Quaternary Geochronology 4, 148–159. https://doi.org/10.1016/j.quageo.2008.08.002

Hearty, P., Kaufman, D., 2000. Whole-Rock Aminostratigraphy and Quaternary Sea-Level History of the Bahamas. Quaternary Research 54, 163–173. https://doi.org/10.1006/qres.2000.2164

Hearty, P., Kindler, P., 1993. New perspectives on Bahamian geology: San Salvador Island, Bahamas. Journal of Coastal Research 577–594.

Hearty, P., Neumann, A., Kaufman, D., 1998. Chevron ridges and runup deposits in the Bahamas from storms late in oxygen-isotope substage 5e. Quaternary Research 50, 309–322.

Hearty, P., O'Leary, M., 2008. Carbonate eolianites, quartz sands, and Quaternary sea-level cycles, Western Australia: A chronostratigraphic approach. Quaternary Geochronology 3, 26–55. https://doi.org/10.1016/j.quageo.2007.10.001

Hearty, P., Schellenberg, S., 2008. Integrated Late Quaternary chronostratigraphy for San Salvador Island, Bahamas: Patterns and trends of morphological change in the land snail Cerion. Palaeogeography, Palaeoclimatology, Palaeoecology 267, 41–58. https://doi.org/10.1016/j.palaeo.2008.06.003

Hearty, P., Tormey, B., 2018a. Listen to the whisper of the rocks, telling their ancient story. Proceedings of the National Academy of Sciences 115, E2902–E2903. https://doi.org/10.1073/pnas.1721253115

Hearty, P., Tormey, B., 2018b. Discussion of: Mylroie, JE, 2018. Superstorms: Comments on Bahamian Fenestrae and Boulder Evidence from the Last Interglacial. Journal of Coastal Research, 34 (6), 1471–1483. Journal of Coastal Research 34, 1503–1511. https://doi.org/10.2112/JCOASTRES-D-18A-00003.1

Hearty, P., Tormey, B., 2017. Sea-level change and superstorms; geologic evidence from the last interglacial (MIS 5e) in the Bahamas and Bermuda offers ominous prospects for a warming Earth. Marine Geology 390, 347–365. https://doi.org/10.1016/j.margeo.2017.05.009

Hearty, P., Tormey, B., Donovan, B., Tselioudis, G., 2015. Reply to Engel, Kindler, and Godefroid's comment on "Ice melt, sea level rise and superstorms: evidence from paleoclimate data, climate modeling, and modern observations that 2°C global warming is highly dangerous" by J. Hansen et al.

Hearty, P., Tormey, B., Neumann, A., 2002. Discussion of "Palaeoclimatic significance of co-occurring wind-and water-induced sedimentary structures in the last-interglacial coastal deposits from Bermuda and the Bahamas"(Kindler and Strasser, 2000, Sedimentary Geology, 131, 1–7). Sedimentary Geology 147, 429–435.

Hearty, P.J., Hollin, J.T., Neumann, A.C., O'Leary, M.J., McCulloch, M., 2007. Global sea-level fluctuations during the Last Interglaciation (MIS 5e). Quaternary Science Reviews 26, 2090–2112. https://doi.org/10.1016/j.quascirev.2007.06.019

Hearty, P.J., Neumann, A.C., 2001. Rapid sea level and climate change at the close of the Last Interglaciation (MIS 5e): evidence from the Bahama Islands. Quaternary Science Reviews 20, 1881–1895. https://doi.org/10.1016/S0277-3791(01)00021-X

Hesp, P., 2013. Conceptual models of the evolution of transgressive dune field systems. Geomorphology 199, 138–149. https://doi.org/10.1016/j.geomorph.2013.05.014

Hesp, P., 2011. Dune Coasts, in: Wolanski, E., McLusky, D. (Eds.), Treatise on Estuarine and Coastal Science. Elsevier, pp. 193–221. https://doi.org/10.1016/B978-0-12-374711-2.00310-7

Hesp, P., 2002. Foredunes and blowouts: initiation, geomorphology and dynamics. Geomorphology 48, 245–268. https://doi.org/10.1016/S0169-555X(02)00184-8

Hesp, P., 2001. The Manawatu dunefield: environmental change and human impacts. New Zealand Geographer 57, 33–40.

Hesp, P., Chape, S., 1984. 1:3 million map of the Coastal Environment of Western Australia.

Hesp, P., Schmutz, P., Martinez, M., Driskell, L., Orgera, R., Renken, K., Revelo, N., Orocio, O., 2010. The effect on coastal vegetation of trampling on a parabolic dune. Aeolian Research 2, 105–111. https://doi.org/10.1016/j.aeolia.2010.03.001

Hesp, P., Walker, I., 2013. Coastal dunes, in: Treatise on Geomorphology.

Hesse, P.P., 2016. How do longitudinal dunes respond to climate forcing? Insights from 25 years of luminescence dating of the Australian desert dunefields. Quaternary International 410, 11–29. https://doi.org/10.1016/j.quaint.2014.02.020

Hesse, P.P., Telfer, M.W., Farebrother, W., 2017. Complexity confers stability: Climate variability, vegetation response and sand transport on longitudinal sand dunes in Australia's deserts. Aeolian Research 17.

Hesse, P.P., Williams, R., Ralph, T.J., Fryirs, K.A., Larkin, Z.T., Westaway, K.E., Farebrother, W., 2018. Palaeohydrology of lowland rivers in the Murray-Darling Basin, Australia. Quaternary Science Reviews 200, 85–105. https://doi.org/10.1016/j.quascirev.2018.09.035

Higgins, M.D., 2000. Measurement of crystal size distributions. American Mineralogist 85, 1105–1116. https://doi.org/10.2138/am-2000-8-901

Hoffman, J.S., Clark, P.U., Parnell, A.C., He, F., 2017. Regional and global sea-surface temperatures during the last interglaciation. Science 355, 276–279. https://doi.org/10.1126/science.aai8464

Hollin, J., 1965. Wilson's Theory of Ice Ages. Nature 208, 12–16. https://doi.org/10.1038/208012a0

Hollin, J., Smith, F., Renouf, J., Jenkins, D., 1993. Sea-cave temperature measurements and amino acid geochronology of British Late Pleistocene Sea stands. Journal of Quaternary Science 8, 359–364. https://doi.org/10.1002/jqs.3390080407

Hoogakker, B.A.A., Smith, R.S., Singarayer, J.S., Marchant, R., Prentice, I.C., Allen, J.R.M., Anderson, R.S., Bhagwat, S.A., Behling, H., Borisova, O., Bush, M., Correa-Metrio, A., de Vernal, A., Finch, J.M., Fréchette, B., Lozano-Garcia, S., Gosling, W.D., Granoszewski, W., Grimm, E.C., Grüger, E., Hanselman, J., Harrison, S.P., Hill, T.R., Huntley, B., Jiménez-Moreno, G., Kershaw, P., Ledru, M.-P., Magri, D., McKenzie, M., Müller, U., Nakagawa, T., Novenko, E., Penny, D., Sadori, L., Scott, L., Stevenson, J., Valdes, P.J., Vandergoes, M., Velichko, A., Whitlock, C., Tzedakis, C., 2016. Terrestrial biosphere changes over the last 120 kyr. Climate of the Past 12, 51–73. https://doi.org/10.5194/cp-12-51-2016

Hoover, R., Gaylord, D., Cooper, C., 2018. Dune mobility in the St. Anthony Dune Field, Idaho, USA: Effects of meteorological variables and lag time. Geomorphology 309, 29–37. https://doi.org/10.1016/j.geomorph.2018.02.018

Hope, G.S., 1994. Quaternary vegetation, in: Hill, R.S., Woinarski, J.C.Z., Williams, J. (Eds.), History of the Australian Vegetation: Cretaceous to Recent. pp. 368–389.

Huang, J., Ji, M., Xie, Y., Wang, S., He, Y., Ran, J., 2016. Global semi-arid climate change over last 60 years. Clim Dyn 46, 1131–1150. https://doi.org/10.1007/s00382-015-2636-8

Huang, J., Li, Y., Fu, C., Chen, F., Fu, Q., Dai, A., Shinoda, M., Ma, Z., Guo, W., Li, Z., Zhang, L., Liu, Y., Yu, H., He, Y., Xie, Y., Guan, X., Ji, M., Lin, L., Wang, S., Yan, H., Wang, G., 2017. Dryland climate change: Recent progress and challenges. Reviews of Geophysics 55, 719–778. https://doi.org/10.1002/2016RG000550

Huang, Jianping, Xie, Y., Guan, X., Li, D., Ji, F., 2017. The dynamics of the warming hiatus over the Northern Hemisphere. Clim Dyn 48, 429–446. https://doi.org/10.1007/s00382-016-3085-8

Hugenholtz, C., 2010. Topographic changes of a supply-limited inland parabolic sand dune during the incipient phase of stabilization. Earth Surface Processes and Landforms 35, 1674–1681. https://doi.org/10.1002/esp.2053

Hunter, R., 1977. Basic types of stratification in small eolian dunes. Sedimentology 24, 361–387.

Hunter, R.E., 1980. Quasi-planar adhesion stratification; an eolian structure formed in wet sand. Journal of Sedimentary Research 50, 263–266. https://doi.org/10.1306/212F79C8-2B24-11D7-8648000102C1865D

IPCC, 2013. Climate change 2013: the physical science basis. Contribution to the Fifth Assessment Report of the Intergovernmental Panel on Climate Change, Cambridge University Press. ed.

IPCC, D., 2014. Summary for Policymakers. Cambridge University Press, Cambridge, United Kingdom and New York, NY, USA.

Itzkin, M., Moore, L.J., Ruggiero, P., Hacker, S.D., Biel, R.G., 2020. The Influence of Dune Aspect Ratio, Beach Width and Storm Characteristics on Dune Erosion for Managed and Unmanaged Beaches. Earth Surface Dynamics Discussions 2020, 1–23. https://doi.org/10.5194/esurf-2020-79

Ivory, S.J., Lézine, A.-M., Vincens, A., Cohen, A.S., 2012. Effect of aridity and rainfall seasonality on vegetation in the southern tropics of East Africa during the Pleistocene/Holocene transition. Quaternary Research 77, 77–86. https://doi.org/10.1016/j.yqres.2011.11.005

Jackson, D.W.T., Costas, S., González-Villanueva, R., Cooper, A., 2019. A global ‘greening’ of coastal dunes: An integrated consequence of climate change? Global and Planetary Change 182, 103026. https://doi.org/10.1016/j.gloplacha.2019.103026

Jackson, P., 1975. A theory for flow over escarpments. Presented at the Fourth International Conf. on Wind Effects on Buildings and Structures, Heathrow, UK, p. 40.

James, N.P., Collins, L.B., Bone, Y., Hallock, P., 1999. Subtropical carbonates in a temperate realm: modern sediments on the southwest Australian shelf. Journal of Sedimentary Research 69, 1297–1321.

Jamison-Todd, S., Stein, N., Overeem, I., Khalid, A., Trower, E.J., 2020. Hurricane Deposits on Carbonate Platforms: A Case Study of Hurricane Irma Deposits on Little Ambergris Cay, Turks and Caicos Islands. Journal of Geophysical Research: Earth Surface 125. https://doi.org/10.1029/2020JF005597

Jansen, E., Overpeck, J., Briffa, K.R., Duplessy, J.-C., Joos, F., Masson-Delmotte, V., Olago, D., Otto-Bliesner, B., Peltier, W.R., Rahmstorf, S., Ramesh, R., Raynaud, D., Rind, D., Solomina, O., Villalba, R., Zhang, D., 2007. Palaeoclimate, in: Climate Change 2007: The Physical Science Basis. Contribution of Working Group I to the Fourth Assessment Report of the Intergovernmental Panel on Climate Change. Cambridge University Press, Cambridge, United Kingdom and New York, NY, USA, pp. 433–497.

Jennings, J., 1967. Cliff-top dunes. Australian Geographical Studies 5, 40–49.

Jennings, J., 1957. On the Orientation of Parabolic or U-Dunes. The Geographical Journal 123, 474. https://doi.org/10.2307/1790349

Jerolmack, D.J., Ewing, R.C., Falcini, F., Martin, R.L., Masteller, C., Phillips, C., Reitz, M.D., Buynevich, I., 2012. Internal boundary layer model for the evolution of desert dune fields. Nature Geoscience 5, 206–209. https://doi.org/10.1038/ngeo1381

Ji, M., Huang, J., Xie, Y., Liu, J., 2015. Comparison of dryland climate change in observations and CMIP5 simulations. Adv. Atmos. Sci. 32, 1565–1574. https://doi.org/10.1007/s00376-015-4267-8

Jiang, X., Pan, Z., Fu, Q., 2001. Regularity of paleowind directions of the Early Cretaceous Desert in Ordos Basin and climatic significance. Sci. China Ser. D-Earth Sci. 44, 24–33. https://doi.org/10.1007/BF02906882

Jiang, X., Pan, Z., Xu, J., Li, X., Xie, G., Xiao, Z., 2008. Late Cretaceous aeolian dunes and reconstruction of palaeo-wind belts of the Xinjiang Basin, Jiangxi Province, China. Palaeogeography, Palaeoclimatology, Palaeoecology 257, 58–66. https://doi.org/10.1016/j.palaeo.2007.09.012

Johnson, D., 1968. Quaternary coastal eolianites: do they have ancient analogues? Presented at the GSA Annual Meeting, Mexico City, pp. 150–151.

Jones, F.H., Scherer, C.M. dos S., Kuchle, J., 2016. Facies architecture and stratigraphic evolution of aeolian dune and interdune deposits, Permian Caldeirão Member (Santa Brígida Formation), Brazil. Sedimentary Geology 337, 133–150. https://doi.org/10.1016/j.sedgeo.2016.03.018

Jorgensen, D., 2012. Quaternary stratigraphy, palaeowinds and palaeoenvironments of carbonate aeolianite on the Garden Island Ridge and in the Naturaliste-Leeuwin region, southwest Western Australia (PhD Thesis). James Cook University, Townsville.

Kar, A., 1993. Aeolian processes and bedforms in the Thar Desert. Journal of Arid Environments 25, 83–96. https://doi.org/10.1006/jare.1993.1044

Kaufman, D., Ager, T., Anderson, N., Anderson, P.M., Andrews, J.T., Bartlein, P.J., Brubaker, L.B., Coats, L.L., Cwynar, L.C., Duvall, M.L., Dyke, A.S., Edwards, M.E., Eisner, W.R., Gajewski, K., Geirsdóttir, A., Hu, F.S., Jennings, A.E., Kaplan, M.R., Kerwin, M.W., Lozhkin, A.V., MacDonald, G., Miller, G.H., Mock, C.J., Oswald, W., Otto-Bliesner, B., Porinchu, D., Rühland, K., Smol, J.P., Steig, E.J., Wolfe, B.B., 2004. Holocene thermal maximum in the western Arctic (0–180°W). Quaternary Science Reviews 23, 529–560. https://doi.org/10.1016/j.quascirev.2003.09.007

Kaufman, D., Manley, W., 1998. A new procedure for determining DL amino acid ratios in fossils using reverse phase liquid chromatography. Quaternary Science Reviews 17, 987–1000.

Kaufman, D., McKay, N., Routson, C., Erb, M., Davis, B., Heiri, O., Jaccard, S., Tierney, J., Dätwyler, C., Axford, Y., Brussel, T., Cartapanis, O., Chase, B., Dawson, A., de Vernal, A., Engels, S., Jonkers, L., Marsicek, J., Moffa-Sánchez, P., Morrill, C., Orsi, A., Rehfeld, K., Saunders, K., Sommer, P.S., Thomas, E., Tonello, M., Tóth, M., Vachula, R., Andreev, A., Bertrand, S., Biskaborn, B., Bringué, M., Brooks, S., Caniupán, M., Chevalier, M., Cwynar, L., Emile-Geay, J., Fegyveresi, J., Feurdean, A., Finsinger, W., Fortin, M.-C., Foster, L., Fox, M., Gajewski, K., Grosjean, M., Hausmann, S., Heinrichs, M., Holmes, N., Ilyashuk, B., Ilyashuk, E., Juggins, S., Khider, D., Koinig, K., Langdon, P., Larocque-Tobler, I., Li, J., Lotter, A., Luoto, T., Mackay, A., Magyari, E., Malevich, S., Mark, B., Massaferro, J., Montade, V., Nazarova, L., Novenko, E., Pařil, P., Pearson, E., Peros, M., Pienitz, R., Płóciennik, M., Porinchu, D., Potito, A., Rees, A., Reinemann, S., Roberts, S., Rolland, N., Salonen, S., Self, A., Seppä, H., Shala, S., St-Jacques, J.-M., Stenni, B., Syrykh, L., Tarrats, P., Taylor, K., van den Bos, V., Velle, G., Wahl, E., Walker, I., Wilmshurst, J., Zhang, E., Zhilich, S., 2020. A global database of Holocene paleotemperature records. Scientific Data 7. https://doi.org/10.1038/s41597-020-0445-3

Kaushal, N., Breitenbach, S.F.M., Lechleitner, F.A., Sinha, A., Tewari, V.C., Ahmad, S.M., Berkelhammer, M., Band, S., Yadava, M., Ramesh, R., Henderson, G.M., 2018. The Indian Summer Monsoon from a Speleothem δ18O Perspective—A Review. Quaternary 1, 29. https://doi.org/10.3390/quat1030029

Kelletat, D., Scheffers, A., 2003. Chevron-shaped accumulations along the coastlines of Australia as potential tsunami evidences. Science of Tsunami Hazards 21, 174–188.

Kelletat, D., Scheffers, A., Scheffers, S., 2004. Holocene tsunami deposits on the Bahaman Islands of Long Island and Eleuthera. Zeitschrift für Geomorphologie 48, 519–540.

Kerans, C., Zahm, C., Bachtel, S., Hearty, P., Cheng, H., 2019. Anatomy of a late Quaternary carbonate island: Constraints on timing and magnitude of sea-level fluctuations, West Caicos, Turks and Caicos Islands, BWI. Quaternary Science Reviews 205, 193–223. https://doi.org/10.1016/j.quascirev.2018.12.010

Kilibarda, Z., Blockland, J., 2011. Morphology and origin of the Fair Oaks Dunes in NW Indiana, USA. Geomorphology 125, 305–318. https://doi.org/10.1016/j.geomorph.2010.10.011

Kilibarda, Z., Kilibarda, V., 2016. Seasonal geomorphic processes and rates of sand movement at Mount Baldy dune in Indiana, USA. Aeolian Research 23, 103–114. https://doi.org/10.1016/j.aeolia.2016.10.004

Kilibarda, Z., Loope, D.B., 1997. Jurassic aeolian oolite on a palaeohigh in the Sundance Sea, Bighorn Basin, Wyoming. Sedimentology 44, 391–404. https://doi.org/10.1111/j.1365-3091.1997.tb01531.x

Kindler, P., 1991. Keystone vugs in coastal dunes: an example from the Pleistocene of Eleuthera, Bahamas. Presented at the Proceedings of the fifth symposium on the geology of the Bahamas., Bahamian Field Station, San Salvador, Bahamas, pp. 117–123.

Kindler, P., Davaud, E., 2001. Recognizing Eolianites in Thin Section. Review and Case Study—The Lower Cretaceous Chambotte Formation, Salève Chain, Southeastern France, in: Modern and Ancient Carbonate Eolianites: Sedimentology, Sequence Stratigraphy, and Diagenesis, SEPM Society for Sedimentary Geology.

Kindler, P., Godefroid, F., Chiaradia, M., Ehlert, C., Eisenhauer, A., Frank, M., Hasler, C.-A., Samankassou, E., 2011. Discovery of Miocene to early Pleistocene deposits on Mayaguana, Bahamas: Evidence for recent active tectonism on the North American margin. Geology 39, 523–526.

Kindler, P., Godefroid, F., Hasler, C.-A., Samankassou, E., 2009. Fenestral porosity in carbonate eolianites: a biological origin? New evidence from the Pleistocene of Providenciales Island (Caicos Platform), in: Pascucci, V., Andreucci, S. (Eds.), Abstract Book of the 27th IAS Meeting of Sedimentology, Alghero, Italy. p. 231.

Kindler, P., Hearty, P., 1996. Carbonate petrography as an indicator of climate and sea-level changes: new data from Bahamian Quaternary units. Sedimentology 43, 381–399. https://doi.org/10.1046/j.1365-3091.1996.d01-11.x

Kindler, P., Mazzolini, D., 2001. Sedimentology and petrography of dredged carbonate sands from Stocking Island (Bahamas). Implications for meteoric diagenesis and aeolianite formation. Palaeogeography, Palaeoclimatology, Palaeoecology 175, 369–379. https://doi.org/10.1016/S0031-0182(01)00380-7

Kindler, P., Mylroie, J., Curran, H., Carew, J., Gamble, D., Rothfus, T., Savarese, M., Sealey, N., 2010. Geology of Central Eleuthera, Bahamas: a field trip guide.

Kindler, P., Strasser, A., 2002. Palaeoclimatic significance of co-occurring wind- and water-induced sedimentary structures in last-interglacial coastal deposits from Bermuda and the Bahamas: response to Hearty et al.'s comment. Sedimentary Geology 147, 437–443. https://doi.org/10.1016/S0037-0738(01)00099-9

Kindler, P., Strasser, A., 2000. Palaeoclimatic significance of co-occurring wind-and water-induced sedimentary structures in the last-interglacial coastal deposits from Bermuda and the Bahamas. Sedimentary Geology 131, 1–7.

Kitoh, A., Murakami, S., 2002. Tropical Pacific climate at the mid-Holocene and the Last Glacial Maximum simulated by a coupled ocean-atmosphere general circulation model: CGCM SIMULATION OF 6 AND 21 KA CLIMATE. Paleoceanography 17, 19-1-19–13. https://doi.org/10.1029/2001PA000724

Knight, M., Thomas, D.S.G., Wiggs, G.F.S., 2004. Challenges of calculating dunefield mobility over the 21st century. Geomorphology 59, 197–213.

Kocurek, G., 1996. Desert aeolian systems, in: Reading, H.G. (Ed.), Sedimentary Environments: Processes, Facies and Stratigraphy. Blackwell Science, Oxford, pp. 125–153.

Kocurek, G., 1991. Interpretation of ancient eolian sand dunes. Annual review of Earth and planetary sciences 19, 43–75.

Kocurek, G., 1988. First-order and super bounding surfaces in eolian sequences—Bounding surfaces revisited. Sedimentary Geology 56, 193–206. https://doi.org/10.1016/0037-0738(88)90054-1

Kocurek, G., 1981. Significance of interdune deposits and bounding surfaces in aeolian dune sands. Sedimentology 28, 753–780.

Kocurek, G., Crabaugh, M., Loope, D.B., 1993. Significance of thin sets of eolian cross-strata; discussion and reply. Journal of Sedimentary Research 63, 1165–1171. https://doi.org/10.1306/D4267CDF-2B26-11D7-8648000102C1865D

Kocurek, G., Dott, R., 1981. Distinctions and uses of stratification types in the interpretation of eolian sand. Journal of Sedimentary Research 51.

Kocurek, G., Fielder, G., 1982. Adhesion structures. Journal of Sedimentary Research 52, 1229–1241. https://doi.org/10.1306/212F8102-2B24-11D7-8648000102C1865D

Kocurek, G., Havholm, K., 1993. Eolian Sequence Stratigraphy—A Conceptual Framework, in: Weimer, P., Posamentier, H. (Eds.), Siliciclastic Sequence Stratigraphy: Recent Developments and Applications. American Association of Petroleum Geologists, p. 0. https://doi.org/10.1306/M58581C16

Kocurek, G., Lancaster, N., 1999. Aeolian system sediment state: theory and Mojave Desert Kelso dune field example. Sedimentology 46, 505–515. https://doi.org/10.1046/j.1365-3091.1999.00227.x

Kohfeld, K.E., Graham, R.M., de Boer, A.M., Sime, L.C., Wolff, E.W., Le Quéré, C., Bopp, L., 2013. Southern Hemisphere westerly wind changes during the Last Glacial Maximum: paleo-data synthesis. Quaternary Science Reviews 68, 76–95. https://doi.org/10.1016/j.quascirev.2013.01.017

Kohfeld, K.E., Harrison, S.P., 2001. DIRTMAP: the geological record of dust 34.

Kohfeld, K.E., Harrison, S.P., 2000. How well can we simulate past climates? Evaluating the models using global palaeoenvironmental datasets. Quaternary Science Reviews 19, 321–346. https://doi.org/10.1016/S0277-3791(99)00068-2

Kopp, R., Simons, F., Mitrovica, J., Maloof, A., Oppenheimer, M., 2009. Probabilistic assessment of sea level during the last interglacial stage. Nature 462, 863–867. https://doi.org/10.1038/nature08686

Kottek, M., Grieser, J., Beck, C., Rudolf, B., Rubel, F., 2006. World Map of the Köppen-Geiger climate classification updated. Meteorologische Zeitschrift 15, 259–263. https://doi.org/10.1127/0941-2948/2006/0130

Krebs, U., Park, W., Schneider, B., 2011. Pliocene aridification of Australia caused by tectonically induced weakening of the Indonesian throughflow. Palaeogeography, Palaeoclimatology, Palaeoecology 309, 111–117. https://doi.org/10.1016/j.palaeo.2011.06.002

Krumbein, W., Pettijohn, F., 1938. Manual of sedimentary petrography, Appleton Century. ed. Appleton Century, London.

Kutzbach, J.E., Street-Perrott, F.A., 1985. Milankovitch forcing of fluctuations in the level of tropical lakes from 18 to 0 kyr BP. Nature 317, 130–134. https://doi.org/10.1038/317130a0

Kylander, M.E., Bindler, R., Martínez Cortizas, A., Gallagher, K., Mörth, C.-M., Rauch, S., 2013. A novel geochemical approach to paleorecords of dust deposition and effective humidity: 8500 years of peat accumulation at Store Mosse (the ``Great Bog''), Sweden. Quaternary Science Reviews 69, 69–82.

Lal, R., 2001. Potential of Desertification Control to Sequester Carbon and Mitigate the Greenhouse Effect, in: Rosenberg, N.J., Izaurralde, R.C. (Eds.), Storing Carbon in Agricultural Soils: A Multi-Purpose Environmental Strategy. Springer Netherlands, Dordrecht, pp. 35–72. https://doi.org/10.1007/978-94-017-3089-1_3

Lancaster, N., 1997. Response of eolian geomorphic systems to minor climate change: examples from the southern Californian deserts. Geomorphology 19, 333–347. https://doi.org/10.1016/S0169-555X(97)00018-4

Lancaster, N., 1994. Dune morphology and dynamics, in: Geomorphology of Desert Environments. Dordrecht, pp. 474–505.

Lancaster, Nicholas, 1994. Dune Morphology and Dynamics, in: Abrahams, A.D., Parsons, A.J. (Eds.), Geomorphology of Desert Environments. Springer Netherlands, Dordrecht, pp. 474–505. https://doi.org/10.1007/978-94-015-8254-4_18

Lancaster, N., 1988. Development of linear dunes in the southwestern Kalahari, Southern Africa. Journal of Arid Environments 14, 233–244.

Lancaster, N., Helm, P., 2000. A test of a climatic index of dune mobility using measurements from the southwestern United States. Earth Surface Processes and Landforms: The Journal of the British Geomorphological Research Group 25, 197–207.

Lancaster, N., Teller, J.T., 1988. Interdune deposits of the Namib Sand Sea. Sedimentary Geology 55, 91–107. https://doi.org/10.1016/0037-0738(88)90091-7

Lancaster, N., Wolfe, S., Thomas, D., Bristow, C., Bubenzer, O., Burrough, S., Duller, G., Halfen, A., Hesse, P., Roskin, J., Singhvi, A., Tsoar, H., Tripaldi, A., Yang, X., Zárate, M., 2016. The INQUA Dunes Atlas chronologic database. Quaternary International 410, 3–10. https://doi.org/10.1016/j.quaint.2015.10.044

Landsberg, S., 1956. The Orientation of Dunes in Britain and Denmark in Relation to Wind. The Geographical Journal 122, 176. https://doi.org/10.2307/1790847

Latrubesse, E., Stevaux, J., Cremon, E., May, J.-H., Tatumi, S., Hurtado, M., Bezada, M., Argollo, J., 2012. Late Quaternary megafans, fans and fluvio-aeolian interactions in the Bolivian Chaco, Tropical South America. Palaeogeography, Palaeoclimatology, Palaeoecology 356–357, 75–88. https://doi.org/10.1016/j.palaeo.2012.04.003

Le Guern, P., 2004. Caractérisation pétrographique et pétrotexturale des éolianites holocènes et pléistocènes. University of Geneva, Geneva.

Lebigre, J.-M., Réaud-Thomas, G., Rejela, M., 2001. Androka (Extrême-Sud de Madagascar) : cartes d’évolution des milieux, CRET. ed. Iles et Archipels, Bordeaux.

Lechleitner, F., Amirnezhad-Mozhdehi, S., Columbu, A., Comas-Bru, L., Labuhn, I., Pérez-Mejías, C., Rehfeld, K., 2018. The Potential of Speleothems from Western Europe as Recorders of Regional Climate: A Critical Assessment of the SISAL Database. Quaternary 1, 30. https://doi.org/10.3390/quat1030030

Lees, B., Yanchou, L., Head, J., 1990. Reconnaissance Thermoluminescence Dating of Northern Australian Coastal Dune Systems. Quaternary Research 34, 169–185. https://doi.org/10.1016/0033-5894(90)90029-K

Lepczyk, X., Arbogast, A., 2005. Geomorphic History of Dunes at Petoskey State Park, Petoskey, Michigan. Journal of Coastal Research 212, 231–241. https://doi.org/10.2112/02-043.1

Lettau, K., 1978. Experimental and micrometeorological field studies of dune migration, in: Exploring in the World's Driest Climate. pp. 110–147.

Levin, N., Ben-Dor, E., Kidron, G., Yaakov, Y., 2008. Estimation of surface roughness (z0) over a stabilizing coastal dune field based on vegetation and topography. Earth Surface Processes and Landforms 33, 1520–1541. https://doi.org/10.1002/esp.1621

Li, H., Yang, X., 2016. Spatial and temporal patterns of aeolian activities in the desert belt of northern China revealed by dune chronologies. Quaternary International 410, 58–68. https://doi.org/10.1016/j.quaint.2015.07.015

Lichter, J., 1995. Lake Michigan beach-ridge and dune development, lake level, and variability in regional water balance. Quaternary Research 44, 181–189.

Lipar, M., Webb, J., 2014. Middle–late Pleistocene and Holocene chronostratigraphy and climate history of the Tamala Limestone, Cooloongup and Safety Bay Sands, Nambung National Park, southwestern Western Australia. Australian Journal of Earth Sciences 61, 1023–1039. https://doi.org/10.1080/08120099.2014.966322

Lipar, M., Webb, J.A., Cupper, M.L., Wang, N., 2017. Aeolianite, calcrete/microbialite and karst in southwestern Australia as indicators of Middle to Late Quaternary palaeoclimates. Palaeogeography, Palaeoclimatology, Palaeoecology 470, 11–29. https://doi.org/10.1016/j.palaeo.2016.12.019

Lisiecki, L.E., Raymo, M.E., 2005. A Pliocene-Pleistocene stack of 57 globally distributed benthic δ 18O records. Paleoceanography 20, n/a-n/a. https://doi.org/10.1029/2004PA001071

Liu, B., Sun, J., Liu, M., Zeng, T., Zhu, J., 2019. The aridity index governs the variation of vegetation characteristics in alpine grassland, Northern Tibet Plateau. PeerJ 7, e7272. https://doi.org/10.7717/peerj.7272

Livingstone, I., 1986. Geomorphological significance of wind flow patterns over a Namib linear dune, in: Nickling, W. (Ed.), Aeolian Geomorphology. pp. 97–112.

Logan, B., 1968. Western Australia, in: Gill, E.D. (Ed.), Quaternary Shoreline Research in Australia and New Zealand Edited, Australian Journal of Science. pp. 106–111.

Lomax, J., Hilgers, A., Radtke, U., 2011. Palaeoenvironmental change recorded in the palaeodunefields of the western Murray Basin, South Australia – New data from single grain OSL-dating. Quaternary Science Reviews 30, 723–736. https://doi.org/10.1016/j.quascirev.2010.12.015

Loope, D., Abegg, F., 2001. Recognition and geologic preservation of ancient carbonate eolianites., in: Modern and Ancient Carbonate Eolianites, SEPM Special Publication. SEPM (Society for Sedimentary Geology). https://doi.org/10.2110/pec.01.71

Loope, D., Simpson, E., 1992. Significance of thin sets of eolian cross-strata. Journal of Sedimentary Research 62, 849–859.

Loucks, R., Patty, K., 2017. Vadose Diagenetic Dissolution Textures, Cementation Patterns, and Aragonite and Mg-Calcite Alteration in the Holocene Isla Cancún Eolianite

Aragonitic Ooids: Modern Analog for Ancient Ooid-Grainstone Pore Networks. Gulf Coast Association of Geological Societies Journal 6, 1–20.

Loucks, R., Ward, W., 2001. Eolian stratification and beach-to-dune transition in a Holocene carbonate eolianite complex, Isla Cancun, Quintana Roo, Mexico., in: Modern and Ancient Carbonate Eolianites, SEPM Special Publication. SEPM (Society of Sedimentary Geology).

Lowdon, J., Robertson, I., Blake, W., 1971. Geological Survey of Canada radiocarbon dates XI. Radiocarbon 13, 255–324.

Lu, J., Vecchi, G.A., Reichler, T., 2007. Expansion of the Hadley cell under global warming. Geophys. Res. Lett. 34, L06805. https://doi.org/10.1029/2006GL028443

Lundberg, J., Ford, D., 1994. Late pleistocene sea level change in the Bahamas from mass spectrometric U-series dating of submerged speleothem. Quaternary Science Reviews 13, 1–14. https://doi.org/10.1016/0277-3791(94)90121-X

Lungershausen, U., Larsen, A., Bork, H.-R., Duttmann, R., 2018. Anthropogenic influence on rates of aeolian dune activity within the northern European Sand Belt and socio-economic feedbacks over the last ~2500 years. The Holocene 28, 84–103. https://doi.org/10.1177/0959683617715693

Lynts, G., 1970. Conceptual model of the Bahamian Platform for the last 135 million years. Nature 225, 1226.

Mackenzie, F., 1964. Bermuda Pleistocene eolianites and paleowinds. Sedimentology 3, 52–64. https://doi.org/10.1111/j.1365-3091.1964.tb00275.x

Madole, R., 1995. Spatial and temporal patterns of late quaternary eolian deposition, Eastern Colorado, U.S.A. Quaternary Science Reviews 14, 155–177. https://doi.org/10.1016/0277-3791(95)00005-A

Maestre, F.T., Salguero-Gómez, R., Quero, J.L., 2012. It is getting hotter in here: determining and projecting the impacts of global environmental change on drylands. Philosophical Transactions of the Royal Society B: Biological Sciences 367, 3062–3075. https://doi.org/10.1098/rstb.2011.0323

Mann, M.E., 2002. Little Ice Age, in: Munn, R.E., MacCracken, M., Perry, J. (Eds.), The Earth System: Physical and Chemical Dimensions of Global Environmental Change, Encyclopedia of Global Environmental Change. Wiley, Chichester ; New York, pp. 504–509.

Mann, M.E., Zhang, Z., Rutherford, S., Bradley, R.S., Hughes, M.K., Shindell, D., Ammann, C., Faluvegi, G., Ni, F., 2009. Global Signatures and Dynamical Origins of the Little Ice Age and Medieval Climate Anomaly. Science 326, 1256–1260. https://doi.org/10.1126/science.1177303

Marcott, S.A., Shakun, J.D., Clark, P.U., Mix, A.C., 2013. A Reconstruction of Regional and Global Temperature for the Past 11,300 Years. Science 339, 1198–1201. https://doi.org/10.1126/science.1228026

Markgraf, V., Dodson, J.R., Kershaw, A.P., McGlone, M.S., Nicholls, N., 1992. Evolution of late pleistocene and holocene climates in the circum-south pacific land areas. Climate Dynamics 6, 193–211. https://doi.org/10.1007/BF00193532

Marsh, W., Marsh, B., 1987. Wind Erosion and Sand Dune Formation on High Lake Superior Bluffs. Geografiska Annaler: Series A, Physical Geography 69, 379–391.

Martínez, J.I., De Deckker, P., Barrows, T.T., 1999. Palaeoceanography of the last glacial maximum in the eastern Indian Ocean: planktonic foraminiferal evidence. Palaeogeography, Palaeoclimatology, Palaeoecology 147, 73–99. https://doi.org/10.1016/S0031-0182(98)00153-9

Marx, S.K., McGowan, H.A., Kamber, B.S., 2009. Long-range dust transport from eastern Australia: A proxy for Holocene aridity and ENSO-type climate variability. Earth and Planetary Science Letters 282, 167–177. https://doi.org/10.1016/j.epsl.2009.03.013

Mason, J., Lu, H., Zhou, Y., Miao, X., Swinehart, J., Liu, Z., Goble, R., Yi, S., 2009. Dune mobility and aridity at the desert margin of northern China at a time of peak monsoon strength. Geology 37, 947–950. https://doi.org/10.1130/G30240A.1

Mason, J., Swinehart, J., Hanson, P., Loope, D., Goble, R., Miao, X., Schmeisser, R., 2011. Late Pleistocene dune activity in the central Great Plains, USA. Quaternary Science Reviews 30, 3858–3870. https://doi.org/10.1016/j.quascirev.2011.10.005

Masse, W., 2007. The archaeology and anthropology of Quaternary period cosmic impact, in: Comet/Asteroid Impacts and Human Society. An Interdisciplinary Approach. Berlin Heidelberg, pp. 25–70.

Masse, W., Bryant, E., Gusiakov, V., Abbott, D., Rambolamana, G., Raza, H., Courty, M., Breger, D., Gerard-Little, P., Burckle, L., 2006. Holocene Indian Ocean cosmic impacts: The megatsunami chevron evidence from Madagascar, in: AGU Fall Meeting Abstracts.

Masse, W., Masse, M., 2007. Myth and catastrophic reality: using myth to identify cosmic impacts and massive Plinian eruptions in Holocene South America. Geological Society, London, Special Publications 273, 177–202.

Masson, V., Vimeux, F., Jouzel, J., Morgan, V., Delmotte, M., Ciais, P., Hammer, C., Johnsen, S., Lipenkov, V.Ya., Mosley-Thompson, E., Petit, J.-R., Steig, E.J., Stievenard, M., Vaikmae, R., 2000. Holocene Climate Variability in Antarctica Based on 11 Ice-Core Isotopic Records. Quaternary Research 54, 348–358. https://doi.org/10.1006/qres.2000.2172

Masson-Delmotte, Valérie, Schulz, M., Abe-Ouchi, A., Beer, J., Ganopolski, A., Fidel, J., Rouco, G., Jansen, E., Lambeck, K., Luterbacher, J., Naish, T., Ramesh, R., Rojas, M., Shao, X., Anchukaitis, K., Arblaster, J., Bartlein, P.J., Benito, G., Clark, P., Comiso, J.C., Crowley, T., Deckker, P.D., de Vernal, A., Delmonte, B., DiNezio, P., Dowsett, H.J., Edwards, R.L., Fischer, H., Fleitmann, D., Foster, G., Fröhlich, C., Hall, A., Hargreaves, J., Haywood, A., Hollis, C., Krinner, G., Landais, A., Li, C., Lunt, D., Mahowald, N., McGregor, S., Meehl, G., Mitrovica, J.X., Moberg, A., Mudelsee, M., Muhs, D.R., Mulitza, S., Müller, S., Overland, J., Parrenin, F., Pearson, P., Robock, A., Rohling, E., Salzmann, U., Savarino, J., Sedláček, J., Shindell, D., Smerdon, J., Solomina, O., Tarasov, P., Vinther, B., Waelbroeck, C., Wolf, D., Yokoyama, Y., Yoshimori, M., Zachos, J., Zwartz, D., Gupta, A.K., Rahimzadeh, F., Raynaud, D., Wanner, H., 2013. Information from Paleoclimate Archives, in: Stocker, T.F., Qin, D., Plattner, M., Tignor, A., Boschung, J., Nauels, A., Xia, Y., Bex, V., Midgley, P. (Eds.), Climate Change 2013: The Physical Science Basis. Contribution of Working Group I to the Fifth Assessment Report of the Intergovernmental Panel on Climate Change. Cambridge, p. 82.

Masson-Delmotte, V., Schulz, M., Abe-Ouchi, A., Beer, J., Ganopolski, A., González Rouco, J., Jansen, E., Lambeck, K., Luterbacher, J., Naish, T., others, 2013. Information from paleoclimate archives. Climate change 383464, 2013.

Mattheus, C., Fowler, J., 2015. Paleotempestite Distribution across an Isolated Carbonate Platform, San Salvador Island, Bahamas. Journal of Coastal Research 314, 842–858. https://doi.org/10.2112/JCOASTRES-D-14-00077.1

May, J.-H., Zech, R., Veit, H., 2008. Late Quaternary paleosol–sediment-sequences and landscape evolution along the Andean piedmont, Bolivian Chaco. Geomorphology 98, 34–54. https://doi.org/10.1016/j.geomorph.2007.02.025

Mayer, J.-H., Mahan, S., 2004. Late Quaternary stratigraphy and geochronology of the western Killpecker Dunes, Wyoming, USA. Quaternary Research 61, 72–84. https://doi.org/10.1016/j.yqres.2003.10.003

Mayle, F.E., Burbridge, R., Killeen, T., 2000. Millennial-Scale Dynamics of Southern Amazonian Rain Forests. Science 290, 2291–2294. https://doi.org/10.1126/science.290.5500.2291

McBride, J., 1987. The Australian summer monsoon. Monsoon Meteorology 203, 13.

McKee, E., 1979. A study of global sand seas. Geological Survey Professional Paper.

McKee, E., 1966. Structures of dunes at White Sands National Monument, New Mexico (and a comparison with structures of dunes from other selected areas). Sedimentology 7, 3–69. https://doi.org/10.1111/j.1365-3091.1966.tb01579.x

McKee, E., Ward, W., 1983. Eolian Environment: Chapter 3, in: M 33: Carbonate Depositional Environments. pp. 131–170.

Mckee, E.D., Bigarella, J.J., 1972. Deformational Structures in Brazilian Coastal Dunes. Journal of Sedimentary Petrology 42, 670–681.

McKenna, W., 2007. An evolutionary model of parabolic dune development: blowout to mature parabolic, Padre Island National Seashore, Texas.

Mercer, J., 1978. West Antarctic ice sheet and CO2 greenhouse effect: a threat of disaster. Nature 271, 321.

Mesbahzadeh, T., Ahmadi, H., 2012. Investigation of Sand Drift Potential (Case Study: Yazd – Ardakan Plain). Journal of Agriculture, Science and Technology 14, 919–928.

Miao, X., Hanson, P., Wang, H., Young, A., 2010. Timing and origin for sand dunes in the Green River Lowland of Illinois, upper Mississippi River Valley, USA. Quaternary Science Reviews 29, 763–773. https://doi.org/10.1016/j.quascirev.2009.11.023

Miao, X., Mason, J., Swinehart, J., Loope, D., Hanson, P., Goble, R., Liu, X., 2007. A 10,000 year record of dune activity, dust storms, and severe drought in the central Great Plains. Geology 35, 119. https://doi.org/10.1130/G23133A.1

Mikolajewicz, U., Scholze, M., Voss, R., 2003. Simulating near-equilibrium climate and vegetation for 6000 cal. years BP. The Holocene 13, 319–326.

Miller, G., Brigham-Grette, J., 1989. Amino acid geochronology: resolution and precision in carbonate fossils. Quaternary International 1, 111–128.

Miller, G.H., Geirsdóttir, Á., Zhong, Y., Larsen, D.J., Otto-Bliesner, B.L., Holland, M.M., Bailey, D.A., Refsnider, K.A., Lehman, S.J., Southon, J.R., Anderson, C., Björnsson, H., Thordarson, T., 2012. Abrupt onset of the Little Ice Age triggered by volcanism and sustained by sea-ice/ocean feedbacks. Geophys. Res. Lett. 39, 5. https://doi.org/10.1029/2011GL050168

Miot da Silva, G., Hesp, P., 2010. Coastline orientation, aeolian sediment transport and foredune and dunefield dynamics of Moçambique Beach, Southern Brazil. Geomorphology 120, 258–278. https://doi.org/10.1016/j.geomorph.2010.03.039

Mirzabaev, A., Wu, J., Evans, J., Garcia-Oliva, F., Hussein, I.A.G., Iqbal, M.H., Kimutai, J., Knowles, T., Meza, F., Nedjroaoui, D., Tena, F., Türkeş, M., Vázquez, R.J., Weltz, M., 2019. Desertification, in: Shukla, P.R., Skeg, J., Calvo Buendia, E., Masson-Delmotte, V., Pörtner, H.-O., Roberts, D.C., Zhai, P., Slade, R., Connors, S., van Diemen, S., Ferrat, M., Haughey, E., Luz, S., Pathak, M., Petzold, J., Portugal Pereira, J., Vyas, P., Huntley, E., Kissick, K., Belkacemi, M., Malley, J. (Eds.), Climate Change and Land: An IPCC Special Report on Climate Change, Desertification, Land Degradation, Sustainable Land Management, Food Security, and Greenhouse Gas Fluxes in Terrestrial Ecosystems.

Morton, R.A., Gelfenbaum, G., Jaffe, B.E., 2007. Physical criteria for distinguishing sandy tsunami and storm deposits using modern examples. Sedimentary Geology 200, 184–207. https://doi.org/10.1016/j.sedgeo.2007.01.003

Mountney, N.P., 2011. A stratigraphic model to account for complexity in aeolian dune and interdune successions 26.

Mountney, N.P., 2006a. Mountney, N. P., Posamentier, H. W., & Walker, R. G. (2006). Eolian facies models. Special Publication-Sepm, 84, 19., in: Walker, R.G., Posamentier, H. (Eds.), Facies Models Revisited, SEPM Special Publication. Oklahoma, pp. 19–83.

Mountney, N.P., 2006b. Periodic accumulation and destruction of aeolian erg sequences in the Permian Cedar Mesa Sandstone, White Canyon, southern Utah, USA. Sedimentology 53, 789–823. https://doi.org/10.1111/j.1365-3091.2006.00793.x

Mourguiart, P., Ledru, M.-P., 2003. Last Glacial Maximum in an Andean cloud forest environment (Eastern Cordillera, Bolivia) 4.

Mueller, D., Jacobs, Z., Cohen, T., Price, D., Reinfelds, I., Shulmeister, J., 2018. Revisiting an arid LGM using fluvial archives: a luminescence chronology for palaeochannels of the Murrumbidgee River, south-eastern Australia: a luminescence chronology for palaeochannels of the Murrumbidgee river. Journal of Quaternary Science 33, 777–793. https://doi.org/10.1002/jqs.3059

Mulder, T., Ducassou, E., Gillet, H., Hanquiez, V., Tournadour, E., Combes, J., Eberli, G.P., Kindler, P., Gonthier, E., Conesa, G., Robin, C., Sianipar, R., Reijmer, J.J.G., François, A., 2012. Canyon morphology on a modern carbonate slope of the Bahamas: Evidence of regional tectonic tilting. Geology 40, 771–774. https://doi.org/10.1130/G33327.1

Mullins, H., Lynts, G., 1977. Origin of the northwestern Bahama Platform: Review and reinterpretation. Geological Society of America Bulletin 88, 1447–1461.

Mylroie, J., 2018a. Superstorms: Comments on Bahamian fenestrae and boulder evidence from the last interglacial. Journal of Coastal Research 34, 1471–1483. https://doi.org/10.2112/JCOASTRES-D-17-00215.1

Mylroie, J., 2018b. Reply to: Hearty, P.J. and Tormey, B.R., 2018. Discussion of: Mylroie, J.E., 2018. Superstorms: Comments on Bahamian Fenestrae and Boulder Evidence from the Last Interglacial. *Journal of Coastal Research,* 34(6), 1471–1483. Journal of Coastal Research 346, 1512–1515. https://doi.org/10.2112/JCOASTRES-D-18A-00004

Mylroie, J.E., 2008. Late Quaternary sea-level position: Evidence from Bahamian carbonate deposition and dissolution cycles. Quaternary International 183, 61–75. https://doi.org/10.1016/j.quaint.2007.06.030

Mylroie, J.E., Carew, J.L., Moore, A.I., 1995. Blue holes: Definition and genesis. Carbonates Evaporites 10, 225–233. https://doi.org/10.1007/BF03175407

Neilson, M., Brockman, G., 1977. The error associated with point-counting. American Mineralogist 62, 1238–1244.

Neumann, A., Hearty, P., 1996. Rapid sea-level changes at the close of the last interglacial (substage 5e) recorded in Bahamian island geology. Geology 24, 775–778.

Newsome, D., 2000. Origin of sandplains in Western Australia: A review of the debate and some recent findings. Australian Journal of Earth Sciences 47, 695–706.

Ngo, T.T., Letchford, C.W., 2009. Experimental study of topographic effects on gust wind speed. J. Wind Eng. Ind. Aerodyn. 13.

Nikolova, I., Yin, Q., Berger, A., Singh, U.K., Karami, M.P., 2013. The last interglacial (Eemian) climate simulated by LOVECLIM and CCSM3. Climate of the Past 9, 1789–1806. https://doi.org/10.5194/cp-9-1789-2013

O’Leary, M., Hearty, P., Thompson, W., Raymo, M., Mitrovica, J., Webster, J., 2013. Ice sheet collapse following a prolonged period of stable sea level during the last interglacial. Nature Geoscience 6, 796–800. https://doi.org/10.1038/ngeo1890

Olson, J.M., Alagarswamy, G., Andresen, J.A., Campbell, D.J., Davis, A.Y., Ge, J., Huebner, M., Lofgren, B.M., Lusch, D.P., Moore, N.J., Pijanowski, B.C., Qi, J., Thornton, P.K., Torbick, N.M., Wang, J., 2008. Integrating diverse methods to understand climate–land interactions in East Africa. Geoforum 39, 898–911. https://doi.org/10.1016/j.geoforum.2007.03.011

Opdyke, N., 1961. The palaeoclimatological significance of desert sandstone, in: Descriptive Palaeoclimatology. New York, NY, pp. 45–60.

Oster, J., Warken, S., Sekhon, N., Arienzo, M., Lachniet, M., 2019. Speleothem Paleoclimatology for the Caribbean, Central America, and North America. Quaternary 2, 5. https://doi.org/10.3390/quat2010005

Palmer, A., Palmer, M., Sasowsky, I. (Eds.), 1999. Karst modeling: Proceedings of the Symposium Held in Charlottesville, Virginia, in: Special Publication. Karst Waters Institute, Charles Town, W. Va.

Past Interglacials Working Group of PAGES, 2016. Interglacials of the last 800,000 years. Reviews of Geophysics 54, 162–219. https://doi.org/10.1002/2015RG000482

Pearce, K., Walker, I., 2005. Frequency and magnitude biases in the ‘Fryberger’ model, with implications for characterizing geomorphically effective winds. Geomorphology 68, 39–55. https://doi.org/10.1016/j.geomorph.2004.09.030

Peel, M., Finlayson, B., McMahon, T., 2007a. Updated world map of the Köppen-Geiger climate classification. Hydrology and earth system sciences discussions 4, 439–473.

Peel, M., Finlayson, B., McMahon, T., 2007b. Updated world map of the Köppen-Geiger climate classification. Hydrol. Earth Syst. Sci. 12.

Peltier, W.R., 2004. Global Glacial Isostasy and the Surface of the Ice-Age Earth: The ICE-5G (VM2) Model and Grace. Annual Review of Earth and Planetary Sciences 32, 111–149. https://doi.org/10.1146/annurev.earth.32.082503.144359

Peña-Monné, J., Sancho-Marcén, C., Sampietro-Vattuone, .M, Rivelli, F., Rhodes, E., Osácar-Soriano, M., Rubio-Fernández, V., García-Giménez, R., 2015. Geomorphological study of the Cafayate dune field (Northwest Argentina) during the last millennium. Palaeogeography, Palaeoclimatology, Palaeoecology 438, 352–363. https://doi.org/10.1016/j.palaeo.2015.08.028

Perlmutter, M., Matthews, M., 1992. Global cyclostratigraphy., University of Chicago. ed. Argonne National Laboratory.

Pessenda, L.C.R., Gomes, B.M., Aravena, R., Ribeiro, A.S., Boulet, R., Gouveia, S.E.M., 1998. The carbon isotope record in soils along a forest-cerrado ecosystem transect: implications for vegetation changes in the Rondonia state, southwestern Brazilian Amazon region. The Holocene 8, 599–603.

Peterson, F., 1988. Pennsylvanian to Jurassic eolian transportation systems in the western United States. Sedimentary Geology 56, 207–260. https://doi.org/10.1016/0037-0738(88)90055-3

Peterson, L.C., Haug, G.H., 2006. Variability in the mean latitude of the Atlantic Intertropical Convergence Zone as recorded by riverine input of sediments to the Cariaco Basin

(Venezuela). Palaeogeography, Palaeoclimatology, Palaeoecology 234, 97–113. https://doi.org/10.1016/j.palaeo.2005.10.021

Petrick, B., Martínez-García, A., Auer, G., Reuning, L., Auderset, A., Deik, H., Takayanagi, H., De Vleeschouwer, D., Iryu, Y., Haug, G.H., 2019. Glacial Indonesian Throughflow weakening across the Mid-Pleistocene Climatic Transition. Sci Rep 9, 16995. https://doi.org/10.1038/s41598-019-53382-0

Pietsch, T., Olley, J., 2005a. Report on the optical dating of sediment samples from Perth and Womerangee, supplied by Brendan Brooke [collected by P Haines and B Brook]: Report to Geoscience Australia and the Geological Survey of Western Australia (unpublished).

Pietsch, T., Olley, J., 2005b. Report on the optical dating of sediment samples from Rottnest Island, supplied by Brendan Brooke [collected by P Haines and PE Playford]: Report to Geoscience Australia and the Geological Survey of Western Australia (unpublished).

Pinter, N., Ishman, S., 2008. Impacts, mega-tsunami, and other extraordinary claims. GSA Today 18, 37. https://doi.org/10.1130/GSAT01801GW.1

Playford, P., 2003. Quaternary tectonism in the Carnarvon Basin, Western Australia. Presented at the Specialist Group: Tectonics and Structural Geology Field Meeting, Kalbarri, Western Australia, p. 89.

Playford, P., Cockbain, A., Berry, P., Robderts, A., Haines, P., Brooke, B., Geological Survey of Western Australia, 2013. The geology of Shark Bay.

Playford, P.E., Cockbain, A., Lowe, G.H., 1976. Geology of the Perth Basin. Western Australia Geological Survey Bulletin 124, 311.

Porat, N., Botha, G., 2008. The luminescence chronology of dune development on the Maputaland coastal plain, southeast Africa. Quaternary Science Reviews 27, 1024–1046. https://doi.org/10.1016/j.quascirev.2008.01.017

Porat, N., Wintle, A., 1995. IRSL dating of aeolianites from the late Pleistocene coastal Kurkar ridge, Israel. Presented at the NQUA XIV, Berlin.

Prager, E., Southard, J., Vivoni-Gallart, E., 1996. Experiments on the entrainment threshold of well-sorted and poorly sorted carbonate sands. Sedimentology 43, 33–40. https://doi.org/10.1111/j.1365-3091.1996.tb01457.x

Prentice, I.C., Webb, T., 1998. BIOME 6000: reconstructing global mid-Holocene vegetation patterns from palaeoecological records. Journal of Biogeography 25, 997–1005. https://doi.org/10.1046/j.1365-2699.1998.00235.x

Price, D., Brooke, B., Woodroffe, C., 2001. Thermoluminescence dating of aeolianites from Lord Howe Island and South-West Western Australian. Quaternary Science Reviews 6.

Psuty, N., Rohr, E., 2000. Coastal dunes: A primer for dune management with models of dune response to storm frequencies. Institute of Marine and Coastal Sciences, Rutgers - The State University of New Jersey.

Pye, K., 1993a. Introduction: the nature and significance of aeolian sedimentary systems. Geological Society, London, Special Publications 72, 1–4. https://doi.org/10.1144/GSL.SP.1993.072.01.01

Pye, K., 1993b. Late Quaternary Development of Coastal Parabolic Megadune Complexes in Northeastern Australia, in: Pye, K., Lancaster, N. (Eds.), Aeolian Sediments. Blackwell Publishing Ltd., Oxford, UK, pp. 23–44. https://doi.org/10.1002/9781444303971.ch3

Pye, K., 1983. Dune formation on the humid tropical sector of the North Queensland Coast, Australia. Earth Surface Processes and Landforms 8, 371–381. https://doi.org/10.1002/esp.3290080409

Pye, K., 1982a. Negatively skewed aeolian sands from a humid tropical coastal Dunefield, Northern Australia. Sedimentary Geology 31, 249–266. https://doi.org/10.1016/0037-0738(82)90060-4

Pye, K., 1982b. Morphological Development of Coastal Dunes in a Humid Tropical Environment, Cape Bedford and Cape Flattery, North Queensland. Geografiska Annaler, Physical Geography 64, 16.

Pye, K., Mazzullo, J., 1994. Effects of Tropical Weathering on Quartz Grain Shape: an Example from Northeastern Australia. SEPM Journal of Sedimentary Research Vol. 64A. https://doi.org/10.1306/D4267DE8-2B26-11D7-8648000102C1865D

Pye, K., Rhodes, E., 1985. Holocene development of an episodic transgressive dune barrier, Ramsay Bay, North Queensland, Australia. Marine Geology 64, 189–202. https://doi.org/10.1016/0025-3227(85)90104-5

Pye, K., Switsur, V., 1981. Radiocarbon dates from the Cape Bedford and Cape Flattery dunefields, North Queensland. Search 12, 225–226.

Pye, K., Tsoar, H., 2008. Aeolian sand and sand dunes, Springer Science & Business Media.

Qiang, M., Chen, F., Song, L., Liu, X., Li, M., Wang, Q., 2013. Late Quaternary aeolian activity in Gonghe Basin, northeastern Qinghai-Tibetan Plateau, China. Quaternary Research 79, 403–412. https://doi.org/10.1016/j.yqres.2013.03.003

Raleigh, C., Urdal, H., 2007. Climate change, environmental degradation and armed conflict. Political Geography 26, 674–694. https://doi.org/10.1016/j.polgeo.2007.06.005

Rawling, J., Hanson, P., Young, A., Attig, J., 2008. Late Pleistocene dune construction in the Central Sand Plain of Wisconsin, USA. Geomorphology 100, 494–505. https://doi.org/10.1016/j.geomorph.2008.01.017

Rea, B.R., Pellitero, R., Spagnolo, M., Hughes, P., Ivy-Ochs, S., Renssen, H., Ribolini, A., Bakke, J., Lukas, S., Braithwaite, R.J., 2020. Atmospheric circulation over Europe during the Younger Dryas. Science Advances 6, eaba4844. https://doi.org/10.1126/sciadv.aba4844

Reeves, J.M., Bostock, H.C., Ayliffe, L.K., Barrows, T.T., De Deckker, P., Devriendt, L.S., Dunbar, G.B., Drysdale, R.N., Fitzsimmons, K.E., Gagan, M.K., Griffiths, M.L., Haberle, S.G., Jansen, J.D., Krause, C., Lewis, S., McGregor, H.V., Mooney, S.D., Moss, P., Nanson, G.C., Purcell, A., van der Kaars, S., 2013. Palaeoenvironmental change in tropical Australasia over the last 30,000 years – a synthesis by the OZ-INTIMATE group. Quaternary Science Reviews 74, 97–114. https://doi.org/10.1016/j.quascirev.2012.11.027

Reitz, M., Jerolmack, D., Ewing, R., Martin, R., 2010. Barchan-parabolic dune pattern transition from vegetation stability threshold. Geophysical Research Letters 37, n/a-n/a. https://doi.org/10.1029/2010GL044957

Richards, D., Smart, P., Edwards, R., 1994. Maximum sea levels for the last glacial period from U-series ages of submerged speleothems. Nature 367, 357.

Ringrose, P., Bentley, M., 2015. Reservoir Model Design. Springer Netherlands, Dordrecht. https://doi.org/10.1007/978-94-007-5497-3

Rodríguez, L., 2008. Después de las desnaturalizaciones: transformaciones socio-económicas y étnicas al sur del valle Calchaquí, Santa María, fines del siglo XVII - fines del XVIII, 1. ed. ed. Ed. Antropofagia, EA, Buenos Aires.

Roduit, N., 2007. JMicroVision: un logiciel d’analyse d’images pétrographiques polyvalent. University of Geneva.

Romain, H.G., Mountney, N.P., 2014. Reconstruction of three-dimensional eolian dune architecture from one-dimensional core data through adoption of analog data from outcrop. Bulletin 98, 1–22. https://doi.org/10.1306/05201312109

Roof, S., 1997. Comparison of isoleucine epimerization and leaching potential in the molluskan genera Astarte, Macoma, and Mya. Geochimica et Cosmochimica Acta 61, 5325–5333. https://doi.org/10.1016/S0016-7037(97)00294-9

Rovere, A., Casella, E., Harris, D., Lorscheid, T., Nandasena, N., Dyer, B., Sandstrom, M., Stocchi, P., D’Andrea, W., Raymo, M., 2018. Reply to Hearty and Tormey: Use the scientific method to test geologic hypotheses, because rocks do not whisper. Proceedings of the National Academy of Sciences 115, E2904–E2905. https://doi.org/10.1073/pnas.1800534115

Rovere, A., Casella, E., Harris, D., Lorscheid, T., Nandasena, N., Dyer, B., Sandstrom, M., Stocchi, P., D’Andrea, W., Raymo, M., 2017. Giant boulders and Last Interglacial storm intensity in the North Atlantic. Proceedings of the National Academy of Sciences 114, 12144–12149. https://doi.org/10.1073/pnas.1712433114

Rowe, M., Bristow, C., 2015a. Sea-level controls on carbonate beaches and coastal dunes (eolianite): Lessons from Pleistocene Bermuda. Geological Society of America Bulletin 127, 1645–1665. https://doi.org/10.1130/B31237.1

Rowe, M., Bristow, C.S., 2015b. Landward-advancing Quaternary eolianites of Bermuda. Aeolian Research 19, 235–249. https://doi.org/10.1016/j.aeolia.2015.06.007

Roy, P., Singhvi, A., 2016. Climate variation in the Thar Desert since the Last Glacial Maximum and evaluation of the Indian monsoon. TIP 19, 32–44. https://doi.org/10.1016/j.recqb.2016.02.004

Rubin, D., Hunter, R., 1983. Reconstructing bedform assemblages from compound crossbedding, in: Developments in Sedimentology. pp. 407–427.

Rubin, D., Hunter, R., 1982. Bedform climbing in theory and nature. Sedimentology 29, 121–138.

Rutter, N., 1985. Dating methods of Pleistocene deposits and their problems. Geological Association of Canada, Toronto, Ontario.

Rutter, N., Crawford, R., Hamilton, R., 1979. Dating methods of Pleistocene deposits and their problems: IV. Amino acid racemization dating. Geoscience Canada 6.

Saint-Smith, E.C., 1912. A geological reconnaissance of a portion of the South-West Division of Western Australia. Western Australia Geological Survey Bulletin 44, 80.

Saji, N.H., Goswami, B.N., Vinayachandran, P.N., Yamagata, T., 1999. A dipole mode in the tropical Indian Ocean. Nature 401, 360–363. https://doi.org/10.1038/43854

Saqqa, W.A., Saqqa, A.W., 2007. A computer program (WDTSRP) designed for computation of sand drift potential (DP) and plotting sand roses. Earth Surf. Process. Landforms 32, 832–840. https://doi.org/10.1002/esp.1451

Sayles, R.W., 1931. Bermuda during the Ice Age. Proceedings of the American Academy of Arts and Sciences 66, 381. https://doi.org/10.2307/20026356

Scheff, J., Seager, R., Liu, H., Coats, S., 2017. Are Glacials Dry? Consequences for Paleoclimatology and for Greenhouse Warming. J. Climate 30, 6593–6609. https://doi.org/10.1175/JCLI-D-16-0854.1

Scheffers, A., Kelletat, D., 2003. Sedimentologic and geomorphologic tsunami imprints worldwide—a review. Earth-Science Reviews 63, 83–92. https://doi.org/10.1016/S0012-8252(03)00018-7

Scheffers, A., Kelletat, D., Scheffers, S., Abbott, D., Bryant, E., 2008. Chevrons – enigmatic sedimentary coastal features. Zeitschrift für Geomorphologie 52, 375–402. https://doi.org/10.1127/0372-8854/2008/0052-0375

Scherer, C.M.S., Goldberg, K., 2007. Palaeowind patterns during the latest Jurassic–earliest Cretaceous in Gondwana: Evidence from aeolian cross-strata of the Botucatu Formation, Brazil. Palaeogeography, Palaeoclimatology, Palaeoecology 250, 89–100. https://doi.org/10.1016/j.palaeo.2007.02.018

Schlager, W., 2005. Carbonate sedimentology and sequence stratigraphy, Concepts in sedimentology and paleontology. SEPM, Soc. for Sedimentary Geology, Tulsa, Okla.

Schmeisser McKean, R., Goble, R., Mason, J., Swinehart, J., Loope, D., 2015. Temporal and spatial variability in dune reactivation across the Nebraska Sand Hills, USA. The Holocene 25, 523–535. https://doi.org/10.1177/0959683614561889

Schwartz, R., 1982. Bedform and stratification characteristics of some modern small-scale washover sand bodies. Sedimentology 29, 835–849.

Scussolini, P., Bakker, P., Guo, C., Stepanek, C., Zhang, Q., Braconnot, P., Cao, J., Guarino, M.-V., Coumou, D., Prange, M., Ward, P.J., Renssen, H., Kageyama, M., Otto-Bliesner, B., Aerts, J.C.J.H., 2019. Agreement between reconstructed and modeled boreal precipitation of the Last Interglacial. Science Advances 5, eaax7047. https://doi.org/10.1126/sciadv.aax7047

Sealey, N., 2006. Bahamian landscapes: an introduction to the geology and physical geography of the Bahamas, Macmillan Education. ed.

Shen, H., Julien, P., 1993. Erosion and sediment transport, in: Handbook of Hydrology. New York, NY.

Sherr, S., Yadav, S.N., 1996. Land degradation in the developing world: implications for foods, agriculture, and the environment to 2020. Food. Agriculture, and the Environment Discussion Paper 14, 42.

Shinn, E., 1983. Birdseyes, Fenestrae, Shrinkage Pores, and Loferites: A Reevaluation. SEPM Journal of Sedimentary Research Vol. 53. https://doi.org/10.1306/212F8247-2B24-11D7-8648000102C1865D

Shinn, E., 1968. Practical significance of birdseye structures in carbonate rocks. Journal of Sedimentary Research 38.

Short, A., 2014. The Australian coast: teacher notes and student activities, Geoscience Australia. ed.

Short, A., 2006. Australian Beach Systems—Nature and Distribution. Journal of Coastal Research 221, 11–27. https://doi.org/10.2112/05A-0002.1

Short, A., 2005. Beaches of the Western Australian Coast: Eucla to Roebuck Bay: A guide to their nature, characteristics, surf and safety, Sydney University Press. ed.

Short, A., 1988. Holocene coastal dune formation in southern Australia: a case study. Sedimentary Geology 55, 121–142.

Shulmeister, J., Lees, B., 1992. Morphology and chronostratigraphy of a coastal dunefield; Groote Eylandt, northern Australia. Geomorphology 5, 521–534. https://doi.org/10.1016/0169-555X(92)90023-H

Shulmeister, J., Lees, B.G., 1995. Pollen evidence from tropical Australia for the onset of an ENSO-dominated climate at c. 4000 BP. The Holocene 5, 10–18. https://doi.org/10.1177/095968369500500102

Silva, G., Hesp, P., Peixoto, J., Dillenburg, S., 2008. Foredune vegetation patterns and alongshore environmental gradients: Moçambique Beach, Santa Catarina Island, Brazil. Earth Surface Processes and Landforms 33, 1557–1573. https://doi.org/10.1002/esp.1633

Singhvi, A., Kar, A., 2004. The aeolian sedimentation record of the Thar desert. Journal of Earth System Science 113, 371–401. https://doi.org/10.1007/BF02716733

Skrivanek, A., Li, J., Dutton, A., 2018. Relative sea-level change during the Last Interglacial as recorded in Bahamian fossil reefs. Quaternary Science Reviews 200, 160–177. https://doi.org/10.1016/j.quascirev.2018.09.033

Smart, P., Richards, D., Edwards, R., 1998. Uranium-series ages of speleothems from South Andros, Bahamas: Implications for quaternary sea-level history and palaeoclimate. Cave and Karst Science 25, 67–74.

Smith, A., Massuel, S., Pollock, D., 2011. Geohydrology of the Tamala Limestone Formation in the Perth region: origin and role of secondary porosity. CSIRO: Water for a Healthy Country National Research Flagship 74.

Smith, L., Al-Tawil, A., Read, J., 2001. High-resolution sequence stratigraphic setting of Mississippian eolianites, Appalachian and Illinois Basins, in: Abegg, F., Harris, P., Loope, D. (Eds.), Modern and Ancient Carbonate Eolianites: Sedimentology, Sequence Stratigraphy, and Diagenesis. pp. 167–181.

Smyth, T., Jackson, D., Cooper, A., 2014. Airflow and aeolian sediment transport patterns within a coastal trough blowout during lateral wind conditions. Earth Surface Processes and Landforms 39, 1847–1854. https://doi.org/10.1002/esp.3572

Spooner, M.I., Barrows, T.T., De Deckker, P., Paterne, M., 2005. Palaeoceanography of the Banda Sea, and Late Pleistocene initiation of the Northwest Monsoon. Global and Planetary Change 49, 28–46. https://doi.org/10.1016/j.gloplacha.2005.05.002

Spooner, M.I., De Deckker, P., Barrows, T.T., Fifield, L.K., 2011. The behaviour of the Leeuwin Current offshore NW Australia during the last five glacial–interglacial cycles. Global and Planetary Change 75, 119–132. https://doi.org/10.1016/j.gloplacha.2010.10.015

Srivastava, A., Thomas, D., Durcan, J., 2019. Holocene Dune Activity in the Thar Desert, India. Earth Surface Processes and Landforms 44, 1407–1418. https://doi.org/10.1002/esp.4583

Srivastava, A., Thomas, D.S.G., Durcan, J.A., Bailey, R.M., 2020. Holocene palaeoenvironmental changes in the Thar Desert: An integrated assessment incorporating new insights from aeolian systems. Quaternary Science Reviews 233, 106214. https://doi.org/10.1016/j.quascirev.2020.106214

Stackhouse, P., Zhang, T., Westberg, D., Barnett, A., Bristow, T., Macpherson, B., Hoell, J., 2018. POWER Release 8 (with GIS Applications) Methodology (Data Parameters, Sources, and Validation—Data Version 8.0. 1). NASA Langley Research Center, Hampton, VA, USA.

Stetler, L., Gaylord, D., 1996. Evaluating eolian-climatic interactions using a regional climate model from Hanford, Washington (USA). Geomorphology 17, 99–113.

Stieglitz, R., Inden, R., 1969. Development of cavernous sediment in a non-beach environment. Journal of Sedimentary Research 39, 342–344.

Street-Perrott, F.A., Harrison, S.P., 1985. Lake Levels and Climate Reconstruction, in: Hecht, A.D. (Ed.), Paleoclimate Analysis and Modeling. New York, NY, pp. 291–331.

Stuut, J.-B.W., Temmesfeld, F., De Deckker, P., 2014. A 550 ka record of aeolian activity near North West Cape, Australia: inferences from grain-size distributions and bulk chemistry of SE Indian Ocean deep-sea sediments. Quaternary Science Reviews 83, 83–94. https://doi.org/10.1016/j.quascirev.2013.11.003

Suppiah, R., 1992. The Australian summer monsoon: a review. Progress in Physical Geography: Earth and Environment 16, 283–318. https://doi.org/10.1177/030913339201600302

Sweet, M.L., Kocurek, G., 1990. An empirical model of aeolian dune lee-face airflow. Sedimentology 37, 1023–1038. https://doi.org/10.1111/j.1365-3091.1990.tb01843.x

Talbot, M., 1984. Late Pleistocene rainfall and dune building in the Sahel, in: Palaeoecology of Africa and the Surrounding Islands. Rotterdam, Netherlands, pp. 203–214.

Tapsell, P., Newsome, D., Bastian, L., 2003. Origin of yellow sand from Tamala Limestone on the Swan Coastal Plain, Western Australia. Australian Journal of Earth Sciences 50, 331–342.

Taylor, C.M., Lambin, E.F., Stephenne, N., Harding, R.J., Essery, R.L.H., 2002. The Influence of Land Use Change on Climate in the Sahel. JOURNAL OF CLIMATE 15, 15.

Tejan-Kella, M., Chittleborough, D., Fitzpatrick, R., Thompson, C., Prescott, J., Hutton, J., 1990. Thermoluminescence dating of coastal sand dunes at Cooloola and North Stradbroke Island, Australia. Soil Research 28, 465. https://doi.org/10.1071/SR9900465

Telfer, M.W., Thomas, D.S.G., 2007. Late Quaternary linear dune accumulation and chronostratigraphy of the southwestern Kalahari: implications for aeolian palaeoclimatic reconstructions and predictions of future dynamics. Quaternary Science Reviews 26, 2617–2630. https://doi.org/10.1016/j.quascirev.2007.07.006

Thomas, D.S.G., Bailey, R.M., 2017. Is there evidence for global-scale forcing of Southern Hemisphere Quaternary desert dune accumulation? A quantitative method for testing hypotheses of dune system development: Southern hemisphere Quaternary desert dune accumulation. Earth Surf. Process. Landforms 42, 2280–2294. https://doi.org/10.1002/esp.4183

Thomas, D.S.G., Knight, M., Wiggs, G.F.S., 2005. Remobilization of southern African desert dune systems by twenty-first century global warming. Nature 435, 1218–1221. https://doi.org/10.1038/nature03717

Thomas, D.S.G., Leason, H.C., 2005. Dunefield activity response to climate variability in the southwest Kalahari. Geomorphology 64, 117–132. https://doi.org/10.1016/j.geomorph.2004.06.004

Thompson, W.G., Allen Curran, H., Wilson, M.A., White, B., 2011. Sea-level oscillations during the last interglacial highstand recorded by Bahamas corals. Nature Geoscience 4, 684–687. https://doi.org/10.1038/ngeo1253

Tian, F., Cao, X., Dallmeyer, A., Lohmann, G., Zhang, X., Ni, J., Andreev, A., Anderson, P.M., Lozhkin, A.V., Bezrukova, E., Rudaya, N., Xu, Q., Herzschuh, U., 2018. Biome changes and their inferred climatic drivers in northern and eastern continental Asia at selected times since 40 cal ka bp. Vegetation History and Archaeobotany 27, 365–379. https://doi.org/10.1007/s00334-017-0653-8

Timmons, E., Fisher, T., Hansen, E., Eisaman, E., Daly, T., Kashgarian, M., 2007. Elucidating aeolian dune history from lacustrine sand records in the Lake Michigan Coastal Zone, USA. The Holocene 17, 789–801. https://doi.org/10.1177/0959683607080520

Tolksdorf, J.F., Kaiser, K., 2012. Holocene aeolian dynamics in the European sand-belt as indicated by geochronological data: Holocene aeolian dynamics in the European sand-belt. Boreas 41, 408–421. https://doi.org/10.1111/j.1502-3885.2012.00247.x

Tomczak, M., Godfrey, J.S., 2003. Regional oceanography: an introduction. Daya Books.

Tormey, B., 1999. EVIDENCE OF RAPID CLIMATE CHANGE DURING THE LAST INTERGLACIAL IN CALCARENITES OF ELEUTHERA, BAHAMAS 154.

Tormey, B.R., Donovan, B.G., Hearty, P.J., 2016. Superstorms of the Last Interglacial: The record from carbonate eolianites of the Bahamas. Presented at the 65th Annual Southeastern GSA Section Meeting. https://doi.org/10.1130/abs/2016SE-273957

Tormey, B.R., Hearty, P.J., Donovan, B.G., 2018. Superstorms deposits in the Bahamas; a record of climate instability from Eleuthera Island during the early peak Last Interglacial (MIS 5e). Presented at the 67th Annual Southeastern GSA Section Meeting - 2018. https://doi.org/10.1130/abs/2018SE-312757

Tormey, D., Donovan, B., 2015. Run over, run up and run out: a storm wave origin for fenestral porosity in last interglacial eolianites of the Bahamas. GSA Abstracts with Programs 47.

Trabucco, A., Zomer, R.J., 2018. Global Aridity Index and Potential Evapo-Transpiration (ET0) Climate Database v2. CGIAR Consortium for Spatial Information (CGIAR-CSI) 10.

Trabucco, A., Zomer, R.J., 2014. Influence of Aridity on Irrigation. International Food Policy Research Institute, Washington, DC. https://doi.org/10.2499/9780896298460_23

Tripaldi, A., Zárate, M., Forman, S., Badger, T., Doyle, M., Ciccioli, P., 2013. Geological evidence for a drought episode in the western Pampas (Argentina, South America) during the early–mid 20th century. The Holocene 23, 1731–1746. https://doi.org/10.1177/0959683613505338

Tsoar, H., 2005. Sand dunes mobility and stability in relation to climate. Physica A: Statistical Mechanics and its Applications 357, 50–56. https://doi.org/10.1016/j.physa.2005.05.067

Tsoar, H., 2001. Types of Aeolian Sand Dunes and Their Formation, in: Balmforth, N., Provenzale, A. (Eds.), Geomorphological Fluid Mechanics. Springer Berlin Heidelberg, Berlin, Heidelberg, pp. 403–429. https://doi.org/10.1007/3-540-45670-8_17

Tsoar, H., 1983. Dynamic processes acting on a longitudinal (seif) sand dune. Sedimentology 30, 567–578. https://doi.org/10.1111/j.1365-3091.1983.tb00694.x

Tsoar, H., Blumberg, D., 2002. Formation of parabolic dunes from barchan and transverse dunes along Israel's Mediterranean coast. Earth Surface Processes and Landforms 27, 1147–1161. https://doi.org/10.1002/esp.417

Tsoar, H., Levin, N., Porat, N., Maia, L.P., Herrmann, H.J., Tatumi, S.H., Claudino-Sales, V., 2009. The effect of climate change on the mobility and stability of coastal sand dunes in Ceará State (NE Brazil). Quaternary Research 71, 217–226. https://doi.org/10.1016/j.yqres.2008.12.001

Uličný, D., 2004. A drying-upward aeolian system of the Bohdašín Formation (Early Triassic), Sudetes of NE Czech Republic: record of seasonality and long-term palaeoclimate change. Sedimentary Geology 167, 17–39. https://doi.org/10.1016/j.sedgeo.2004.01.014

UNDRR, 2021. GAR Special Report on Drought 2021. Geneva, Switzerland.

Vallis, G.K., Zurita-Gotor, P., Cairns, C., Kidston, J., 2015. Response of the large-scale structure of the atmosphere to global warming: Response of Atmospheric Structure to Global Warming. Q.J.R. Meteorol. Soc. 141, 1479–1501. https://doi.org/10.1002/qj.2456

van der Kaars, S., De Deckker, P., 2003. Pollen distribution in marine surface sediments offshore Western Australia. Review of Palaeobotany and Palynology 124, 113–129. https://doi.org/10.1016/S0034-6667(02)00250-6

van der Kaars, S., De Deckker, P., 2002. A Late Quaternary pollen record from deep-sea core Fr10/95, GC17 offshore Cape Range Peninsula, northwestern Western Australia. Review of Palaeobotany and Palynology 120, 17–39. https://doi.org/10.1016/S0034-6667(02)00075-1

Vance, R.E., Beaudoin, A.B., Luckman, B.H., 2007. The Paleoecological Record of 6 ka BP Climate in the Canadian Prairie Provinces. GPQ 49, 81–98. https://doi.org/10.7202/033031ar

Vanoni, V., 1975. Sediment discharge formulas, in: Sedimentation Engineering. pp. 190–229.

Vaz, D.A., Silvestro, S., 2014. Mapping and characterization of small-scale aeolian structures on Mars: An example from the MSL landing site in Gale Crater. Icarus 230, 151–161. https://doi.org/10.1016/j.icarus.2013.08.007

Verheul, J., Becker, D., Zickel, M., Yasa Yener, Willmes, C., 2016. Megabiome changes over the last 120kyr (HadCM3). https://doi.org/10.5880/SFB806.30

Vicente-Serrano, S.M., Cuadrat-Prats, J.M., Romo, A., 2006. Aridity influence on vegetation patterns in the middle Ebro Valley (Spain): Evaluation by means of AVHRR images and climate interpolation techniques. Journal of Arid Environments 66, 353–375. https://doi.org/10.1016/j.jaridenv.2005.10.021

Vimpere, L., Kindler, P., Castelltort, S., 2019. Chevrons: Origin and relevance for the reconstruction of past wind regimes. Earth-Science Reviews 193, 317–332. https://doi.org/10.1016/j.earscirev.2019.04.005

Vimpere, L., Watkins, S.E., Castelltort, S., 2021. Continental interior parabolic dunes as a potential proxy for past climates. Global and Planetary Change 206, 24. https://doi.org/10.1016/j.gloplacha.2021.103622

Viret, G., 2008. Mégablocs au nord d'Eleuthera (Bahamas): preuve de vagues extrêmes au sous-stade isotopique 5e ou restes érosionnels ? (MSc Thesis). University of Geneva, Switzerland.

Wakelin-King, G.A., Webb, J.A., 2020. Origin, geomorphology and geoheritage potential of Australia's longest coastal cliff lines. Australian Journal of Earth Sciences 67, 649–661. https://doi.org/10.1080/08120099.2020.1742202

Walker, I., 1999. Secondary airflow and sediment transport in the lee of a reversing dune. Earth Surface Processes and Landforms 24, 437–448. https://doi.org/10.1002/(SICI)1096-9837(199905)24:5<437::AID-ESP999>3.0.CO;2-Z

Walker, I.J., 1999. Secondary airflow and sediment transport in the lee of a reversing dune 12.

Walker, I.J., Nickling, W.G., 2002. Dynamics of secondary airflow and sediment transport over and in the lee of transverse dunes. Progress in Physical Geography: Earth and Environment 26, 47–75. https://doi.org/10.1191/0309133302pp325ra

Walker, M., 2005. Quaternary dating methods. J. Wiley, Chichester, West Sussex, England.

Wanless, H., Dravis, J., Tedesco, L., Rossinsky Jr, V., 1989. Carbonate Environments and Sequences of Caicos Platform, International Geological Congress Field Trip Guidebook.

Wanner, H., Beer, J., Bütikofer, J., Crowley, T.J., Cubasch, U., Flückiger, J., Goosse, H., Grosjean, M., Joos, F., Kaplan, J.O., Küttel, M., Müller, S.A., Prentice, I.C., Solomina, O., Stocker, T.F., Tarasov, P., Wagner, M., Widmann, M., 2008. Mid- to Late Holocene climate change: an overview. Quaternary Science Reviews 27, 1791–1828. https://doi.org/10.1016/j.quascirev.2008.06.013

Ward, W., 2006. Coastal dunes and strandplains in southeast Queensland: Sequence and chronology. Australian Journal of Earth Sciences 53, 363–373. https://doi.org/10.1080/08120090500507354

Wasson, R., Hyde, R., 1983. Factors determining desert dune type. Nature 304, 337.

Wasson, R., Rajagury, S., Misra, V., Agrawal, D., Dhir, R., 1983. Geomorphology, late Quaternary stratigraphy and paleoclimatology of the Thar dunefield. Zeitschrift für Geomorphologie 45, 117–151.

Webb, T., Bartlein, P.J., Harrison, S.P., Anderson, K.H., 1993. Vegetation, lake levels, and climate in eastern North America for the past 18,000 years, in: Wright Jr, H., Kutzbach, J.E., Webb, T., Ruddiman, W., Street-Perrott, F.A., Bartlein, P.J. (Eds.), Global Climates since the Last Glacial Maximum. pp. 415–467.

Webster, P.J., Moore, A.M., Loschnigg, J.P., Leben, R.R., 1999. Coupled ocean–atmosphere dynamics in the Indian Ocean during 1997–98. Nature 401, 356–360. https://doi.org/10.1038/43848

Wessel, B., Huber, M., Wohlfart, C., Marschalk, U., Kosmann, D., Roth, A., 2018. Accuracy assessment of the global TanDEM-X Digital Elevation Model with GPS data. ISPRS Journal of Photogrammetry and Remote Sensing 139, 171–182. https://doi.org/10.1016/j.isprsjprs.2018.02.017

Whitacre, K., Kaufman, D., Kosnik, M., Hearty, P., 2017. Converting A/I values (ion exchange) to D/L values (reverse phase) for amino acid geochronology. Quaternary Geochronology 37, 1–6. https://doi.org/10.1016/j.quageo.2016.10.004

White, B., Curran, H., 1989. The Holocene Carbonate Eolianites of North Point and the Modern Environments between North Point and Cut Cay, San Salvador Island, Bahamas. pp. 17–22. https://doi.org/10.1029/FT175p0017

Wijffels, S., Sprintall, J., Fieux, M., Bray, N., 2002. The JADE and WOCE I10/IR6 Throughflow sections in the southeast Indian Ocean. Part 1: water mass distribution and variability. Deep Sea Research Part II: Topical Studies in Oceanography 49, 1341–1362. https://doi.org/10.1016/S0967-0645(01)00155-2

Williams, H.F.L., 2011. Shell bed tempestites in the Chenier Plain of Louisiana: late Holocene example and modern analogue. Journal of Quaternary Science 26, 199–206. https://doi.org/10.1002/jqs.1444

Williams, J., Day, M., Chojnacki, M., Rice, M., 2020. Scarp orientation in regions of active aeolian erosion on Mars. Icarus 335, 113384. https://doi.org/10.1016/j.icarus.2019.07.018

Wilson, A., 1964. Origin of ice ages: an ice shelf theory for Pleistocene glaciation 3.

Wolcott, D., Donner, D., Brown, D., Ribic, C., 2018. Kirtland's warbler winter habitat changes across the Bahamian Archipelago in response to future climate-condition scenarios. Caribbean Naturalist 1–20.

Wolfe, S., Hugenholtz, C., 2009. Barchan dunes stabilized under recent climate warming on the northern Great Plains. Geology 37, 1039–1042. https://doi.org/10.1130/G30334A.1

Wolfe, S., Hugenholtz, C., Evans, C., Huntley, D., Ollerhead, J., 2007a. Potential Aboriginal-Occupation-Induced Dune Activity, Elbow Sand Hills, Northern Great Plains, Canada 17, 21.

Wolfe, S., Huntley, D., David, P., Ollerhead, J., Sauchyn, D., MacDonald, G., 2001. Late 18th century drought-induced sand dune activity, Great Sand Hills, Saskatchewan. Canadian Journal of Earth Sciences 38, 105–117. https://doi.org/10.1139/cjes-38-1-105

Wolfe, S., Huntley, D., Ollerhead, J., 2004. Relict Late Wisconsinan Dune Fields of the Northern Great Plains, Canada. Géographie physique et Quaternaire 58, 323. https://doi.org/10.7202/013146ar

Wolfe, S., Huntley, D., Ollerhead, J., 2002a. Optical Dating of Modern and Late Holocene Dune Sands in the Brandon Sand Hills, Southwestern Manitoba. Géographie physique et Quaternaire 56, 203. https://doi.org/10.7202/009106ar

Wolfe, S., Nickling, W., 1993. The protective role of sparse vegetation in wind erosion. Progress in Physical Geography: Earth and Environment 17, 50–68. https://doi.org/10.1177/030913339301700104

Wolfe, S., Ollerhead, J., Huntley, D., Lian, O., 2006. Holocene dune activity and environmental change in the prairie parki and and boreal forest, central Saskatchewan, Canada. The Holocene 16, 17–29.

Wolfe, S., Ollerhead, J., Lian, O., 2002b. Holocene Eolian Activity in South-central Saskatchewan and the Southern Canadian Prairies. Géographie physique et Quaternaire 56, 215. https://doi.org/10.7202/009107ar

Wolfe, S., Paulen, R., Smith, I., Lamothe, M., 2007b. Age and paleoenvironmental significance of Late Wisconsinan dune fields in the Mount Watt and Fontas River map areas, northern Alberta and British Columbia (No. 2007). https://doi.org/10.4095/223690

Wolfe, S., Walker, I., Huntley, D., 2008. Holocene coastal reconstruction, Naikoon peninsula, Queen Charlotte Islands, British Columbia (No. 2008–12). https://doi.org/10.4095/225498

Wolman, M., Miller, J., 1960. Magnitude and Frequency of Forces in Geomorphic Processes. The Journal of Geology 68, 54–74. https://doi.org/10.1086/626637

Woodroffe, C., 2002. Coasts: form, process, and evolution. Cambridge University Press, Cambridge ; New York.

Xue, Y., Shukla, J., 1993. The influence of land surface properties on Sahel climate. Part 1: desertification. Journal of Climate 6, 2232–2245.

Yalin, M., 1977. Mechanics of sediment transport, Pergamon press. ed. New York, NY.

Yan, N., Baas, A., 2017. Environmental controls, morphodynamic processes, and ecogeomorphic interactions of barchan to parabolic dune transformations. Geomorphology 278, 209–237. https://doi.org/10.1016/j.geomorph.2016.10.033

Yan, N., Baas, A., 2015. Parabolic dunes and their transformations under environmental and climatic changes: Towards a conceptual framework for understanding and prediction. Global and Planetary Change 124, 123–148. https://doi.org/10.1016/j.gloplacha.2014.11.010

Yan, X.-H., Ho, C.-R., Zheng, Q., Klemas, V., 1992. Temperature and Size Variabilities of the Western Pacific Warm Pool. Science 258, 1643–1645. https://doi.org/10.1126/science.258.5088.1643

Yang, X., Wang, X., Liu, Z., Li, H., Ren, X., Zhang, D., Ma, Z., Rioual, P., Jin, X., Scuderi, L., 2013. Initiation and variation of the dune fields in semi-arid China – with a special reference to the Hunshandake Sandy Land, Inner Mongolia. Quaternary Science Reviews 78, 369–380. https://doi.org/10.1016/j.quascirev.2013.02.006

Yizhaq, H., Xu, Z., Ashkenazy, Y., 2020. The effect of wind speed averaging time on the calculation of sand drift potential: New scaling laws. Earth and Planetary Science Letters 544, 116373. https://doi.org/10.1016/j.epsl.2020.116373

Yu, G., Harrison, S.P., Xue, B., 2001. Lake status records from China: Data Base Documentation, Max-Planck-Institut for Biogeochemie. ed, Technical Reports.

Yu, L., Lai, Z., 2014. Holocene climate change inferred from stratigraphy and OSL chronology of aeolian sediments in the Qaidam Basin, northeastern Qinghai–Tibetan Plateau. Quaternary Research 81, 488–499. https://doi.org/10.1016/j.yqres.2013.09.006

Zhou, L., Williams, M.A.J., Peterson, J.A., 1994. Late Quaternary aeolianites, palaeosols and depositional environments on the Nepean Peninsula, Victoria, Australia. Quaternary Science Reviews 13, 225–239. https://doi.org/10.1016/0277-3791(94)90027-2

Zhuravleva, A., Bauch, H.A., 2018. Last interglacial ocean changes in the Bahamas: climate teleconnections between low and high latitudes. Climate of the Past 14, 1361–1375. https://doi.org/10.5194/cp-14-1361-2018

Zieliński, P., Sokołowski, R., Fedorowicz, S., Jankowski, M., 2011. Stratigraphic position of fluvial and aeolian deposits in the Żabinko site (W Poland) based on TL dating. Geochronometria 38, 64–71. https://doi.org/10.2478/s13386-011-0005-x

Zou, L., Wang, L., Li, J., Lu, Y., Gong, W., Niu, Y., 2019. Global surface solar radiation and photovoltaic power from Coupled Model Intercomparison Project Phase 5 climate models. Journal of Cleaner Production 224, 304–324. https://doi.org/10.1016/j.jclepro.2019.03.268

Zular, A., Sawakuchi, A., Guedes, C., Mendes, V., Nascimento, D., Giannini, P., Aguiar, V., DeWitt, R., 2013. Late Holocene intensification of colds fronts in southern Brazil as indicated by dune development and provenance changes in the São Francisco do Sul coastal barrier. Marine Geology 335, 64–77. https://doi.org/10.1016/j.margeo.2012.10.006

Appendices

Appendix 1: Compilation of all dating data available in literature for chevrons. (1) sample taken at -0.6m; (2) sample taken at -2m; (3) sample taken at -10m; (4) sample taken at -20m; (5) sample taken at -25m; (6) sample taken at -8m, minimum age; (7) sample taken at -6 to -8m; (8) sample taken just below (7); (9) reliable age; (10) minimum age; (11) maximum age; (12) High U and Th content; (13) High U and Th content.

Country	Region	Location	Stratigraphy	Method	Age	Reference
Bahamas	Long Island	Miller's Settlement	French Bay Member	WR A/I	Late Pleistocene, MIS 5e	Hearty et al., 1998
Egypt	S-Egypt	Selima sand sheet	Actual	Sattelite images and field study	Actual	Maxwell and Haynes, 1989
Madagascar	S-Madagascar	Ampalaza Bay		Geomorphic indicators and archeologic dating	Mid Holocene to 500 AD	Gusiakov et al., 2009
		Fenambosy		Geomorphic indicators and archeologic dating	Mid Holocene to 500 AD	Gusiakov et al., 2009
		Cap St. Marie		Geomorphic indicators and archeologic dating	Mid Holocene to 500 AD	Gusiakov et al., 2009
		Faux Cap		Geomorphic indicators and archeologic dating	Mid Holocene to 500 AD	Gusiakov et al., 2009
		Ambazoa		Geomorphic indicators	3000-2000 BP or 18000 BP	Clark et al., 1998
W-Australia		Quobba		Geomorphic indicators	Younger Pleistocene	Scheffers et al., 2008
		South Coral Bay		Geomorphic indicators	Pleistocene	Scheffers et al., 2008
		West Albany		Geomorphic indicators	Pleistocene	Scheffers et al., 2008
N-Australia		Groote Eylandt		Geomorphic indicators	Holocene	Scheffers et al., 2008
E-Australia	Cape Bedord-Cape Flattery dunefield	NW of Cape Flattery	First unit (oldest)	^{14}C	>48'000	Pye and Switsur, 1981
		Near Cape Flattery Mining Camp	Second unit	^{14}C	7’480 ± 75 BP	Pye and Switsur, 1981
				^{14}C	7’560 ± 90 BP	Pye and Switsur, 1981
				^{14}C	8’200 ± 85 BP	Pye and Switsur, 1981
			Third unit (youngest); A for Lee et al., 1990	Aerial photographs	300 - 500	Pye, 1993
		Near Red Hill	A	^{14}C	220 ± 70 BP (1)	Lee et al., 1990
			B	TL	2’000 ± 1000 BP (2)	Lee et al., 1990
			C	TL	19’200 ± 3400 BP (3)	Lee et al., 1990
			D	TL	22’700 ± 2800 BP (4)	Lee et al., 1990
			E	TL	19’800 ± 2300 BP (5)	Lee et al., 1990
			F	TL	171’000 ± 13000 BP	Lee et al., 1990

		G	TL	>66’000 BP	Lee et al., 1990
Shelburne Bay dunefield	Red Cliffs	C	TL	17’600 ± 1400 BP (6)	Lee et al., 1990
		D	TL	28’400 ± 1300 BP (7)	Lee et al., 1990
		D	TL	29’900 ±2400 BP (8)	Lee et al., 1990
		D	^{14}C	29’740 ± 3030 BP (9)	Lee et al., 1990
	Double Point	C	TL	23’800 ± 2400 BP	Lee et al., 1990
	Conical Hill	C	TL	15’000 ± 1110 BP (10)	Lee et al., 1990
	?	A	^{14}C	930 ± 135 BP (11)	Lee et al., 1990
Arnhem Land dunefields	Cobourg Peninsula	B	TL	1’900 ± 400 BP	Lee et al., 1990
		C	TL	2’600 ± 300 BP	Lee et al., 1990
		C	TL	2’800 ± 500 BP	Lee et al., 1990
			TL	8’600 ± 1400 BP	Lee et al., 1990
		E	TL	9’300 ± 1100 BP (12)	Lee et al., 1990
		E	TL	81’400 ± 8500 BP (13)	Lee et al., 1990
Hinchinbrook Island	Ramsay Bay		^{14}C	9’000 BP	Pye, 1993
			^{14}C	900 BP	Pye, 1993

Appendix 2: Geomorphology and stratigraphy of the extreme S-Madagascar (from Lebigre et al., 2001)

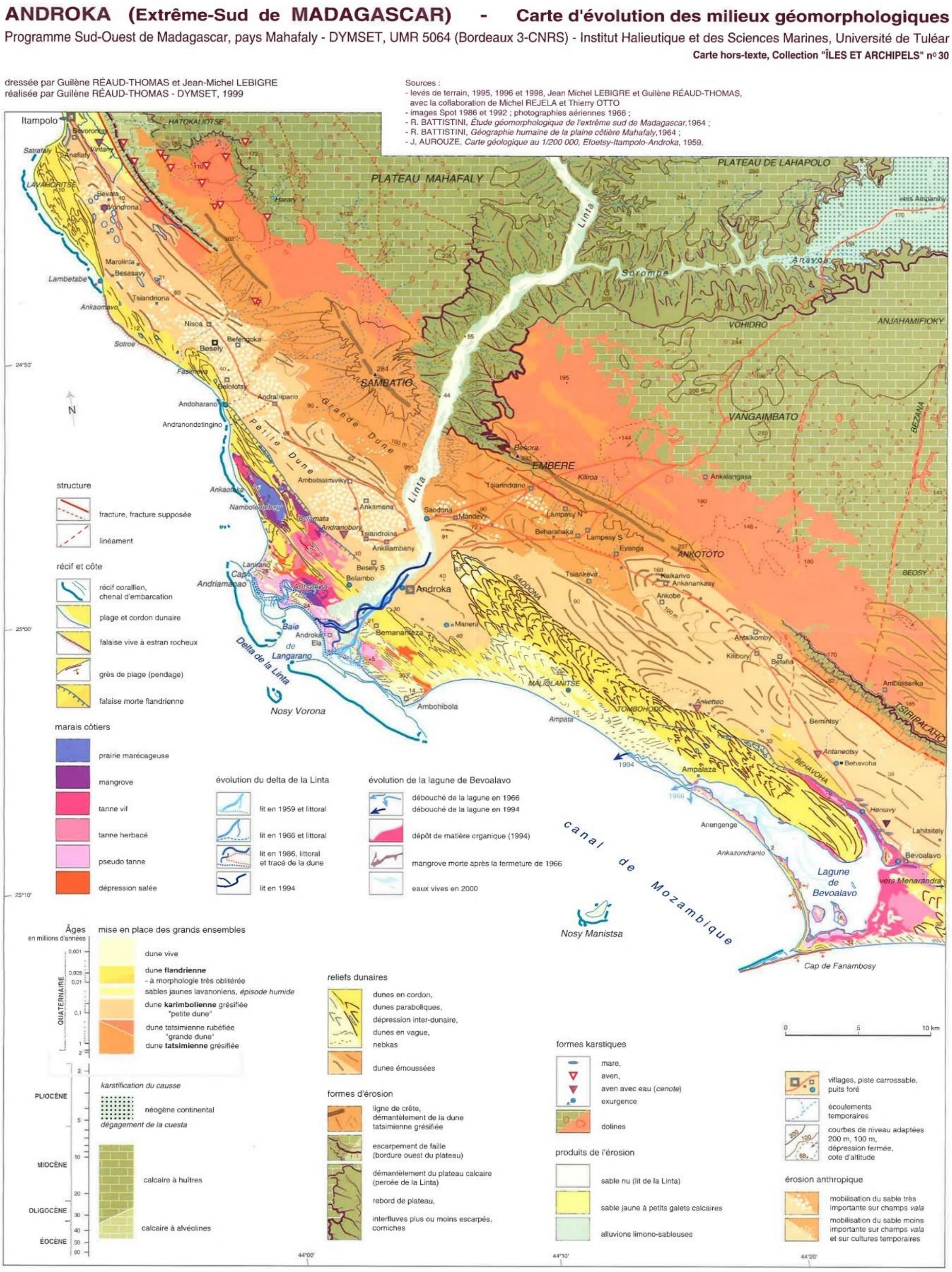

Appendix 3: Map of Madagascar, the Bahamas and Australia showing the studied locations.

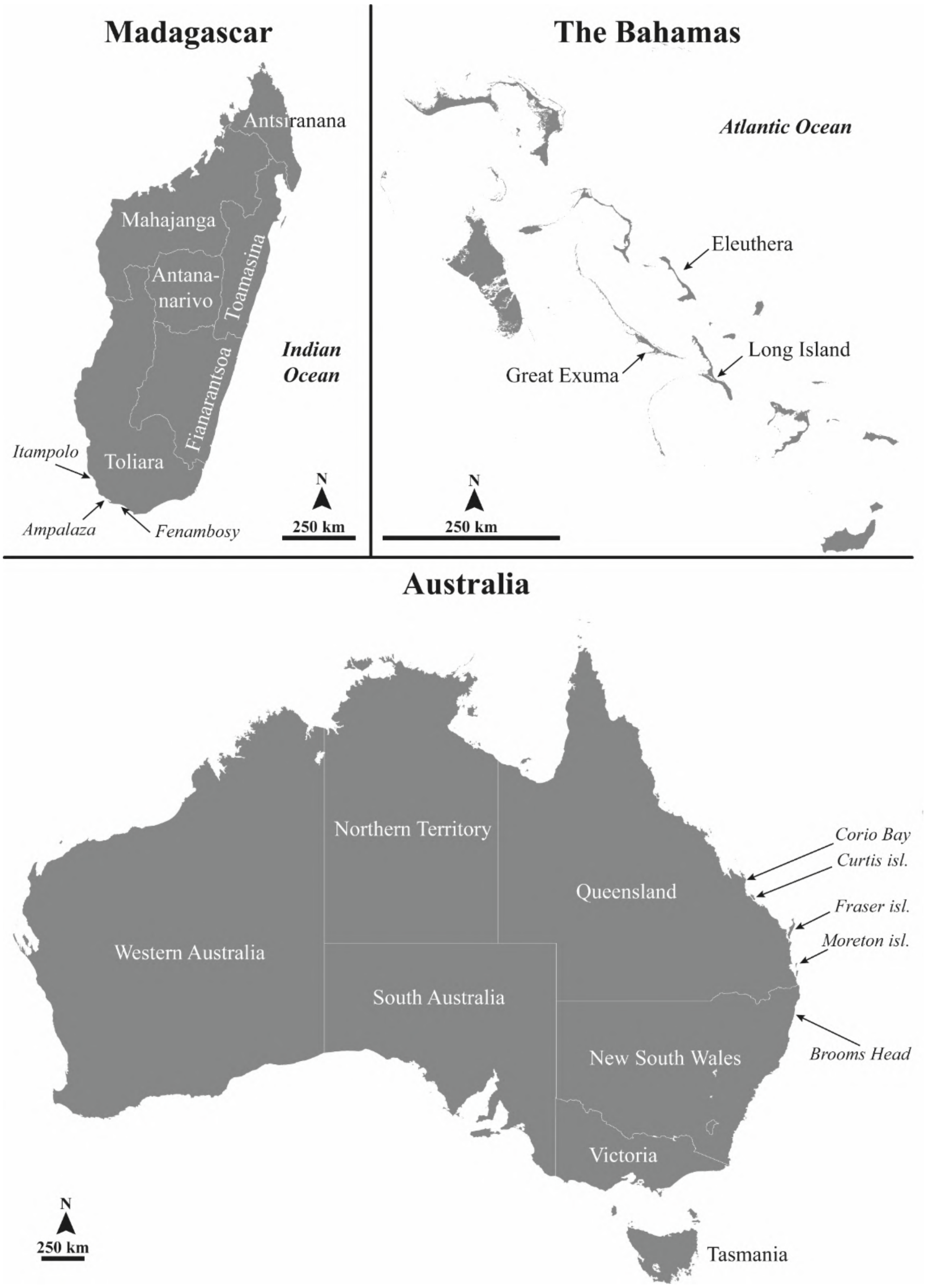

Appendix 4: Morphological parameters measured on Bahamian “chevrons”.

Country	Location	#	Lat.	Long.	Length (km)	Width (km)	Height (m)	L/W	L/H	W/H	Perimeter (km)	Pile Volume (m3)	Enclosed Area (km2)	α (°)	ϕ (°)
Bahamas	Acklins Island	BA-AK-1	-73.921	22.454	1.7	0.7	21	2.5	79.8	32.5	5.192	5.67E+06	1.351	12	1
	Great Exuma	BA-EX-1	23.601	-75.909	2.0	0.9	33	2.1	59.1	27.9	5.589	8.56E+06	1.530	14	3
		BA-EX-2	23.613	-75.934	2.3	1.2	21	1.8	109.9	60.0	6.993	9.08E+06	2.360	14	5
	Long Island	BA-LI-1	23.394	-75.160	1.7	0.5	10	3.2	178.7	56.4	4.267	1.66E+06	1.015	11	2
		BA-LI-2	23.390	-75.149	0.4	0.4	7	1.0	62.3	60.0	1.647	8.08E+05	0.180	12	3
		BA-LI-3	23.385	-75.148	0.8	0.5	7	1.7	127.5	74.8	2.689	1.90E+06	0.413	11	1
		BA-LI-4	23.209	-75.105	3.0	0.6	11	5.3	281.8	53.3	6.732	7.38E+06	1.754	9	1
		BA-LI-5	23.492	-75.215	2.0	0.4	13	5.1	147.4	28.9	4.959	4.50E+06	0.967	8	3
		BA-LI-6	23.500	-75.212	0.7	0.3	19	1.9	33.7	17.4	2.202	2.55E+06	0.315	12	2
		BA-LI-7	23.556	-75.239	1.4	0.6	32	2.1	42.8	20.1	4.281	7.59E+06	0.903	10	2

Appendix 5: Morphological parameters measured on 95 parabolic dunes around the world.

Country	Location	#	Orien. (°)	Lat.	Long.	L (km)	W (km)	H (m)	L/W	L/H	W/H	Perimeter (km)	Pile Volume (m3)	Enclosed Area (km2)	α (°)	ϕ (°)
Australia	Brooms Head	A-NSW-BH1	354	-29.699	153.304	1.5	0.2	36	8.2	40.6	5.0	3.799	3.01E+06	0.394	13	2
	Corio Bay	A-QL-CB1	315	-22.903	150.761	1.9	0.4	47	4.8	40.0	8.3	4.722	6.27E+06	0.960	8	2
		A-QL-CB2	306	-22.900	150.773	0.8	0.3	44	2.6	18.4	7.2	2.265	3.49E+06	0.293	13	4
		A-QL-CB3	309	-22.892	150.766	1.8	0.4	58	4.8	31.1	6.5	4.83	1.81E+07	0.978	17	6
		A-QL-CB4	314	-22.869	150.744	2.1	0.5	35	4.6	61.1	13.3	6.334	N/A	1.118	18	5
		A-QL-CB4 Bis	312	-22.872	150.748	2.4	0.5	20	4.7	119.8	25.2	6.171	N/A	1.192	18	1
		A-QL-CB4 Ter	311	-22.879	150.756	1.1	0.4	31	2.8	34.1	12.3	3.522	4.90E+06	0.450	16	5
		A-QL-CB5	308	-22.864	150.760	2.9	0.9	34	3.3	86.6	26.4	7.55	2.40E+07	2.782	8	1
		A-QL-CB6	309	-22.819	150.747	4.2	1.0	31	4.1	134.7	32.6	11.118	N/A	4.596	15	3
		A-QL-CB6 Bis	308	-22.837	150.772	2.0	0.8	43	2.6	46.0	17.8	6.935	1.39E+07	1.268	18	4
		A-QL-CB7	312	-22.817	150.782	1.4	0.2	24	8.3	59.0	7.1	4.159	1.89E+06	0.277	26	11
	Curtis Island	A-QL-CI1	312	-23.585	151.219	0.7	0.2	19	4.6	39.3	8.6	2.03	1.11E+06	0.177	18	5
		A-QL-CI2	309	-23.572	151.218	0.7	0.1	19	5.0	38.5	7.7	2.23	6.15E+05	0.151	14	6
		A-QL-CI3	307	-23.566	151.214	1.4	0.4	25	3.4	56.4	16.6	4.038	3.72E+06	0.691	18	6
		A-QL-CI4	310	-23.554	151.213	1.9	0.4	27	4.8	70.3	14.7	5.414	5.40E+06	0.994	21	6
		A-QL-CI5	310	-23.532	151.210	2.7	0.6	49	4.7	56.3	12.0	6.832	2.10E+07	1.921	19	2
	Fraser Island	A-QL-FI4	316	-25.626	153.002	5.6	3.2	57	1.8	99.5	56.6	20.439	1.52E+08	17.510	13	3
		A-QL-FI4 Bis	313	-25.663	153.035	3.4	1.1	50	3.0	67.1	22.6	12.025	4.09E+07	3.737	25	3
		A-QL-FI5	314	-25.319	153.196	1.4	0.8	50	1.8	28.9	16.2	4.48	1.23E+07	1.272	28	5
		A-QL-FI6	321	-25.219	153.187	4.1	1.2	58	3.4	70.4	20.4	11.649	8.95E+07	4.926	20	2
		A-QL-FI7	320	-24.811	153.202	3.8	1.7	75	2.2	50.3	22.9	18.615	1.07E+08	10.754	15	4
		A-QL-FI8	314	-24.824	153.248	1.7	0.7	32	2.5	51.8	20.8	4.528	1.10E+07	1.217	14	3

	Nigaloo	A-WA-NI1	7	-22.704	113.676	1.4	0.4	8	3.4	169.4	49.8	3.907	1.40E+06	0.638	5	1
		A-WA-NI2	5	-22.697	113.684	0.7	0.3	22	2.6	33.0	12.8	2.037	1.42E+06	0.237	12	5
		A-WA-NI3	6	-22.703	113.683	1.0	0.4	27	2.4	38.0	15.7	3.164	3.30E+06	0.522	19	4
		A-WA-NI4	6	-22.725	113.732	0.7	0.4	18	1.9	38.4	20.0	2.127	9.16E+05	0.255	20	5
		A-WA-NI5	15	-22.761	113.766	1.5	0.5	24	3.2	62.6	19.6	4.027	5.00E+06	0.828	14	3
		A-WA-NI6	13	-22.778	113.775	1.5	0.3	25	4.5	60.4	13.6	3.313	2.49E+06	0.495	13	3
	S Wide Bay	A-QL-FI1	315	-26.120	153.093	1.9	0.4	33	4.8	56.4	11.8	4.786	7.77E+06	0.928	22	4
		A-QL-FI2	321	-26.088	153.102	1.5	0.2	26	6.8	58.9	8.7	4.602	3.64E+06	0.421	26	4
		A-QL-FI3	326	-25.999	153.133	2.0	0.9	33	2.3	59.9	26.6	6.709	8.09E+06	1.741	22	1
Brazil	Fortaleza	BR-NE-FO1	282	-3.975	-38.276	1.8	0.4	64	4.7	28.0	6.0	5.055	8.18E+06	1.139	23	5
		BR-NE-FO2	284	-3.955	-38.282	1.3	0.4	90	3.8	14.7	3.9	3.899	1.15E+07	0.671	22	6
		BR-NE-FO3	284	-3.925	-38.344	0.5	0.3	28	1.8	17.4	9.4	1.419	1.12E+06	0.139	16	8
		BR-NE-FO4	290	-3.842	-38.410	0.7	0.4	43	1.8	15.0	8.1	2.624	4.43E+06	0.370	13	8
Denmark	Blåvand	DK-VA-BL1	91	55.563	8.180	1.0	0.6	17	1.8	56.6	32.1	2.806	3.35E+05	0.440	11	5
		DK-VA-BL2	94	55.563	8.180	0.3	0.3	7	1.2	43.5	37.0	1.153	5.75E+04	0.092	13	6
		DK-VA-BL3	112	55.563	8.180	1.0	0.6	16	1.7	63.6	36.5	2.979	1.05E+06	0.574	15	3
		DK-VA-BL4	103	55.563	8.180	1.6	0.3	15	5.1	107.5	21.0	4.02	6.56E+05	0.553	10	3
Lybia	Marsa el Brega	LY-CY-MB1	137	30.549	19.827	1.8	0.8	33	2.2	53.5	23.9	6.018	7.54E+06	1.597	10	3
		LY-CY-MB2	118	30.561	19.849	1.0	0.6	25	1.6	39.1	24.8	3.1	2.02E+06	0.574	13	3
		LY-CY-MB3	115	30.588	19.877	1.3	0.7	38	1.9	34.2	18.3	0.778	4.81E+06	4.224	10	4
		LY-CY-MB4	120	30.577	19.936	2.3	0.9	19	2.5	120.2	48.7	6.527	4.97E+06	2.318	6	3
		LY-CY-MB5	113	30.613	19.932	2.3	0.7	19	3.4	119.6	35.2	5.747	3.21E+06	1.622	6	4

		LY-CY-MB6	127	30.654	19.961	1.2	0.7	35	1.9	35.9	19.0	3.739	3.95E+06	0.840	21	3
		LY-CY-MB7	137	30.768	20.035	1.1	0.5	24	2.1	45.6	21.4	3.214	2.04E+06	0.639	13	3
		LY-CY-MB8	123	30.782	20.030	1.6	0.5	22	3.0	73.8	24.9	4.732	1.87E+06	0.933	16	3
		LY-CY-MB9	109	30.851	20.119	1.0	0.7	27	1.3	35.6	27.3	3.529	2.17E+06	0.757	19	4
Netherlands	Ijmuiden	N-NH-IJ1	60	52.431	4.583	0.4	0.2	18	2.0	23.3	11.5	1.646	2.61E+05	0.126	28	8
Scotland	Newburgh	S-AS-NB1	66	57.329	-1.981	0.2	0.2	12	0.9	13.3	14.8	0.765	3.57E+04	0.033	25	10
		S-AS-NB2	330	57.329	-1.981	0.2	0.1	15	1.4	12.9	9.1	0.73	7.19E+04	0.029	16	6
Spain	Suances	SP-CT-SU1	96	43.447	-3.967	0.2	0.1	8	1.6	27.3	16.6	0.734	6.47E+04	0.033	9	3
		SP-CT-SU2	88	43.445	-3.972	0.2	0.1	19	1.4	8.1	5.8	0.611	4.95E+04	0.022	22	10
		SP-CT-SU3	107	43.445	-3.969	0.2	0.2	14	1.1	13.9	12.5	0.846	6.82E+04	0.047	11	7
USA	Cape Cod	US-MA-CC1	112	42.073	-70.184	0.4	0.2	4	1.6	90.0	54.6	1.387	1.16E+05	0.107	5	2
		US-MA-CC2	109	42.073	-70.184	0.3	0.1	5	2.3	65.7	28.3	0.922	3.82E+04	0.048	4	2
		US-MA-CC3	123	42.073	-70.184	0.7	0.4	6	1.5	121.1	78.4	2.15	1.83E+05	0.286	4	1
		US-MA-CC4	116	42.073	-70.184	0.4	0.4	5	1.1	89.7	78.0	1.663	1.64E+05	0.170	5	2
	Eureka	US-CA-EU1	156	40.834	-124.178	0.5	0.3	8	1.7	69.0	40.6	1.634	2.69E+05	0.131	6	1
		US-CA-EU2	162	40.834	-124.178	0.3	0.1	4	3.0	80.6	26.9	0.993	4.17E+04	0.043	5	1
		US-CA-EU3	167	40.834	-124.178	0.4	0.1	4	3.2	96.7	30.4	1.068	4.24E+04	0.054	6	2
	Grand Marais	US-MI-GM1	135	46.686	-85.895	0.3	0.1	N/A	2.0	N/A	N/A	0.893	1.75E+05	0.041	23	6
	Holland	US-MI-HO1	73	42.759	-86.204	0.4	0.2	54	2.2	8.2	3.7	1.538	7.27E+05	0.099	31	13
		US-MI-HO2	79	42.759	-86.204	0.2	0.1	47	2.3	3.5	1.5	0.602	1.18E+05	0.020	32	17
		US-MI-HO3	81	42.759	-86.204	0.3	0.1	44	2.6	6.2	2.4	0.815	4.69E+05	0.041	31	11
		US-MI-HO4	80	42.759	-86.204	0.3	0.1	49	2.8	6.3	2.2	0.852	5.30E+05	0.040	31	11

	US-MI-HO5	63	42.759	-86.204	0.4	0.1	37	2.9	9.5	3.3	1.055	8.31E+05	0.068	32	10
	US-MI-HO6	75	42.759	-86.204	0.4	0.2	45	2.1	9.4	4.5	1.408	9.11E+05	0.102	29	10
Lompoc	US-CA-LO1	121	34.803	-120.590	0.4	0.1	7	3.6	61.2	16.8	1.023	4.79E+04	0.057	7	2
	US-CA-LO2	114	34.803	-120.590	0.4	0.2	7	2.9	62.2	21.7	1.213	6.70E+04	0.084	7	2
	US-CA-LO3	102	34.803	-120.590	0.5	0.1	8	3.3	57.9	17.6	1.271	7.14E+04	0.082	6	2
	US-CA-LO4	107	34.803	-120.590	2.0	0.4	11	5.4	192.4	35.5	4.97	3.18E+05	0.835	5	0
P.J. Hoffmaster	US-MI-PJ1	82	43.131	-86.274	0.5	0.2	57	3.0	8.8	2.9	1.677	1.19E+06	0.125	29	14
	US-MI-PJ2	76	43.131	-86.274	0.4	0.1	65	2.5	5.4	2.1	1.398	7.96E+05	0.087	33	17
	US-MI-PJ3	69	43.131	-86.274	0.3	0.1	56	2.3	6.1	2.7	1.144	7.99E+05	0.068	31	13
Petoskey	US-MI-PE1	96	45.408	-84.908	0.2	0.1	N/A	4.3	N/A	N/A	0.642	7.16E+04	0.017	29	20
	US-MI-PE2	81	45.408	-84.908	0.2	0.1	N/A	2.9	N/A	N/A	0.64	1.33E+05	0.019	31	10
Point Reyes Seashore	US-CA-PR1	128	38.094	-122.966	0.8	0.1	14	7.2	60.7	8.4	2.007	1.04E+05	0.131	5	1
	US-CA-PR2	128	38.094	-122.966	0.4	0.1	11	3.9	40.2	10.2	1.134	4.98E+04	0.052	8	3
	US-CA-PR3	129	38.094	-122.966	0.5	0.1	N/A	6.5	N/A	N/A	1.085	1.92E+04	0.042	2	2
Van Buren	US-MI-VB1	68	42.335	-86.304	0.3	0.2	N/A	1.9	N/A	N/A	1.087	3.62E+05	0.066	26	4
	US-MI-VB2	69	42.335	-86.304	0.4	0.3	N/A	1.4	N/A	N/A	1.48	1.67E+06	0.125	31	10
Warren Dunes	US-MI-WI1	92	41.913	-86.588	0.6	0.1	30	5.0	20.4	4.1	1.683	1.04E+06	0.115	31	7
	US-MI-WI2	97	41.913	-86.588	0.4	0.2	37	2.3	9.4	4.2	1.04	N/A	0.076	31	9
	US-MI-WI3	74	41.913	-86.588	0.2	0.1	21	2.5	10.2	4.0	0.626	1.61E+05	0.024	30	7
	US-MI-WD1	73	41.913	-86.588	0.4	0.1	35	3.0	12.9	4.3	1.332	8.77E+05	0.086	32	16

		US-MI-WD2	81	41.913	-86.588	0.4	0.1	69	3.0	5.8	1.9	1.309	1.18E+06	0.087	32	12
		US-MI-WD3	88	41.913	-86.588	0.5	0.1	50	3.4	10.0	2.9	1.559	1.31E+06	0.116	31	9
		US-MI-WD4	82	41.913	-86.588	0.4	0.2	54	2.6	7.5	2.8	1.216	1.09E+06	0.083	29	11
Wales	Newborough	WA-IA-NB1	23	53.142	-4.366	0.1	0.1	8	1.8	17.0	9.5	0.46	1.21E+04	0.011	22	9
		WA-IA-NB2	22	53.142	-4.366	0.1	0.0	8	3.3	18.3	5.5	0.405	1.18E+04	0.008	21	12
		WA-IA-NB3	24	53.142	-4.366	0.1	0.0	9	3.3	15.9	4.8	0.41	1.00E+04	0.008	22	5
		WA-IA-NB4	22	53.142	-4.366	0.1	0.1	14	2.1	8.8	4.3	0.467	1.28E+04	0.008	32	18
		WA-IA-NB5	25	53.142	-4.366	0.1	0.1	5	2.2	24.4	11.3	0.382	3.98E+03	0.008	22	9
		WA-IA-NB6	53	53.142	-4.366	0.1	0.1	13	1.3	7.6	5.9	0.378	8.25E+03	0.008	34	24

Appendix 6: Grain-size classification implanted in GRADISTAT v.8 and used in this study.

Size			**Sediment size class terminology**	
mm	µm	φ	**(after Friedman & Sanders, 1978)**	
2048		-11	very large boulders	boulders
1024		-10	large boulders	
512		-9	medium boulders	
256		-8	small boulders	
128		-7	large cobbles	
64		-6	small cobbles	
32		-5	very coarse pebbles	gravels
16		-4	coarse pebbles	
8		-3	medium pebbles	
4		-2	fine pebbles	
2	2000	-1	very fine pebbles	
1	1000	0	very coarse sand	sand
0.5	500	1	coarse sand	
0.25	250	2	medium sand	
0.125	125	3	fine sand	
0.063	63	4	very fine sand	
0.031	31	5	very coarse silt	
0.016	16	6	coarse silt	silt
0.008	8	7	medium silt	
0.004	4	8	fine silt	
0.002	2	9	very fine silt	
			clay	clay

Appendix 7: DEM of Long Island showing the locations of all the "chevrons" for which morphological parameters have been measured (see Appendix 4).

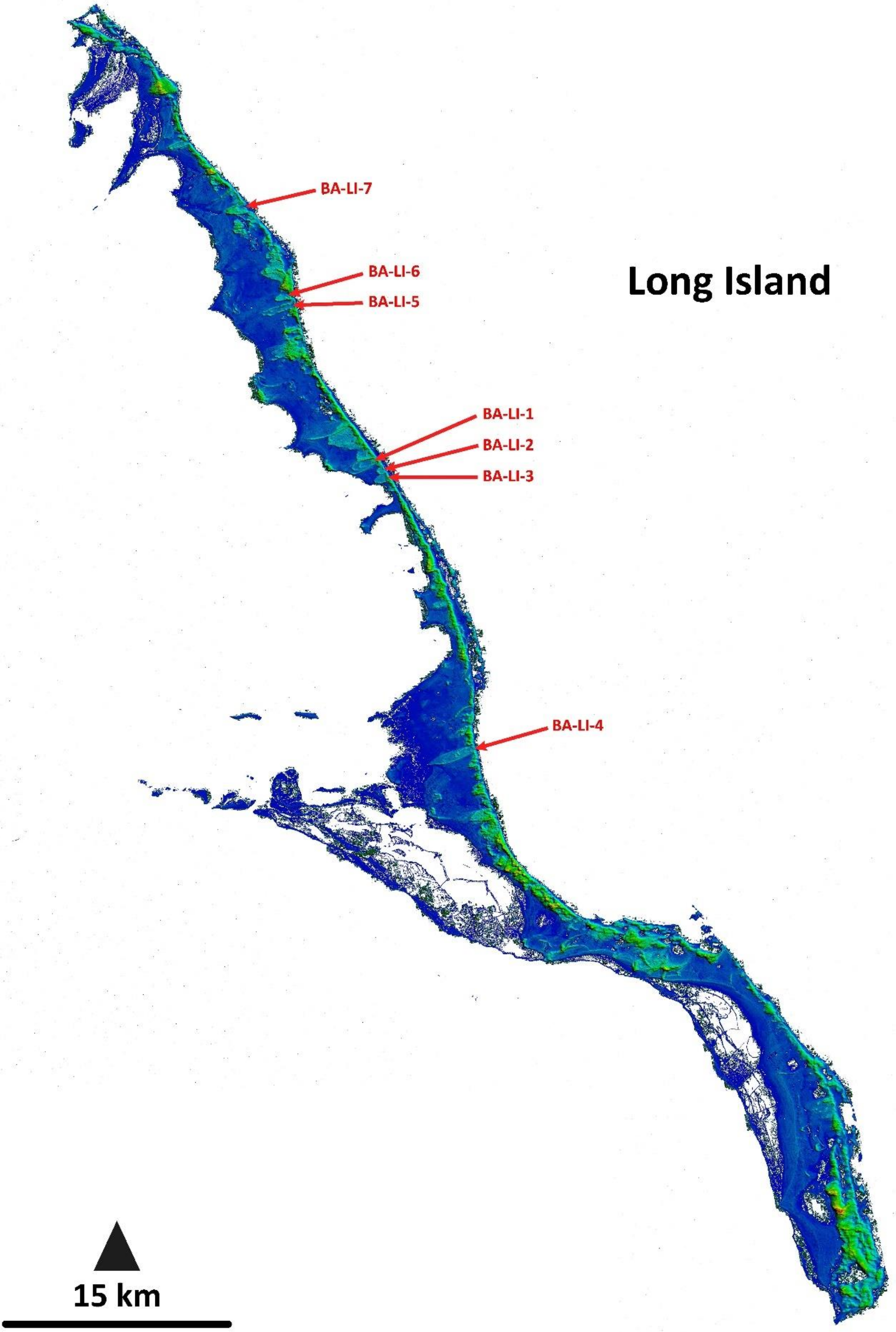

Appendix 8: Statistics obtained with the Excel macro GRADISTAT v.8 (Blott and Pye, 2001) on the grain-size distributions of "chevrons", aeolianites and beaches by applying the Folk and Ward (1957) method.

SAMPLE IDENTITY:	**Chevrons**
SAMPLE TYPE:	Bimodal, Moderately Well Sorted
SEDIMENT NAME:	Moderately Well Sorted Fine Sand
TEXTURAL GROUP:	Sand

-	-	-	-
	Geometric	**Logarithmic**	**Description**
MEAN:	272.4	1.876	Medium Sand
SORTING (s):	1.593	0.671	Moderately Well Sorted
SKEWNESS (Sk):	0.131	-0.131	Coarse Skewed
KURTOSIS (K):	0.927	0.927	Mesokurtic

Stats	**mm**	**φ**
MODE 1:	196.0	2.356
MODE 2:	327.5	1.616
MODE 3:		
D_{10}:	157.0	0.997
MEDIAN or D_{50}:	261.4	1.936
D_{90}:	500.9	2.672
(D_{90} / D_{10}):	3.192	2.679
(D_{90} - D_{10}):	344.0	1.674
(D_{75} / D_{25}):	1.946	1.683
(D_{75} - D_{25}):	183.5	0.961

GRAIN SIZE DISTRIBUTION			
GRAVEL:	0.0%	**COARSE SAND:**	9.9%
SAND:	100.0%	**MEDIUM SAND:**	42.7%
MUD:	0.0%	**FINE SAND:**	44.2%
		V FINE SAND:	3.1%
V COARSE GRAVEL:	0.0%	**V COARSE SILT:**	0.0%
COARSE GRAVEL:	0.0%	**COARSE SILT:**	0.0%
MEDIUM GRAVEL:	0.0%	**MEDIUM SILT:**	0.0%
FINE GRAVEL:	0.0%	**FINE SILT:**	0.0%
V FINE GRAVEL:	0.0%	**V FINE SILT:**	0.0%
V COARSE SAND:	0.1%	**CLAY:**	0.0%

SAMPLE IDENTITY:	**Aeolianites**
SAMPLE TYPE:	Bimodal, Moderately Well Sorted
SEDIMENT NAME:	Moderately Well Sorted Fine Sand
TEXTURAL GROUP:	Sand

-	-	-	-
	Geometric	**Logarithmic**	**Description**
MEAN:	271.3	1.882	Medium Sand
SORTING (s):	1.542	0.625	Moderately Well Sorted
SKEWNESS (Sk):	0.228	-0.228	Coarse Skewed
KURTOSIS (K):	1.159	1.159	Leptokurtic

Stats	**mm**	**φ**
MODE 1:	231.0	2.1

GRAIN SIZE DISTRIBUTION			
GRAVEL:	0.0%	**COARSE SAND:**	10.3%

MODE 2:	655.0	0.6
MODE 3:		
D_{10}:	166.3	0.9
MEDIAN or D_{50}:	258.4	2.0
D_{90}:	527.3	2.6
(D_{90} / D_{10}):	3.2	2.8
(D_{90} - D_{10}):	361.0	1.7
(D_{75} / D_{25}):	1.7	1.5
(D_{75} - D_{25}):	140.4	0.8

SAND:	100.0%	**MEDIUM SAND:**	42.1%
MUD:	0.0%	**FINE SAND:**	45.3%
		V FINE SAND:	1.5%
V COARSE GRAVEL:	0.0%	**V COARSE SILT:**	0.0%
COARSE GRAVEL:	0.0%	**COARSE SILT:**	0.0%
MEDIUM GRAVEL:	0.0%	**MEDIUM SILT:**	0.0%
FINE GRAVEL:	0.0%	**FINE SILT:**	0.0%
V FINE GRAVEL:	0.0%	**V FINE SILT:**	0.0%
V COARSE SAND:	0.7%	**CLAY:**	0.0%

[redacted]

SAMPLE IDENTITY:	**Beaches**	-
SAMPLE TYPE:	Polymodal, Moderately Sorted	
SEDIMENT NAME:	Slightly Very Fine Gravelly Medium Sand	
TEXTURAL GROUP:	Slightly Gravelly Sand	

	-	-	-
	Geometric	**Logarithmic**	**Description**
MEAN:	377.2	1.407	Medium Sand
SORTING (s):	1.954	0.966	Moderately Sorted
SKEWNESS (*Sk*):	0.254	-0.254	Coarse Skewed
KURTOSIS (*K*):	0.870	0.870	Platykurtic

Stats	**mm**	**φ**
MODE 1:	231.0	2.1
MODE 2:	327.5	1.6
MODE 3:	655.0	0.6
D_{10}:	181.2	0.0
MEDIAN or D_{50}:	340.4	1.6
D_{90}:	983.6	2.5
(D_{90} / D_{10}):	5.4	103.3
(D_{90} - D_{10}):	802.4	2.4
(D_{75} / D_{25}):	2.8	3.2
(D_{75} - D_{25}):	404.6	1.5

GRAIN SIZE DISTRIBUTION			
GRAVEL:	1.8%	**COARSE SAND:**	24.3%
SAND:	98.2%	**MEDIUM SAND:**	34.3%
MUD:	0.0%	**FINE SAND:**	30.7%
		V FINE SAND:	1.1%
V COARSE GRAVEL:	0.0%	**V COARSE SILT:**	0.0%
COARSE GRAVEL:	0.0%	**COARSE SILT:**	0.0%
MEDIUM GRAVEL:	0.0%	**MEDIUM SILT:**	0.0%
FINE GRAVEL:	0.0%	**FINE SILT:**	0.0%
V FINE GRAVEL:	1.8%	**V FINE SILT:**	0.0%
V COARSE SAND:	7.8%	**CLAY:**	0.0%

Appendix 9: Annual wind frequency rose (A); wind speed annual (B) and monthly distribution (C) andat False Entrance. The greyed zones represent the threshold velocity of wind from which sand transport is initiated (Fryberger and Dean, 1979). D to O show the monthly wind frequency roses. All the graphs were generated based on daily-averaged (from 1990 to 2017) wind speed and direction data collected from the Power-8 NOAA database (Stackhouse et al., 2018).

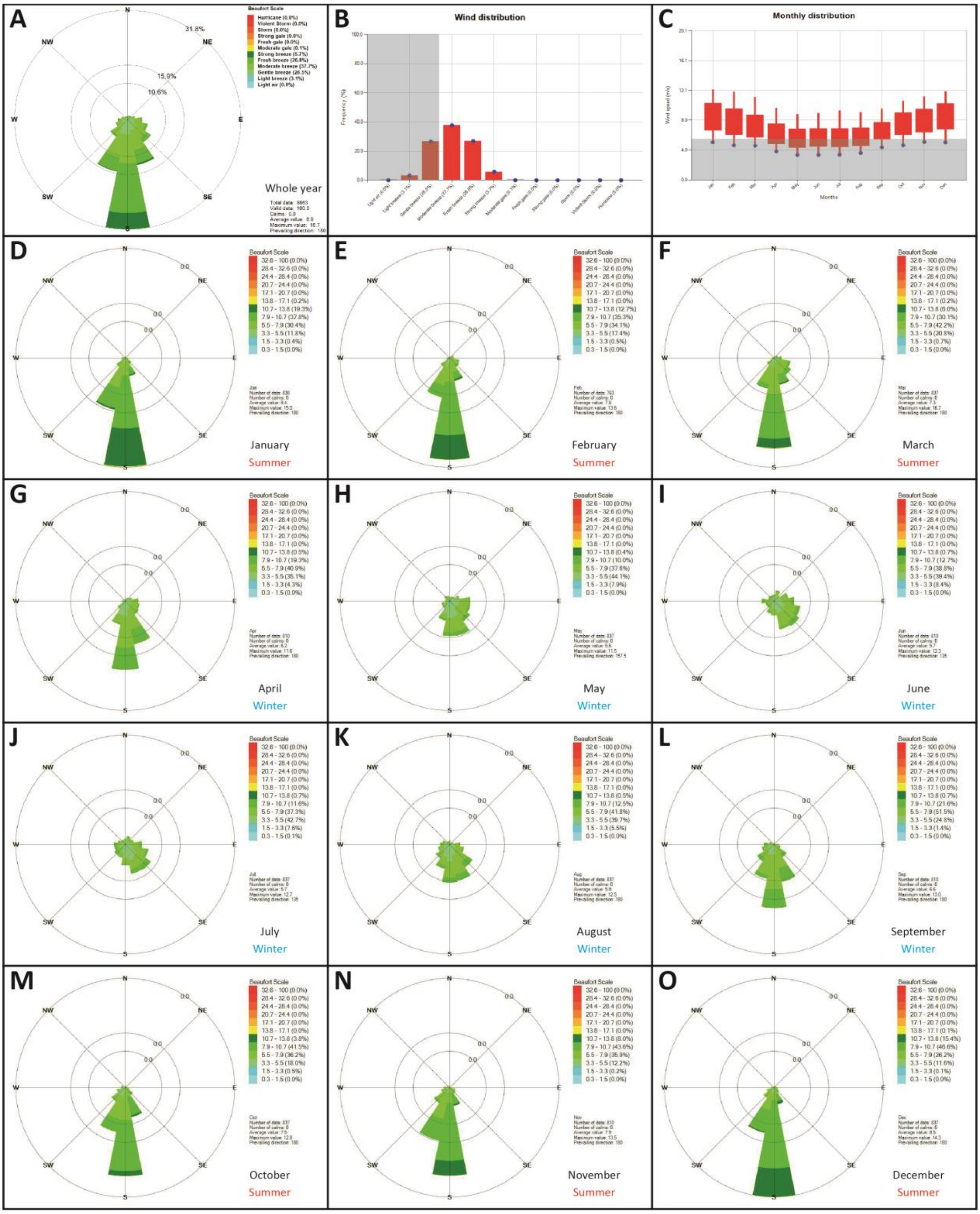

Appendix 10: List of the 109 publications reviewed for this study that mention parabolic dunes and provide a luminescence age, along with their area of focus.

Country	Region	Ref.
Argentina	Buenos Aires	Latrubesse, E., Ramonell, C., 2010. Landforms and chronology in the Pampean Sand Sea, Argentina. Abstracts Volumen, 18 International Sedimentological Congress, p.529. Mendoza, Argentina.
	Salta Province	Peña-Monné, J.L., Sancho-Marcén, C., Sampietro-Vattuone, M.M., Rivelli, F., Rhodes, E.J., Osácar-Soriano, M.C., Rubio-Fernández, V., García-Giménez, R., 2015. Geomorphological study of the Cafayate dune field (Northwest Argentina) during the last millennium. Palaeogeography, Palaeoclimatology, Palaeoecology 438, 352-363.
	San Luis	Tripaldi, A., Zárate, M.A., Forman, S.L., Badger, T., Doyle, M., Ciccioli, P.L., 2013. Geological evidence for a drought episode in the western Pampas (Argentina, South America) during the early-mid 20th century. The Holocene 23(12): 1729-1744.
Australia	New South Wales	Hesse, P.P., Williams, R., Ralph, T.J., Fryirs, K.A., Larkin, Z.T., Westaway, K.E., Farebrother, W., accepted September 2018. Palaeohydrology of lowland rivers in the Murray-Darling Basin, Australia. Quaternary Science Reviews. Thom, B., Hesp, P.,Bryant, E., 1994. Last glacial 'coastal' dunes in Eastern Australia and implications for landscape stability during the Last Glacial Maximum. Palaeogeography, Palaeoclimatology, Palaeoecology 111, 229-248. Mueller, D., Jacobs, Z., Cohen, T.J., Price, D.M., Reinfelds, I.V., Shulmeister, J., 2018. Revisiting an arid LGM using fluvial archives: a luminescence chronology for palaeochannels of the Murrumbidgee River, south-eastern Australia. Journal of Quaternary Science 0
	Northern Australia	Shulmeister, J., Lees, B., 1992. Morphology and chronostratigraphy of a coastal dunefield; Groote Eylandt, northern Australia. Geomorphology 5, 521–534. https://doi.org/10.1016/0169-555X(92)90023-H
	Queensland	Lees, B., Yanchou, L., Head, J., 1990. Reconnaissance Thermoluminescence Dating of Northern Australian Coastal Dune Systems. Quat. Res. 34, 169–185. https://doi.org/10.1016/0033-5894(90)90029-K Pye, K., Switsur, V., 1981. Radiocarbon dates from the Cape Bedford and Cape Flattery dunefields, North Queensland. Search 12, 225–226. Tejan-Kella, M., Chittleborough, D., Fitzpatrick, R., Thompson, C., Prescott, J., Hutton, J., 1990. Thermoluminescence dating of coastal sand dunes at Cooloola and North Stradbroke Island, Australia. Soil Res. 28, 465. https://doi.org/10.1071/SR9900465 Pye, K., Rhodes, E., 1985. Holocene development of an episodic transgressive dune barrier, Ramsay Bay, North Queensland, Australia. Mar. Geol. 64, 189–202. https://doi.org/10.1016/0025-3227(85)90104-5
	South Australia	Dutkiewicz, A., Prescott, J., 1997. Thermoluminescence ages and palaeoclimate from the lake Malata-Lake Greenly Complex, Eyre Peninsula, South Australia. Quat. Sci. Rev. 16, 367–385. https://doi.org/10.1016/S0277-3791(97)89532-7 Murray-Wallace, C., Bourman, R., Prescott, J., Williams, F., Price, D., Belperio, A., 2010. Aminostratigraphy and thermoluminescence dating of coastal aeolianites and the later Quaternary history of a failed delta: The River Murray mouth region, South Australia. Quat. Geochronol. 5, 28–49. https://doi.org/10.1016/j.quageo.2009.09.011 Lomax, J., Hilgers, A. and Radtke, U., 2011. Palaeoenvironmental change recorded in the palaeodunefields of the western Murray Basin, South Australia - New data from single grain OSL-dating. Quaternary Science Reviews, 30: 723-736.
Belgium	West Flanders	De Ceunynck, R., 1985. The evolution of the coastal dunes in the western Belgian coastal plain. Eiszeitalt. Ggw. 35, 33–41.

		Depuydt, F., 1967. Bijdrage tot de geomorfologische en fytogeografische studie van het domaniaal natuurreservaat De Westhoek. Ministere de l’agriculture, Administration des eaux et forets, Service des reserves naturelles domaniales et de la conservation de la nature.
Bolivia	Bolivian Chaco	May, J.-H., Zech, R., Veit, H., 2008. Late Quaternary paleosol–sediment-sequences and landscape evolution along the Andean piedmont, Bolivian Chaco. Geomorphology 98, 34–54. https://doi.org/10.1016/j.geomorph.2007.02.025
	Santa Cruz de la Sierra	Latrubesse, E.M., Stevaux, J.C., Cremon, E.H., May, J.-H., Tatumi, S.H., Hurtado, M.A., Bezada, M., Argollo, J.B., 2012. Late Quaternary megafans, fans and fluvio-aeolian interactions in the Bolivian Chaco, Tropical South America. Palaeogeography, Palaeoclimatology, Palaeoecology 356-357, 75-88.
Brazil	Bahia	De Olivera, P.E., Barreto, A.M.F., Suguio K., 1999. Late Pleistocene/Holocene climatic and vegetational history of the Brazilian caatinga: the fossil dunes of the middle São Francisco River. Palaeogeography, Palaeoclimatology, Palaeoecology 152(3-4): 319-337
	Santa Catarina	Zular, A., Sawakuchi, A., Guedes, C., Mendes, V., Nascimento, D., Giannini, P., Aguiar, V., DeWitt, R., 2013. Late Holocene intensification of colds fronts in southern Brazil as indicated by dune development and provenance changes in the São Francisco do Sul coastal barrier. Mar. Geol. 335, 64–77. https://doi.org/10.1016/j.margeo.2012.10.006
Canada	Alberta	Wolfe, S. A., J. Ollerhead, R. Smith, and M. Lamothe. 2002. Age and paleoenvironmental significance of Late Wisconsinan dune fields in the Mount Watt (84-K) and Fontas River (94-I) map sheets, northern Alberta and British Columbia. Geological Survey of Canada, Current Research 2007-B4: 12 p..
	British Columbia	Wolfe, S.A. I. J. Walker and D.J. Huntley. 2008. Holocene coastal reconstruction, Naikoon Peninsula, northern Graham Island, Queen Charlotte Islands, British Columbia. Geological Survey of Canada, Current Research, 2008-12, 16 p.
	Manitoba	Wolfe, S.A., Muhs, D.R., David, P.P., McGeehin, J.P., 2000. Chronology and geochemistry of late Holocence eolian deposits in the Brandon Sand Hills, Manitoba, Canada. Quaternary International 67, 61-74. Wolfe, S. A., D. J. Huntley, and J. Ollerhead. 2002. Optical dating of modern and late Holocene dune sands in the Brandon Sand Hills, southwestern Manitoba. Geographie physique et Quaternaire 56(2-3): 203-214.
	Northwest Territories	McNeely, R, 2005. Geological Survey of Canada Radiocarbon Dates XXXIV. GSC Current Research 2005. Michaud, Y. and C. Begin 2000. Past environmental change recorded in dune fields. Geological Survey of Canada; The Physical Environment of the Mackenzie Valley, Northwest Territories: a Base Line for the Assessment of Environmental Change Bulletin 547(79-87). Rampton, V. N., 1988. Quaternary Geology of the Tuktoyaktuk coastlines, Northwest Territories. Geological Survey of Canada Memoir 423. Wolfe, S. A., D. J. Huntley, and J. Ollerhead. 2004. Relict late Wisconsinan dune fields of the Northern Great Plains, Canada" Geographie physique et Quaternaire 58(2-3): 323-336.
	Ontario	Loope, H.M., Loope, W.L., Goble, R.J., Fisher, T.G., Jol, H.M., Seong, J.C., 2010. Early Holocene dune activity linked with final destruction of Glacial Lake Minong, eastern Upper Michigan, USA. Quaternary Research, 74(1), 73-81.
	Quebec	Lowdon, J. A., Robertson, I. M., 1971. Geological Survey of Canada Radiocarbon Dates XI. Geological Survey of Canada Paper(71-7), 269-270.

		Filion, L., 1987. Holocene development of parabolic dunes in the central St. Lawrence lowland, Quebec. Quaternary Research 28, 196-209. Carcaillet, C., Richard, P.J.H., Asnong, H., Capece, L., Bergeron, Y., 2006. Fire and soil erosion history in East Canadian boreal and temperate forests. Quaternary Science Reviews 25, 1489-1500. Fillion, L., 1987. Holocene development of parabolic dunes in the Central St. Lawrence Lowland, Québec. Quat. Res. 28, 196–209.
	Saskatchewan	Wolfe, S.A. Huntley, D.J., Ollerhead, J., 1994. Recent and late Holocene sand dune activity in southwestern Saskatchewan. Geological Survey of Canada, Current Research 1995-B, 131-140 Wolfe, S. A., J. Ollerhead, and O. Lian. 2002. Holocene eolian activity in south-central Saskatchewan and the southern Canadian prairies. Geographie physique et Quaternaire 56(2-3): 215-227. Wolfe, S.A.. C. Hugenholtz, C. Evans, D. Huntley and J. Ollerhead. 2007. Potential aboriginal occupation-induced dune activity, Elbow Sand Hills, northern Great Plains, Canada. Great Plains Research. v. 17, 173-192. Wolfe, S.A., J. Ollerhead, D.J. Huntley and O.B. Lian. 2006. Holocene dune activity and environmental change in the prairie parkland and boreal forest, central Saskatchewan, Canada. The Holocene, v. 16, p. 17- 29 Morlan, R.E., McNeely, R., Nielsen, E., Wolfe, S. A., Schreiner, B.T., 2002. Quaternary dates and vertebrate faunas in Saskatchewan. Geological Survey of Canada, Open File 3888, 139p. Wolfe, S.A., J. Bond and M. Lamothe. 2011. Dune stabilization in central and southern Yukon in relation to early Holocene environmental change, northwestern North America. Quaternary Science Review, 30, 324-334. Wolfe, S. A., D. J. Huntley, et al. 2001. Late 18th century drought-induced sand dune activity, Great Sand Hills, Saskatchewan. Canadian Journal of Earth Sciences 38(1): 105-117.
China	Gonghe Basin	Qiang, M., Chen, F., Song, L., Liu, X., Li, M., Wang, Q., 2013. Late Quaternary aeolian activity in Gonghe Basin, northeastern Qinghai-Tibetan Plateau, China. Quaternary Research, 79(3), 403-412.
	Hulun Buir	Guo, L., Xiong, S., Dong, X., Ding, Z., Yang, P., Zhao, H., Wu, J., Ye, W., Jin, G., Wu, W., Zheng, L., 2018. Linkage between C4 vegetation expansion and dune stabilization in the deserts of NE China during the late Quaternary. Quat. Int. https://doi.org/10.1016/j.quaint.2018.10.026
	Inner Mongolia	Li, S., Sun, J., Zhao, H., 2002. Optical dating of dune sands in the northeastern deserts of China. Palaeogeography, Palaeoclimatology, Palaeoecology 181, 419-429. Mason, J. A., Lu, H., Zhou, Y., Miao, X., Swinehart, J. B., Liu, Z., Goble, R. J., Yi, S., 2009. Dune mobility and aridity at the desert margin of northern China at a time of peak monsoon strength. Geology 37, 947 - 950. Yang, X., Wang, X., Liu, Z., Li, H., Ren, X., Zhang, D., Ma, Z., Rioual, P., Jin, X., Scuderi, L., 2013. Initiation and variation of the dune fields in semi-arid China - with a special reference to the Hunshandake Sandy Land, Inner Mongolia. Quaternary Science Reviews Yang, X., Zhu, B., Wang, X., Li, C., Zhou, Z., Chen, J., Wang, X., Yin, J., Lu, Y., 2008. Late Quaternary environmental changes and organic carbon density in the Hunshandake Sandy Land, eastern Inner Mongolia, China. Global and Planetary Change 61, 70-78.
	Qaidam Basin	Yu, L., Lai, Z., 2014. Holocene climate change inferred from stratigraphy and OSL chronology of aeolian sediments in the Qaidam Basin, northeastern Qinghai,Tibetan Plateau. Quaternary Research, 81(3), 488-499.

	Qinghai	Lu, H., Zhao, C., Mason, J., Yi, S., Zhao, H., Zhou, Y., unfeng, J., Swinehart, J., Wang, C., 2011. Holocene climatic changes revealed by aeolian deposits from the Qinghai Lake area (northeastern Qinghai-Tibetan Plateau) and possible forcing mechanisms. Holocene, 21, 297-304
Denmark	Anholt Island	Clemmensen, L., Bjørnsen, M., Murray, A., Pedersen, K., 2007. Formation of aeolian dunes on Anholt, Denmark since AD 1560: A record of deforestation and increased storminess. Sediment. Geol. 199, 171–187. https://doi.org/10.1016/j.sedgeo.2007.01.042
	Jutland	Clemmensen, L., Andreasen, F., Nielsen, S., Sten, E., 1996. The late Holocene coastal dunefield at Vejers, Denmark: characteristics, sand budget and depositional dynamics. Geomorphology 17, 79–98. https://doi.org/10.1016/0169-555X(95)00096-N Jonassen, H., 1957. Bidrag til Filsøegnens naturhistorie 14. Clemmensen, L., Pye, K., Urray, R., 2001. Sedimentology, stratigraphy and landscape evolution of a Holocene coastal dune system, Lodbjerg, NW Jutland, Denmark 25.
Finland	Saarijärvi-Viitsasaari	Mäkelä, J., Illmer, K., 1990. The parabolic blowout dune of Kangasjärvi in Saarijärvi, central Finland. Bull. Geol. Soc. Finl. 62, 135–147. https://doi.org/10.17741/bgsf/62.2.004
France	Aquitaine	Bertran, P., Bateman, M., Hernandez, M., Mercier, N., Millet, D., Sitzia, L., Tastet, J.-P., 2011. Inland aeolian deposits of south-west France: facies, stratigraphy and chronology. J. Quat. Sci. 26, 374–388. https://doi.org/10.1002/jqs.1461
India	Rajasthan	Srivastava, A., Thomas, D.S.G., Durcan, J.A., 2019. Holocene dune activity in the Thar Desert, India. Earth Surface Processes and Landforms Singhvi, A.K., Kar, A., 2004. The aeolian sedimentation record of the Thar Desert. Proceedings of the Indian Academy of Sciences (Earth Sciences) 113, 371-401.
Mozambique	Maputo	Armitage, S. J., Botha, G. A., Duller, G. A. T., Wintle, A. G., Rebêlo, L. P., & Momade, F. J. (2006). The formation and evolution of the barrier islands of Inhaca and Bazaruto, Mozambique. *Geomorphology*, *82*(3-4), 295-308.
Poland	Glogów-Baruth Urstromtal	Hilgers, A., 2007. The chronology of Late Glacial and Holocene dune development in the northern Central European lowland reconstructed by optically stimulated luminescence (OSL) dating, Geographisches Institut. Universität zu Köln, Köln, Germany, p. 353.
	Sandomierz Basin	Wojtanowicz, J., 1999. Problem of occurrence and age (TL) of inland Plenivistulian dunes in Poland (on the example of Sandiomierz Basin. In: W. Schirmer (Ed.), Dunes and Fossil Soils. Geo Archaeo Rhein. Lit Verlag, Münster, Germany, pp. 43-54.
	Warta Pradolina	Zieliński.P., Sokołowski, R., Fedorowicz, S., Jankowski, M., 2011. Stratigraphic position of fluvial and aeolian deposits in the Żabinko site (W Poland) based on TL dating. Geochronometria 38, 64-71.
South Africa	Kwazulu-Natal	Porat, N., Botha, G., 2008. The luminescence chronology of dune development on the Maputaland coastal plain, southeast Africa. Quat. Sci. Rev. 27, 1024–1046. https://doi.org/10.1016/j.quascirev.2008.01.017
	Northern Cape	Stokes, S., Thomas D.S.G., Washington R., 1997. Multiple episodes of aridity in southern Africa since the last interglacial period. Nature 388: 154-158.
Sudan	Wadi Howar	Bubenzer, O., Besler, H., Hilgers, A., 2007. Filling the gap: OSL data expanding 14C chronologies of late Quaternary environmental change in the Lybian Desert. Quaternary International 175, 41-52

Sweden	Jämtland	Bernhardson, M., Alexanderson, H., 2018. Early Holocene NW-W winds reconstructed from small dune fields, central Sweden. Boreas 47, 869–883. https://doi.org/10.1111/bor.12307
	Värmland	Alexanderson, H., Fabel, D., 2015. Holocene Chronology of the Brattforsheden Delta and Inland Dune Field, Sw Sweden. Geochronometria 42. https://doi.org/10.1515/geochr-2015-0001
United States	Alaska	Reuther, J.D., Potter, B.A., Holmes, C.E., Feathers, J.K., Lanoë, F.B., Kielhofer, J., 2016. The Rosa-Keystone Dunes Field: The geoarchaeology and paleoecology of a late Quaternary stabilized dune field in Eastern Beringia. The Holocene.
		Wiles, G., McAllister, R., Davi, N., Jacoby, G., 2003. Eolian Response to Little Ice Age Climate Change, Tana Dunes, Chugach Mountains, Alaska, U.S.A. Arct. Antarct. Alp. Res. 35, 67–73. https://doi.org/10.1657/1523-0430(2003)035[0067:ERTLIA]2.0.CO;2
	California	Stokes, S., Kocurek, G., Pye, K., Winspear, N.R., 1997. New evidence for the timing of aeolian sand supply to the Algodones dunefield and East Mesa area, southeastern California, USA. Palaeogeography, Palaeoclimatology, Palaeocology 128, 63-75.
	Colorado	Forman, S.L., Oglesby, R., Markgraf, V., Stafford, T., 1995. Paleoclimatic significance of Late Quaternary eolian deposition on the Piedmont and High Plains, Central United States. Global and Planetary Change 11, 35–55.
		Madole, R.F., 1995. Spatial and temporal patterns of late Quaternary eolian deposition, eastern Colorado, USA. Quaternary Science Reviews 14, 155–177.
		Forman, S.L., Spaeth, M., Marin, L., Pierson, J., Gómez, J., Bunch, F., Valdez, A., 2006. Episodic Late Holocene dune movements on the sand sheet area, Great Sand Dunes National Park and Preserve, San Luis Valley, Colorado, USA. Quaternary Research 66, 119-132.
		Forman, S., Goetz, A., Yuhas, R., 1992. Large-scale stabilized dunes on the High Plains of Colorado: Understanding the landscape response to Holocene climates with the aid of images from space. Geology 20, 145. https://doi.org/10.1130/0091-7613(1992)020<0145:LSSDOT>2.3.CO;2
		Forman, S.L., Maat, P., 1990. Stratigrahic evidence for late Quaternary dune activity near Hudson on the the Piedmont of northern Colorado. Geology 18, 745–748.
	Georgia	Leigh, D.S., Srivastava, P., Brook, G.A., 2004. Late Pleistocene braided rivers of the Atlantic Coastal Plain, USA. Quaternary Science Reviews 23, 65-84.
		Ivester, A.H., Leigh, D.S., Godfrey-Smith, D.I., 2001. Chronology of Inland Eolian Dunes on the Coastal Plain of Georgia, USA. Quaternary Research 55, 293-302.
		Leigh, D.S., 2008. Late Quaternary climates and river channels of the Atlantic Coastal Plain, Southeastern USA. Geomorphology 101, 90-108.
	Idaho	Forman, S.L., Pierson, J., 2003. Formation of linear and parabolic dunes on the eastern Snake River Plain, Idaho in the nineteenth century. Geomorphology 56, 189-200.
		Rich, J., Rittenour, T.M., Nelson, M.S., Owen, J., 2015. OSL chronology of middle to late Holocene aeolian activity in the St. Anthony dune field, southeastern Idaho, USA. Quaternary International 362, 77-86.
	Illinois	Miao, X., Hanson, P.R., Wang, H., Young, A.R., 2010. Timing and origin for sand dunes in the Green River Lowland of Illinois, upper Mississippi River Valley, USA. Quaternary Science Reviews 29, 763–773

Indiana	Kilibarda, Z., Blockland, J., 2011. Morphology and origin of the Fair Oaks Dunes in NW Indiana, USA. Geomorphology 125, 305–318
	Fisher, T.G., Horton, J., Lepper, K., Loope, H.M., 2019. Aeolian activity during Late Glacial time, with an example from Mongo, Indiana, USA. Canadian Journal of Earth Sciences 56, 175-182.
Kansas	Arbogast, A., 1996. Stratigraphic evidence for late-Holocene aeolian sand mobilization and soil formation in south-central Kansas, U.S.A. J. Arid Environ. 34, 403–414. https://doi.org/10.1006/jare.1996.0120
	Halfen, A.F., Johnson, W.C., Hanson, P.R., Woodburn, T.L., Young, A.R., Ludvigson, G.A., 2012. Activation history of the the Hutchinson dunes in east-central Kansas, USA during the past 2200 years. Aeolian Research 5, 9-20.
Massachusetts	Forman, S., Sagintayev, Z., Sultan, M., Smith, S., Becker, R., Kendall, M., Marìn, L., 2008. The twentieth-century migration of parabolic dunes and wetland formation at Cape Cod National Sea Shore, Massachusetts, USA: landscape response to a legacy of environmental disturbance. The Holocene 18, 765–774. https://doi.org/10.1177/0959683608091796
Michigan	Arbogast, A.F., Packman, S.C., 2004. Middle-Holocene mobilization of aeolian sand in western upper Michigan and the potential relationship with climate and fire. The Holocene 14, 464–471
	Hansen, E.C., Arbogast, A.F., Packman, S.C., Hansen, B., 2002. Post-Nipissing origin of a backdune complex along the southeastern shore of Lake Michigan. Physical Geography 23, 233–244.
	Timmons, E., Fisher, T., Hansen, E., Eisaman, E., Daly, T., Kashgarian, M., 2007. Elucidating aeolian dune history from lacustrine sand records in the Lake Michigan Coastal Zone, USA. The Holocene 17, 789–801. https://doi.org/10.1177/0959683607080520
	Arbogast, A.F., Bigsby, M.E., CeVisser, M.H., Langley, S.A., Hanson, P.R., Daly, T.A., Young, A.R., 2010. Reconstructing the age of coastal sand dunes along the northwestern shore of Lake Huron in Lower Michigan: Paleoenvironmental implications and regional comparisons. Aeolian Research 2, 83–92
	Arbogast, A.F., Wintle, A.G., Packman, S.C., 2002. Widespread middle holocene dune formation in the Upper Peninsula of Michican and the relationship to climate and the outlet-controlled lake level. Geology 30, 55–58.
	Colgan, P.M., Amidon, W.H., Thurkettle, S.A., 2017. Inland dunes on the abandoned bed of Glacial Lake Chicago indicate eolian activity during the Pleistocene-Holocene transition, southwestern Michigan, USA. Quaternary Research 87, 66-81.
	Hansen, E., Fisher, T., Arbogast, A., Bateman, M., 2010. Geomorphic history of low-perched, transgressive dune complexes along the southeastern shore of Lake Michigan. Aeolian Res. 1, 111–127. https://doi.org/10.1016/j.aeolia.2009.08.001
	Lepczyk, X., Arbogast, A., 2005. Geomorphic History of Dunes at Petoskey State Park, Petoskey, Michigan. J. Coast. Res. 212, 231–241. https://doi.org/10.2112/02-043.1
	Arbogast, A.F., Luehmann, M.D., Miller, B.A., Wernette, P.A., Adams, K.M., Waha, J.D., O'Neil, G.A., Tang, Y., Boothroyd, J.J., Babcock, C.R., Hanson, P.R., Young, A.R., 2015. Late-Pleistocene paleowinds and aeolian sand mobilization in north-central Lower Michigan. Aeolian Research 16, 109-116.
	Lichter, J., 1995. Lake Michigan beach-ridge and dune development, lake level, and variability in regional water balance. Quat. Res. 44, 181–189.
Nebraska	Miao, X., Manson, J.A., Swinehart, J.B., Loope, D.B., Hanson, P.R., Goble, R.J., Liu, X., 2007. A 10,000 year record of dune activity, dust storms, and severe drought in the central Great Plains. Geology 35, 119–122

	Schmeisser McKean, R.L., Goble, R.J., Mason, J.B., Swinehart, J.B., Loope, D.B., 2015. Temporal and spatial variability in dune reactivation across the Nebraska Sand Hills, USA. The Holocene, 25(3), 523-535.
	Mason, J.A., Swinehart, J.B., Hanson, P.R., Loope, D.B., Goble, R.J., Miao, X., Schmeisser, R.L., 2011. Late Pleistocene dune activity in the central Great Plains, USA. Quaternary Science Reviews, 30, 3858-3870
	Forman, S.L., Marin, L., Pierson, J., Gomez, J., Miller, G.H., Webb, R.S., 2005. Aeolian sand depositional records from western Nebraska: landscape response to droughts in the past 1500 years. The Holocene 15, 973–981.
New Mexico	Smith, G.D., McFaul, M.D., 1997. Paleoenvironmental and geoarchaeologic implications of late Quaternary sediments and paleosols: north-central to southwestern San Juan basin, New Mexico. Geomorphology 21, 107-138.
	Hall, S.A., Goble, R.G., 2016. Permian Basin Research Design 2016-2026 Volume II: Quaternary and Archaeological Geology of Southeastern New Mexico. SWCA Environmental Consultants, Albuquerque, New Mexico, p. 151.
South Carolina	Swezey, C.S., Schultz, A.P., González, W.A.n., Bernhardt, C.E., Doar Iii, W.R., Garrity, C.P., Mahan, S.A., McGeehin, J.P., 2013. Quaternary eolian dunes in the Savannah River valley, Jasper County, South Carolina, USA. Quaternary Research 80, 250-264.
South Dakota	Baldauf, P.E., Burkhart, P.A., Hanson, P.R., Miles, M., Larsen, A., 2019. Chronology of dune development in the White River Badlands, northern Great Plains, USA. Aeolian Research 37, 14-24.
	Rawling, J.E., Fredlund, G.G., Mahan, S.A., 2003. Aeolian cliftop deposits and buried soils in the White River Badlands, South Dakota, USA. The Holocene 13, 121–129.
Texas	Forman, S.L., Nordt, L., Gomez, J., Pierson, J., 2009. Late Holocene dune migration on the south Texas sand sheet. Geomorphology 108, 159–170.
Virginia	Markewich, H.W., Litwin, R.J., Pavich, M.J., Brook, G.A., 2009. Late Pleistocene eolian features in southeastern Maryland and Chesapeake Bay region indicate strong WNW-NW winds accompanied growth of the Laurentide Ice Sheet. Quaternary Research 71, 409-425.
Wisconsin	Rawling III, J.E., Hanson, P.R., Young, A.R., Attig, J.W., 2008. Late Pleistocene dune construction in the Central Sand Plain of Wisconsin, USA. Geomorphology 100, 494–505
Wyoming	Halfen, A.F., Fredlund, G.G., Mahan, S.A., 2010. Holocene stratigraphy and chronology of the Casper Dune Field, Casper, Wyoming, USA. Holocene 20, 773–783
	Stokes, S., Gaylord, D.R., 1993. Optical dating of Holocen dune sands in the Ferris Dune Field, Wyoming. Quaternary Research 39, 274–281.
	Mayer, J.H., Mahan, S.A., 2004. Late Quaternary stratigraphy and geochronology of the western Killpecker Dunes, Wyoming, USA. Quaternary Research 61, 72–84.

Appendix 11: List of ages obtained for dunes active during the last 1 ka BP, their location, the corresponding luminescence method, and protocol applied. The main associated publications are also listed, along with the interpretations of the factor(s) triggering dune activity.

Country	Region	Location	Lab. Id	Depth (m)	Age	±	Lat.	Long.	Dating Type	Protocol	Cause
Argentina	Salta Province	Cafayate	K0159	1.2	220	60	-26.050	-65.885	OSL	SAR	Drought. Potentially amplified by spanish occupation with overgrazing in the lowlands of the region because the valley was used to breed mules for the Alto Perú (Peña-Monné et al., 2015; Rodríguez, 2008).
			K0160	1.5	230	50	-26.050	-65.885	OSL	SAR	
			K0161	2.5	350	50	-26.051	-65.887	OSL	SAR	
			K0162	3.0	410	40	-26.051	-65.887	OSL	SAR	
			K0160	1.2	990	80	-26.050	-65.885	OSL	SAR	
	San Luis	Pampean sand sea	UIC2372	1.0	60	5	-33.967	-65.576	OSL	SAR	Drought. Amplified with european settlers replacing native grasses and woodland trees by wheat for agriculture (Tripaldi et al., 2013).
			UIC2376	3.0	70	10	-33.854	-65.405	OSL	SAR	
			UIC2805	0.6	70	10	-33.534	-65.331	OSL	SAR	
			UIC3281	0.4	70	10	-33.142	-65.363	OSL	SAR	
			UIC3286	2.8	75	10	-33.142	-65.363	OSL	SAR	
			UIC2377	2.8	200	20	-33.854	-65.405	OSL	SAR	
Australia	South Australia	Mallee	BM1	1.0	0	0	-34.227	139.656	OSL	SGR	Drought period inducing more frequent bushfires, which removed vegetation (Lomax et al., 2011).
	New South Wales	Rhyola	UOW1550	0.9	140	30	-35.116	144.518	OSL	SGR	N/A (Mueller et al., 2018).
Brazil	Bahia	rio São Francisco dunes	P-5	0.3-0.5	900		-10.400	-43.220	TL	N/A	Arid Late Holocene linked with a northward displacement of the ITCZ (De Oliveira et al., 1999).

Canada	Saskatchewan	Bigstick	SFU-O-130	0.8	85	5	50.181	-109.157	IRSL	MAAD	Drought (Wolfe et al., 2001).
			SFU-O-125	4.0	91	5	50.185	-109.211	IRSL	MAAD	
			SFU-O-154	0.6	117	6	50.182	-109.160	IRSL	MAAD	
			SFU-O-155	0.7	151	5	50.182	-109.160	IRSL	MAAD	
		Burstall	SFU-O-146	0.5	92	7	50.707	-109.907	IRSL	MAAD	
			SFU-O-149	3.2	163	7	50.703	-109.911	IRSL	MAAD	
			SFU-O-129	3.0	168	9	50.703	-109.911	IRSL	MAAD	
		Elbow	SFU-O-223	2.5	145	20	51.025	-106.528	IRSL	MAAD	Drought (Wolfe et al., 2002b).
			SFU-O-229	2.0	215	17	51.022	-106.526	IRSL	MAAD	
			SFU-O-254	0.8	140	20	51.050	-106.445	IRSL	MAAD	Drought amplified by bison grazing (Wolfe et al., 2007a).
			SFU-O-255	0.8	235	15	51.051	-106.455	IRSL	MAAD	
			SFU-O-256	0.8	320	20	51.054	-106.460	IRSL	MAAD	
		Great Sand Hills	SFU-O-150	0.8	115	5	50.703	-109.303	IRSL	MAAD	Drought (Wolfe et al., 2001).
			SFU-O-153	1.0	116	5	50.703	-109.303	IRSL	MAAD	
			SFU-O-152	0.8	129	6	50.703	-109.303	IRSL	MAAD	
			SFU-O-151	0.9	143	9	50.703	-109.303	IRSL	MAAD	
			SFU-O-128	4.0	216	11	50.693	-109.283	IRSL	MAAD	
			SFU-O-126	3.0	640	60	50.518	-109.144	IRSL	MAAD	

	SFU-O-127	6.0	930	50	50.529	-109.135	IRSL	MAAD
Seward	SFU-O-132	0.5	94	6	50.230	-108.253	IRSL	MAAD
	SFU-O-134	0.5	94	6	50.230	-108.253	IRSL	MAAD
	SFU-O-124	8.0	109	8	50.240	-108.253	IRSL	MAAD
	SFU-O-133	0.5	116	7	50.230	-108.253	IRSL	MAAD
	SFU-O-141	0.5	117	7	50.233	-108.253	IRSL	MAAD
	SFU-O-131	0.5	123	6	50.230	-108.253	IRSL	MAAD
	SFU-O-136	0.5	125	5	50.230	-108.253	IRSL	MAAD
	SFU-O-140	0.5	137	9	50.233	-108.253	IRSL	MAAD
	SFU-O-135	0.5	152	8	50.230	-108.253	IRSL	MAAD
	SFU-O-139	0.5	160	10	50.233	-108.253	IRSL	MAAD
	SFU-O-138	0.5	168	7	50.233	-108.253	IRSL	MAAD
	SFU-O-137	0.5	174	8	50.233	-108.253	IRSL	MAAD
	SFU-O-156	1.0	180	8	50.233	-108.253	IRSL	MAAD
	SFU-O-157	1.5	185	8	50.233	-108.253	IRSL	MAAD
Tunstall	SFU-O-123	6.0	68	12	50.154	-108.256	IRSL	MAAD
Westerham	SFU-O-144	0.5	105	8	50.918	-109.653	IRSL	MAAD
	SFU-O-143	0.5	129	9	50.918	-109.653	IRSL	MAAD

China	Horqin	NM-02	2.0	80	10	43.320	121.377	OSL	SAR	Climatic deterioration (historical droughts) and/or poor land use (overcultivation or overgrazing). (Guo et al., 2018).
		NM-01	0.4	110	30	43.320	121.377	OSL	SAR	
		NM-03	5.9	320	30	43.320	121.377	OSL	SAR	
	Hulun Buir Desert	XBH-02	0.7	130	10	47.732	119.317	OSL	SAR	
		XBH-03	1.1	150	30	47.732	119.317	OSL	SAR	
		HHNR-02	1.0	200	50	49.131	118.849	OSL	SAR	
		XBH-05	2.1	270	40	47.732	119.317	OSL	SAR	
	Otindag	SGDA-01	0.2	130	20	42.670	115.987	OSL	SAR	
		WRTB-01	0.8	130	10	43.046	116.007	OSL	SAR	
		WRTD-01	2.5	180	10	43.176	116.131	OSL	SAR	
		NRTL-01	0.2	710	40	42.913	116.634	OSL	SAR	
		XLHT-01	0.4	900	200	43.504	115.715	OSL	SAR	
		PKU-L219	0.4	140	10	43.251	116.133	OSL	SAR	Increased occurrence of strong dry cold fronts in spring and growing human impact (Mason et al., 2009).
		UNL-1227	6.0	630	40	42.974	115.954	OSL	SAR	
		UNL-1228	8.0	630	40	42.974	115.954	OSL	SAR	
		B-1	0.5	1000	60	43.123	114.482	OSL	SAR	Increasing of aridity due to the decrease in the intensity of East Asian summer monsoon in response to the decrease in solar radiation (Yang et al., 2013).
	Tiekui Desert	SYK1-0	0.3	23	2	36.361	97.900	IRSL	N/A	Increase of aridity (Yu and Lai, 2014).

India	Rajastan	Thar	Thar 18/1/2	1.0	50	10	26.579	72.814	OSL	post-IR blue SAR	Human activity (Srivastava et al., 2019).
			Thar 16/9/2	2.5	60	10	26.669	72.570	OSL	post-IR blue SAR	
			Thar 16/10/1	1.0	70	10	26.819	72.303	OSL	post-IR blue SAR	
			Thar 16/10/4	3.7	70	10	26.819	72.303	OSL	post-IR blue SAR	
			Thar 16/6/1	0.5	70	10	26.602	72.289	OSL	post-IR blue SAR	
			Thar 16/6/5	5.0	70	10	26.602	72.289	OSL	post-IR blue SAR	
			Thar 16/9/1	1.5	70	10	26.669	72.570	OSL	post-IR blue SAR	
			Thar 16/9/5	5.5	130	10	26.669	72.570	OSL	post-IR blue SAR	Low precipitation and human activity (Srivastava et al., 2019)
			Thar 16/9/4	4.5	140	20	26.669	72.570	OSL	post-IR blue SAR	
			Thar 18/1/4	2.0	150	30	26.579	72.814	OSL	post-IR blue SAR	
			Thar 16/4/2	1.0	160	30	26.331	72.288	OSL	post-IR blue SAR	
			Thar 16/4/1	0.3	200	30	26.331	72.288	OSL	post-IR blue SAR	
			Thar 16/1/2	0.7	390	30	26.584	72.816	OSL	post-IR blue SAR	
			Thar 16/1/1	0.5	450	60	26.584	72.816	OSL	post-IR blue SAR	
			Thar 16/1/4	6.0	550	50	26.584	72.816	OSL	post-IR blue SAR	
			Thar 16/10/8	8.2	670	10	26.819	72.303	OSL	post-IR blue SAR	
			Thar 16/4/4	2.0	840	80	26.331	72.288	OSL	post-IR blue SAR	
			TR-80	0.0	63	11	28.810	74.676	OSL	MAAD	Less rainfall during Little Ice Age and human activiy (cultivation and grazing, fuelwood collection). (Singhvi

											and Kar, 2004).
			TR-69	0.0	100	10	28.895	74.609	OSL	MAAD	
			TR-81	0.0	108	65	28.810	74.676	OSL	MAAD	
			TR-82	0.0	133	27	28.810	74.676	OSL	MAAD	
			TR-83	0.0	150	21	28.810	74.676	OSL	MAAD	
			TR-84	0.0	189	21	28.810	74.676	OSL	MAAD	
			TR-63	0.6	200	40	28.895	74.609	TL	MAAD	
			TR-77	0.0	300	100	28.895	74.609	OSL	MAAD	
			TR89	0.8	300	30	28.244	73.401	OSL	MAAD	
			TR-78	1.2	350	590	28.895	74.609	TL	MAAD	
			TR-70	0.0	400	250	28.895	74.609	OSL	MAAD	
			TR-68	0.8	400	180	28.895	74.609	TL	MAAD	
			TR-69	1.0	450	510	28.895	74.609	TL	MAAD	
			TR-77	1.0	470	170	28.895	74.609	TL	MAAD	
			TR-78	0.0	500	100	28.895	74.609	OSL	MAAD	
			TR-64	0.9	500	50	28.895	74.609	TL	MAAD	
			TR-70	1.9	830	330	28.895	74.609	TL	MAAD	
Sweden	Dalarna	Haftaheden	L15120	0.5	150	10	60.456	13.887	OSL	SAR	Increased storminess and/or land-use changes (Bernhardson and Alexanderson, 2018).

	Jämtland	Svegssjön	R061356	0.1	160	160	62.094	14.129	OSL	SAR	
	Värmland	Brattforsheden	Risø 061328	1.4	270	40	59.718	13.878	OSL	SAR	Human activity (charcoal production and slash-and-burn agriculture). (Alexanderson and Fabel, 2015).
			Risø 061329	1.2	180	10	59.718	13.878	OSL	SAR	
			Risø 061330	0.7	180	10	59.718	13.878	OSL	SAR	
United States	Colorado	Great Sand Dunes	UIC1077	2.0	16	2	37.691	-105.586	OSL	SAR	Drought (Forman et al., 2006).
			UIC1259	0.8	120	20	37.694	-105.570	OSL	SAR	
			UIC1235	0.5	170	30	37.694	-105.571	OSL	SAR	
			UIC1238	1.0	210	30	37.694	-105.571	OSL	SAR	
			UIC1138	0.8	230	30	37.694	-105.571	OSL	SAR	
			UIC1137	1.2	700	75	37.694	-105.571	OSL	SAR	
			UIC1260	1.7	710	70	37.694	-105.570	OSL	SAR	
			UIC1258	1.5	735	90	37.694	-105.570	OSL	SAR	
			UIC1086	2.0	940	80	37.694	-105.571	OSL	SAR	
		Wray Dune Field	UNL-1103	2.3	700	60	40.510	-102.359	OSL	SAR	N/A (Mason et al., 2011).
	Idaho	Snake River Plain	UIC681B	1.5	130	20	43.898	-112.372	OSL	SAR	Drought (Forman and Pierson, 2003).
			UIC681	1.5	150	30	43.898	-112.372	OSL	SAR	
	Illinois	Green River Lowlands	UNL-2135	0.5	430	110	41.486	-90.349	OSL	SAR	Droughts, wild fire, bison grazing, and aboriginal land use (Miao et al., 2010).
			UNL-2024	0.5	430	110	41.486	-90.349	OSL	SAR	

		UNL-2026	0.3	840	210	41.465	-89.906	OSL	SAR	
Indiana	Fair Oaks	UNL-2474	0.9	60	20	41.021	-87.134	OSL	SAR	Changes in land use following European settlement (Kilibarda and Blockland, 2011).
		UNL-2474	0.9	220	40	41.021	-87.134	OSL	SAR	
Kansas	Hutchinson Dunes	UNL-2555	1.6	10	20	38.133	-97.883	OSL	SAR	Arid Little Ice Age (Halfen et al., 2012).
		UNL-2556	1.7	80	80	38.130	-97.887	OSL	SAR	
		UNL-2560	1.6	80	10	38.081	-97.665	OSL	SAR	
		UNL-2698	1.8	80	10	38.176	-97.950	OSL	SAR	
		UNL-2981	1.9	80	10	38.142	-97.928	OSL	SAR	
		UNL-2983	2.1	90	10	38.143	-97.928	OSL	SAR	
		UNL-2562	1.6	100	10	38.104	-97.844	OSL	SAR	
		UNL-2696	1.8	100	10	38.085	-97.796	OSL	SAR	
		UNL-2987	2.1	100	10	38.256	-97.968	OSL	SAR	
		UNL-2558	1.8	110	10	38.084	-97.667	OSL	SAR	
		UNL-2969	1.9	110	10	38.157	-97.945	OSL	SAR	
		UNL-2091	1.8	120	10	38.098	-97.847	OSL	SAR	
		UNL-2561	5.9	140	30	38.081	-97.665	OSL	SAR	
		UNL-2985	6.4	140	20	38.230	-97.971	OSL	SAR	
		UNL-2984	2.1	140	10	38.230	-97.971	OSL	SAR	

UNL-2557	6.2	160	20	38.130	-97.887	OSL	SAR
UNL-2982	6.6	160	20	38.142	-97.928	OSL	SAR
UNL-2551	1.6	180	20	38.077	-97.788	OSL	SAR
UNL-2553	1.6	180	10	38.133	-97.884	OSL	SAR
UNL-2552	6.2	190	20	38.077	-97.788	OSL	SAR
UNL-2702	1.7	190	20	38.070	-97.802	OSL	SAR
UNL-2699	7.0	190	20	38.176	-97.950	OSL	SAR
UNL-2554	6.2	200	20	38.133	-97.884	OSL	SAR
UNL-2686	1.7	200	20	38.124	-97.885	OSL	SAR
UNL-2689	5.4	200	20	38.124	-97.886	OSL	SAR
UNL-2691	6.9	200	20	38.072	-97.757	OSL	SAR
UNL-2988	6.8	200	20	38.256	-97.968	OSL	SAR
UNL-2976	1.7	210	20	38.211	-97.995	OSL	SAR
UNL-2986	6.6	220	30	38.230	-97.971	OSL	SAR
UNL-2559	6.3	220	20	38.084	-97.667	OSL	SAR
UNL-2692	1.9	220	20	38.074	-97.822	OSL	SAR
UNL-2690	2.0	220	20	38.072	-97.757	OSL	SAR
UNL-2693	5.7	240	30	38.074	-97.822	OSL	SAR

UNL-2687	7.4	240	20	38.124	-97.885	OSL	SAR	
UNL-2700	1.8	240	20	38.061	-97.812	OSL	SAR	
UNL-2688	6.7	260	30	38.124	-97.886	OSL	SAR	
UNL-2977	5.1	270	50	38.211	-97.995	OSL	SAR	
UNL-1874	3.2	270	30	38.173	-97.944	OSL	SAR	
UNL-1881	1.5	290	20	38.118	-97.958	OSL	SAR	
UNL-1883	2.4	300	30	38.119	-97.848	OSL	SAR	
UNL-1875	2.7	320	50	38.173	-97.944	OSL	SAR	
UNL-1878	4.0	320	30	38.088	-97.855	OSL	SAR	
UNL-1879	6.7	320	30	38.088	-97.855	OSL	SAR	
UNL-1876	9.8	330	40	38.173	-97.944	OSL	SAR	
UNL-2090	7.4	350	30	38.119	-97.848	OSL	SAR	
UNL-2092	7.0	390	50	38.098	-97.847	OSL	SAR	
UNL-2703	6.5	420	50	38.070	-97.802	OSL	SAR	
UNL-1877	1.3	450	50	38.088	-97.855	OSL	SAR	
UNL-2563	6.3	520	50	38.104	-97.844	OSL	SAR	
UNL-2697	7.0	600	50	38.085	-97.796	OSL	SAR	
UNL-2701	6.9	920	90	38.061	-97.812	OSL	SAR	Arid Medieval Climatic Anomaly (Halfen et al., 2012).

		UNL-1882	7.7	920	80	38.118	-97.958	OSL	SAR	
		UNL-2694	1.7	960	80	38.082	-97.813	OSL	SAR	
		UNL-2695	7.0	960	80	38.082	-97.813	OSL	SAR	
Nebraska	Nebraska Sand Hills	UNL-896	0.5	500	40	41.831	-102.576	OSL	SAR	Arid Medieval Climatic Anomaly (Miao et al., 2007)
		UNL-929	1.4	830	50	41.531	-100.503	OSL	SAR	
		UNL-896	0.5	354	39	41.831	-102.576	OSL	SAR	Arid Medieval Climatic Anomaly (Schmeisser McKean et al., 2015).
		UNL-929	1.2	597	31	41.531	-100.503	OSL	SAR	
		UNL-1217	5.1	724	42	41.531	-100.503	OSL	SAR	
		UNL-1216	2.7	741	43	41.531	-100.503	OSL	SAR	
		UNL-930	8.2	748	44	41.531	-100.503	OSL	SAR	
		UNL-901	7.0	915	52	41.831	-102.576	OSL	SAR	
		UNL-900	5.3	917	56	41.831	-102.576	OSL	SAR	
	South of Sand Hills	UNL-1097	1.0	540	50	40.749	-101.626	OSL	SAR	N/A (Mason et al., 2011).
	Wray Dune Field	UIC993	1.0	70	10	40.040	-101.510	OSL	SAR	Dust Bowl drought (Forman et al., 2005)
		UIC986	2.0	80	10	40.040	-101.510	OSL	SAR	
		UIC992	2.5	420	30	40.040	-101.510	OSL	SAR	Megadrought in North America (16th cent.). (Forman et al., 2005)
		UIC991	3.9	540	40	40.040	-101.510	OSL	SAR	
New Mexico	Mescalero Sand Sheet	UNL-4110	0.1	110	120	32.121	-103.360	OSL	SAR	Arid Little Ice Age caused the expansion of mesquite, which changed the area into a semi-arid shrubland (Hall

										and Goble, 2016)
		UNL-4123	0.1	120	10	32.180	-103.360	OSL	SAR	
		UNL-3972	0.4	160	40	32.313	-103.812	OSL	SAR	
		UNL-3969	0.8	170	40	32.313	-103.812	OSL	SAR	
		UNL-3930	0.3	220	40	32.169	-103.833	OSL	SAR	
		UNL-4108	0.8	230	80	32.121	-103.360	OSL	SAR	
		UNL-3929	0.8	280	20	32.169	-103.833	OSL	SAR	
		UNL-4109	0.5	440	70	32.121	-103.360	OSL	SAR	
South Dakota	White River Badlands	UNL-4306	1.5	0	20	43.536	-102.633	OSL	SAR	Arid mid-Holocene period (Medevial Climate Anomaly + Little Ice Age). (Baldauf et al., 2019).
		UNL-4380	1.0	210	20	43.660	-102.271	OSL	SAR	
		UNL-4381	1.4	210	20	43.660	-102.271	OSL	SAR	
		UNL-4304	2.1	250	20	43.536	-102.633	OSL	SAR	
		UNL-4305	2.7	260	40	43.536	-102.633	OSL	SAR	
		UNL-4291	0.8	300	40	43.660	-102.271	OSL	SAR	
		UNL-4058	1.2	350	50	43.694	-102.438	OSL	SAR	
		UNL-4293	1.0	400	40	43.660	-102.271	OSL	SAR	
		UNL-4060	1.2	420	50	43.694	-102.438	OSL	SAR	
		UNL-4056	1.1	420	50	43.694	-102.438	OSL	SAR	

		UNL-4292	1.9	600	60	43.660	-102.271	OSL	SAR	
		UNL-4288	1.0	600	50	43.660	-102.271	OSL	SAR	
		UNL-4379	1.3	720	70	43.660	-102.271	OSL	SAR	
Wyoming	Casper	6055	1.5	410	190	42.926	-106.004	OSL	SAR	Drought (Halfen et al., 2010).
		6061	0.4	410	50	43.037	-106.810	OSL	SAR	
		6062	0.9	420	40	43.037	-106.810	OSL	SAR	
		6056	3.6	1000	220	42.926	-106.004	OSL	SAR	
	Killpecker Dunes	KRM-1B	0.5	615	225	42.016	-109.362	TL	MAAD	Arid Medieval Climatic Anomaly (Mayer and Mahan, 2004).
		KRM-1A	0.5	670	45	42.016	-109.362	IRSL	MAAD	

Appendix 12: List of ages obtained for dunes active during the mid-Holocene period (7.5 to 4.5 ka BP), their location, the corresponding luminescence method and protocol applied, and the main associated publication.

Country	Region	Location	Lab. Id	Depth (m)	Age	±	Lat.	Long.	Dating Type	Protocol	Ref.
Australia	New South Wales	Dry Lake	Yanco-1	3.6	5000	1000	-34.716	146.323	OSL	SGR	(Hesse et al., 2018)
	South Australia	Big Desert	CD4	0.75	7200	600	-35.548	140.789	OSL	SGR	(Lomax et al., 2011)
Bolivia	Bolivian Chaco	Andean Piedmont	PCN3-K	3.0	5614	28	-18.599	-63.095	14C	N/A	(May et al., 2008)
	Santa Cruz de la Sierra	Río Grande	BOL TL-3		6500	1100	-19.620	-62.627	OSL	MAR	(Latrubesse et al., 2012)
		Río Parapetí	BOL TL-1		6600	1400	-19.620	-62.627	OSL	MAR	(Latrubesse et al., 2012)
			BOL TL-11		5600	1200	-19.620	-62.627	OSL	MAR	(Latrubesse et al., 2012)
Canada	Alberta	Stony Plain	SFU-O-269	1.2	6200	600	53.447	-113.806	IRSL	MAAD	(Wolfe et al., 2004)
	Manitoba	Brandon Sand Hills	SFU-O-173	2.6	5600	270	49.925	-99.590	IRSL	MAAD	(Wolfe et al., 2002a)
	Québec	Lac St. Jean	GSC-1213	3.9	7160	70	48.850	-72.683	14C	N/A	(Lowdon et al., 1971)
		St. Lawrence Lowlands	I-13217	1.7	7440	270	46.552	-71.600	14C	N/A	(Filion, 1987)
		Villemontel	UQ-2113	2.2	5525	72	48.700	-78.361	14C	N/A	(Carcaillet et al., 2006)
	Saskatchewan	Elbow	SFU-O-224	5.6	5690	240	51.022	-106.526	IRSL	MAAD	(Wolfe et al., 2002b)
		Fort a la Corne	SFU-O-240	3.3	6620	310	53.292	-104.724	IRSL	MAAD	(Wolfe et al., 2006)
			SFU-O-212	2.0	6810	300	53.293	-104.724	IRSL	MAAD	(Wolfe et al., 2006)
		Manito Lake	SFU-O-221	14.5	6940	310	52.703	-109.902	IRSL	MAAD	(Wolfe et al., 2006)
			SFU-O-220	10.0	6070	310	52.703	-109.902	IRSL	MAAD	(Wolfe et al., 2006)
			SFU-O-219	7.0	4960	190	52.703	-109.902	IRSL	MAAD	(Wolfe et al., 2006)
		Nisbet	SFU-O-214	1.3	5230	250	53.285	-105.616	IRSL	MAAD	(Wolfe et al., 2006)
		North Battleford	SFU-O-216	5.9	6510	280	52.715	-108.374	IRSL	MAAD	(Wolfe et al., 2006)
			SFU-O-217	1.3	5580	270	52.715	-108.374	IRSL	MAAD	(Wolfe et al., 2006)
China	Gonghe Basin	Mugetan	MGT-A-02	1.9	5700	200	35.678	100.622	OSL	SAR	(Qiang et al., 2013)
			MGT-A-01	0.9	4500	500	35.678	100.622	OSL	SAR	(Qiang et al., 2013)
			MGT-B-01	2.0	5500	300	35.778	100.796	OSL	SAR	(Qiang et al., 2013)
	Inner Mongolia	Hulun Buir	HHNR-05	2.2	7240	600	49.131	118.849	OSL	SAR	(Guo et al., 2018)
		Hunshandake Sandy Land	PKU-L221	1.8	5020	380	43.251	116.133	OSL	SAR	(Guo et al., 2018)
		Otindag	NRTA-05	1.7	5800	400	42.899	115.636	OSL	SAR	(Guo et al., 2018)
			JPB-04	6.5	7420	340	43.075	117.123	OSL	SAR	(Guo et al., 2018)
			WRTC-04	1.9	6100	400	43.119	116.092	OSL	SAR	(Guo et al., 2018)
			JP-03	1.2	5800	300	43.183	117.283	OSL	SAR	(Guo et al., 2018)
			CGNR-05	1.1	6750	350	43.251	114.468	OSL	SAR	(Guo et al., 2018)
			CGNR-04	0.5	6430	320	43.251	114.468	OSL	SAR	(Guo et al., 2018)
			CGNR-03	0.2	6000	350	43.251	114.468	OSL	SAR	(Guo et al., 2018)
			XLHT-03	1.4	6000	300	43.504	115.715	OSL	SAR	(Guo et al., 2018)
			XLHT-02	0.7	5600	300	43.504	115.715	OSL	SAR	(Guo et al., 2018)

			BYXL-03	7.4	6770	380	43.687	116.638	OSL	SAR	(Guo et al., 2018)
	Qaidam Basin	Tiekui Desert	SYK1-5	2.6	6900	500	36.361	97.900	OSL	SAR + SGC	(Yu and Lai, 2014)
India	Rajastan	Thar	Thar 16/1/6	20.0	6860	490	26.584	72.816	OSL	post-IR blue SAR	(Srivastava et al., 2019)
			Thar 16/10/10	10.2	5430	400	26.819	72.303	OSL	post-IR blue SAR	(Srivastava et al., 2019)
			Thar 16/10/9	9.2	5190	510	26.819	72.303	OSL	post-IR blue SAR	(Srivastava et al., 2019)
			KD	155.0	7000	700	25.372	71.810	IRSL	MAAD	(Singhvi and Kar, 2004)
			TR140	1.4	5400	1300	28.244	73.401	OSL	MAAD	(Singhvi and Kar, 2004)
			TR99	3.9	5300	700	28.244	73.401	OSL	MAAD	(Singhvi and Kar, 2004)
			TR93	2.2	5200	1800	28.244	73.401	OSL	MAAD	(Singhvi and Kar, 2004)
			TR98	3.7	5100	1400	28.244	73.401	OSL	MAAD	(Singhvi and Kar, 2004)
			TR92	2.0	4700	900	28.244	73.401	OSL	MAAD	(Singhvi and Kar, 2004)
			TR-71	2.5	5350	690	28.895	74.609	TL	MAAD	(Singhvi and Kar, 2004)
			TR-79	1.4	5300	700	28.895	74.609	TL	MAAD	(Singhvi and Kar, 2004)
			TR-67	2.0	5080	680	28.895	74.609	TL	MAAD	(Singhvi and Kar, 2004)
			TR-66	1.5	4500	480	28.895	74.609	TL	MAAD	(Singhvi and Kar, 2004)
			TR-72	0.0	7500	80	28.895	74.609	OSL	MAAD	(Singhvi and Kar, 2004)
			TR-76	0.0	7200	3000	28.895	74.609	OSL	MAAD	(Singhvi and Kar, 2004)
			TR-67	0.0	6600	2400	28.895	74.609	OSL	MAAD	(Singhvi and Kar, 2004)
			TR-79	0.0	5100	1000	28.895	74.609	OSL	MAAD	(Singhvi and Kar, 2004)
			TR-66	0.0	4600	1900	28.895	74.609	OSL	MAAD	(Singhvi and Kar, 2004)
Sudan	Wadi Howar	Wadi Howar	C-L3357	2.0	7330	1210	17.283	26.750	OSL	MAR	(Bubenzer et al., 2007)
			C-L3355	2.1	7370	1140	17.600	27.500	OSL	MAAD	(Bubenzer et al., 2007)
			C-L1199	0.3	6780	480	17.600	28.117	OSL	SAR	(Bubenzer et al., 2007)
			C-L3353	3.0	6570	870	17.600	27.500	OSL	MAAD	(Bubenzer et al., 2007)
			C-L3354	2.1	6280	860	17.600	27.500	OSL	MAAD	(Bubenzer et al., 2007)
Sweden	Dalarna	Haftaheden	L15105	1.3	7500	500	60.473	13.924	OSL	SAR	(Bernhardson and Alexanderson, 2018)
	Jämtland	Svegssjön	R061354	1.9	6500	1200	62.094	14.129	OSL	SAR	(Bernhardson and Alexanderson, 2018)
			R061353	0.7	6200	700	62.094	14.129	OSL	SAR	(Bernhardson and Alexanderson, 2018)
United States	Colorado	Fort Morgan Dune Field	OTL-369	6.7	6700	700	40.101	-103.977	TL	PM	(Forman et al., 1995)
			OTL-311	2.4	6600	600	40.101	-103.977	TL	PM	(Forman et al., 1995)
			OTL-379	9.7	6600	600	40.101	-103.977	TL	PM	(Forman et al., 1995)

		OTL-378	11.0	6400	800	40.101	-103.977	TL	PM	(Forman et al., 1995)
		OTL-371	10.0	5600	700	40.101	-103.977	TL	PM	(Forman et al., 1995)
		OTL-267	5.6	6100	500	40.122	-104.617	TL	PM	(Forman et al., 1995)
		OTL-273	5.7	5300	500	40.122	-104.617	TL	PM	(Forman et al., 1995)
				6940	1300	40.230	-104.658	OSL	N/A	(Madole, 1995)
	Hudson Dune Field	GX-15840	2.0	4765	305	40.122	-104.617	14C	N/A	(Forman et al., 1992)
		GX-15785	5.5	5515	410	40.122	-104.617	14C	N/A	(Forman et al., 1992)
Illinois	Green River Lowlands	UNL-1869	0.6	5490	410	41.454	-89.908	OSL	SAR	(Miao et al., 2010)
		UNL-1863	1.4	7060	550	41.465	-89.906	OSL	SAR	(Miao et al., 2010)
		UNL-1864	1.5	6790	500	41.465	-89.906	OSL	SAR	(Miao et al., 2010)
Michigan	Eraga Dunefield	ABER-38/4	6.5	7000	700	46.606	-88.578	OSL	SAR	(Arbogast and Packman, 2004)
		ABER-38/3	1.5	6800	700	46.606	-88.578	OSL	SAR	(Arbogast and Packman, 2004)
		ABER-38/6	2.5	7300	800	46.612	-88.611	OSL	SAR	(Arbogast and Packman, 2004)
		ABER-38/5	1.5	6200	600	46.612	-88.611	OSL	SAR	(Arbogast and Packman, 2004)
		ABER-38/8	7.0	7200	800	46.632	-88.588	OSL	SAR	(Arbogast and Packman, 2004)
		ABER-38/7	1.5	7100	600	46.632	-88.588	OSL	SAR	(Arbogast and Packman, 2004)
		ABER-38/9	1.5	6500	1000	46.634	-88.614	OSL	SAR	(Arbogast and Packman, 2004)
		ABER-38/2	3.5	7100	800	46.646	-88.557	OSL	SAR	(Arbogast and Packman, 2004)
		ABER-38/1	1.5	6600	800	46.646	-88.557	OSL	SAR	(Arbogast and Packman, 2004)
	Holland Dune Field	NSRL-10345		4840	65	42.739	-86.206	14C	SAR	(Timmons et al., 2007)
	Manitou Beach Dunes	UNL-2294	2.0	6000	500	45.490	-83.978	OSL	SAR	(Arbogast et al., 2010)
	Newberry Dune Field	30/Mic6	4.0	5700	900	46.211	-84.920	OSL	SAR	(Arbogast et al., 2002b)
		30/Mic1	5.0	6800	1200	46.314	-85.911	OSL	SAR	(Arbogast et al., 2002b)
		30/Mic2	1.5	6800	800	46.314	-85.911	OSL	SAR	(Arbogast et al., 2002b)
		30/Mic3	1.0	6200	700	46.454	-85.461	OSL	SAR	(Arbogast et al., 2002b)
		30/Mic4	7.0	5100	130	46.454	-85.461	OSL	SAR	(Arbogast et al., 2002b)
		30/Mic18	1.5	6700	1200	46.457	-86.176	OSL	SAR	(Arbogast et al., 2002b)
		30/Mic19	5.0	6600	1000	46.457	-86.176	OSL	SAR	(Arbogast et al., 2002b)
		30/Mic5	4.0	5700	1200	46.625	-85.201	OSL	SAR	(Arbogast et al., 2002b)
	Petoskey State Park	Beta 132995		4620	195	45.396	-84.906	14C	SAR	(Lepczyk and Arbogast, 2005)
Nebraska	Nebraska Sand Hills	UNL-899	10.3	5650	370	41.831	-102.576	OSL	SAR	(Miao et al., 2007)
	South of Sand Hills	UNL-1366	0.8	7500	500	40.525	-101.215	OSL	SAR	(Mason et al., 2011)

South Dakota	White River Badlands	UNL-4307	1.9	7200	500	43.536	-102.633	OSL	SAR	(Baldauf et al., 2019)
		UNL-4290	1.6	6300	500	43.660	-102.271	OSL	SAR	(Baldauf et al., 2019)
		UNL-4062	1.3	7400	600	43.694	-102.438	OSL	SAR	(Baldauf et al., 2019)
		UNL-4064	1.7	6100	500	43.694	-102.438	OSL	SAR	(Baldauf et al., 2019)
Wisconsin	Central Sand Plain	UNL-1566	0.5	5800	400	44.184	-89.856	OSL	SAR	(Rawling et al., 2008)
	Casper	6059	9.3	7020	220	42.926	-106.004	OSL	SAR	(Halfen et al., 2010)
		6060	3.1	6100	230	43.120	-107.029	OSL	SAR	(Halfen et al., 2010)
		6065	1.5	6670	450	43.125	-107.367	OSL	SAR	(Halfen et al., 2010)

Appendix 13: Accuracies of the collected DEMs.

Country	State	Location	Fundamental Horizontal Accuracy (FHA,m)	Fundamental Vertical Accuracy (FVA,m)
Australia			5	0.8
Bahamas			>10	2
Brazil			>10	2
Denmark			0.4	0.05
Lybia			>10	2
Madagascar			>10	2
Netherlands			0.5	0.1
Scotland			1	
Spain			1	
USA	California	Eureka	5	
USA	California	Lompoc	5	
USA	California	Mackerricher State Park	5	
USA	California	Point Reyes Seashore	5	
USA	Colorado	Great Sand Dunes National Park	3	
USA	Idaho	St Anthony	10	
USA	Massachusetts	Cape Code	5	
USA	Michigan	Grand Marais	1	
USA	Michigan	Holland	1	
USA	Michigan	P J Hoffmaster State Park	1	
USA	Michigan	Petoskey State Park	1	
USA	Michigan	Van Buren State Park	1	
USA	Michigan	Warren Dunes State Park	1	
USA	Michigan	Wilderness State Park	1	
USA	New Mexico	White Sands National Park	1	
USA	New York	Long Island	5	
USA	Oregon	Cape Lookout	5	
USA	Oregon	Florence	5	
USA	Oregon	North Spit	5	
USA	South Carolina	Garnett	5	
USA	Texas	Baffin Bay	5	
USA	Washington	Hanford	10	
Wales			0.5	

Appendix 14: Morphological measurements and sand drift potential analysis results. For DP: white, yellow, and orange correspond to low, intermediate, and high wind energy, respectively (Fryberger and Dean, 1979). For RDP/DP: white, yellow, and orange correspond to a low, intermediate, and high directional variability of winds, respectively (Fryberger and Dean, 1979).

Country	Location	Lat.	Long.	Class (Pye, 1993)	Class (Scheffers et al., 2008)	Orient. (°)	L (km)	W (km)	H (m)	L/W	L/H	W/H	Perim. (km)	Area (km2)	DP	RDP	RDP/DP	RDD
Australia	Brooms Head	-29.699	153.304	Elongated	3	354	1.45	0.18	36	8.2	40.6	5.0	3.799	0.394	41	21	0.5	344
Australia	Cape Flattery	-15.058	145.203	Elongated	3 to 5	316	2.25	0.43	71	5.2	31.7	6.1	5.159	1.060	330	309	0.9	290
Australia	Cape Flattery	-15.058	145.203	Elongated	3 to 5	312	1.93	0.36	55	5.3	35.1	6.6	4.591	0.999	330	309	0.9	290
Australia	Cape Flattery	-15.058	145.203	Lobate	3 to 5	318	1.49	0.51	44	2.9	34.1	11.7	3.776	0.734	330	309	0.9	290
Australia	Cape Flattery	-15.058	145.203	Elongated	3 to 5	316	5.84	0.84	68	7.0	85.8	12.3	13.615	3.721	330	309	0.9	290
Australia	Cape Flattery	-15.058	145.203	Elongated	3 to 5	313	7.76	0.85	67	9.2	115.7	12.6	21.735	7.599	330	309	0.9	290
Australia	Cape Flattery	-15.058	145.203	Elongated	3 to 5	316	6.36	1.17	90	5.4	70.5	13.0	14.719	7.306	330	309	0.9	290
Australia	Cape Flattery	-15.058	145.203	Elongated	3 to 5	313	5.46	1.16	76	4.7	71.8	15.2	15.536	6.491	330	309	0.9	290
Australia	Cape Flattery	-15.058	145.203	Lobate	3 to 5	313	3.09	1.46	72	2.1	43.0	20.3	8.431	3.382	330	309	0.9	290
Australia	Cape Flattery	-15.058	145.203	Elongated	3 to 5	319	4.98	1.58	76	3.2	65.5	20.8	14.251	7.848	330	309	0.9	290
Australia	Cape Manifold	-22.782	150.781	Elongated	3 to 5	316	5.98	1.23	155	4.9	38.6	7.9	15.174	5.795	162	141	0.9	296
Australia	Cape Manifold	-22.782	150.781	Elongated	3 to 5	306	1.73	0.52	49	3.3	35.2	10.6	4.343	0.964	162	141	0.9	296
Australia	Cape Manifold	-22.587	150.770	Elongated	3 to 5	310	1.63	0.51	41	3.2	39.8	12.3	4.155	0.758	162	141	0.9	296
Australia	Cape Manifold	-22.782	150.781	Elongated	3 to 5	310	2.83	0.93	75	3.0	37.7	12.5	6.903	2.137	162	141	0.9	296
Australia	Cape Manifold	-22.782	150.781	Elongated	3 to 5	312	3.95	1.18	85	3.3	46.4	13.9	9.238	3.974	162	141	0.9	296
Australia	Cape Manifold	-22.782	150.781	Lobate	3 to 5	307	3.63	1.34	95	2.7	38.3	14.1	9.050	3.843	162	141	0.9	296
Australia	Cape Manifold	-22.782	150.781	Lobate	3 to 5	311	7.95	2.66	148	3.0	53.7	18.0	20.278	18.580	162	141	0.9	296
Australia	Cape Manifold	-22.391	150.674	Lobate	3 to 5	311	2.62	0.88	43	3.0	60.8	20.5	6.319	1.747	162	141	0.9	296
Australia	Cape Manifold	-22.782	150.781	Elongated	3 to 5	307	5.76	1.30	63	4.4	91.5	20.6	13.430	7.138	162	141	0.9	296
Australia	Cape Manifold	-22.587	150.770	Lobate	3 to 5	312	1.65	0.90	32	1.8	51.6	28.1	4.661	1.104	162	141	0.9	296
Australia	Cape Manifold	-22.782	150.781	Elongated	3 to 5	312	8.02	2.38	59	3.4	135.9	40.4	19.079	16.223	162	141	0.9	296
Australia	Cape Manifold	-22.782	150.781	Lobate	3 to 5	302	3.69	2.36	56	1.6	65.9	42.1	10.945	7.362	162	141	0.9	296
Australia	Cape Manifold	-22.587	150.770	Lobate	3 to 5	316	1.73	1.54	32	1.1	53.9	48.1	5.806	2.068	162	141	0.9	296
Australia	Corio Bay	-22.892	150.766	Elongated	3	309	1.80	0.38	58	4.8	31.1	6.5	4.830	0.978	412	360	0.9	296
Australia	Corio Bay	-22.817	150.782	Elongated	3	312	1.40	0.17	24	8.3	59.0	7.1	4.159	0.277	412	360	0.9	296
Australia	Corio Bay	-22.900	150.773	Lobate	5	306	0.81	0.32	44	2.6	18.4	7.2	2.265	0.293	412	360	0.9	296
Australia	Corio Bay	-22.903	150.761	Elongated	5	315	1.87	0.39	47	4.8	40.0	8.3	4.722	0.960	412	360	0.9	296
Australia	Corio Bay	-22.879	150.756	Lobate	5	311	1.05	0.38	31	2.8	34.1	12.3	3.522	0.450	412	360	0.9	296
Australia	Corio Bay	-22.869	150.744	Elongated	5	314	2.14	0.46	35	4.6	61.1	13.3	6.334	1.118	412	360	0.9	296
Australia	Corio Bay	-22.837	150.772	Lobate	2	308	1.96	0.76	43	2.6	46.0	17.8	6.935	1.268	412	360	0.9	296

Australia	Corio Bay	-22.872	150.748	Elongated	5	312	2.39	0.50	20	4.7	119.8	25.2	6.171	1.192	412	360	0.9	296
Australia	Corio Bay	-22.864	150.760	Elongated	5	308	2.92	0.89	34	3.3	86.6	26.4	7.550	2.782	412	360	0.9	296
Australia	Corio Bay	-22.819	150.747	Elongated	2	309	4.22	1.02	31	4.1	134.7	32.6	11.118	4.596	412	360	0.9	296
Australia	Curtis Island	-23.543	151.222	Elongated	3 to 5	308	1.28	0.42	55	3.1	23.3	7.6	2.986	0.469	162	141	0.9	296
Australia	Curtis Island	-23.572	151.218	Elongated	3	309	0.72	0.15	19	5.0	38.5	7.7	2.230	0.151	162	141	0.9	296
Australia	Curtis Island	-23.585	151.219	Elongated	3	312	0.73	0.16	19	4.6	39.3	8.6	2.030	0.177	162	141	0.9	296
Australia	Curtis Island	-23.532	151.210	Elongated	5	310	2.74	0.59	49	4.7	56.3	12.0	6.832	1.921	162	141	0.9	296
Australia	Curtis Island	-23.543	151.222	Lobate	3 to 5	311	3.00	1.12	77	2.7	38.9	14.5	7.228	2.530	162	141	0.9	296
Australia	Curtis Island	-23.554	151.213	Elongated	5	310	1.91	0.40	27	4.8	70.3	14.7	5.414	0.994	162	141	0.9	296
Australia	Curtis Island	-23.543	151.222	Lobate	3 to 5	312	2.12	0.75	50	2.8	42.4	15.1	5.428	1.395	162	141	0.9	296
Australia	Curtis Island	-23.566	151.214	Elongated	5	307	1.40	0.41	25	3.4	56.4	16.6	4.038	0.691	162	141	0.9	296
Australia	Curtis Island	-23.543	151.222	Lobate	3 to 5	305	1.59	0.66	35	2.4	45.4	18.8	4.024	0.891	162	141	0.9	296
Australia	Francois Peron National Park	-25.961	113.629	Elongated	5	2	20.07	4.24	53	4.7	380.3	80.4	43.251	62.863	586	493	0.8	9
Australia	Francois Peron National Park	-25.961	113.629	Elongated	5	6	25.32	6.73	46	3.8	551.1	146.4	59.354	149.940	586	493	0.8	9
Australia	Fraser Island	-24.804	153.228	Elongated	3 to 5	313	2.45	0.66	59	3.7	41.6	11.2	5.657	1.249	366	277	0.8	311
Australia	Fraser Island	-24.804	153.228	Lobate	3 to 5	313	3.78	1.35	92	2.8	41.1	14.7	9.948	4.077	366	277	0.8	311
Australia	Fraser Island	-24.804	153.228	Lobate	3 to 5	313	3.58	1.32	84	2.7	42.6	15.7	8.509	3.749	366	277	0.8	311
Australia	Fraser Island	-25.319	153.196	Lobate	5	314	1.45	0.81	50	1.8	28.9	16.2	4.480	1.272	366	277	0.8	311
Australia	Fraser Island	-24.804	153.228	Lobate	3 to 5	313	3.13	1.47	87	2.1	36.0	16.9	8.566	3.757	366	277	0.8	311
Australia	Fraser Island	-25.376	153.130	Lobate	3 to 5	317	6.40	2.49	131	2.6	48.8	19.0	16.465	12.730	366	277	0.8	311
Australia	Fraser Island	-25.376	153.130	Elongated	3 to 5	324	6.20	1.84	95	3.4	65.2	19.4	14.765	9.311	366	277	0.8	311
Australia	Fraser Island	-25.219	153.187	Elongated	3	321	4.08	1.18	58	3.4	70.4	20.4	11.649	4.926	366	277	0.8	311
Australia	Fraser Island	-24.824	153.248	Lobate	5	314	1.66	0.67	32	2.5	51.8	20.8	4.528	1.217	366	277	0.8	311
Australia	Fraser Island	-24.804	153.228	Lobate	3 to 5	322	5.84	2.10	97	2.8	60.2	21.6	14.406	10.488	366	277	0.8	311
Australia	Fraser Island	-25.376	153.130	Lobate	3 to 5	313	3.58	1.60	73	2.2	49.0	21.9	9.772	5.131	366	277	0.8	311
Australia	Fraser Island	-25.663	153.035	Lobate		313	3.39	1.14	50	3.0	67.1	22.6	12.025	3.737	366	277	0.8	311
Australia	Fraser Island	-24.811	153.202	Lobate		320	3.78	1.72	75	2.2	50.3	22.9	18.615	10.754	366	277	0.8	311
Australia	Fraser Island	-24.804	153.228	Lobate	3 to 5	309	1.45	1.43	62	1.0	23.3	23.1	6.549	2.052	366	277	0.8	311
Australia	Fraser Island	-25.376	153.130	Lobate	3 to 5	322	4.22	1.83	74	2.3	57.1	24.8	10.387	5.651	366	277	0.8	311
Australia	Fraser Island	-25.376	153.130	Lobate	3 to 5	321	6.01	2.61	105	2.3	57.3	24.9	16.657	13.655	366	277	0.8	311
Australia	Fraser Island	-24.804	153.228	Lobate	3 to 5	318	2.62	1.26	49	2.1	53.5	25.6	6.807	2.497	366	277	0.8	311
Australia	Fraser Island	-25.376	153.130	Lobate	3 to 5	318	7.88	3.61	120	2.2	65.7	30.1	20.567	19.947	366	277	0.8	311
Australia	Fraser Island	-25.376	153.130	Lobate	3 to 5	321	5.25	1.84	60	2.9	87.4	30.6	13.436	7.720	366	277	0.8	311
Australia	Fraser Island	-25.376	153.130	Lobate	3 to 5	324	4.84	2.64	85	1.8	57.0	31.0	12.846	8.668	366	277	0.8	311
Australia	Fraser Island	-24.804	153.228	Lobate	3 to 5	313	5.24	4.01	93	1.3	56.3	43.1	17.226	15.783	366	277	0.8	311
Australia	Fraser Island	-25.626	153.002	Lobate		316	5.62	3.20	57	1.8	99.5	56.6	20.439	17.510	366	277	0.8	311

Australia	Moreton Island	-27.083	153.432	Elongated	3 to 5	339	3.30	0.80	79	4.1	41.8	10.1	7.529	2.159	74	46	0.6	322
Australia	Moreton Island	-27.083	153.432	Lobate	3 to 5	324	1.98	0.79	62	2.5	31.9	12.8	5.089	1.307	74	46	0.6	322
Australia	Moreton Island	-27.083	153.432	Lobate	3 to 5	325	3.06	1.15	68	2.7	45.3	17.0	7.607	3.092	74	46	0.6	322
Australia	Ningaloo	-22.697	113.684	Lobate	5	5	0.74	0.29	22	2.6	33.0	12.8	2.037	0.237	573	481	0.8	9
Australia	Ningaloo	-22.778	113.772	Lobate	5	18	1.37	0.63	48	2.2	28.5	13.1	3.399	0.616	573	481	0.8	9
Australia	Ningaloo	-22.778	113.775	Elongated	3	13	1.50	0.34	25	4.5	60.4	13.6	3.313	0.495	573	481	0.8	9
Australia	Ningaloo	-22.703	113.683	Lobate	3	6	1.04	0.43	27	2.4	38.0	15.7	3.164	0.522	573	481	0.8	9
Australia	Ningaloo	-22.778	113.772	Lobate	5	12	1.57	0.74	47	2.1	33.4	15.8	4.538	0.908	573	481	0.8	9
Australia	Ningaloo	-22.778	113.772	Lobate	5	16	1.42	0.60	37	2.4	38.4	16.2	3.741	0.556	573	481	0.8	9
Australia	Ningaloo	-22.778	113.772	Lobate	5	17	1.54	0.55	29	2.8	53.0	19.0	3.819	0.757	573	481	0.8	9
Australia	Ningaloo	-22.761	113.766	Elongated	3	15	1.52	0.48	24	3.2	62.6	19.6	4.027	0.828	573	481	0.8	9
Australia	Ningaloo	-22.778	113.772	Lobate	5	15	0.81	0.46	23	1.8	35.1	20.0	2.328	0.337	573	481	0.8	9
Australia	Ningaloo	-22.725	113.732	Lobate	5	6	0.70	0.36	18	1.9	38.4	20.0	2.127	0.255	573	481	0.8	9
Australia	Ningaloo	-22.704	113.676	Elongated	5	7	1.40	0.41	8	3.4	169.4	49.8	3.907	0.638	573	481	0.8	9
Australia	Point Quobba	-24.571	113.509	Elongated	3	6	2.55	0.85	34	3.0	75.1	25.0	6.228	1.788	579	487	0.8	9
Australia	Point Quobba	-24.571	113.509	Lobate	3	1	1.73	0.88	35	2.0	49.3	25.1	4.469	1.028	579	487	0.8	9
Australia	Point Quobba	-24.571	113.509	Lobate	3	12	1.08	0.89	35	1.2	30.8	25.3	3.711	0.679	579	487	0.8	9
Australia	Point Quobba	-24.571	113.509	Lobate	3	1	1.98	0.84	28	2.4	70.6	30.0	4.769	1.167	579	487	0.8	9
Australia	Point Quobba	-24.571	113.509	Elongated	3	0	1.88	0.57	19	3.3	98.9	30.1	4.734	0.826	579	487	0.8	9
Australia	Point Quobba	-24.571	113.509	Elongated	3	2	1.79	0.39	12	4.7	149.3	32.1	4.663	0.551	579	487	0.8	9
Australia	Point Quobba	-24.571	113.509	Lobate	3	3	3.01	1.05	27	2.9	111.5	38.7	7.552	2.251	579	487	0.8	9
Australia	S Wide Bay	-26.088	153.102	Elongated	7	321	1.54	0.23	26	6.8	58.9	8.7	4.602	0.421	366	277	0.8	311
Australia	S Wide Bay	-26.120	153.093	Elongated		315	1.88	0.39	33	4.8	56.4	11.8	4.786	0.928	366	277	0.8	311
Australia	S Wide Bay	-25.999	153.133	Lobate	5	326	2.00	0.89	33	2.3	59.9	26.6	6.709	1.741	366	277	0.8	311
Bahamas	Acklins Island	22.306	-74.122	Lobate	5	258	1.67	0.68	21	2.5	79.8	32.5	5.192	1.351	411	296	0.7	254
Bahamas	Crooked	22.454	-73.921	Lobate	5	254	1.88	0.89	14	2.1	134.1	63.4	4.871	1.268	411	296	0.7	254
Bahamas	Exumas	23.479	-75.760	Hemicyclic	5	230	0.79	0.99	20	0.8	39.5	49.7	2.826	0.466	398	275	0.7	254
Bahamas	Exumas	23.602	-75.905	Lobate	3	242	2.05	1.01	16	2.0	127.8	63.3	5.225	1.369	398	275	0.7	254
Bahamas	Exumas	23.612	-75.933	Lobate	2	236	2.16	1.97	30	1.1	72.0	65.5	7.712	3.354	398	275	0.7	254
Bahamas	Exumas	23.612	-75.933	Lobate	5	241	3.30	1.97	23	1.7	143.3	85.5	9.328	4.332	398	275	0.7	254
Bahamas	Exumas	24.159	-76.455	Lobate	5	255	5.09	1.69	15	3.0	339.5	112.7	11.513	6.214	398	275	0.7	254
Bahamas	Great Exuma	23.601	-75.909	Lobate	3	245	1.97	0.93	33	2.1	59.1	27.9	5.589	1.530	398	275	0.7	254
Bahamas	Great Exuma	23.613	-75.934	Lobate	3	244	2.27	1.24	21	1.8	109.9	60.0	6.993	2.360	398	275	0.7	254
Bahamas	Long Island	23.500	-75.212	Lobate	5	253	0.65	0.34	19	1.9	33.7	17.4	2.202	0.315	425	317	0.7	254
Bahamas	Long Island	23.556	-75.239	Lobate	3	254	1.36	0.64	32	2.1	42.8	20.1	4.281	0.903	425	317	0.7	254

Bahamas	Long Island	23.238	-75.093	Lobate	3	245	1.23	0.42	17	2.9	72.4	24.8	3.258	0.579	425	317	0.7	254
Bahamas	Long Island	23.492	-75.215	Elongated	3	252	1.99	0.39	13	5.1	147.4	28.9	4.959	0.967	425	317	0.7	254
Bahamas	Long Island	23.493	-75.212	Elongated	5	251	1.98	0.43	14	4.7	141.7	30.4	4.462	0.728	425	317	0.7	254
Bahamas	Long Island	23.394	-75.159	Lobate	5	243	2.02	0.70	21	2.9	96.0	33.2	4.761	1.138	425	317	0.7	254
Bahamas	Long Island	23.556	-75.237	Lobate	3	253	1.51	0.74	22	2.1	68.7	33.5	3.863	0.807	425	317	0.7	254
Bahamas	Long Island	23.210	-75.100	Elongated	5	248	1.29	0.30	9	4.2	143.4	33.8	2.865	0.351	425	317	0.7	254
Bahamas	Long Island	23.417	-75.180	Elongated	5	249	2.97	0.73	19	4.1	156.2	38.2	6.637	1.662	425	317	0.7	254
Bahamas	Long Island	23.210	-75.100	Elongated	5	249	3.02	0.64	13	4.7	232.2	49.2	6.476	1.520	425	317	0.7	254
Bahamas	Long Island	23.209	-75.105	Elongated	5	250	2.98	0.56	11	5.3	281.8	53.3	6.732	1.754	425	317	0.7	254
Bahamas	Long Island	23.394	-75.160	Elongated	5	251	1.73	0.55	10	3.2	178.7	56.4	4.267	1.015	425	317	0.7	254
Bahamas	Long Island	23.390	-75.149	Lobate	5	254	0.44	0.43	7	1.0	62.3	60.0	1.647	0.180	425	317	0.7	254
Bahamas	Long Island	23.385	-75.148	Lobate	5	249	0.83	0.49	7	1.7	127.5	74.8	2.689	0.413	425	317	0.7	254
Brazil	Fortaleza	-3.955	-38.282	Elongated	3	284	1.32	0.35	90	3.8	14.7	3.9	3.899	0.671	55	54	1.0	281
Brazil	Fortaleza	-3.975	-38.276	Elongated	3	282	1.80	0.39	64	4.7	28.0	6.0	5.055	1.139	55	54	1.0	281
Brazil	Fortaleza	-3.842	-38.410	Lobate	2	290	0.65	0.35	43	1.8	15.0	8.1	2.624	0.370	55	54	1.0	281
Brazil	Fortaleza	-3.925	-38.344	Lobate	3	284	0.49	0.27	28	1.8	17.4	9.4	1.419	0.139	55	54	1.0	281
Denmark	Blåvand	55.563	8.180	Elongated		103	1.62	0.32	15	5.1	107.5	21.0	4.020	0.553	1005	518	0.5	71
Denmark	Blåvand	55.563	8.180	Lobate	5	91	0.98	0.56	17	1.8	56.6	32.1	2.806	0.440	1005	518	0.5	71
Denmark	Blåvand	55.563	8.180	Lobate	2	112	1.01	0.58	16	1.7	63.6	36.5	2.979	0.574	1005	518	0.5	71
Denmark	Blåvand	55.563	8.180	Lobate	5	94	0.32	0.27	7	1.2	43.5	37.0	1.153	0.092	1005	518	0.5	71
Lybia	Marsa el Brega	30.588	19.877	Lobate	3	115	1.28	0.69	38	1.9	34.2	18.3	0.778	4.224	153	78	0.5	121
Lybia	Marsa el Brega	30.654	19.961	Lobate	5	127	1.25	0.66	35	1.9	35.9	19.0	3.739	0.840	153	78	0.5	121
Lybia	Marsa el Brega	30.768	20.035	Lobate	3	137	1.12	0.53	24	2.1	45.6	21.4	3.214	0.639	153	78	0.5	121
Lybia	Marsa el Brega	30.549	19.827	Lobate	3	137	1.77	0.79	33	2.2	53.5	23.9	6.018	1.597	153	78	0.5	121
Lybia	Marsa el Brega	30.561	19.849	Lobate	3	118	0.99	0.63	25	1.6	39.1	24.8	3.100	0.574	153	78	0.5	121
Lybia	Marsa el Brega	30.782	20.030	Lobate	3	123	1.59	0.54	22	3.0	73.8	24.9	4.732	0.933	153	78	0.5	121
Lybia	Marsa el Brega	30.851	20.119	Lobate	3	109	0.97	0.74	27	1.3	35.6	27.3	3.529	0.757	153	78	0.5	121
Lybia	Marsa el Brega	30.613	19.932	Elongated	3	113	2.27	0.67	19	3.4	119.6	35.2	5.747	1.622	153	78	0.5	121
Lybia	Marsa el Brega	30.577	19.936	Lobate	3	120	2.32	0.94	19	2.5	120.2	48.7	6.527	2.318	153	78	0.5	121
Madagascar	Ampalaza	-25.085	44.275	Lobate	3	325	0.61	0.28	27	2.2	22.3	10.2	1.919	0.199	662	580	0.9	293
Madagascar	Ampalaza	-25.085	44.275	Lobate	3	330	0.98	0.41	39	2.4	25.1	10.4	2.951	0.467	662	580	0.9	293
Madagascar	Ampalaza	-25.085	44.275	Lobate	3	328	0.73	0.29	26	2.5	28.2	11.2	2.333	0.260	662	580	0.9	293

Madagascar	Ampalaza	-25.085	44.275	Lobate	3	329	1.07	0.51	34	2.1	31.5	15.1	2.755	0.484	662	580	0.9	293
Madagascar	Ampalaza	-25.034	44.187	Elongated	3	318	2.44	0.73	46	3.3	52.9	15.8	5.982	1.798	662	580	0.9	293
Madagascar	Ampalaza	-25.034	44.187	Lobate	5	336	1.29	0.56	32	2.3	40.3	17.3	3.649	0.746	662	580	0.9	293
Madagascar	Ampalaza	-25.085	44.275	Lobate	2	326	0.86	0.41	21	2.1	40.7	19.2	2.510	0.367	662	580	0.9	293
Madagascar	Ampalaza	-25.034	44.187	Elongated	5	318	1.67	0.49	25	3.4	66.8	19.5	4.143	0.787	662	580	0.9	293
Madagascar	Ampalaza	-25.034	44.187	Lobate	5	337	1.51	0.57	29	2.7	51.9	19.6	3.751	0.554	662	580	0.9	293
Madagascar	Ampalaza	-25.034	44.187	Lobate	2	340	1.10	0.96	47	1.1	23.3	20.5	6.712	1.325	662	580	0.9	293
Madagascar	Ampalaza	-25.034	44.187	Elongated	5	339	2.20	0.56	27	3.9	81.6	20.7	4.018	0.632	662	580	0.9	293
Madagascar	Ampalaza	-25.085	44.275	Lobate	3	307	0.65	0.43	19	1.5	33.8	22.5	2.674	0.401	662	580	0.9	293
Madagascar	Ampalaza	-25.034	44.187	Lobate	3	317	0.64	0.55	24	1.2	26.8	22.9	2.020	0.235	662	580	0.9	293
Madagascar	Ampalaza	-25.034	44.187	Elongated	5	325	5.11	1.27	54	4.0	94.6	23.5	12.114	2.341	662	580	0.9	293
Madagascar	Ampalaza	-25.085	44.275	Lobate	2	317	1.08	0.48	20	2.3	53.6	23.7	3.839	0.659	662	580	0.9	293
Madagascar	Ampalaza	-25.034	44.187	Hemicyclic	3	336	0.64	0.76	30	0.8	21.2	25.4	2.430	0.382	662	580	0.9	293
Madagascar	Ampalaza	-25.034	44.187	Lobate	5	331	1.66	0.74	29	2.2	57.2	25.4	4.090	0.756	662	580	0.9	293
Madagascar	Ampalaza	-25.034	44.187	Hemicyclic	3	324	0.91	0.97	38	0.9	24.0	25.5	3.242	0.677	662	580	0.9	293
Madagascar	Ampalaza	-25.034	44.187	Lobate	3	329	0.97	0.88	34	1.1	28.6	26.0	2.954	0.529	662	580	0.9	293
Madagascar	Ampalaza	-25.034	44.187	Lobate	3	334	1.43	1.10	41	1.3	34.9	26.9	4.724	0.952	662	580	0.9	293
Madagascar	Ampalaza	-25.085	44.275	Lobate	2	324	0.93	0.77	23	1.2	39.6	32.8	3.506	0.730	662	580	0.9	293
Madagascar	Ampalaza	-25.034	44.187	Lobate	3	329	4.30	1.59	48	2.7	89.5	33.1	10.695	3.747	662	580	0.9	293
Madagascar	Ampalaza	-25.034	44.187	Lobate	2	324	1.53	1.15	33	1.3	46.4	34.8	4.901	1.365	662	580	0.9	293
Madagascar	Ampalaza	-25.034	44.187	Lobate	3	325	3.52	1.92	48	1.8	73.3	40.0	10.365	5.221	662	580	0.9	293
Madagascar	Ampalaza	-25.034	44.187	Lobate	3	328	1.41	1.32	31	1.1	45.6	42.6	4.859	1.470	662	580	0.9	293
Madagascar	Fenambosy	-25.246	44.638	Lobate	3	322	0.76	0.41	52	1.9	14.7	7.9	2.241	0.255	469	410	0.9	287
Madagascar	Fenambosy	-25.246	44.638	Lobate	3	318	1.07	0.47	59	2.3	18.1	7.9	3.985	0.530	469	410	0.9	287
Madagascar	Fenambosy	-25.240	44.622	Lobate	3	319	0.92	0.37	30	2.5	30.9	12.3	2.709	0.337	469	410	0.9	287
Madagascar	Fenambosy	-25.240	44.622	Lobate	5	307	0.72	0.33	25	2.2	29.5	13.6	2.374	0.278	469	410	0.9	287
Madagascar	Fenambosy	-25.246	44.638	Lobate	3	319	0.67	0.63	46	1.1	14.6	13.8	2.364	0.331	469	410	0.9	287
Madagascar	Fenambosy	-25.246	44.638	Lobate	3	312	1.01	0.51	33	2.0	30.5	15.3	2.773	0.439	469	410	0.9	287
Madagascar	Fenambosy	-25.240	44.622	Lobate	3	317	0.86	0.29	19	3.0	46.4	15.5	2.422	0.303	469	410	0.9	287
Madagascar	Fenambosy	-25.246	44.638	Lobate	3	317	0.68	0.70	45	1.0	15.1	15.5	2.507	0.410	469	410	0.9	287
Madagascar	Fenambosy	-25.240	44.622	Lobate	3	304	1.08	0.39	25	2.8	43.4	15.5	3.075	0.455	469	410	0.9	287
Madagascar	Fenambosy	-25.246	44.638	Lobate	3	317	0.90	0.68	43	1.3	20.8	15.7	3.019	0.551	469	410	0.9	287
Madagascar	Fenambosy	-25.246	44.638	Elongated	3	298	17.20	3.10	183	5.6	94.0	16.9	38.871	45.371	469	410	0.9	287
Madagascar	Fenambosy	-25.246	44.638	Elongated	3	315	2.24	0.71	41	3.2	54.5	17.2	5.416	1.200	469	410	0.9	287
Madagascar	Fenambosy	-25.246	44.638	Lobate	3	311	0.63	0.59	32	1.1	19.7	18.6	2.187	0.342	469	410	0.9	287
Madagascar	Fenambosy	-25.246	44.638	Lobate	3	316	1.14	0.80	43	1.4	26.6	18.6	3.347	0.619	469	410	0.9	287

Madagascar	Fenambosy	-25.246	44.638	Lobate	3	312	0.67	0.36	18	1.9	37.4	20.2	2.577	0.265	469	410	0.9	287
Madagascar	Fenambosy	-25.246	44.638	Lobate	3	316	1.21	0.78	38	1.6	31.9	20.4	3.395	0.629	469	410	0.9	287
Madagascar	Fenambosy	-25.240	44.622	Lobate	5	309	0.80	0.57	28	1.4	28.6	20.4	3.150	0.528	469	410	0.9	287
Madagascar	Fenambosy	-25.246	44.638	Lobate	3	315	1.45	0.83	40	1.7	36.3	20.8	5.886	1.274	469	410	0.9	287
Netherlands	Ijmuiden	52.431	4.583	Lobate		60	0.41	0.20	18	2.0	23.3	11.5	1.646	0.126	1024	609	0.6	63
Scotland	Newburgh	57.329	-1.981	Lobate	3	30	0.19	0.14	15	1.4	12.9	9.1	0.730	0.029	1312	547	0.4	57
Scotland	Newburgh	57.329	-1.981	Hemicyclic	1	66	0.16	0.18	12	0.9	13.3	14.8	0.765	0.033	1312	547	0.4	57
Spain	Mallorca	39.715	3.211	Lobate		187	0.28	0.12	14	2.4	20.9	8.9	0.856	0.040	357	155	0.4	161
Spain	Mallorca	39.704	3.206	Lobate		180	0.49	0.21	17	2.3	29.1	12.5	1.458	0.125	357	155	0.4	161
Spain	Mallorca	39.700	3.214	Lobate		193	0.31	0.20	15	1.6	20.4	13.0	1.001	0.063	357	155	0.4	161
Spain	Mallorca	39.720	3.226	Lobate		187	0.20	0.12	8	1.7	24.6	14.5	0.654	0.025	357	155	0.4	161
Spain	Mallorca	39.720	3.210	Lobate		195	0.33	0.25	9	1.3	34.8	27.0	1.177	0.082	357	155	0.4	161
Spain	Suances	43.445	-3.972	Lobate	3	88	0.15	0.11	19	1.4	8.1	5.8	0.611	0.022	235	149	0.6	161
Spain	Suances	43.445	-3.969	Lobate		107	0.20	0.18	14	1.1	13.9	12.5	0.846	0.047	235	149	0.6	161
Spain	Suances	43.447	-3.967	Lobate	5	96	0.22	0.13	8	1.6	27.3	16.6	0.734	0.033	235	149	0.6	161
USA	Bromela	35.039	-120.614	Lobate	5	122	0.57	0.30	33	1.9	17.4	9.1	1.502	0.134	24	8	0.3	42
USA	Bromela	35.014	-120.614	Elongated	5	121	1.94	0.33	32	6.0	59.9	10.0	4.302	0.564	24	8	0.3	42
USA	Bromela	35.014	-120.614	Lobate	5	120	0.85	0.50	44	1.7	19.3	11.3	2.318	0.315	24	8	0.3	42
USA	Bromela	35.033	-120.623	Lobate	3	123	0.54	0.26	22	2.1	24.3	11.5	1.449	0.108	24	8	0.3	42
USA	Bromela	35.014	-120.614	Lobate	5	112	0.98	0.38	30	2.6	32.7	12.5	2.637	0.300	24	8	0.3	42
USA	Bromela	35.014	-120.614	Lobate	3	116	1.03	0.44	31	2.3	33.7	14.5	2.519	0.328	24	8	0.3	42
USA	Bromela	35.014	-120.614	Lobate	3	121	0.80	0.60	33	1.3	24.1	18.1	3.586	0.418	24	8	0.3	42
USA	Bromela	35.014	-120.614	Elongated	5	119	2.49	0.64	34	3.9	74.2	19.1	6.934	1.496	24	8	0.3	42
USA	Bromela	35.062	-120.609	Elongated	5	106	2.24	0.60	30	3.7	73.9	19.9	5.134	0.993	24	8	0.3	42
USA	Bromela	35.014	-120.614	Lobate	2	128	1.10	0.53	23	2.1	47.0	22.6	2.917	0.469	24	8	0.3	42
USA	Bromela	35.014	-120.614	Elongated	5	119	2.28	0.69	30	3.3	75.4	22.9	5.479	0.960	24	8	0.3	42
USA	Bromela	35.081	-120.610	Lobate	3	106	1.63	0.61	25	2.7	66.2	24.9	4.413	0.868	24	8	0.3	42
USA	Bromela	35.014	-120.614	Lobate	2	129	1.01	0.78	31	1.3	32.4	25.0	3.569	0.723	24	8	0.3	42
USA	Cape Cod	42.073	-70.184	Lobate	3	109	0.30	0.13	5	2.3	65.7	28.3	0.922	0.048	1304	468	0.4	111
USA	Cape Cod	42.073	-70.184	Lobate	5	112	0.40	0.24	4	1.6	90.0	54.6	1.387	0.107	1304	468	0.4	111
USA	Cape Cod	42.073	-70.184	Lobate	5	116	0.44	0.39	5	1.1	89.7	78.0	1.663	0.170	1304	468	0.4	111
USA	Cape Cod	42.073	-70.184	Lobate	5	123	0.67	0.43	6	1.5	121.1	78.4	2.150	0.286	1304	468	0.4	111
USA	Coos Bay	43.444	-124.252	Lobate		174	0.33	0.12	8	2.7	41.8	15.6	0.984	0.054	22	20	0.9	12
USA	Coos Bay	43.482	-124.238	Elongated		172	0.53	0.17	5	3.1	96.5	30.8	1.599	0.108	22	20	0.9	12
USA	Coos Bay	43.496	-124.236	Lobate		173	0.73	0.34	8	2.1	91.2	42.9	2.257	0.258	22	20	0.9	12
USA	Eureka	40.834	-124.178	Lobate	3	162	0.32	0.11	4	3.0	80.6	26.9	0.993	0.043	148	18	0.1	189
USA	Eureka	40.834	-124.178	Elongated	3	167	0.40	0.12	4	3.2	96.7	30.4	1.068	0.054	148	18	0.1	189

USA	Eureka	40.834	-124.178	Lobate	3	156	0.54	0.32	8	1.7	69.0	40.6	1.634	0.131	148	18	0.1	189
USA	Grand Marais	46.679	-85.922			136	0.25	0.12	23	2.1	10.7	5.1	0.793	0.035	145	73	0.5	118
USA	Grand Marais	46.677	-85.894			132	0.32	0.15	24	2.2	13.7	6.3	0.970	0.061	145	73	0.5	118
USA	Grand Marais	46.658	-86.050			132	0.26	0.13	19	2.0	13.4	6.7	0.893	0.041	145	73	0.5	118
USA	Grand Marais	46.680	-85.931			135	0.29	0.13	19	2.2	14.7	6.8	0.884	0.041	145	73	0.5	118
USA	Grand Marais	46.682	-85.921			122	0.27	0.12	16	2.2	17.0	7.7	0.732	0.033	145	73	0.5	118
USA	Grand Marais	46.678	-85.904			126	0.27	0.11	13	2.4	21.1	8.8	0.738	0.035	145	73	0.5	118
USA	Grand Marais	46.675	-85.872			130	0.45	0.25	25	1.8	17.8	9.8	1.268	0.109	145	73	0.5	118
USA	Grand Marais	46.681	-85.924			137	0.29	0.19	16	1.5	18.4	12.4	0.941	0.054	145	73	0.5	118
USA	Grand Marais	46.680	-85.894			118	0.26	0.14	10	1.8	24.7	13.9	0.791	0.039	145	73	0.5	118
USA	Grand Marais	46.686	-85.895			123	0.34	0.24	16	1.4	21.8	15.1	1.199	0.087	145	73	0.5	118
USA	Grand Marais	46.684	-85.885			120	0.54	0.41	22	1.3	25.0	18.6	1.964	0.255	145	73	0.5	118
USA	Grand Marais	46.685	-85.880			117	0.40	0.32	16	1.3	24.8	19.8	1.425	0.133	145	73	0.5	118
USA	Great Sand Dunes	37.707	-105.581	Elongated		34	0.26	0.06	8	4.6	31.9	6.9	0.692	0.018	19	17	0.9	72
USA	Great Sand Dunes	37.705	-105.571	Elongated		31	0.14	0.04	6	3.3	23.8	7.3	0.367	0.008	19	17	0.9	72
USA	Great Sand Dunes	37.703	-105.575	Lobate		35	0.25	0.09	12	2.8	21.1	7.4	0.658	0.021	19	17	0.9	72
USA	Great Sand Dunes	37.716	-105.582	Lobate		35	0.23	0.08	11	2.9	21.3	7.5	0.702	0.027	19	17	0.9	72
USA	Great Sand Dunes	37.690	-105.573	Elongated		29	0.21	0.06	8	3.4	26.2	7.6	0.632	0.015	19	17	0.9	72
USA	Great Sand Dunes	37.706	-105.579	Lobate		35	0.14	0.06	8	2.1	17.1	8.1	0.457	0.011	19	17	0.9	72
USA	Great Sand Dunes	37.691	-105.573	Lobate		38	0.13	0.05	6	2.5	21.0	8.5	0.360	0.007	19	17	0.9	72
USA	Great Sand Dunes	37.719	-105.584	Lobate		36	0.34	0.16	12	2.1	28.0	13.3	1.070	0.059	19	17	0.9	72
USA	Great Sand Dunes	37.698	-105.584	Elongated		35	0.63	0.16	9	3.9	69.7	17.8	1.958	0.102	19	17	0.9	72
USA	Great Sand Dunes	37.693	-105.587	Elongated		29	0.77	0.23	11	3.3	69.8	21.2	1.898	0.158	19	17	0.9	72
USA	Great Sand Dunes	37.700	-105.601	Lobate		33	0.49	0.41	15	1.2	32.6	27.3	1.789	0.176	19	17	0.9	72
USA	Hanford	46.381	-119.321	Hemicyclic		73	0.17	0.21	13	0.8	13.4	16.2	0.745	0.035	23	10	0.4	50
USA	Hanford	46.381	-119.321	Lobate		58	0.27	0.16	9	1.7	31.3	18.5	0.905	0.054	23	10	0.4	50
USA	Hanford	46.381	-119.321	Lobate		69	0.42	0.23	12	1.8	35.2	19.1	1.439	0.103	23	10	0.4	50

USA	Hanford	46.381	-119.321	Lobate		72	0.39	0.18	9	2.1	43.7	20.4	1.099	0.072	23	10	0.4	50
USA	Hanford	46.381	-119.321	Hemicyclic		88	0.23	0.28	8	0.8	27.9	33.2	0.986	0.063	23	10	0.4	50
USA	Holland	42.759	-86.204	Lobate	3	79	0.16	0.07	47	2.3	3.5	1.5	0.602	0.020	23	10	0.4	50
USA	Holland	42.759	-86.204	Lobate	3	80	0.31	0.11	49	2.8	6.3	2.2	0.852	0.040	23	10	0.4	50
USA	Holland	42.759	-86.204	Lobate	3	81	0.27	0.11	44	2.6	6.2	2.4	0.815	0.041	23	10	0.4	50
USA	Holland	42.759	-86.204	Lobate	3	63	0.36	0.12	37	2.9	9.5	3.3	1.055	0.068	23	10	0.4	50
USA	Holland	42.759	-86.204	Lobate	3	73	0.44	0.20	54	2.2	8.2	3.7	1.538	0.099	23	10	0.4	50
USA	Holland	42.759	-86.204	Lobate		75	0.43	0.21	45	2.1	9.4	4.5	1.408	0.102	23	10	0.4	50
USA	Lompoc	34.803	-120.590	Elongated	5	121	0.40	0.11	7	3.6	61.2	16.8	1.023	0.057	24	8	0.3	50
USA	Lompoc	34.803	-120.590	Elongated	3	102	0.47	0.14	8	3.3	57.9	17.6	1.271	0.082	24	8	0.3	50
USA	Lompoc	34.803	-120.590	Lobate	5	114	0.44	0.15	7	2.9	62.2	21.7	1.213	0.084	24	8	0.3	50
USA	Lompoc	34.803	-120.590	Elongated	3	107	2.04	0.38	11	5.4	192.4	35.5	4.970	0.835	24	8	0.3	50
USA	Manila	40.895	-124.146	Lobate	5	159	0.55	0.22	17	2.5	32.9	13.3	1.465	0.103	148	18	0.1	189
USA	Manila	40.902	-124.140	Lobate	5	163	0.46	0.28	16	1.6	27.7	17.0	1.327	0.106	148	18	0.1	189
USA	Manila	40.855	-124.164	Hemicyclic	5	148	0.23	0.38	9	0.6	26.3	43.0	1.188	0.081	148	18	0.1	189
USA	Marina	36.693	-121.809	Lobate	5	133	0.44	0.23	33	1.9	13.1	7.0	1.189	0.091	148	18	0.1	189
USA	Marina	36.693	-121.809	Lobate	5	116	0.46	0.31	39	1.5	11.9	8.0	1.534	0.123	148	18	0.1	189
USA	Marina	36.693	-121.809	Lobate	5	108	0.55	0.25	28	2.3	19.6	8.7	1.406	0.112	148	18	0.1	189
USA	Marina	36.693	-121.809	Lobate	5	103	0.54	0.27	27	2.0	19.7	9.8	1.353	0.104	148	18	0.1	189
USA	Marina	36.693	-121.809	Lobate	5	113	0.51	0.22	21	2.4	24.5	10.4	1.535	0.104	148	18	0.1	189
USA	Marina	36.693	-121.809	Lobate	5	112	0.53	0.47	28	1.1	18.8	16.9	1.722	0.206	148	18	0.1	189
USA	New York	41.013	-72.038	Lobate	3	119	0.20	0.08	4	2.5	47.2	18.6	0.627	0.017	593	235	0.4	119
USA	New York	41.013	-72.036	Lobate	3	115	0.34	0.12	4	3.0	83.9	28.3	1.175	0.056	593	235	0.4	119
USA	New York	41.008	-72.029	Lobate	5	132	0.73	0.57	8	1.3	87.0	67.7	2.474	0.368	593	235	0.4	119
USA	P.J. Hoffmaster	43.131	-86.274	Lobate		76	0.35	0.14	65	2.5	5.4	2.1	1.398	0.087	356	156	0.4	119
USA	P.J. Hoffmaster	43.131	-86.274	Lobate		69	0.34	0.15	56	2.3	6.1	2.7	1.144	0.068	356	156	0.4	119
USA	P.J. Hoffmaster	43.131	-86.274	Elongated		82	0.50	0.17	57	3.0	8.8	2.9	1.677	0.125	356	156	0.4	119
USA	Pacific City	45.310	-123.950	Elongated	5	21	2.86	0.92	47	3.1	60.5	19.4	6.886	2.082	1.3	1	0.9	18
USA	Pacific City	45.310	-123.950	Lobate	5	27	4.15	1.72	31	2.4	134.9	55.9	11.288	6.215	1.3	1	0.9	18
USA	Petoskey	45.408	-84.908	Elongated	3	96	0.23	0.05	41	4.3	5.5	1.3	0.642	0.017	100	54	0.5	82
USA	Petoskey	45.408	-84.908	Lobate	3	81	0.18	0.06	5	2.9	36.9	12.6	0.640	0.019	100	54	0.5	82
USA	Point Reyes Beach North	38.093	-122.964	Lobate	3	131	0.27	0.11	21	2.4	13.2	5.5	0.765	0.027	7.2	3	0.4	66

USA	Point Reyes Beach North	38.100	-122.961	Lobate	5	129	0.96	0.33	38	2.9	25.5	8.8	2.397	0.280	7.2	3	0.4	66
USA	Point Reyes Seashore	38.094	-122.966	Elongated	5	128	0.85	0.12	14	7.2	60.7	8.4	2.007	0.131	7.2	3	0.4	66
USA	Point Reyes Seashore	38.094	-122.966	Elongated	5	128	0.43	0.11	11	3.9	40.2	10.2	1.134	0.052	7.2	3	0.4	66
USA	Point Reyes Seashore	38.094	-122.966	Elongated	5	129	0.48	0.07	2	6.5	208.8	32.1	1.085	0.042	7.2	3	0.4	66
USA	Sand Lake	45.306	-123.954	Lobate		23	0.92	0.33	13	2.8	70.8	25.3	2.453	0.284	1.3	1	0.9	18
USA	Sand Lake	45.324	-123.941	Lobate		30	3.54	1.35	15	2.6	238.7	90.9	11.372	5.949	1.3	1	0.9	18
USA	Sand Lake	45.317	-123.948	Elongated		20	2.93	0.56	5	5.2	545.7	104.4	6.775	1.536	1.3	1	0.9	18
USA	Savannah River Valley	32.517	-81.213	Elongated		92	0.63	0.13	1	4.8	441.2	92.6	1.586	0.119	0.3	0	0.9	48
USA	Savannah River Valley	32.517	-81.213	Lobate		80	0.54	0.30	3	1.8	197.2	110.7	1.851	0.205	0.3	0	0.9	48
USA	Savannah River Valley	32.517	-81.213	Lobate		88	0.56	0.26	2	2.1	352.9	164.5	1.523	0.138	0.3	0	0.9	48
USA	Savannah River Valley	32.517	-81.213	Elongated		92	1.43	0.34	2	4.2	779.6	185.7	3.429	0.534	0.3	0	0.9	48
USA	Savannah River Valley	32.517	-81.213	Lobate		82	0.85	0.45	2	1.9	524.6	279.5	2.559	0.350	0.3	0	0.9	48
USA	Siuslaw River North	44.074	-124.111	Lobate		155	0.57	0.20	7	2.8	81.4	29.1	1.735	0.119	102	83	0.8	20
USA	Siuslaw River North	44.067	-124.111	Lobate		151	0.87	0.37	9	2.3	98.1	42.1	2.564	0.371	102	83	0.8	20
USA	Siuslaw River North	44.037	-124.115	Lobate		157	1.37	1.03	6	1.3	244.3	183.5	5.330	1.457	102	83	0.8	20
USA	Umpqua River North	43.791	-124.159	Elongated		170	0.63	0.14	26	4.5	24.6	5.5	1.869	0.170	22	20	0.9	12
USA	Umpqua River North	43.796	-124.152	Elongated		157	0.49	0.16	19	3.1	26.1	8.5	1.727	0.147	22	20	0.9	12
USA	Umpqua River North	43.791	-124.154	Elongated		152	0.88	0.25	25	3.5	35.4	10.0	2.307	0.286	22	20	0.9	12
USA	Umpqua River South	43.596	-124.184	Hemicyclic		31	0.66	0.86	9	0.8	76.2	99.9	2.859	0.283	22	20	0.9	12
USA	Van Buren	42.335	-86.304	Lobate	5	69	0.41	0.29	7	1.4	57.6	40.9	1.480	0.125	313	153	0.5	74
USA	Van Buren	42.335	-86.304	Lobate	3	68	0.34	0.18	4	1.9	84.4	44.5	1.087	0.066	313	153	0.5	74
USA	Warren Dunes	41.913	-86.588	Elongated	3	97	0.40	0.13	69	3.0	5.8	1.9	1.309	0.087	275	128	0.5	73
USA	Warren Dunes	41.913	-86.588	Lobate	3	73	0.40	0.15	54	2.6	7.5	2.8	1.216	0.083	275	128	0.5	73

USA	Warren Dunes	41.913	-86.588	Elongated	3	74	0.50	0.15	50	3.4	10.0	2.9	1.559	0.116	275	128	0.5	73
USA	Warren Dunes	41.913	-86.588	Lobate	2	82	0.21	0.08	21	2.5	10.2	4.0	0.626	0.024	275	128	0.5	73
USA	Warren Dunes	41.913	-86.588	Elongated	3	81	0.61	0.12	30	5.0	20.4	4.1	1.683	0.115	275	128	0.5	73
USA	Warren Dunes	41.913	-86.588	Lobate	2	88	0.35	0.16	37	2.3	9.4	4.2	1.040	0.076	275	128	0.5	73
USA	Warren Dunes	41.913	-86.588	Lobate	3	92	0.44	0.15	35	3.0	12.9	4.3	1.332	0.086	275	128	0.5	73
USA	White Sands	32.863	-106.193	Lobate	3	63	0.19	0.09	8	2.1	23.5	11.3	0.579	0.016	12	8	0.6	53
USA	White Sands	32.863	-106.193	Lobate	3	49	0.31	0.16	12	1.9	25.5	13.5	0.913	0.046	12	8	0.6	53
USA	White Sands	32.863	-106.193	Lobate	3	61	0.26	0.14	10	1.9	25.8	13.5	0.722	0.026	12	8	0.6	53
USA	White Sands	32.863	-106.193	Lobate	3	60	0.22	0.11	8	2.0	27.4	13.9	0.693	0.022	12	8	0.6	53
USA	White Sands	32.863	-106.193	Lobate	3	59	0.17	0.13	9	1.4	19.3	13.9	0.608	0.019	12	8	0.6	53
USA	White Sands	32.863	-106.193	Lobate	3	54	0.29	0.18	12	1.6	24.0	14.7	0.805	0.036	12	8	0.6	53
USA	White Sands	32.863	-106.193	Lobate	3	59	0.21	0.11	7	2.0	30.1	15.0	0.605	0.019	12	8	0.6	53
USA	White Sands	32.863	-106.193	Hemicyclic	3	66	0.19	0.20	12	1.0	15.9	16.4	0.689	0.030	12	8	0.6	53
USA	White Sands	32.863	-106.193	Lobate	3	60	0.24	0.15	9	1.6	26.9	16.8	0.699	0.031	12	8	0.6	53
USA	White Sands	32.863	-106.193	Lobate	3	62	0.23	0.16	9	1.4	25.8	18.0	0.733	0.034	12	8	0.6	53
USA	White Sands	32.863	-106.193	Lobate	3	58	0.33	0.15	8	2.2	40.6	18.1	0.872	0.040	12	8	0.6	53
USA	White Sands	32.863	-106.193	Lobate	3	57	0.25	0.19	10	1.3	24.5	19.1	0.914	0.046	12	8	0.6	53
USA	White Sands	32.863	-106.193	Lobate	3	67	0.32	0.20	10	1.6	32.4	19.8	0.928	0.053	12	8	0.6	53
USA	White Sands	32.863	-106.193	Lobate	3	69	0.18	0.14	7	1.3	26.1	20.3	0.568	0.020	12	8	0.6	53
USA	White Sands	32.863	-106.193	Lobate	3	59	0.19	0.14	7	1.4	27.4	20.3	0.641	0.021	12	8	0.6	53
USA	White Sands	32.863	-106.193	Lobate	3	66	0.41	0.22	11	1.8	37.3	20.4	1.116	0.072	12	8	0.6	53
USA	White Sands	32.863	-106.193	Lobate	3	56	0.23	0.13	6	1.7	38.0	21.8	0.689	0.024	12	8	0.6	53
USA	White Sands	32.863	-106.193	Lobate	3	59	0.26	0.18	8	1.5	32.8	22.0	0.720	0.030	12	8	0.6	53
USA	White Sands	32.863	-106.193	Lobate	3	57	0.39	0.22	10	1.8	39.1	22.1	1.090	0.070	12	8	0.6	53
USA	White Sands	32.863	-106.193	Lobate	3	53	0.34	0.23	10	1.5	33.7	22.6	0.989	0.063	12	8	0.6	53
USA	White Sands	32.863	-106.193	Lobate	3	57	0.27	0.23	10	1.1	26.5	23.2	0.832	0.044	12	8	0.6	53
USA	White Sands	32.863	-106.193	Hemicyclic	3	62	0.17	0.19	8	0.9	21.5	24.0	0.551	0.020	12	8	0.6	53
USA	White Sands	32.863	-106.193	Lobate	3	59	0.33	0.28	11	1.2	29.9	25.3	1.062	0.075	12	8	0.6	53
USA	White Sands	32.863	-106.193	Lobate	3	57	0.37	0.26	10	1.4	36.8	26.3	1.122	0.077	12	8	0.6	53
USA	White Sands	32.863	-106.193	Lobate	3	48	0.39	0.22	8	1.8	49.0	26.9	1.238	0.079	12	8	0.6	53
USA	White Sands	32.863	-106.193	Lobate	3	57	0.36	0.26	9	1.4	40.4	28.6	1.076	0.068	12	8	0.6	53
USA	White Sands	32.863	-106.193	Lobate	3	60	0.34	0.33	11	1.0	31.0	29.6	1.151	0.079	12	8	0.6	53
Wales	Newborough	53.142	-4.366	Lobate	5	22	0.12	0.06	14	2.1	8.8	4.3	0.467	0.008	1181	770	0.7	53
Wales	Newborough	53.142	-4.366	Elongated	3	24	0.15	0.04	9	3.3	15.9	4.8	0.410	0.008	1181	770	0.7	53
Wales	Newborough	53.142	-4.366	Elongated	3	22	0.15	0.04	8	3.3	18.3	5.5	0.405	0.008	1181	770	0.7	53
Wales	Newborough	53.142	-4.366	Lobate		53	0.10	0.08	13	1.3	7.6	5.9	0.378	0.008	1181	770	0.7	53

Wales	Newborough	53.142	-4.366	Lobate		23	0.14	0.08	8	1.8	17.0	9.5	0.460	0.011	1181	770	0.7	53
Wales	Newborough	53.142	-4.366	Lobate	3	25	0.11	0.05	5	2.2	24.4	11.3	0.382	0.008	1181	770	0.7	53